CIVIL ENGINEERING JOURNAL

číslo 4/2022

Obsah:

CIVIL ENGINEERING JOURNAL

Article no. 39

THE CIVIL ENGINEERING JOURNAL 4-2022

STABILITY DETERIORATION OF CLIFF FACES DUE TO HISTORICAL MINING IN THE ELBE SANDSTONES PROTECTED AREA

Zuzana Vařilová[1], Kamil Podroužek[2], Natálie Belisová[1] and Jan Horák[2]

1. *Municipal Museum of Ústí nad Labem, Masarykova 1000/3, 40001 Ústí nad Labem, Czech Republic; varilova@muzeumusti.cz*
2. *Faculty of Arts of Jan Evangelista Purkyně University in Ústí nad Labem, Pasteurova 13, 400 96 Ústí nad Labem, Czech Republic; kamil.podrouzek@ujep.cz*

ABSTRACT

The paper is a methodological study for registering abandoned mining sites and for the assessment of stability of artificial sandstone outcrops. The study presents partial results of the expert cooperation between geologists and historians in the Bohemian Switzerland (Elbe Sandstones) area focused on mapping and documentation of old quarries and mining pits. More than three thousand abandoned quarries for building stone were newly mapped and registered within the study area. Attention was given not only to the preserved relics after mining and their historical context: methods of stone extraction were also described, and the current state of quarries and mining areas was documented. Many of them represent unstable quarry faces prone to rockfall. The present survey and documentation of old quarries identified hitherto unknown sites of potential hazard, where old quarry faces or their parts are endangered by rockfall and can represent a potential risk in populated or tourist-visited areas (e.g., the Elbe River canyon between Děčín and the state border, Suchá Kamenice River valley, Rabštejnské údolí Valley, Kvádrberk Hill, Děčín–Podmokly, Děčín–Dolní Oldřichov, Ludvíkovice and Janská areas, Pekelský důl Valley, etc). Catastrophic events have already occurred in some quarries, and several localities had to be technically secured by stabilizing works recently, fresh rockfalls from 2021/2022 were also registered. One of the aims was therefore to create an inventory map of risk related to old quarries and the assessment of the present-day degree of hazard. Three-dimensional models of selected quarry faces were created using modern technology including calculation of cubic capacity of excavated material and collapsed masses. The complete results are included in the map geodatabase, which is under construction and which will be exploitable for an implementation within the information-educational and state-administration systems.

KEYWORDS

Quarry, Sandstone mining, Rockfall, Rock slope stability, Risk assessment and risk zoning, Map database, 3D modelling

INTRODUCTION

The area of Bohemian Switzerland lies in the north western part of the Bohemian Cretaceous Basin, being represented mainly by quartzose sandstones with isolated occurrences of Tertiary volcanics. Although under a strict supervision by conservationists today with unique sandstone geomorphology (Bohemian Switzerland National Park, Elbe Sandstones Protected Area), this territory was under long-lasting influence of human activities. Their impact has been mostly obscured by natural processes again. An inter-disciplinary survey and a detailed documentation of relics after

old mining activities in a broad area of interest was performed in 2021–2022. Attention was given to the extracted rocks, archival materials related to mining history, relict landforms after anthropogenic activities preserved in the landscape, the employed mining techniques, effects on sandstone relief, and possible hazard associated with abandoned quarries. More than 3 000 old quarries and mine workings, including exploratory workings, have been as yet registered in the territories of the National Park (80 km^2 in area) and the Protected Landscape Area (248 km^2 in area). These are represented mainly by quarries exploiting building stone (primarily sandstone), crushed stone (basalt, granitoids), and – to a lesser degree – by workings related to the prospection and exploitation of iron ore (with local extraction of limestone, dolerite, fluorite, quartz, sand and gravel and other minerals).

The area of Bohemian Switzerland is known for the high dynamics of sandstone relief which poses favourable conditions for slope movement activity (especially block movements linked with steep edges of plateaus – e.g. [1]. However, the lack of stability of the local sandstone massifs, manifested *inter alia* by rockfall events in the last few decades, has been largely induced by human interventions, especially by unremediated historical mining. Old mining sites seek their new balance on their way from cultural to natural existence in a succession of natural relief. Around 2 200 abandoned quarries for sandstone building stone (more than 1 380 shelf quarries) are currently registered, many of them being represented by unstable quarry faces. Abandoned quarries are often associated with elevated hazard of catastrophic rockfall, the preparatory stage of which has been shortened considerably relative to that of natural dynamics of rocky-slope evolution [2]. The aim of the study is, in addition to a comprehensive description and characteristics of old quarries, also the identification of possible threats associated with old quarrying. This is achieved through field research with special regard to sedimentary rocks (selection of high-risk areas around quarries, hazard appraisals and basic risks assessment).

METHODS OF BUILDING STONE EXPLOITATION

The former methods of mining, hence also of rock massif disintegration, are directly linked with the present stability state of previously quarried valley slopes. We therefore provide a brief review of the different methods of historical sandstone extraction, primarily based on the observation of the traces they left behind on the former quarry faces (Figure 1).

The oldest encountered mining techniques are derived from observed natural processes of spontaneous rockfall. These early anthropogenic interventions in the landscape are therefore hardly discernible from natural processes in the field. Such old workings are generally revealed only by the presence of unnatural landforms, rare traces of quarryman tools and techniques, or by the occurrence of otherwise improbable rockfall at these sites.

Artificial falls of sandstone blocks

The technique of induced fall of sandstone blocks was usually started by cleaning of joints and scraping of bedding-parallel fissures using forged iron hooks. Boulders and stones from talus-filled joints and fracture zones were then released and removed by iron crowbars and rolled away from the cliff face downhill using nailed wooden bars. Scavenging of transverse and longitudinal joints in the fractured rock massif resulted in the formation of separate rock pillars. The pillars were then forced to a downhill fall by **undercutting – undermining at the level of their bases**. The technique of undercutting of the cliff face created artificial overhangs as much as 20 m in depth and over 40 m in width [3] and was considered a high-risk activity. Fallen blocks were stopped in their downhill movement by drystone terraces and further **disintegrated** mostly by wedging along bedding-parallel fissures or minor tectonic joints. Bags after cutting wedges, earlier wooden ones or later iron ones, have been preserved in some cases in unfinished fallen boulders and blocks, providing valuable evidence of the employed mining technique. Extensive incisions are left behind in the cliff faces, being turned into short gullies due to natural weathering processes. Horizontally levelled rock plateaus are then visible at the cliff bases – floors of the undercuts. Prematurely abandoned mining sites are characterized primarily by the presence of half-disintegrated blocks with

undercuts, many tons in weight. Unfinished undercuts have the form of overhangs with flat ceilings and even floors. These unfinished undercuts pose the main hazard of spontaneous rockfall in the future (Figure 2), together with unreclaimed breakups of fracture zones and free-lying fallen boulders on the slope [4]. The extent of this technique of building-stone extraction is exceptional. Its biggest boom dates to the 18–19th century. It was applied especially to the right-bank slopes of the Elbe River canyon from the mouth of the Suchá Kamenice River to the south across Belvedér and Podskalí as far as to Loubí. It was also practiced in the adjacent part of the valley of the Suchá Kamenice River, the channel of which is buried beneath incompletely worked boulders in its lower reach. This mining method can be equally identified in the valleys of the Olešnička and Kamenice rivers, and was widely used also on the Saxonian side of the Elbe River canyon [5].

Fig. 1 - Methods of sandstone mining inducing instabilities in rock massifs (examples from the Suchá Kamenice River valley and the adjacent part of the Elbe River canyon: a) a shelf quarry in the valley of the Suchá Kamenice River with well visible traces after quarry-face mining using the technique of undercutting, b) Zlomiskova věž Pillar, produced by extraction of joints and surrounding sandstone blocks, primed for induced fall to the Elbe River canyon by undercutting its base, c) a crevice (dilated tensional joint) formed by unloading of the massif by mining in the Comiteebruch Quarry, d) borings for loading explosive cartridges, e) bags after the insertion of splitters (photo by K. Podroužek)

Bank method

Instabilities of cliff faces are also induced by the bank method, focusing on the extraction of serial rock outcrops. The techniques of building-stone extraction make use of the orthogonal jointing of sandstone. Three techniques were applied in the area under survey. Of the lowest negative impact on cliff-face stability is **chiselling of sandstone ashlars by benches (benching)**. This technique, typical for the 19th century, was applied to the face between two joints. Besides stepped benches, typical anthropogenic traces include rectangular cut-offs with vertical quarry faces, running across the full height of the outcrop [6]. **Wedging along joints and fissures** was applied specially to inclined beds. Cut-offs after this technique are irregular but respect the courses of joints. Extraction of cliff faces by undercutting is common in such cases. Again, the danger of rockfall occurs particularly at sites with unfinished quarrying activities. The third method of disintegration of cliff faces and blocks is blasting with the use of gunpowder and, since 1870s, also dynamite. A typical anthropogenic trace after **blasting** is a spherical blast-firing hole, accompanied by a series of cracks

extending radially into the rest of the block. A half-groove after drilling by a borer to lay the explosive cartridge is often preserved. The damage made by the explosives induces secondary disintegration of the massif and a gradual spontaneous deterioration of the block. Such blocks pose a major threat of spontaneous rockfall. The above techniques of cliff-face extraction are well visible in the Elbe River canyon, where they represent the younger layer of mining activities. At upper quarry levels, they produced faces up to 35 m in height.

Fig. 2 - Unfinished mining using the undercutting technique in the Elbe River canyon: left) in the area of the Comiteebruch Quarry, preserved as a deep "overhang" 7×3 m in size; right: unstable rock wall in the whetstone quarry near Podskalí (photo by Z. Vařilová)

Tab. 1 - Basic classification of all mining techniques in the study area

Type of mining object registered	Character of hazard	Degree of threat
Haphazard disintegration of free-lying blocks and boulders	downhill movement due to bedrock weathering / gravity and unloading	none / low
Quarrying and disintegration of small outcrops	falls of disintegrated rock fragments	low
Bank quarry	falls of blocks, rockfalls	moderate / high
Pit quarry, surface pit	---	none
Underground mine working (adit, chamber, shaft)	subsidence	moderate
Cut	minor falls, cave-ins	low

EFFECTS OF MINING ON NATURAL EVOLUTION OF ROCKY SLOPES

The occurrences of rockfall are mostly associated with high cliff faces and outcrops formed by rather resistant quartzose sandstones of Upper Cretaceous age (Lower to Middle Turonian age, corresponding to the Bílá hora and Jizera formations). At places most affected by stone extraction, the cliffs are formed by sub-horizontally stratified fine- to coarse-grained quartzose sandstones with only low amounts of kaolinite matrix. A typical "block" disintegration proceeds along a system of orthogonal joints. The types of rockfalls and their incidence are controlled by the geomorphic character of present relief (degree of rocky slope evolution), the intensity of tectonic fragmentation of the rock massif. The most frequent mass movements of rockfall type are associated with zones of deep-reaching disintegration of the rock massif in the slopes of the of the Elbe River canyon, which are, moreover, affected by long-lasting mining activities. Quarrying of building stone also resulted in changes in the gradient and height of the rocky slopes and in the formation of new discontinuities. The quarry faces, often extending across several natural cliff levels, often reach several tens of metres in height. It is specifically these sites that are endangered by catastrophic waste rockfalls. In contrast with natural evolution, rock massif at such sites is fragmented without being weathered. Therefore, the usual stage of gradual lowering of rock strength is skipped, and the whole process of stability deterioration becomes accelerated [2]. The main reason for mass movement activation in sandstones is the vast redistribution of loading stress, reaching as far as

tens of metres beyond the quarry faces. Artificial relief "rejuvenation" by quarrying created conditions favourable for the occurrence of catastrophic rockfalls even in those portions of the rocks slopes where these would never occur under natural conditions.

Tab. 2 - Main hazards in abandoned shelf quarries

Observed phenomenon in parts of rocky slopes affected by historical mining	**Consequence and potential hazards**
Variations in the gradient and height of rocky slopes due to quarrying	Effect on natural development of rocky slopes, resulting in potential deterioration of stability conditions
Extreme height of quarry faces, which often extend across several natural outcrop levels, often reaching several tens of meters (in some parts up to 40 meters)	Loss of cliff-face stability due to unloading and stress redistribution, activation of slope movements in the interior of damaged rock mass (tens of meters behind the quarry face), risk of catastrophic rockfalls of large volumes
Zones of intensive deep weakening of rock massifs	Opening of old tensile fractures, creation of new discontinuities, loosening and falling of blocks
Exposure of surface / subsurface parts of rock massif and fracturing of unweathered rock massif	Acceleration of rock deterioration processes, loss of stability
Undercutting of cliff/quarry faces (artificial overhang)	Loss of rock strength due to prolonged weathering, loss of stability due to the rock weight itself
Secondary failure of rock massifs due to the use explosive methods of rock disintegration	Secondary fissures and cracks with effect on stability, rockfall initiation
Other negative factors and conditions present	**Consequence and potential risk**
Uprooted trees from the cliff/quarry face or the upper edge of the face	Falling of sub-blocks and parts of the cliff/quarry face
Disintegration of quarry facilities (buildings, terraces, unstable piles of unused material from the quarry)	Fall of stones (smaller blocks) in the accumulation parts of the rocky slopes

Historical rockfall events and their remediation

The largest concentrations of unstable cliff faces are clearly located in steep slopes of the Elbe River canyon in areas of intensive building-stone extraction substantially altering the natural cliff-face morphology. Human-induced undercutting and secondary fragmentation of the rock massif are common phenomena here. This is evidenced by catastrophic rockfall events as well as the need of emergency remediation works in recent times. Recurrent threats at almost identical places are not an exception, as indicated by archival sources of information.

For example, repeated rockfalls were encountered at **Kvádberk Hill** (cadastre of Děčín) at the site of former sandstone quarrying above the municipal pasture of "Kühweg" (Viehweide) in years 1835, 1893 and 1931. Another catastrophic event at the same site was the big rockfall of 1938 (Figure 3) which induced damage to the local water-supply tank and a part of the forest and city park [7, 8]. This event was induced not only by stability degradation due to a giant artificial incision in the rock massif contributed by unfavourable weather conditions but also, most importantly, by the improper location of the quarry at the intersection of two tectonic fractures. Based on an expert opinion from 1960s [9], safety measures were proposed for separate parts of the hill and selected unstable objects. The above-mentioned shelf quarry was evaluated as the highest-risk portion by these reports. Based on an updated stability study (2003), extensive remediation measures were realized in the area of this quarry face degraded by fracturing and shearing to avert the threat of a rockfall thousands of m^3 in volume (removal of high-risk blocks, fixing of blocks by basal walls, rod rock bolting, filling of joints by gunite, construction of a retaining wall). Remediation of another rock pillar in the former quarry took place in 2013. The area of the old quarry continues to pose, despite all realized technical measures, potential risk of fall of stones and smaller loose parts of the rock massif.

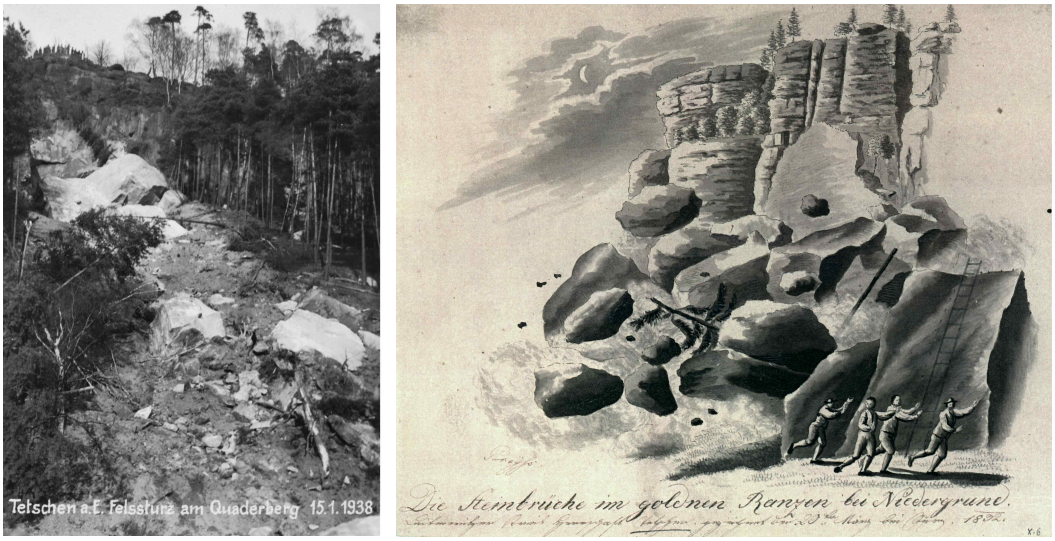

Fig. 3 - Left: A historical photograph of rockfall in a quarry at Kvádrberk Hill in 1938 (archive of P. Joza); Right: A wash drawing by J. Preyss, the parish priest of Hřensko, showing the rockfall of March 20, 1832 in the Goldenen Ranzen Quarry (near the Suchá Kamenice River); then, blocks at the foot of the slope were quarried by wedging, and a spontaneous fall of the quarry face occurred in the upper part of the slope (collections of the Municipal Museum of Ústí nad Labem)

Possibly the best example to demonstrate this type of hazard is the serial rock exposure over 300 m long south of the confluence of the Suchá Kamenice and Elbe rivers. It represents **the area of several quarry faces** known as **Goldene Ranzen (Elbleiten)**. Rock extraction was started in the 18th century here, and the building stone was used, e.g., for the construction of the fort of Terezín or for buildings in the near town of Děčín. The rocky slope is strongly weakened down to considerable depths and, moreover, affected by old quarrying. The intense, deep-reaching disintegration of rock massif is also evidenced by the presence of extensive systems of crevice caves. The area is therefore subject to long-term monitoring by engineering geologists. Repeated rockfall events were encountered here at the time of the quarry operation and thereafter – e.g., in 1832 (Figure 3), 1862, 1864, 1882, 1962 and 1980. One of the last big rockfalls, 1 360 m³ in volume, in January 1984 (Figure 4) was successfully predicted based on block-movement monitoring, and the affected road could be closed in time [10]. Remediation of a part of the quarry face pillar was made to avert threat to road traffic again in 1986. Two years later, a prelude to another catastrophic rockfall was accelerated by controlled downing of a part of the face. Another emergency remediation (quarries Goldene Ranzen_1 and 2) was realized based on data from revision monitoring in 1999. In a part of the area ("P31" corresponding to quarry Goldene Ranzen_3), technically demanding security measures were adopted for several rock massifs (volume about 3 000 m^3) threatening to fall onto the road in 2007 [11]. Detachment and fall of a fractured portion of the rock massif directly from the face of the former quarry Goldene Ranzen_2 occurred in the neighbourhood of the remediated area in autumn 2010; this event was induced by the degradation of the rock massif by mining, intensive fracturing and saturation with precipitation (Figure 4). Processes like joint dilation, rock deformation and tensional joint formation, loosening and removal of blocks or rock plates continue to the present. The broader area of these old quarry faces still belongs to the most hazardous portions of the Elbe River canyon.

Fig. 4 - Left: A face of the Goldene Ranzen_1 Quarry near the mouth of the Suchá Kamenice River to the Elbe River (a historical photograph from the 1980s during remedial work); Middle/Right: A catastrophic rockfall of 1984 and a smaller-volume rockfall of 2010 at the site of an old quarry face in the Goldene Ranzen_2 mining area (photo from [12] and by Z. Vařilová 2022)

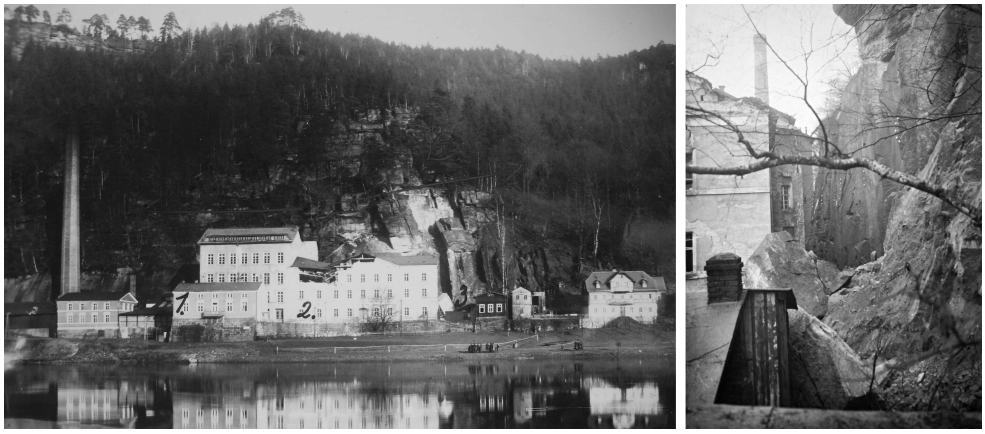

Fig. 5 - Zwirnfabrik Eiselt (Duty free shop) site – photographic documentation is available for the rockfall event of 1938, when sandstone mass from an old quarry face 400 m^3 in volume induced damage to the adjacent building [14]

Another exemplary site is the cliff face behind the **Duty-free shop** building – the original spinning mill of Zwirnfabrik Eiselt at Hřensko. It experienced repeated catastrophic rockfalls in 1886, 1938 (Figure 5) and 1944. New threat, identified in years 2002/2003, called for technically demanding security measures. Repeated rockfall events and extensive remediation works preclude any precise determination of the original shape and size of the quarry face.

Similarly, the threat of fall of large rock masses from an old quarry face directly **above international Road I/62** in the developed part of the village of Hřensko was observed in 2010–2011. Sandstone extraction at this site was probably conducted in 1938–1945 with the use of reckless blasting operations (numerous explosions in core runs). The quarry forms a trapezoidal niche in a serial outcrop with prominent primary orthogonal jointing. These joints were subjected to dynamic effects of rock extraction, generating secondary detachment planes and cracks. Traffic on the road was constrained for a long time due to the imminent risk of rockfall [15], and an impact bed was constructed in one lane. Multi-stage remediation works were then performed (2011–2013) with the aim to secure the parts of the cliff face endangered by imminent rockfall. As much as 1 200 tonnes of unstable rock were removed, a concrete collar was built in the most fractured part of the quarry face at the height of 25 m, the face was strengthened by bolt mandrels (bolting to a depth of 24 m), joints were injected with gunite and a high-load barrier was installed [16].

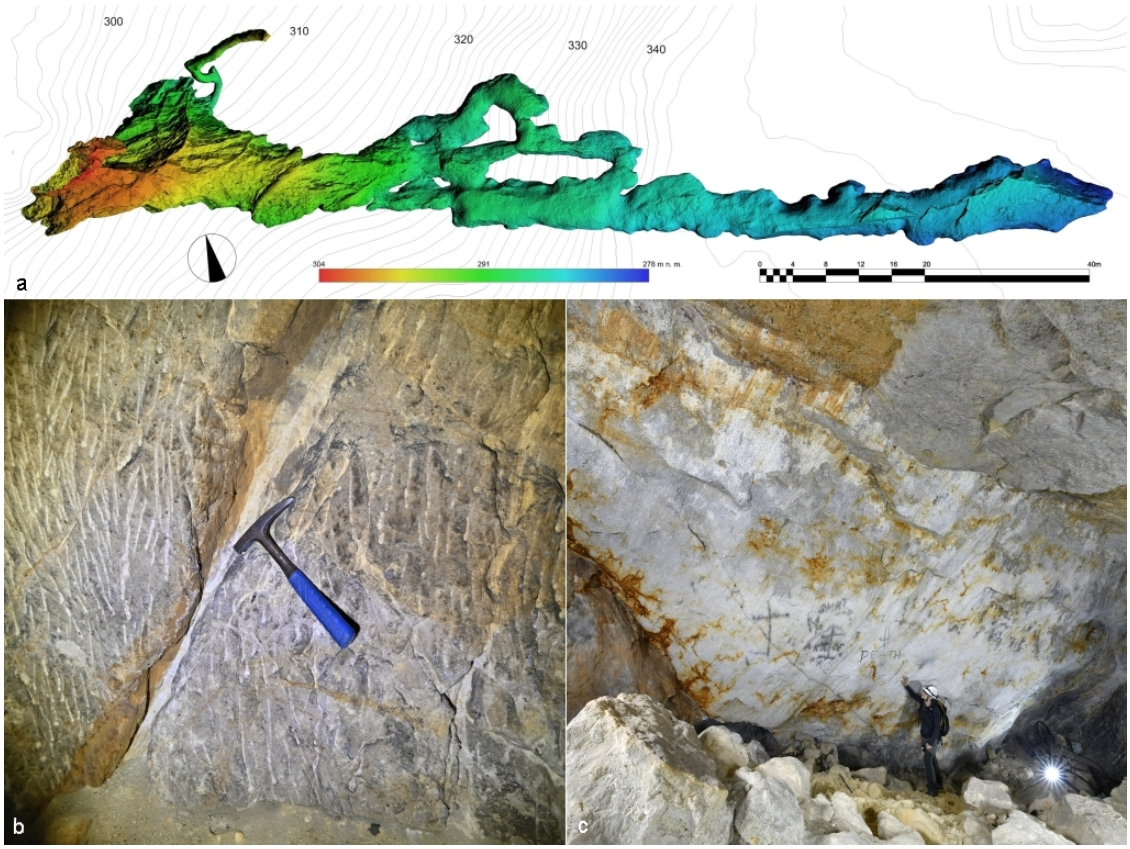

Fig. 6 a) - Hypsometric analysis of surfaces of excavated underground spaces at Ludvíkovice, b) a minor shear fault in a side of the adit, c) an exposed striated shear plane now forming the wall of the terminal dome at the site of repeated ceiling collapses and deadly rockfalls (photo by Z.Vařilová and J. Preclík)

Underground sand pits exploiting friable sandstone represent a specific type of mining objects. One of the largest excavated objects in the area of interest is the Labyrinth or **Sandloch** site (cadastre of Ludvíkovice, Figure 6). This Labyrinth was originally promoted as a point of interest in tourist guidebooks in the second half of the 19th century. After a fatal injury by fallen rock mass during sand extraction in 1914, mining operations were stopped and the entrance to the adit was closed [17, 18]. The entrance to the underground sand pit lies at the foot of a hill in an immediate proximity of the developed area of Ludvíkovice. The overall length of all documented underground spaces is 132 m, maximum height is 6.5 m (height of artificially carved corridor max. 5.5 m). The present size is markedly affected by repeated falls of the ceiling and parts of walls even at recent times (traces of fresh fallout). The extracted material was low-strength quartzose sandstone, showing dips of strata of max. 20° and intensive fracturing. Shear faults and their intersections, fractures and prominent lithological boundaries functioned as detachment surfaces of rockfalls. Fresh-looking detachment surfaces in the entrance dome and the terminal dome confirm the presence of imminent risk. A potential threat of subsidence of a part of the undermined slope cannot be excluded.

Other selected documented rockfall events at sites of old quarrying according to [19–25]:
Dolní Kamenice, Rabštejnské údolí Valley, Vrchnostenský Quarry (Pr_7): April 1912, January 2022
Janská, Rabštejnské údolí Valley: 1861 rockfall at spinning mill
Děčín, Teplická St. – Pastýřský vrch Hill (Lerchenbruch / Kargel Quarry): 1869, fall of a block; 1898, repeated rockfall and rock fragment detachment in 20th century, 2021 rockfall and remediation
Děčín, Spitzhüttel (a historical quarry): 1872, fall of the quarry face and remediation
Děčín, Pastýřská stěna Cliff: 1877, rockfall and remediation

Hřensko (former cadastre of Dolní Žleb), Komitee Steinbruch Quarry: 1874, fatal injury of a quarryman under a suddenly released block
Hřensko, near the Labe Hotel: 1843, fall of a block; 1900, rockfall; 2010–2011 remediation
Hřensko, near the Zlodějská stezka Path: 1876, risk of rockfall from the face
Hřensko, near the Březový důl Valley: 1889, remediation of a high-risk block necessary
Hřensko, near the Malinový důl Valley: 1851 rockfall; 1855 rockfall followed by remediation by chiselling; 1896 fall of a block followed by remediation
Martiněves, Windrich Quarry: 1899, collapse of the face, death of three quarrymen working under the face

Present signs of stability deterioration of quarry faces

Besides rockfalls documented by archival data, several new events from the break of 2021/2022 were identified (e.g. Figure 7, 11). These mass movements were induced by a combination of factors: intensive fracturing of the rock massif and artificial overhangs, saturation with precipitation water or meltwater, often facilitated by uprooting and wedging of the root system of adult trees on top edges of quarry faces. The problem of stability of old quarry faces is, however, not restricted only to the selected sections of the right slopes of the Elbe River canyon between Děčín and the state border. The present survey and documentation of old quarries identified hitherto unknown sites of potential hazard, where old quarry faces or their parts are endangered by rockfall (Suchá Kamenice River valley, Rabštejnské údolí Valley, close to the network of tourist trails leading to the Dolský Mill, above buildings and roads at Děčín-Podmokly and Dolní Oldřichov, Martiněves, Růžová, Ludvíkovice and Janská areas, Pekelský důl Valley and other sites). In only a few cases, however, potential rockfalls pose a threat to inhabited and man-frequented areas.

Fig. 7 - A collapse of a part of a cliff face, 2.6 m³ in volume, caused by a tree uprooting at the model site of Bruckgraben (Vysoká Lípa cadastral area) – a comparison with the use of a photogrammetric quarry model (June 2021 and March 2022)

QUARRY DOCUMENTATION AND HAZARD CLASSIFICATION

The existing published methodologies (e.g., [26]) were found to be inadequate for a uniform and representative description of abandoned quarries in sandstone rocks. On the basis of field documentation, a typology and terminology of old quarries and their components was developed in comparison with written sources and literature. All quarries and mine work were described using basic typology and defined parameters: site description (extent of mining activities, size and shape of the quarry, geological description, direction of mining progress, present state) and object type (shelf quarry / pit quarry / artificial disintegration and benching in small outcrops / wedging of boulders / underground mining / prospection etc.), character of the extracted material and the deposit, historical data (time interval of quarry operation, quarry operator/lease-holder), extraction method,

description of relics of buildings and equipment, semi-finished products and engravings including a list of all recovered archival sources and literature for each registered site.

Representative quarry areas were chosen as model sites and characterized in detail, beyond the extent of routine documentation. At these sites, an inventory of features related to mining history and preserved relics after human activities was extended by the study of the degree of interventions in the sandstone landscape and by the assessment of mining impacts.

Documentation of model quarry faces using photogrammetry

Geodetic documentation of the quarries employed routinely practised techniques, based primarily on the polar method [25]. This was performed with the use of a total station or a stabilized laser range meter (two range meters at known positions allow the use of the forward intersection method). Polar measurement is intended to provide, depending on the desired output for the given site, marker coordinates for subsequent photogrammetry measurement, or laser scanning, or direct determination of detailed points as a basis for the creation of the plans [28]. With respect to the character of relief in quarries, the manual direct linear measuring technique was only rarely used.

Similarly, the coordinate system of the geodetic survey was chosen depending on the requirements stipulated for the given site. If a total station is used, it is advisable to use – apart from the local S-JTSK system. The connection was realized using the GNSS RTK receiver, the limits of which are especially sensible in the environment of historical quarries. Densely forested terrain, narrow valley profiles and underground mine workings preclude any fixation of the measured points at some sites. Planimetry and altitude data were checked against the detailed Digital Elevation Model / DEM [29].

Where a digital 3D model was required for the given site, its creation is based on photogrammetry method SfM (Structure from Motion; [30]; for output examples see Figure 8). This photogrammetry method was based on an automated optical correlation in a series of digital photographs, generating 3D data in the form of a point cloud. The point clouds were evaluated and processed into a form of a polygonal mesh with a photorealistic texture. This method is limited, above all, by the need of good visibility of the photographed object. This implies that some sites are not suitable for processing by this method, and some other sites can be detected by this method only in a vegetation-free period. 3D data obtained by this method were combined with data from a detailed DEM [29] complete the final scene.

3D models were used not only for presentation purposes but also as a basis for the creation of other outputs. These include especially plan documentation, which can show a much closer detail, if aided by 3D models, than plans constructed solely on the basis of geodetic measurements. The plan documentation was created in the environment of CAD system and other vector graphic editors. 3D models were further used to create orthophoto mosaics, DEMs with hypsometric analyses, to compare models and to calculate areas and volumes [31]. The task to calculate the volume of wasted or excavated part of the quarry is relatively straightforward if models of the quarry before and after the event are available (see Figure 7): the differential body has to be created first at the given level of detail (post-modelling is sometimes needed to eliminate the effect of spaces covered with fallen material in the post-event model), and its volume is subsequently calculated using at least two different programs independent of each other for its corroboration (for large-scale projects with periodically surveyed areas, automated procedures are available; [32]). If the volume of fallen / excavated part is to be calculated without a prior geodetic documentation, collaboration of the surveyor with a geologist is necessary to produce a qualified estimate of this volume.

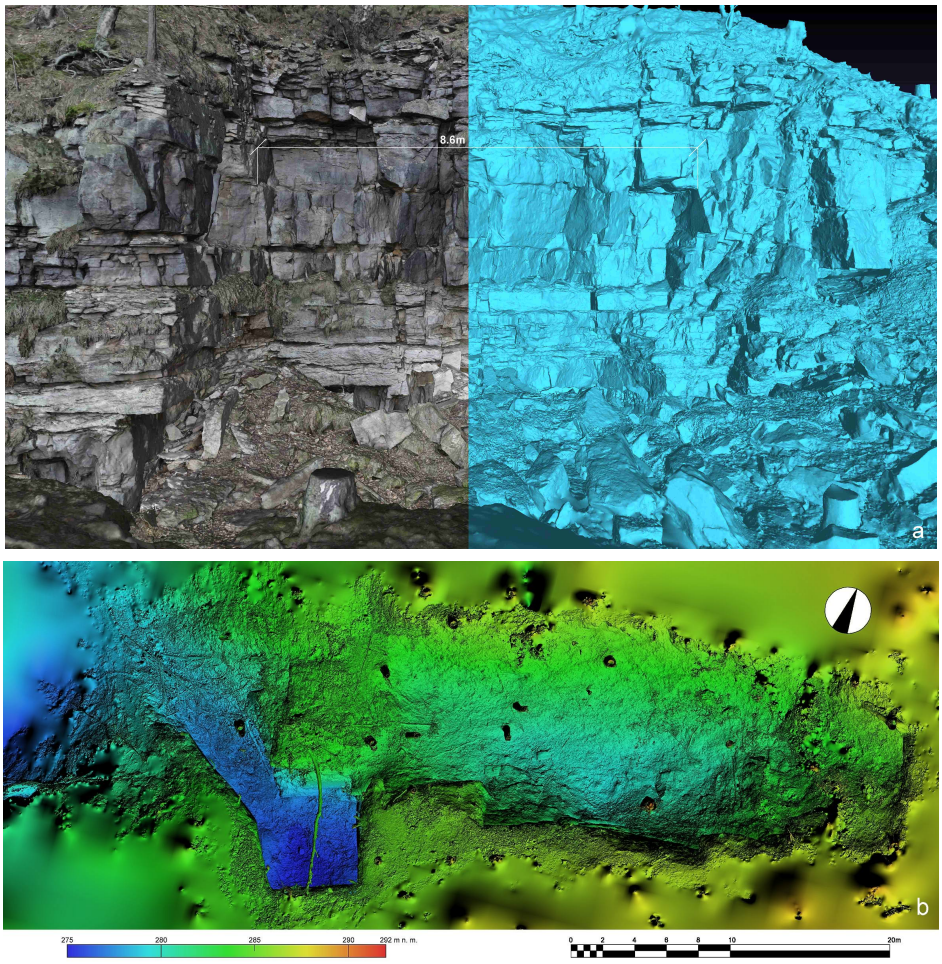

Fig. 8. a) - A 3-D computer model of a whetstone quarry near Podskalí in the Děčín area – an image with phototexture (left) compared with monochrome colour with simple shading (right); b) A digital model of the surface of an excavated quarry near Janská with a hypsometric visualization of relief.

Assessment of present-day stability and risk classification

An assessment of potential risk from mass movements was made, and present-day stability degrees were attributed to different sites. Due to the large quantity of mining sites, the risk evaluation was made for whole quarries or mining areas within the full limits of their exploitation. Only the sections of rocks massif affected by human activity and their integral parts were assessed. A more detailed risk classification was performed for selected model sites, distinguishing among individual risk zones within the quarry area/quarry face – e.g., the Goldene Ranzen and Comiteebruch quarries in the Elbe River canyon or the Vrchnostenský Quarry in the Rabštejnské údolí Valley. Unlike in a detailed engineering-geological study of stability conditions (e.g. [33]), the aim of the present activity was to provide a basic assessment of the degree of present-day risk and the presumed damage inflicted. Therefore, the main evaluation criterion was the probability of damage to the road network, buildings, local population or visitors by rockfalls. Other classification criteria included local conditions and controlling factors, such as the position, height and character of cliff faces (intensity of tectonic and human-induced fragmentation of outcrops, intensity of weathering, etc.), slope gradient or the presence of spontaneously established woody plants. Last but not least, the documented history of rockfall events and data on previous remediation measures were also considered. A specific type of threat related to sandstone mining relicts is represented by waste stone deposits, remains of retaining walls or disintegrating relics of buildings, which may release

smaller sandstone blocks. On the other hand, major slope adjustments (e.g., artificial terraces or protective ramparts of quarried stone) can play a positive role in retaining the loose masses in some cases.

The degrees of risk (0 to 3) were assessed individually based on field reconnaissance considering the specific conditions at each site, making use of basic point evaluation. A list of all evaluated parameters is given in Table 3.

Tab. 3 - Evaluation criteria for a quarry face risk assessment

Parameter (controlling factor / condition)	Point
Presence of roads, tourist trails and forest roads or developed areas in the presumed rockfall trajectory (targets of potential threat)	1
Documented history of rockfall / relatively frequent rockfall events above 3 m^3 in volume	1
Presence of tectonic fractures affecting stability (faults, joints) / gravitational dilation / tensional joints / fracturing / intensive weathering of inner parts of rock massif	1
Overhanging portions of cliff face / artificial undercutting	1
Adult trees and vegetation growing on the cliff face or its upper edge (wedging by roots)	1
Larger volume of unstable parts of the cliff face or individual blocks (with a potential catastrophic impact, 5 m^3 to tens of m^3)	1
Position of unstable components of the rock massif in upper part of the quarry face or at its upper edge (higher energy of the fall can be expected)	1
Slope gradient (above 30°) and aspect allowing for the movement of fallen masses, blocks moving downhill will probably reach its base, with a minimum possibility of their stopping	1
Presence of safety and retaining elements (impact bed – e.g., horizontal manipulation terraces or prominent terrain depressions under the quarry, prominent rock steps and a dense cover of adult trees, a.o.)	-1
Completed technical remediation, installed functional safety elements	-1

Tab. 4 - Assessment and classification of rockfall risk

Risk degree	Colour of symbol in map	Points
0	white	0
1	yellow	1–2
2	orange	3–5
3	red	6–8

GIS-aided presentation of results and their applications

Collection and processing of geo-spatial data for quarry sites adopted an approach based on collaborative mapping in the ArcGIS technological environment, the solution is based on the cloud platform of ArcGIS Online. The emerging information database is based on various types of background maps together with a DEM. The emerging map database contains, besides the inventory of old mine workings and their geological and mining-historical characteristics, the assessment of stability of old quarries.

Besides point- and polygon-defined registries of old quarries (Figure 9) and mining-related anthropogenic relict landforms, the database also includes an independent data layer called “Stability of cliff faces”, reflecting the attributed present-day rockfall risk together with a description of any potential threat (Figure 10). Places of high risk, endangered by falls of old quarry faces into populated or man-used areas were indicated. Potential risk was identified not only in the deeply incised canyon of the Elbe River and its tributaries, but also at other sites in a broader region of interest. The selected model mining areas were documented in detail using geodetical and photogrammetric methods (Figure 11).

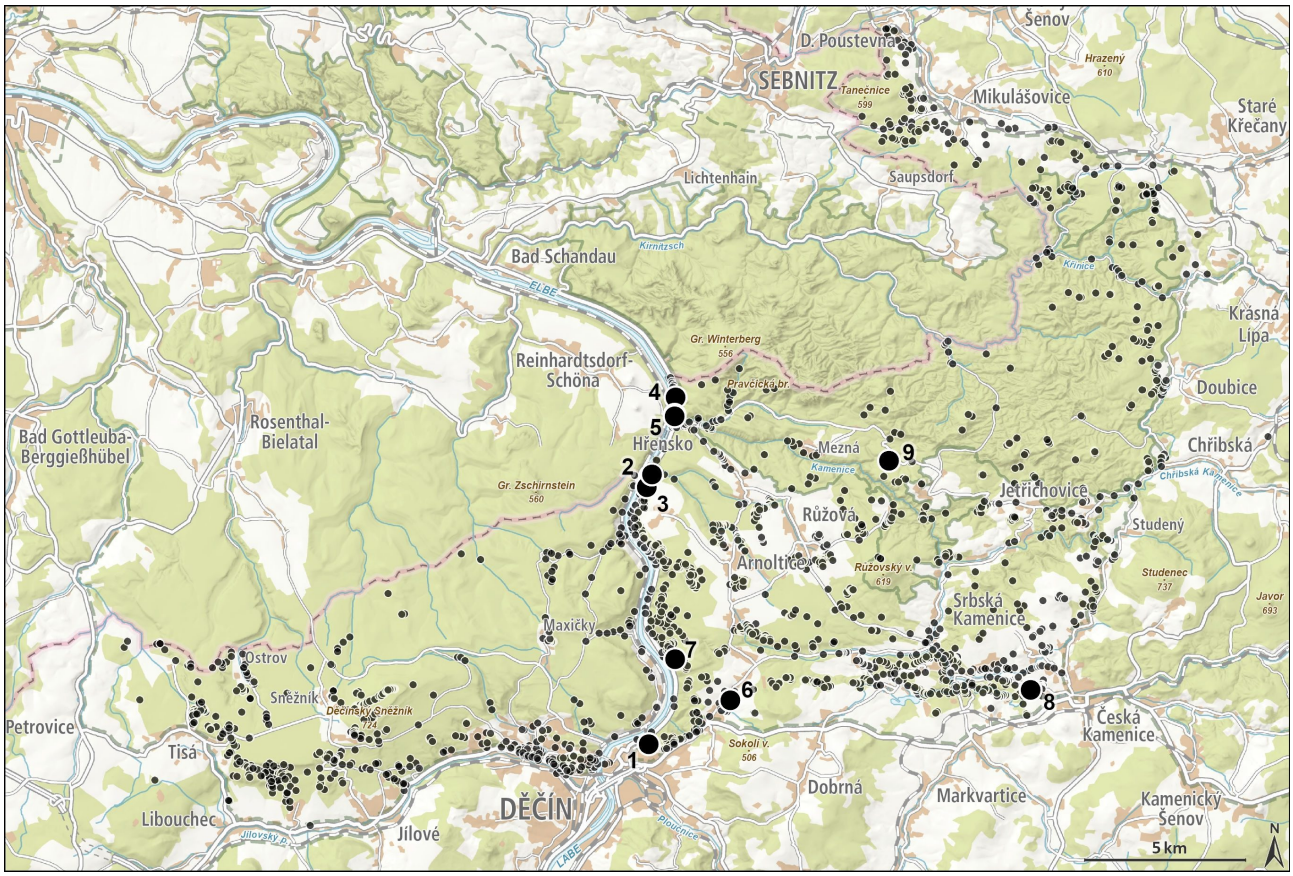

Fig. 9 - A map of the study area with identified quarries (black points) and selected localities: 1) Kvádberk Hill (Děčín), 2) Goldene Ranzen Quarry, 3) Comiteebruch Quarry, 4) Duty free shop (Hřensko), 5) Quarry above Road I/62 (Hřensko), 6) Sandloch (Ludvíkovice), 7) Quarry near Podskalí, 8) Vrchnostenský Quarry (Rabštejnské údolí Valley), 9) Bruckgraben (Vysoká Lípa); Map: © Bohemian Switzerland NP Administration; Source data: © ČÚZK, © IPF TUD, © GeoSN, © BKG, © LFULG

RESULTS AND DISCUSSION

Rock massifs of the Bohemian Switzerland NP and Elbe Sandstones PLA have been extensively affected by historical mining – although this fact is not visible at a first look. The number of currently mapped quarries exceeded initial expectations of the research team by an order of magnitude. The results of study provide an integral set of information on the distribution of quarries in the landscape and the history of minerals utilization. For the purpose of uniform and representative characteristics of quarries in this specific sandstone region, it was necessary to create a new methodology using the sporadic existing literature (e.g., [26, 34]). The emerging map database contains, besides the inventory of old mine workings and their geological and mining-historical characteristics, the assessment of stability of old quarries. Extraction-induced areas of instability of rocky slopes were recognized during the field mapping, for which we recommend an additional detailed engineering-geological evaluation of massifs, risk analysis and rockfall simulations (e.g., [34, 35, 36, 37]). The threat was not determined for a number of old sandstone quarries (and for quarries in other types of rocks) because there were no objects at risk identified.

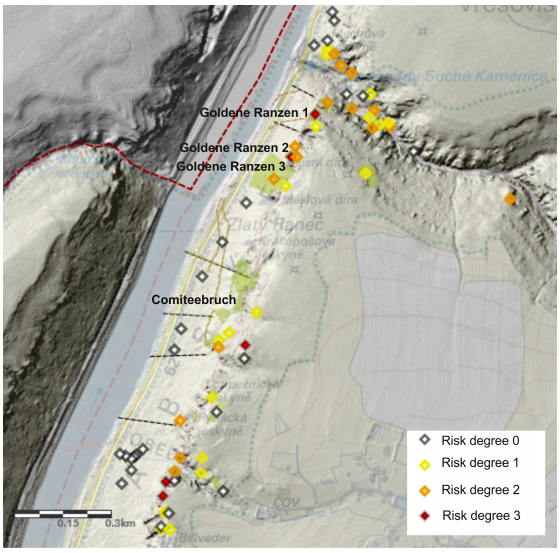

Fig. 10 - The Suchá Kamenice River valley and a part of the right bank of the Elbe River canyon with marked positions of surveyed quarries with inferred rockfall risk degrees (the green polygons correspond to the Goldene Ranzen_1–3 and Comiteebruch mining areas); based on the DEM of Bohemian Switzerland [29]

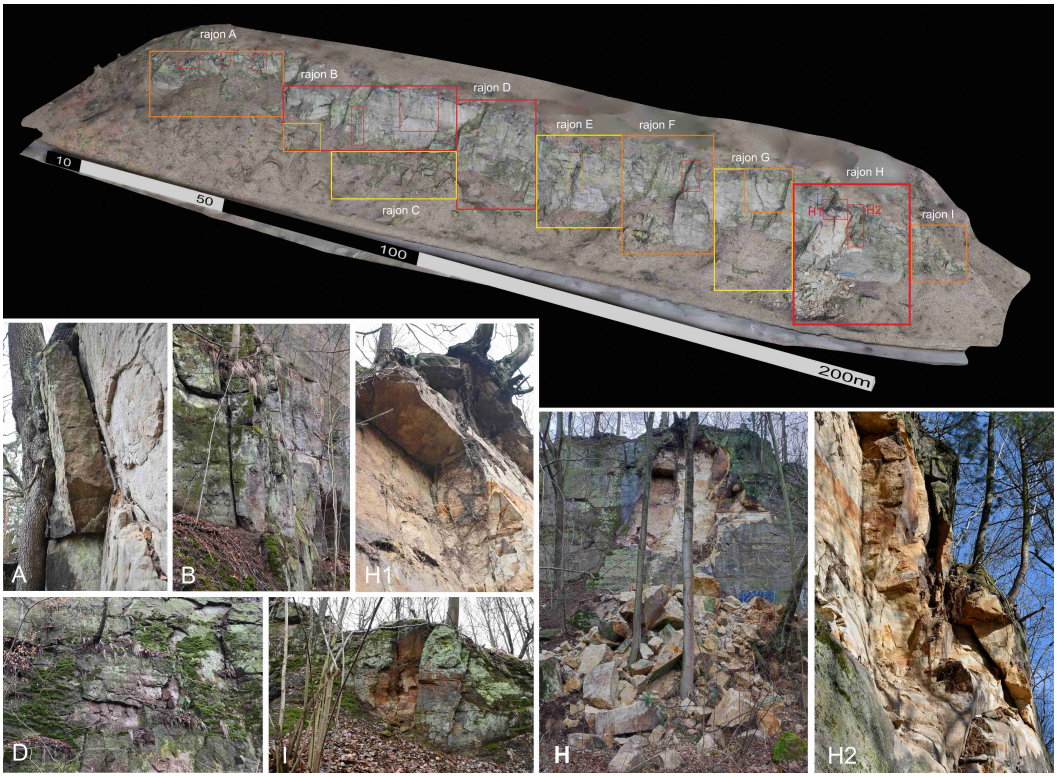

Fig. 11 - Model locality – a quarry face in Rabštejnské údolí Valley divided into individual parts according to the determined degree of risk, and examples of unstable parts of the cliff face (old parts of rock wall A, B, D, I and fresh risk zones H1, H2 corresponding to the shear surface of the rockfall); a rockfall 78 m³ in volume occured here in February 2022 (H) (cadastral area of Dolní Kamenice, photo by Z.Vařilová)

High-risk areas and sites should be given more attention by the users/managers of the potentially affected land. The main recommendations include: Awareness of land owners, authorities, forest managers, nature protection authorities; continuous monitoring of the state of high-risk sites (3–5 years); elimination of mature trees from quarry faces and their upper edges; proper marking of risk and safeguarding the entrances to dangerous quarries /underground spaces. Recommendations in the case of endangering buildings, roads/railways, and frequented tourist routes: detailed engineering-geological survey of selected quarry sites; securing the slopes under the quarry faces (impact beds, terraces, retaining walls and fences); control monitoring of the faces of abandoned quarries (e.g. [38]); remediation of immediately dangerous parts of the rock massif; revitalization and repair of original structures (buildings, retaining walls, roads, skids, etc.); taking into consideration old mining remains in the management of forestry interventions.

CONCLUSION

The set of knowledge will be further extended by consequential research. The current study targeted at maximum applicability of the obtained results and their implementation in the information-educational system. Presentation of the complex results via an online map database (scheduled for the turn of the year 2023/2024) will be guided by practical needs of the Administration of the PLA and NP, local governments and administrative bodies.

ACKNOWLEDGEMENTS

The herein presented results were achieved within the project TL05000407 “Database of old quarries and mine workings in the territories of the Bohemian Switzerland National Park and the Elbe Sandstones Protected Area”. This project is co-financed from the state budget by the Technology agency of the Czech Republic under the ÉTA Progamme.

REFERENCES AND LIST OF ARCHIVAL SOURCES:

[1] Vařilová Z., Zvelebil J., 2007. Catastrophic and episodic events in sandstone landscapes: slope movements and weathering. In: Sandstone Landscapes, eds. Härtel H., Cílek V., Herben T., Williams R., Academia, Praha, 115-128.
[2] Zvelebil J., 1990. Vliv historické lomové těžby na současnou stabilitu pískovcových skalních svahů v Děčínské vrchovině, Sbor. “38. Fórum pro nerudy“, Čs. Spol. Min. Geol.,124-173, Praha.
[3] Stein K., 1988. Příspěvek k historii těžby pískovce v údolí Labe v Děčínské vrchovině, Historia 9, Sborník Severočeského muzea, Liberec, p. 71-88.
[4] Podroužek K., 2012. Těžba pískovců – typy, způsoby, příklady, Péče o historická důlní díla vzniklá do konce 19. století, eds. Tomáš Brož, Jiří Bureš, NPÚ ÚOP v Ústí n. L. 2012, p. 31-46.
[5] Kutschke D., 2000. Steinbrüche und Steinbrecher in der Sächsischen Schweiz, Pirna, p. 1-21.
[6] Podroužek K., 2006. Štuky a kopáky – těžba, užití a význam kvádrového pískovcového zdiva. In: Opracování kamene, eds. Jahn John, Miroslav Kovář, Plzeň, p. 85-95.
[7] SOkA Děčín, AM Děčín: K 246.
[8] Joza, P., 2009. Kvádrberk, Malá děčínská vlastivěda, Děčín, p. 59-60, 62-64.
[9] Zajíc J., Král J., Daniel J., 1975. Průzkum skalních stěn a svahů na Děčínsku, Sborník geol. věd, řada Hydrogeologie, inženýrská geologie, 12: 137-176.
[10] Zvelebil J., 1984. Skalní řícení u Hřenska a jeho prognóza, Geologický průzkum 10/1984, p.294-296.
[11] Komín M., 2003. Hřensko – sanace skalního masivu P31, MS, Project documentation, AZCONSULT, Ústí nad Labem.
[12] Zvelebil J., 1984. Inženýrskogeologická prognóza rizik katastrofálních skalních řícení, MS, part C – photographic appendix, photo 15.
[13] Kropáčková D. 1988. Petrologické studium křemenných pískovců z údolí Labe severně od Děčína, MS, Diploma thesis, Faculty of Science UK Praha, p. 31.
[14] SOkA Děčín, LR Děčín, K 16
[15] Zvelebil J., 2010. Upozornění na bezprostředně nestabilní objekty ohrožující chodník a silnici I/62 na pravém břehu Labe v obci Hřensko, MS, 2 p. + 11 appendices, Zdiby.

[16] Komárek M., 2011. Hřensko, Sanace skalního masivu Lomová stěna nad silnicí I/62. MS/PD, AZ CONSULT, Ústí nad Labem.
[17] John, F., 1980. Chronik der Gemeinde Losdorf, Chronik Ausschuß der Gemeinde Losdorf, 1980, p. 22, Laufen/Ob B.
[18] Veselý M., 2010. "Ludvíkovická jeskyně" podzemní pískovna v Ludvíkovicích, Děčínské vlastivědné zprávy: časopis pro vlastivědu Děčínska a Šluknovska / Děčín: Oblastní muzeum v Děčíně, 1212-6918 Vol. 20, No. 1 (2010), p. 39-48.
[19] SOkA Děčín, OU Děčín: K 101, 11-53/286; K 103, 11-53/719; K 504, 11-53/ N 154; 11/ 2-28; 11/ 2-98; K 103, 11-53/682;
[20] SOkA Děčín, OU Děčín: AF Hřensko, pamětní kniha II, unpaged.
[21] SOA Litoměřice, pob. Děčín: VS Bynovec, K 130, inv. č. 337, K 140, K 143;
[22] SOA Litoměřice, pob. Děčín: ÚS Clary Teplice, K 5, I - 1889/233; K 11, I- 1896/369.
[23] Nordböhmischer Gebirgsbote, 19. 11. 1861.
[24] Tetschner Anzeiger, 5. 9. 1874.
[25] Leitmeritzer Zeitung, roč. 29, č. 38, 17. 5. 1899.
[26] Večeřa J. et al., 2020. Návrh popisu a vyhodnocení historických důlních děl, ČGS, Praha.
[27] Sokol, P. et al., 2017. Metodika terénní prostorové identifikace, dokumentace a popisu nemovitých archeologických památek, p. 96-111.
[28] Veselý, J. et al., 2014. Měřická dokumentace historických staveb pro průzkum v památkové péči, edice odborné a metodické publikace, sv. 49, Národní památkový ústav, 120 p.
[29] IPF TUD, 2005. Digital terrain model created from airborne laser scanning data in the frame of the EU INTERREG IIIA project „Geoinformation Networks for the cross-border National Park Region of Saxon-Bohemian Switzerland“.Remote Sensing, Institute for Photogrammetry and Remote Sensing, Dresden University of Technology.
[30] Ullman S., 1979. The Interpretation of Structure from Motion, Proceedings of the Royal Society of London. Series B, Biological Sciences 203, n. 1153, 1979, p. 405-426.
[31] Westoby, M. J. et al., 2012. Structure-from-Motion' photogrammetry: A low-cost, effective tool for geoscience applications, Geomorphology, Volume 179, 2012, p. 300-314.
[32] Farmakis I. et al., 2022. Rockfall detection using LiDAR and deep learning, Rockfall detection using LiDAR and deep learning, Engineering Geology, Volume 309, 106836.
[33] Zvelebil, J., Stemberk, J., 2000. Inženýrskogeologické mapování stability skalních svahů v obci Hřensko. In: Nebezpečí svahových pohybů v údolí Labe na okrese Děčín, Šebesta, J. et al., díl F: 1-28. Hřensko. MS, Český geologický ústav. Praha.
[34] Matheson, G.D., Reeves G.M., 2011. The identification, appraisal and assessment of hazards on quarry rock faces in terms of the UK Quarries Regulations. Quarterly Journal of Engineering Geology and Hydrogeology, 44 (2), 259-275.
[35] Robotham M.E., Wand H., Walton G., 1995. Assessment of risk from rockfall from active and abandoned quarry slopes. Transactions of the Institution of Mining and Metallurgy, Sect. A, Mining Industry, 104, A25-A33|
[36] Blahůt J., Klimeš J., Vařilová Z., 2013. Quantitative rockfall hazard and risk analysis in selected municipalities of the Ceske Svycarsko National Park, northwestern Czechia. Geografie, 118 (3), 205-220.
[37] Kusák M., Valagussa A., Frattini P., 2019. Key issues in 3D rockfall modelling, natural hazard and risk assessment for rockfall protection in Hrensko (Czechia). - Acta Geodynamica et Geomaterialia, 16 (4), 393-408.
[38] Zvelebil J., Vařilová Z., Paluš M., 2005. Tools for rock fall risk integrated management in sandstone landscape of the Bohemian Switzerland National Park, Czech Republic (M121). 1st General Assembly of the International Consortium on Landslides. Landslides: risk analysis and sustainable disaster management, 119-126.

List of symbols:

BKG – Bundesamt für Kartographie und Geodäsie, Datenlizenz Deutschland
CAD – Computer-Aided Design
ČÚZK – Český úřad zeměměřický a katastrální
DEM – Digital Elevation Model
IPF TUD – Institute of Photogrammetry and Remote Sensing, Technische Universität Dresden
GeoSN – Staatsbetrieb Geobasisinformation und Vermessung Sachsen
GIS – Geographic information system

GNSS – Global Navigation Satellite System
LFULG – Sächsisches Landesamt für Umwelt, Landwirtschaft und Geologie
NP – National Park; PLA – Protected Area
RTK – Real-Time Kinematic positioning
SfM – Structure from Motion
S-JTSK – System of the Unified Trigonometric Cadastral Network (geodetic system, mandatory for the territory of the Czech Republic)
SOA – State Regional Archive; SOkA – State District Archive

CIVIL ENGINEERING JOURNAL

Article no. 40

THE CIVIL ENGINEERING JOURNAL 4-2022

RESEARCH ON SAFETY EVALUATION OF ASSEMBLY BUILDING CONSTRUCTION BY INTEGRATING ENTROPY POWER METHOD AND NETWORK ANALYSIS MODEL

Luying Li

Hubei Light Industry Technology Institute, Wuhan, Hubei 430070, China; zhiying78861@126.com

ABSTRACT

Unlike the traditional construction mode of rough operation, assembly building construction implements the concept of green development in terms of energy consumption and environmental adaptability. Although assembly construction can effectively reduce construction energy consumption and improve the environmental resilience of building construction work, there is an urgent need for an effective safety assessment model for construction development due to the imperfect operation system and harsh construction environment in the construction industry. Therefore, the study analyzes the relationship of construction safety factors by using Analytic Network Process (ANP) to filter safety evaluation indexes according to the importance ranking. At the same time, the objective weights of safety indicators were determined by the entropy weight method, and the subjective weights determined by the ANP method were combined to construct the safety evaluation model for the construction of assembled buildings. The experiment shows that the maximum similarity between the comprehensive evaluation results of the model in the simulation of safety evaluation of high-rise residential construction and the actual evaluation criteria is 0.772. The experiment proves the reliability of the evaluation of the model, which reduces the safety loopholes and operation hazards for the construction of assembled buildings.

KEYWORDS

Assembly building construction, Entropy power method, Network analysis method, Construction safety index

INTRODUCTION

As the structural transformation and optimization of the building construction industry proceeds, the disadvantages of the traditional construction model with poor risk resistance and high energy consumption become more and more prominent, and the progress of the assembled building construction model adapts to the requirements of economic and social development for the efficiency of residential construction [1]. The assembled building construction model focuses on the individual needs of the customer for accessories and the logistics management of accessories, while considering the planning and control of the delivery and assembly of prefabricated building systems. Peng Li, a domestic scholar, proposed a case-based reasoning based multi-objective optimization model for clustering construction suppliers. This method can optimize the management of the construction party and guide the construction into green transformation. At the same time, foreign scholars [2]. Anna Adamczak, Bugno and others tested the flexural strength of fiber cement building materials and proposed the possibility of using acoustic emission and wavelet analysis to test cellulose fiber reinforced cement plates [3]. Based on the frontier achievements of the academic community, the study determined the safety index assessment system for assembly building construction and the subjective weights of the indexes based on text mining and network analysis, introduced CR values to modify the weight matrix, and used the entropy weighting method to

determine the objective weights of the indexes. After calculating the comprehensive weights, the cloud model was used to characterize the quantitative scores as the degree of risk, and the similarity was used to evaluate the performance of the ANP-EW model constructed by the study. Through the combined application of the subjective and objective weights and the cloud conversion algorithm, it is expected to provide an effective and accurate risk assessment method for the emerging development of assembled buildings.

RELATED WORKS

The application of entropy weight method, network analysis and cloud transformation model by domestic and foreign scholars has become mature. Yu K et al. established an index system of factors influencing coal miners' unsafe behavior and used the weights determined by ANP as the influence coefficients among variables to construct a system dynamics (SD) model of coal miners' unsafe behavior. Experiments showed that the method provides theoretical support and methodological guidance for improving coal miners' safety [4]. Zheng used ANP to derive subjective weights in multi-attribute decision making and proposed a hybrid hesitant fuzzy language factor analysis method to cluster attributes as principal factors. Experiments show that the method can be applied to physical health assessment with graduate students [5]. Abedin S F et al. prioritize different QoS requirements of heterogeneous IoT applications in fog networks by using an AHP implementation analysis framework to initiate stable associations between fog network infrastructure (i.e., fog devices) and IoT devices. The results show that the association of the method possesses stability and higher efficiency in resource allocation with high utility gain [6]. Li Z et al. proposed a data-driven algorithm based on the entropy and TOPSIS methods for analyzing the applicability potential of shallow geothermal energy. Experiments showed that the algorithm can overcome the subjectivity of expert experience and is suitable for selecting the best site [7]. Liang Wei et al. proposed an entropy method with a multi-step reverse cloud transformation algorithm based on sampling replacement (MBCT-SR) for a risk assessment model of long-distance gas transmission pipelines in mines [8]. Chen J Q et al. A transformer bushing fault prediction method based on entropy-weighted TOPSIS and gray prediction theory, using TOPSIS assessment method to convert the insulation assessment problem into a vector space distance problem, and verified the effectiveness of the method by example [9]. Luo J used entropy-weighted TOPSIS and barrier based on 2016 statistical data and population flow data degree model to measure the centrality of cities in the Yangtze River Economic Belt (YREB) and the factors affecting the centrality [10]. Sivaprasad P V et al. constructed an optimization model for alloy-X laser microdrilling process variables based on a joint entropy-based-Dunn's similarity algorithm. It was shown that the method can account for the thermal effects during the metallurgical processing performed in the micro-hole [11].

Akter S. et al. investigated the increasing convergence of artificial intelligence, blockchain, cloud transformation, and data analytics for technology operations and value propositions [12]. Symvoulidis C. et al. presented a cloud-based system for electronic health records (EHR) that uses an object storage architecture to store healthcare data and enable authenticated healthcare professionals to accelerate the delivery of health services in an emergency, in an automated but secure manner [13]. Wu Q et al. developed an entropy-weighted cloud evaluation model to calculate evaluation metrics for the energy utilization potential of air conditioners based on the results of the analysis of the structure and operating mechanisms of large building air conditioners [14]. Fang et al. proposed a four-dimensional hyperchaotic system with large key space and chaotic dynamics performance, and combined it with a cloud model to construct a more complex random sequence as a keystream to solve the chaotic periodicity problem [15]. Qian J et al. developed an R-packet tranSurv and estimated the phase dependent truncation under One model of the survival function is a structural transition model that relates potential quasi-independent truncation times to observed dependent truncation times and event times [16]. Muhic M et al. developed a staged business model innovation model related to the adoption and continued use of cloud outsourcing, and the model identifies three business model innovation stages by characterizing specific capability types. The

model was experimentally demonstrated to help better understand the evolution of dynamic capabilities and the evolution of cloud sourcing companies and cloud-based business model innovation [17]. Cui et al. proposed a cloud model-based risk assessment method for the ambiguity and stochastic nature of qualitative and quantitative knowledge transformation in the risk assessment process, which was experimentally demonstrated to fully consider risk itself and the uncertainty in the inference process [18].

In summary, there are few examples of the entropy power method, network analysis, and the integrated optimization application of cloud conversion model in safety evaluation, and the same lack of experience in constructing safety indicators for assembled buildings, so the study constructs the EW-ANP model to make up for the shortage of related studies.

CONSTRUCTION OF EW-ANP SAFETY ASSESSMENT MODEL FOR ASSEMBLED BUILDING CONSTRUCTION

Selection of construction safety assessment indexes based on network analysis method

Due to the diverse safety influencing factors and complicated construction procedures of assembly building construction, its safety assessment indexes need to meet the principles of comprehensiveness, practicality and dynamism. Therefore, the research constructs the safety assessment index system of assembly building construction firstly, the construction safety indexes are screened out by text mining method, the network construction reports and accident causes are analyzed by Text Miner tool, the high-frequency words in the reports are summarized work, and the Text Miner software is used to clean up the word-sense relationship and summarize the accident causes and high-frequency words to ensure the safety assessment index system is comprehensive comprehensiveness as well as practical and reasonable [19]. Secondly, the network analysis method was used to determine the subjective weights of safety evaluation indexes, and the relationship between construction safety factors was initially judged based on the questionnaire survey, and the safety indexes derived from the text mining method were correlated with the comprehensive construction safety factors derived from the questionnaire to determine the hierarchical relationship and importance ranking between the indexes. The network structure model and judgment matrix of the network analysis method are used to divide the main criteria and secondary indicators, and their unweighted matrix is shown in equation (1).

$$X_{ic} = \begin{pmatrix} x_{i1}(\mathrm{c1}) & x_{i1}(\mathrm{c2}) & \ldots & x_{i1}(cn) \\ x_{i2}(\mathrm{c1}) & x_{i2}(\mathrm{c2}) & \ldots & x_{i2}(cn) \\ \ldots & \ldots & \ldots & \ldots \\ x_{in}(\mathrm{c1}) & x_{in}(\mathrm{c2}) & \ldots & x_{in}(cn) \end{pmatrix} \quad (1)$$

In equation (1), X_{ic} is the unweighted evaluation factor index matrix, x_{ij} is the normalized eigenvector of the j evaluation factor of the i level decision criteria, and cn is the influence factor. Next, the weights are coupled with the matrix and multiplication is performed to derive the weighting matrix, and the weighting formula is shown in equation (2).

$$W = \bar{X}_{ic} = a_{ic} X_{ic} (i = 1, 2..., n; c = 1, 2..., n) \quad (2)$$

In equation (2), W indicates the weighting matrix, $\bar{X}_{ic}$ indicates the weighting result of the evaluation factor index matrix, and a_{ij} indicates the weight of the j evaluation factor of the decision criteria at the i level. After the weights are obtained, the network structure model is used to rank the importance of the indicators, and four first-level indicators are derived, including personnel indicators, equipment indicators, environmental indicators, and policy indicators. In the process of assembly

building construction, the occurrence of safety accidents is accompanied by the injury of construction personnel and the loss of material equipment. Among the personnel indicators, those that have an impact on the safety factors of the construction process of building projects include the degree of operational standardization of construction personnel, the management experience of management personnel, the awareness of safety standardization of construction personnel and the completion of their safety training. Among the indicators of equipment and things, they include the degree of strict factory security inspection of materials, frequency of regular inspection of equipment safety, number of simulations of equipment component assembly, and fixed measures of equipment component installation and transportation. The specific index system is shown in Figure 1.

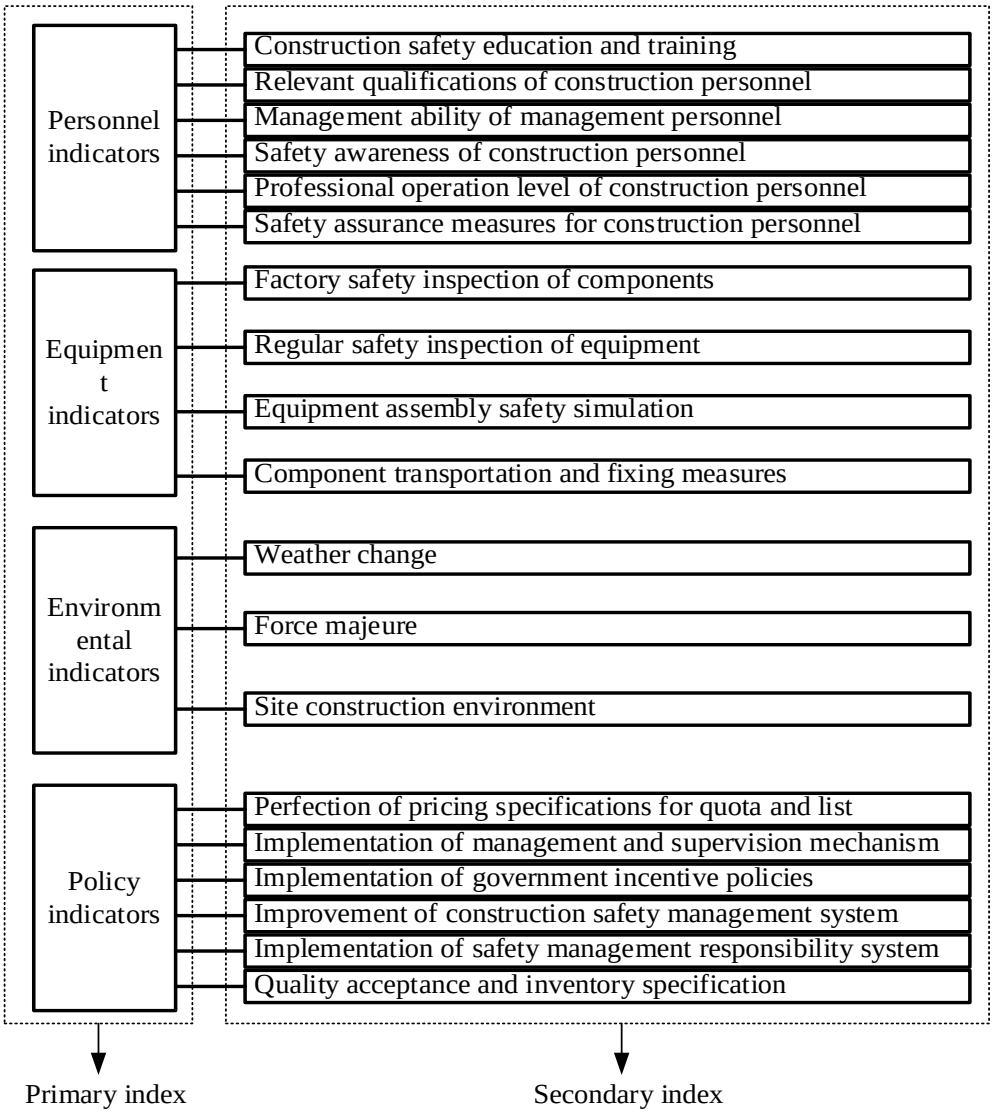

Fig. 1 – Safety evaluation index system of prefabricated building construction

As can be seen from Figure 1, in addition to personnel indicators and equipment indicators, the safety evaluation index system of the assembly building project also includes two first-level indicators of environmental factors and policy factors, and a total of 19 second-level indicators. The environmental indicators include weather changes, force majeure level construction environment conditions such as temperature, humidity and ventilation, while the policy indicators include six secondary indicators such as the specification of quality acceptance inventory, the perfection of pricing specification of quotas and lists, the implementation of safety management responsibility

system, the perfection of construction safety management system, and the implementation of government incentive policies. Therefore, the study derived the above safety evaluation index system for assembly building construction based on the correlation analysis of text mining and questionnaire survey, which can comprehensively identify the safety factors in the construction process from four perspectives: human, material, environment and policy.

Construction of safety assessment model of assembly building construction by entropy power method and ANP

After constructing the safety evaluation index system of assembly building construction, the study determined the objective weights of the indexes by entropy weight (EW) method. Since the entropy weight method has the advantages of clear data processing, reduction of the influence of subjective factors and clear operation steps, the objective weights of the entropy weight method and the subjective weights of the network analysis method are combined [20]. Firstly, the interval range of indicator data is unified by the extreme criteria method to enhance the comparability of the model, and its formula is shown in equation (1).

$$x_{ij}^{'} = \frac{x_{ij} - \min x_{ij}}{\max x_{ij} - \min x_{ij}} \tag{3}$$

In equation (3), equation (1) $\max x_{ij}$ denotes the maximum value of the initial data of the indicator in the influence factor ; i j $\min x_{ij}$ denotes the minimum value of the initial data of the i indicator in the influence factor ; j x_{ij} denotes the initial data of the i indicator in the influence factor ; j $x_{ij}^{'}$ denotes the normalized data of the i indicator in the influence factor j . After standardizing the indicator values, the data are normalized and the entropy value of the risk indicator is calculated based on the standardization matrix with the formula shown in equation (4).

$$E_i = -K \sum_{j=1}^{m} P_{ij} \ln P_{ij} \tag{4}$$

In equation (4), the indicator E_i denotes the weight of the factor i , K is the Boltzmann constant, $K = 1/\ln m$, m denotes the sample size, and P denotes the number of indicators whose calculation formula is shown in equation (5).

$$P_{ij} = \frac{y_{ij}}{\sum_{i=1}^{m} y_{ij}} \tag{5}$$

In equation (5), y_{ij} denotes the normalized indicator value after normalization, and the variance coefficient of risk indicator $g_i = 1 - E_i$ can be calculated based on the entropy value of risk indicator, and the entropy weight of risk indicator of variance coefficient can be derived, and its mathematical expression is shown in equation (6).

$$WO_i = \frac{g_i}{\sum_{i=1}^{n} g_i} \tag{6}$$

After the objective weight is calculated, the subjective weight is calculated through network analysis, and the CR value is introduced to judge the consistency of the weight matrix. Modify the matrix until the CR value meets the consistency requirements, multiply the rows of the influencing factors of the optimized matrix, and square the results n times to obtain the matrix vector. Normalize the subjective weight of the indicator. The method of network analysis to calculate the subjective weight is shown in formula (7).

$$W_i = \frac{\sqrt[n]{\prod_{j=1}^{n} b_{ij}}}{\sum_{i=1}^{n} \sqrt[n]{\prod_{j=1}^{n} b_{ij}}} \tag{7}$$

In equation (7), b_{ij} is the initial weight of the influencing factors of the weight matrix. Finally, according to the subjective weight coefficient $W = [W_1, W_2, ..., W_n]$ and the objective weight coefficient $WO = [WO_1, WO_2, ..., WO_n]$, the comprehensive weight of the index is derived, and its calculation formula is shown in equation (8).

$$WC_j = \frac{W_i WO_i}{\sum_{1}^{n} W_i WO_i} \tag{8}$$

After deriving the comprehensive weights, the probabilistic statistical cloud model is used to analyze each safety index of construction by feedback and calculate the comprehensive safety score. Using the cloud model of fuzzy mathematics in the quantitative conversion of qualitative generators reflect the natural language in the safety evaluation questionnaire, first determine the evaluation criteria grading, the formation of the standard cloud, the mathematical model is shown in equation (9).

$$\begin{cases} E_x = \dfrac{\max x + \min x}{2} \\ E_n = \dfrac{\max x + \min x}{6} \\ H_e = f \end{cases} \tag{9}$$

In formula (9), E_x indicates the evaluation expectation value, which is the qualitative concept quantification point of the evaluation results, and its calculation method is to take the absolute center of the maximum and minimum values of the security score. E_n is the rating entropy value, which indicates the randomness and fuzziness of the evaluation model, and the larger the entropy value is, the fuzzier the qualitative concept month of the evaluation results. Finally, H_e is the super entropy, which indicates the randomness of the entropy value and reflects the discrete nature of the evaluation results, and f is a constant. After the standard cloud is determined, the evaluation cloud is calculated, and the evaluation data is produced according to the secondary index i, whose model is expressed as equation (10).

$$\begin{cases} E_x u_i = \dfrac{1}{n}\sum_{q=1}^{n} x_q \\ E_n u_i = \dfrac{1}{n}\sqrt{\dfrac{\prod}{2}}\sum_{q=1}^{n}\left|x_q - E_x u\right| \\ H_e u_i = \sqrt{\left|S^2 - E_n^2 u\right|} \end{cases} \tag{10}$$

In equation (10), $E_x u_i$ is the evaluation expectation value of indicator i , x_q is the q th rating under the second level indicator, $E_n u_i$ is the rating entropy value of the indicator, $H_e u_i$ is the super entropy of the indicator rating, and S^2 is the variance of the sample to absolute center distance of the indicator. Finally, the evaluation results are calculated according to the evaluation cloud and the integrated weight, and the mathematical model is expressed as shown in equation (11).

$$\begin{cases} E_X = \sum_{i=1}^{m} WC_i E_x u_i \\ E_N = \sqrt{\sum_{i=1}^{m} WC_i E_n^2 u_i} \\ H_E = \sum_{i=1}^{m} WC_i H_e u_i \end{cases} \tag{11}$$

In equation (11), E_X , E_N , and H_E denote the comprehensive evaluation results of the secondary index i , respectively. In the comprehensive evaluation result, the comprehensive result of the evaluation cloud is valid when the similarity between the evaluation cloud and the standard cloud is large. According to the above research method, the operation flow of the summarized EW-ANP model is shown in Figure 2.

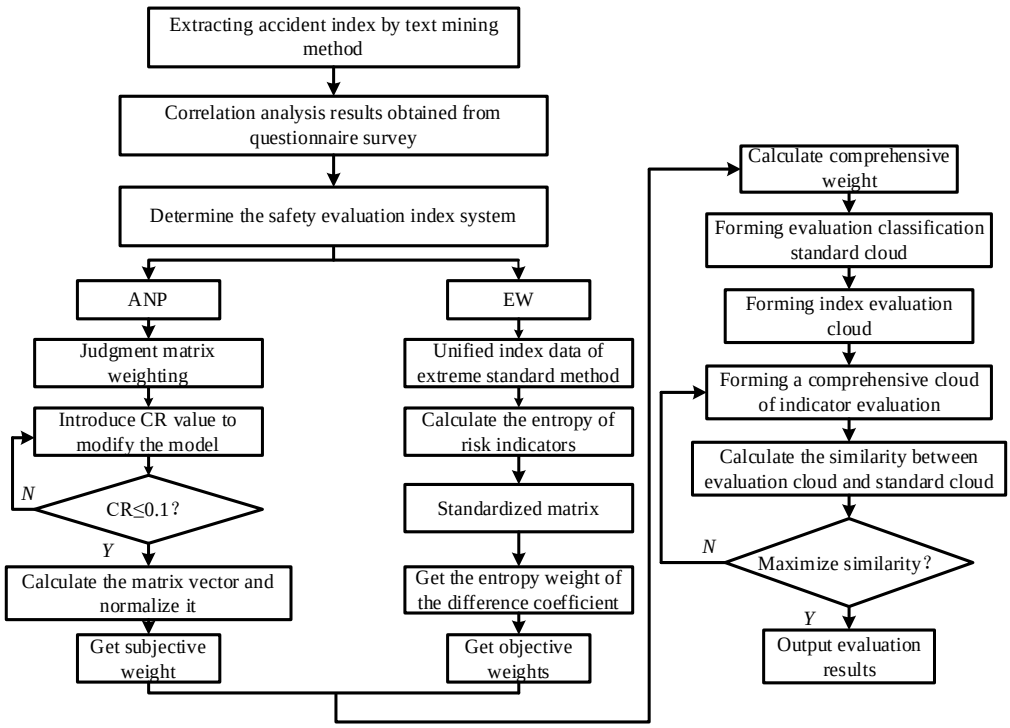

Fig. 2 – Ew-ANP model operation flow chart

From Figure 2, it can be seen that the optimization of this study to construct the safety evaluation index system lies in the modification of CR values introduced in the subjective weight matrix and the comparison of the maximum similarity of quantitative scores to qualitative transformation of the cloud conversion algorithm. The subjective weights determined by ANP and the objective weights determined by the entropy weighting method yield the comprehensive weights, and finally the evaluation cloud and the standard cloud are derived using the cloud model (Shuai Li, 2019) [21]. The research method was constructed to ensure the validity of the safety evaluation indexes and the accuracy of the safety assessment of the construction of assembled buildings.

PRACTICAL STUDY OF THE EW-ANP SECURITY ASSESSMENT MODEL

Analysis of EW-ANP index algorithm in high-rise residential construction

In order to verify the practical performance of the EW-ANP safety indicator assessment model constructed by the research method, the study selected a high-rise residential assembly construction project in a city as an example. The subjective weights of the safety index system constructed by the text mining method in this experiment relied on the expert survey method to complete, and the personnel distribution of 205 experts practicing in the construction industry who participated in this experiment is shown in Figure 3.

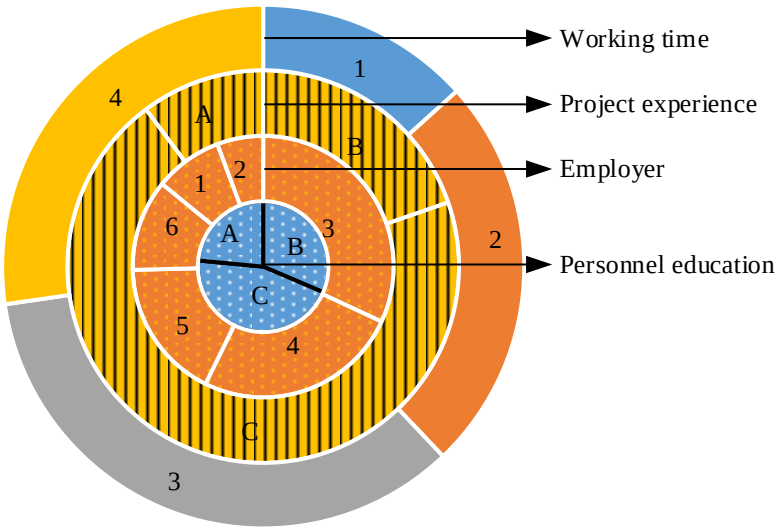

Fig. 3 – Distribution of experts participating in the questionnaire

In Figure 3, from the outer ring to the inner ring, the length of time in the field, construction project experience, organization in the field, and education level of the 2000 experts are indicated respectively. Outer ring 1 indicates the number of people who have been in the field for less than 1 year, accounting for 13.3%, outer ring 2 indicates the number of people who have been in the field for 2-4 years, accounting for 24.6%, outer ring 3 and outer ring 4 indicate the number of people who have been in the field for 5-10 years and more than 10 years, accounting for 34.8% and 27.3%, respectively. The outer ring A indicates the number of personnel involved in construction projects more than 10, accounting for 10.2%, the outer ring B and outer ring C respectively white man involved in construction projects 0-1 and 2-10, the number of people accounted for 19.7% and 70.1%. Inner ring 1-6 indicate BIM consulting units, build manufacturers, construction units, construction units, and design units and residential service units, respectively, and the number of people accounted for 8.4%, 5.7%, 31.9%, 25.4%, and 11.3%. The inner rings A, B and C denote specialist degree, bachelor's degree and graduate degree, respectively, and the number of people accounted

for is 31.4%, 45.1% and 23.5%, respectively. The weights of 19 secondary indicators and 4 level 1 indicators were derived from the experts' questionnaires as shown in Table 1.

Tab. 1 - Subjective weight of safety index system for prefabricated buildings

Primary index	Secondary index	Number	Subjective weight of secondary indicators	Subjective weight of primary indicators
Personnel index evaluation	Construction safety education and training	c1	0.1482	0.2818
	Relevant qualifications of construction personnel	c2	0.1736	
	Management ability of management personnel	c3	0.1705	
	Safety awareness of construction personnel	c4	0.1673	
	Professional operation level of construction personnel	c5	0.1834	
	Safety assurance measures for construction personnel	c6	0.1570	
Equipment index evaluation	Factory safety inspection of components	c7	0.2312	0.0827
	Regular safety inspection of equipment	c8	0.1865	
	Equipment assembly safety simulation	c9	0.3193	
	Component transportation and fixing measures	c10	0.2630	
Environmental index evaluation	Weather change	c11	0.3259	0.2141
	Force majeure	c12	0.3418	
	Site construction environment	c13	0.3323	
Evaluation of policy indicators	Perfection of pricing specifications for quota and list	c14	0.1921	0.4214
	Implementation of management and supervision mechanism	c15	0.1643	
	Improvement of construction safety management system	c16	0.1752	
	Implementation of safety management responsibility system	c17	0.1625	
	Quality acceptance and inventory specification	c18	0.1493	
	Implementation of government incentive policies	c19	0.1566	

As can be learned from Table 1, the subjective weights of the four Level 1 indicators of personnel, equipment, environment, and policy indicators are 28.18%, 8.27%, 21.41%, and 42.14%, respectively. The results indicated that the policy indicators and personnel indicators had the highest weighting, and the number of secondary indicators within both level 1 indicators was 6. Among the personnel indicators, the professional operation level of construction personnel has the highest weight, with a value of 0.1834; the safety education and safety training of construction personnel has the lowest weight, with a weight of 0.1482. Among the equipment indicators, the assembly safety simulation of construction equipment has the highest weight, with a value of 0.3193; the regular safety inspection of equipment has the lowest weight, with a weight of 0.1865. Among the environmental indicators, force majeure Among the environmental indicators, force majeure has the highest weight, with a value of 0.3418; weather changes have the lowest weight, with a value of 0.3259. Finally, among the normal indicators, the highest weight, with a value of 0.1921, is given to the situation of perfecting the fixed list pricing specifications, and the lowest weight, with a value of 0.1493, is given to the situation of quality acceptance and inventory specifications. The calculation results are shown in Figure 4.

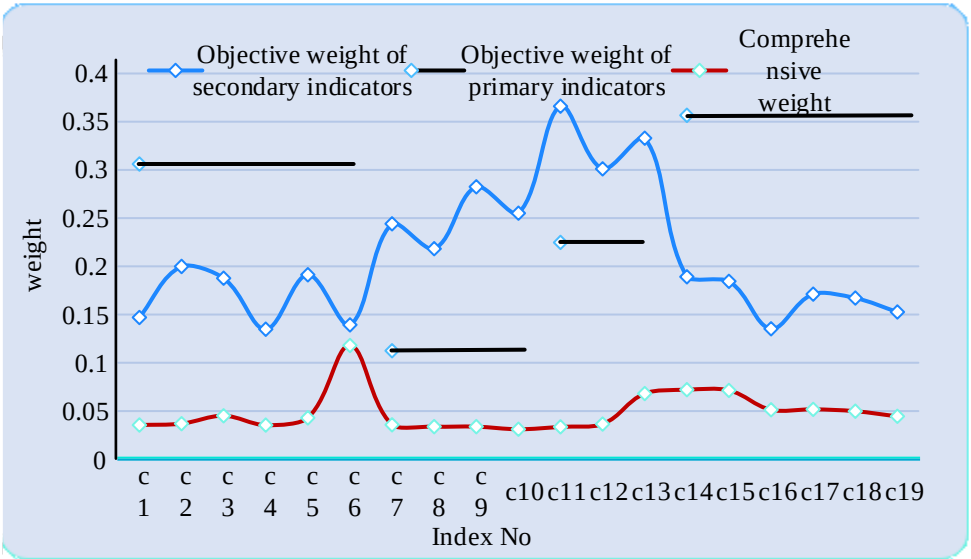

Fig. 4 – Objective weight of safety index system for prefabricated buildings

As can be seen from Figure 4, the subjective weights of the four Level 1 indicators of personnel indicators, equipment indicators, environmental indicators, and policy indicators are 30.61%, 11.25%, 22.48%, and 35.66%, respectively. Compared with the subjective weights, the objective weights of personnel indicators, equipment indicators and environmental indicators have increased, and the increase is within the range of 1%-3%, indicating that the calculation results of the subjective and objective weights are relatively unified, while the objective weight of policy indicators among the level 1 indicators has decreased by 6.48% compared with the subjective weights, indicating that the introduction of objective weights has effectively increased the applicability and effectiveness of the model. The overall evaluation index of assembly building construction safety is set as Bn, and the four first-level indicators of personnel, equipment, environment and policy indicators are set as B1, B2, B3 and B4, then the results of the subjective weight validity test of the index system are shown in Figure 5.

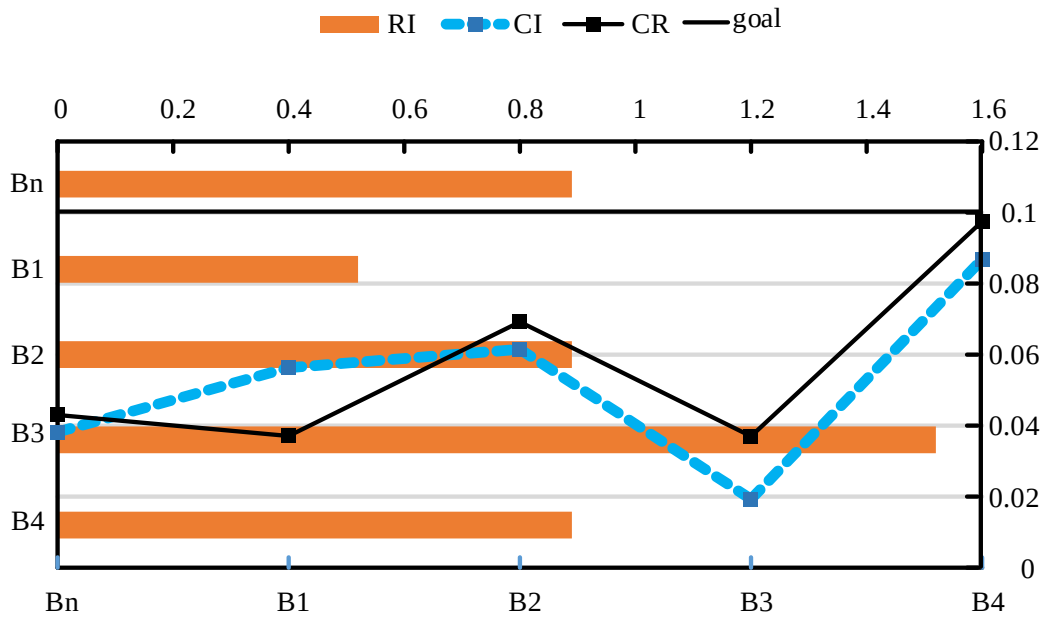

Fig. 5 – Introduction of CR value of subjective weight of index system and modification results of weight matrix

As can be seen from Figure 5, the CR values of the overall consistency tests of the index system are all less than 0.1, and the consistency test results of the overall weights of the safety evaluation indexes of assembly building construction are 0.043, and the consistency test results of the subjective weights of the four primary indexes of personnel indexes, equipment indexes, environmental indexes, and policy indexes are 0.0371, 0.0692, 0.037, and 0.0975. The CR values of indicator weights are all less than 0.1, indicating that the results of subjective weight calculation are true and valid, and have reliability in the safety evaluation of assembly building construction.

Simulation experiment of EW-ANP model for safety assessment in high-rise residential construction

According to the actual situation of the high-rise construction project and the feedback from experts, the safety evaluation level of the assembly building construction is divided into five levels: dangerous, mildly dangerous, generally safe, relatively safe and very safe. The specific evaluation criteria cloud for construction are shown in Table 2.

Tab. 2 - Standard cloud model for safety evaluation of high-rise building construction projects

Evaluation criterion	Scoring range	Ex	En	He
Danger	[0,40]	20	6.67	0.5
Mild hazard	[40,60]	50	3.33	0.5
General safety	[60,75]	67.5	2.5	0.5
Relatively safe	[75,90]	82.5	2.5	0.5
Very safe	[90,100]	95	1.67	0.5

The calculated standard cloud model for construction safety of building projects is shown in Table 2, and the intervals of safety scores for the five safety evaluation levels are 0-40 for dangerous, 40-60 for mildly dangerous, 60-75 for generally safe, 75-90 for relatively safe, and 90-100 for very

safe. After deriving the standard cloud model, 10 experts who participated in the questionnaire were invited to rate the 19 secondary indicators of the high-rise construction project as shown in Figure 6.

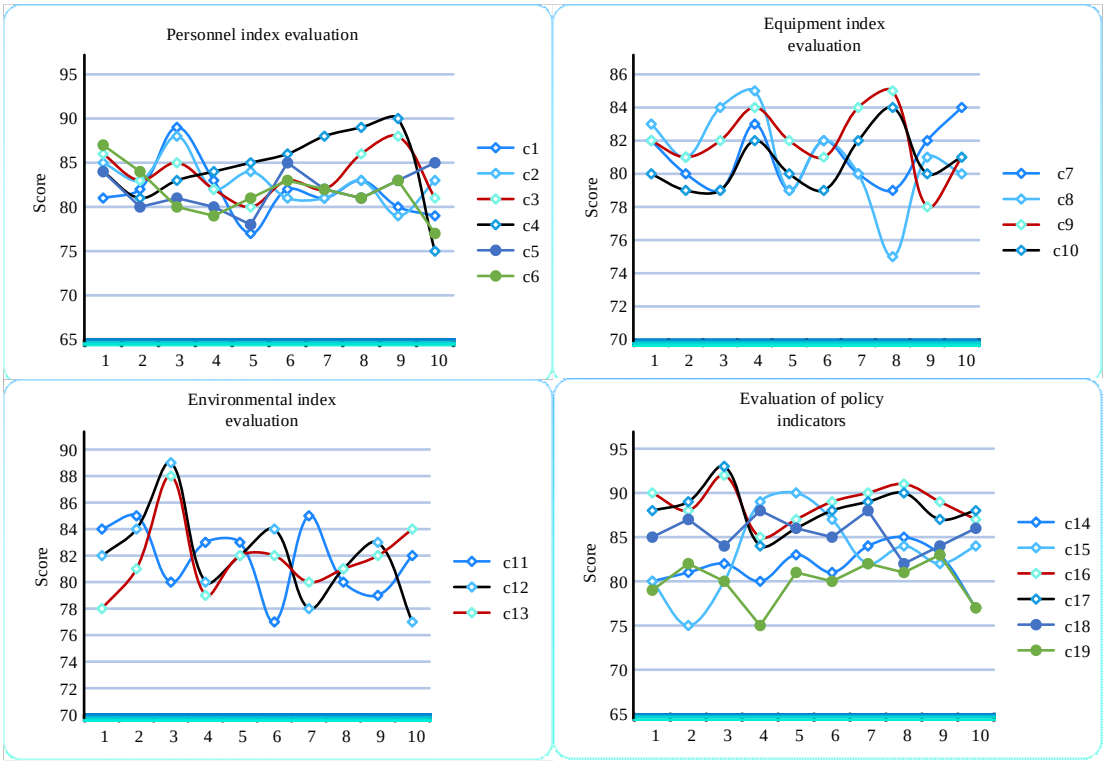

Fig. 6 – Experts' scores on 19 secondary indicators of high-rise building construction projects

As can be seen from Figure 6, the average ratings of 19 safety indicators of building construction projects by 10 experts are in the range of 81-84, with the minimum rating of 75 and the maximum rating of 93, which exist in the indicators of regular safety inspection of equipment and the indicators of implementation of safety management responsibility system, respectively, and the evaluation cloud model of building construction is derived according to the ratings, as shown in Table 3.

Tab. 3 - Evaluation cloud model of building construction

Index No	E_x u	E_n u	H_e u
c1	81.7	2.632	1.7405
c2	82.9	2.1557	0.9813
c3	83.6	2.657	1.1004
c4	84.5	3.8853	1.9548
c5	81.9	2.3813	0.8528
c6	81.7	2.632	1.5031
c7	81	1.88	0.5586
c8	81	2.5066	1.128
c9	82	1.7546	0.9598
c10	80.6	1.6544	0.2566

c11	81.8	2.8074	1.0633
c12	82	3.008	1.5836
c13	81.7	2.3813	0.7728
c14	81.6	2.256	0.0629
c15	83.3	4.3866	0.4749
c16	88.8	2.1306	0.5474
c17	88.2	2.0554	1.2264
c18	85.5	1.888	2.8826
c19	80.2	2.8826	1.5558

Based on the above standard cloud model, the average expert score and the median distance score within the evaluation cloud model were calculated to derive the similarity between the two, and the similarity results are shown in Figure 7.

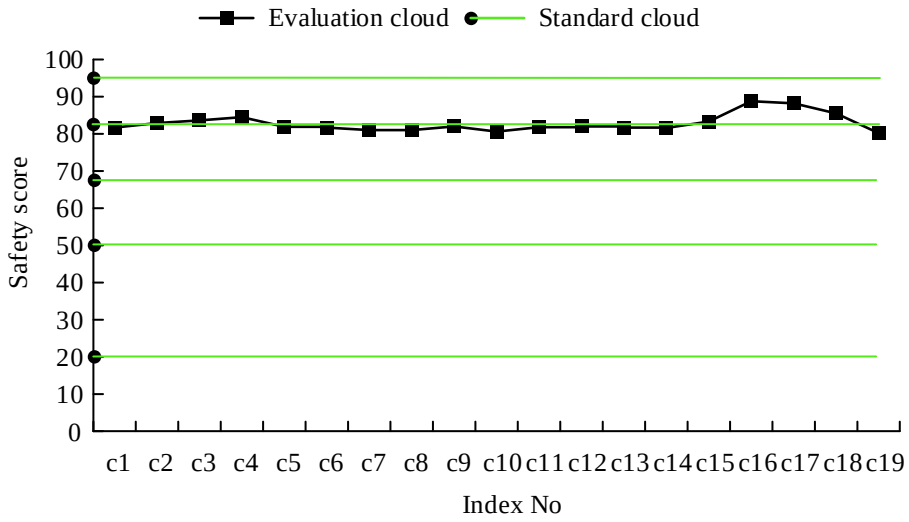

Fig. 7 – Comparison of similarity between building safety standard cloud and evaluation cloud

As can be seen from Figure 7, the rating fold of the evaluation cloud is closest to the straight line of the comparative security evaluation level in the standard cloud, and the similarity calculation results in the similarity between the evaluation cloud model and the five security levels of the standard cloud model in the order of 0.0094, 0.0691, 0.257, 0.772, and 0.3341.Finally, the subjective and objective weight evaluation model proposed in this study is compared with the traditional data survey weight evaluation model for evaluation vectors, and the specific results are shown in Figure 8.

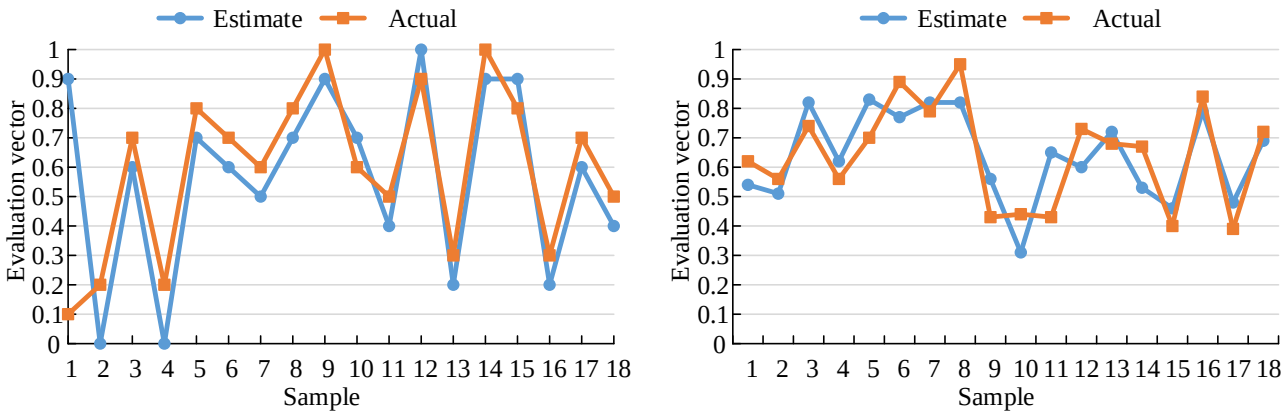

（a）Evaluation and prediction of traditional subjective and objective weight matrix

（b）Evaluation and prediction of optimizing subjective and objective weight matrix

Fig. 8 – Comparison of evaluation matrix vector between traditional method and optimization method

It can be seen from Figure 8 that in the weight matrix of the subjective and objective weight safety evaluation model of prefabricated buildings constructed in this study, the fluctuation range and error of the evaluation prediction value are smaller than those of the traditional evaluation methods. The experimental data show that the error between the predicted value of the optimized model and the actual safety evaluation vector is between 0.05-0.1, while the error of the traditional method is between 0.1-0.15. The experimental results show that the safety evaluation model is more accurate in the safety measurement of prefabricated buildings.

CONCLUSION

Through the calculation and algorithm analysis of the subjective and objective weights of the high-rise building project, the study concluded that the subjective and objective weight gap of the three secondary indicators is within the range of 1%-3%, and the subjective and objective weight gap is 6.5% only in the policy indicators, and the experiment shows that the calculation results of the subjective and objective weights corroborate each other and compensate each other, which can effectively improve the reliability of the index construction. At the same time, the CR value was introduced to analyze the consistency of the weights of the model, and the results showed that the consistency of the subjective weights of the four first-level indicators of personnel, equipment, environment and policy indicators were 0.0371, 0.0692, 0.037 and 0.0975, indicating that the construction of the subjective weight matrix has validity. In addition, the study analyzed the evaluation performance of the cloud conversion model by example, and concluded that the similarity of the five safety levels of the evaluation cloud model and the standard cloud model are 0.0094, 0.0691, 0.257, 0.772, 0.3341 in order, and the maximum similarity is 0.772, which indicates that the safety index of the example project of high-rise building is evaluated as relatively safe. The shortcoming of this experiment is that the empirical examples were selected as random results, and other influencing factors such as the geographic location of the dwelling were not considered enough.

REFERENCES

[1] Bortolini R., Formoso C.T., Viana D.D., 2019. Site logistics planning and control for engineer-to-order prefabricated building systems using BIM 4D modeling. Automation in Construction, vol. 98: 248-264.

[2] Peng Li,Huizhen Chen.Evaluation of green building suppliers based on IVPLTS-CBR decision-making method[J].International Journal of Intelligent Computing and Cybernetics,2022,15(1):17-40

[3] Anna Adamczak,Bugno,Aleksandra,Krampikowska.The basics of a system for evaluation of fiber-cement materials based on acoustic emission and time-frequency analysis.[J].Mathematical biosciences and engineering : MBE,2020,17(3):2218-2235
[4] Yu K., Cao Q., Xie C., Qu N., Zhou L., 2019. Analysis of intervention strategies for coal miners' unsafe behaviors based on analytic network process and system dynamics. Safety Science, vol. 118: 145-157.
[5] Zheng Y.Y., Xu Z., He Y., 2021. A novel weight-derived method and its application in graduate students' physical health assessment. International Journal of Intelligent Systems, vol. 36: 200-236.
[6] Abedin S.F., Alam M., Kazmi S., Tran N.H., Niyato D., Hong C.S., 2019. Resource Allocation for Ultra-Reliable and Enhanced Mobile Broadband IoT Applications in Fog Network. IEEE Transactions on Communications, vol. 67: 489-502.
[7] Li Z., Luo Z., Wang Y., Fan G., Zhang J., 2022. Suitability evaluation system for the shallow geothermal energy implementation in region by Entropy Weight Method and TOPSIS method. Renewable Energy, vol. 184: 564-576.
[8] Liang X., Liang W., Zhang L., Guo X., 2019. Risk assessment for long-distance gas pipelines in coal mine gobs based on structure entropy weight method and multi-step backward cloud transformation algorithm based on sampling with replacement. Journal of Cleaner Production, vol. 227: 218-228.
[9] Chen J.Q., 2019. Fault Prediction of a Transformer Bushing Based on Entropy Weight TOPSIS and Gray Theory. Computing in Science & Engineering, vol. 21: 55-62.
[10] Luo J., Chen S., Sun X., Zhu Y., Zeng J., Chen G., 2020. Analysis of city centrality based on entropy weight TOPSIS and population mobility: A case study of cities in the Yangtze River Economic Belt. Journal of Geographical Sciences, vol. 30: 515-534.
[11] Sivaprasad P.V., Haq N.A., 2019. An Entropy-Deng's Similarity-based technique for Modeling and Optimization of Process Variables for Laser Micro Drilling of Alloy-X. Journal of Scientific & Industrial Research, vol. 78: 223-230.
[12] Akter S., Michael K., Uddin M.R., McCarthy G., Rahman M., 2022. Transforming business using digital innovations: the application of AI, blockchain, cloud and data analytics. Annals of Operations Research, vol. 308: 7-39.
[13] Symvoulidis C., Kiourtis A., Mavrogiorgou A., Kyriazis D., 2021. Healthcare Provision in the Cloud: An EHR Object Store-based Cloud Used for Emergency. HEALTHINF, vol. 1: 435-442.
[14] Wu Q., Qi A., Zhao G., 2022. Evaluation of energy utilisation efficiency of central air conditioning in large buildings based on entropy weight-cloud model. International Journal of Global Energy Issues, vol. 44: 198-216.
[15] Fang P.F., Liu H., Wu C., Liu M., 2022. Neural-mechanism-driven image block encryption algorithm incorporating a hyperchaotic system and cloud model. Chinese Physics B, vol. 31: 197-212.
[16] Qian J., Chiou S.H., Betensky R.A., 2022. Transformation model-based regression with dependently truncated and independently censored data. Journal of the Royal Statistical Society Series C, vol. 71: 395-416.
[17] Muhic M., Bengtsson L., Ewert R., 2021. Dynamic capabilities triggered by cloud sourcing: a stage-based model of business model innovation. Springer, vol. 15: 33-54.
[18] Cui C.Q., Wang B., Zhao Y.X., Zhang Y.J., Xue L.M., 2020. Risk management for mine closure: A cloud model and hybrid semi-quantitative decision method. Mineral Metallurgy and Materials, vol. 27: 1021-1035.
[19] Tachibana S., Tsuda K., 2020. A Study of a Method to Understand the Intention of Taste Expressions through Text Mining. Procedia Computer Science, vol. 176: 1793-1802.
[20] Huan J., Ma D., Wang W., Guo X., Wang Z., Wu L., 2020. Safety-state evaluation model based on structural entropy weight-matter element extension method for ancient timber architecture. Advances in Structural Engineering, vol. 23: 1087-1097.
[21] Li S., Wang G., Yang J., 2019. Survey on cloud model-based similarity measure of uncertain concepts. Journal of Intelligent Technology, vol. 4: 223-230.

CIVIL ENGINEERING JOURNAL

Article no. 41

THE CIVIL ENGINEERING JOURNAL 4-2022

DEVELOPING A VIRTUAL OPEN-AIR MUSEUM OF VERNACULAR ARCHITECTURE

Tomáš Bouček[1], Martin Landa[1] and Petr Soukup[1]

Czech Technical University of Prague, Faculty of Civil Engineering, Department of Geomatics, Prague, Thakurova 7/2077, Czech Republic; tomas.boucek@fsv.cvut.cz

ABSTRACT

Vernacular architecture is an integral part of the national cultural heritage. Today, however, many of these buildings exist only on old plans or photographs and the average citizen has no opportunity to get acquainted with this part of the national identity. Therefore, in our work, we present the development of two web applications with the aim of creating a virtual open-air museum for presenting vernacular architecture in the Czech Republic. The applications were created using open-source technologies, and are implemented with methods that allow easy transfer from one operating system to another. The presented content is a carefully selected sub-sample of more than 10,000 available records representing all regional types of vernacular architecture. The result is one application designed for editors to manage the presented content and one application allowing interactive viewing of the available geo-located records designed for the general public. Individual records can be searched either directly using the map window or by querying the attribute table. These records contain descriptive information about the object, as well as historical photographs and plans and, for some objects, additional information in the form of 3D models, PDF documents and other files. The applications are designed in such a way that their content can be freely expanded in the future and thus contribute to the popularization of vernacular architecture among the general public, which was the main reason for their creation.

KEYWORDS

Web application, Deployment, Docker, Map application, Open-air museum, Open source, QGIS, Gisquick, Vernacular architecture, 3D model, Component-Based Software Engineering, Dynamic architecture, Web-based DBMS

INTRODUCTION

The use of open-source software technologies is increasingly popular across almost all fields related to the development of software tools, web application development is not an exception. Therefore, in this paper, we present two web applications that were created using a combination of several open-source software packages. Both applications were developed within the VISKALIA (Virtual open-air museum of vernacular architecture) project, which is supported by the Ministry of Culture of the Czech Republic [1].

The main objective of the VISKALIA project is to document and present the vernacular architecture in the Czech Republic. Vernacular architecture can be considered an important part of regional and national identity. In the collections of the National Museum of the Czech Republic and the Institute of Ethnology of the Czech Academy of Sciences, there is a large number of historical documents from this field (plans, photographs, drawings, textual descriptions) in several separate collections. Within the framework of the project, these documents were digitized, stored in a unified manner in a database (hereinafter referred to as a central database) and made available to the public on the web. The central database contains more than 10,000 records and its web interface allows

users to search for records according to several basic criteria (e.g. location, regional type, purpose, object material).

The comprehensive set of records in the central database is a unique source of information, especially for the professional public. The general public finds it more difficult to navigate such a large and structured database. Therefore, the virtual museum VISKALIA was created to present the basic features of the cultural heritage contained in vernacular architecture in a clearer way. It contains approximately 200 carefully selected buildings (objects) representing all regional types of vernacular architecture in the Czech Republic. All the documents (records) registered for these objects in the central database are also available in the virtual open-air museum in the form of a database (hereinafter referred to as a selective database). In addition, other specific information such as text documents or photographs, as well as spatial models, can be recorded for the objects in the selective database.

Spatial models have a great potential in terms of visualization and attractiveness for users. However, the creation of detailed models of building objects is a very laborious task, complicated in our case by the fact that the selected historical objects usually no longer exist, or their original (modelled) state has been changed by reconstruction. It is therefore necessary to rely on the surviving documents, which are most often plan documentation and period photographs or drawings. Colleagues from the National Museum and the Institute of Ethnology selected a total of 15 buildings (Appendix Table A1), which represent all regional types of rural buildings. Details of the creation of models from plan documentation are described in a separate article [2].

Physical models of buildings, which have already been created for some objects in the past and are stored in the archives of the National Museum, can also be a specific type of basis for digital modelling. For this purpose, a total of three objects were selected (Appendix Table A2), one of which contains an interior that was also the subject of digitisation.

The creation of a web application with a focus on vernacular architecture is also discussed by Ammendola et al. [3], mentioning that this way of disseminating information is the best option to reach the attention of the general public. Another advantage mentioned is the possibility of constant improvement and integration of other records. Other authors also mention the importance of sharing cultural heritage. Dhonju et al. [4] describe the creation of an online geo-crowdsourcing system designed for large-scale documentation and sharing of cultural heritage. One of the authors' reasons for creating such a system was the fact that cultural heritage around the world is under considerable risk from natural and anthropogenic threats. The creation of a web application for cultural heritage has also been addressed by Mantegari et al. [5] and Chalkidou et al. [6]. An important part of documenting cultural heritage is the creation of 3D models and their subsequent presentation. Therefore, Guarnieri et al. [7] deal in their work with a case study regarding the development of a web-based application for the interactive exploration of 3D models. Nishanbaev [8] also deals with 3D models of cultural heritage in his work. Specifically, his goal was to create a web repository for 3D models. Recently, augmented and virtual reality has become increasingly popular. Their usage in the presentation and preservation of cultural heritage has been addressed in the works of Rattanarungrot et al. [9] and Selmanović et al. [10] respectively.

Another example of web application development is described in the work of Jílková & Cajthaml [11], who worked on the creation of a database of historical atlases in the Czech Republic. Web application with similar content has already been created in another project called “A Transformation of Rural Architecture with Emphasis on the Development of the 19th and 20th Centuries” [12]. Specifically, this is a map application (available from https://country.fsv.cvut.cz/) that has been discussed as a possible basis for our map application, although the technologies used in its creation are not exactly state-of-the-art nowadays (framework based on PHP). The development of the application was preceded by the creation of the web database described in the article by Soukup & Sýkora [13]. The second option was to start with the map application from scratch, which we eventually chose. Our inspiration was a map application dealing with hydrological data (available from https://rain.fsv.cvut.cz/webapp/gisquick/), which partly uses the same open-source technologies as in our case, as described by Landa et al. [14].

Based on the topic that our web applications address and the requirements that the applications should meet, we set the overall goal divided into the following objectives:

- attractive presentation of rural architecture in virtual space;
- separate user interfaces for editors and visitors;
- easy deployment of the whole system.

METHODS

A high-level static architecture of our solution was designed based on system requirements and the objectives highlighted in the introduction section. The system design comes from Component-Based Software Engineering (CBSE) [15]. Based on the static architecture of the system, a dynamic architecture was developed. It allows the evaluation of the interaction between system components in a sequential order. Workflow diagrams were designed in the Unified Modeling Language (UML). The system was programmed using Bash, Python, Structured Query Language (SQL), and JavaScript. Web applications were designed using Django and Gisquick frameworks. Spatial models were visualized using Three.js library [16]. For system deployment Docker technology [17] was used.

RESULTS

System design

This section describes the system design. A high-level static architecture presents the core software components of the system. A system dynamic architecture shows interaction between the core components.

High-level system architecture

The high-level system architecture is based on a client-server model. System software components (Table 1, Figure 1) are decomposed into three layers: persistence, application and client layer the persistence layer provides selective (P1) and publication (P2) databases. Software components in this layer preserve the data for further processing and publication. The application layer contains a deployment package (A1) which controls system deployment of two web applications and related databases. The first web application is dedicated to the editors (A2). The application provides access to the data stored in the selective database (P1). The second web application (A3) presents data from the publication database (P2), which is deployed from the selective database (P1) by A1 package. The functionality of web applications A2 and A3 is provided in the client layer via a web browser (C1).

The system design considers three types of users: system administrator, editor and visitor. The system administrator may easily deploy and manage the system. The editor may add or modify additional information served by the selective database (P1) using web application A2. The visitor may interactively browse data content provided by the publication database (P2) via map application A3.

Tab. 1 - System components overview.

ID	Component name	Layer	Description
P1	Selective DB	Persistence	Store selected data from central DB
P2	Publication DB	Persistence	Store geospatial data for publication
A1	Deployment package	Application	Deploy the system
A2	Editorial App	Application	Web application for editors
A3	Map App	Application	Web map application for the public
C1	Web browser	Client	Software component to access A2, A3

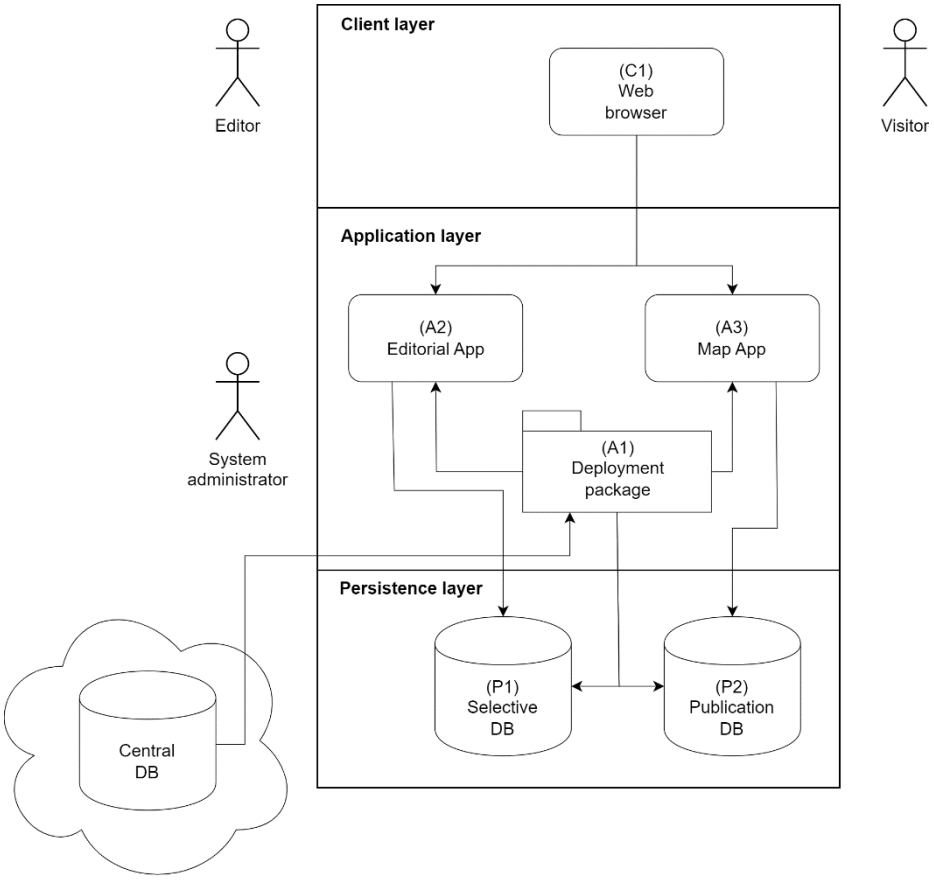

Fig. 1 – Static high-level system architecture.

Dynamic system architecture

The dynamic architecture design reflects the interactions of the system software components (Table 1) in time. The UML sequential diagram Figure 2 shows the interaction between the software components A1, A2, A3 (application layer) and P1, P2 (persistence layer). The deployment process starts with the initial configuration of the system. Next, the deployment package (A1) performs four major operations. First, the selective database (P1) is deployed. By this operation selected data records are imported from the central database into the selective database, the data is normalized and a synchronization process between central and selective databases is activated. It ensures that data provided by the selective database will always be synchronized with the central database content. Second, the editorial web application (A2) is deployed. Third, the publication database (P2) is deployed and geospatial features, required for the visualization of the objects in the interactive map, are created. Four, the web map application (A3) is deployed.

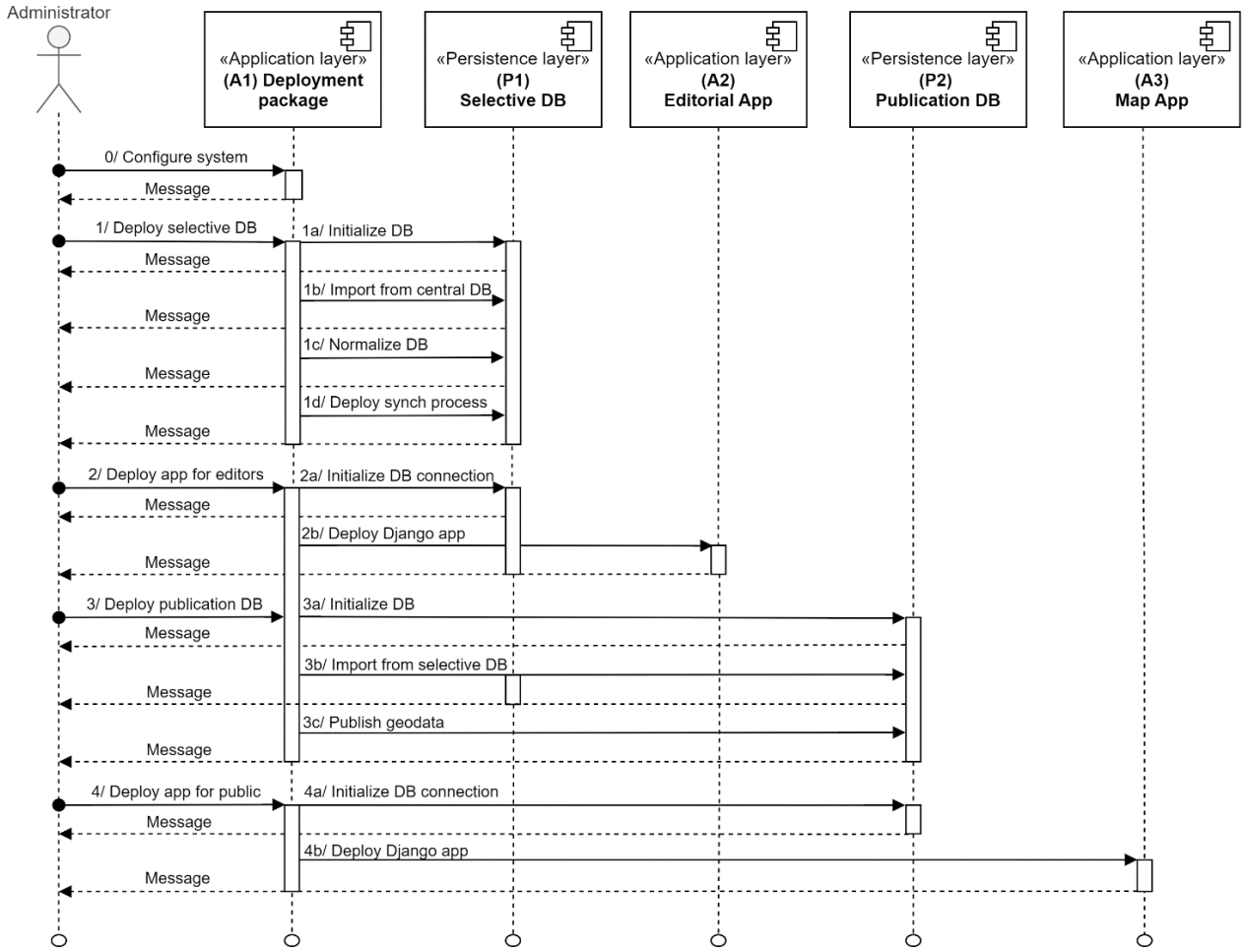

Fig. 2 – Dynamic system architecture.

Implementation

Two web applications were created - the editorial and the map application. Only open-source software components were used to achieve the desired outcomes. In the following sections, both applications including the deployment package and related databases are described in more detail in terms of development and functionality.

Deployment package

The deployment package was programmed in Bash, Python and SQL. The deployment process is controlled by Docker containers and a docker-compose tool. There are five deployed services (Docker containers):

- db: responsible for the selective database (P1);
- syncdb: responsible for synchronization between the selective (P1) and the central database;
- phpmyadmin: provides access to the selective database (P1) via web interface for system administrators;
- editapp: responsible for editorial web application deployment (A2);
- mapapp: responsible for web map application (A3) and the publication database (P2) deployment;

The deployment of the complete system is done by a command below:

```
$ docker-compose up
```

Selective and Publication databases

The selective database is provided by object-relational database management system MariaDB. The database contains three relations:

- objects_of_interest: the main relation describing objects of interest (buildings)
- files_central: information about files (photographs, plans) taken from the central database
- files_selective: files (spatial models, photographs, documents, etc.) managed by the selective database

Records from files_central and files_selective are linked to objects_of_interests via the foreign key defined by the OID attribute (Figure 3).

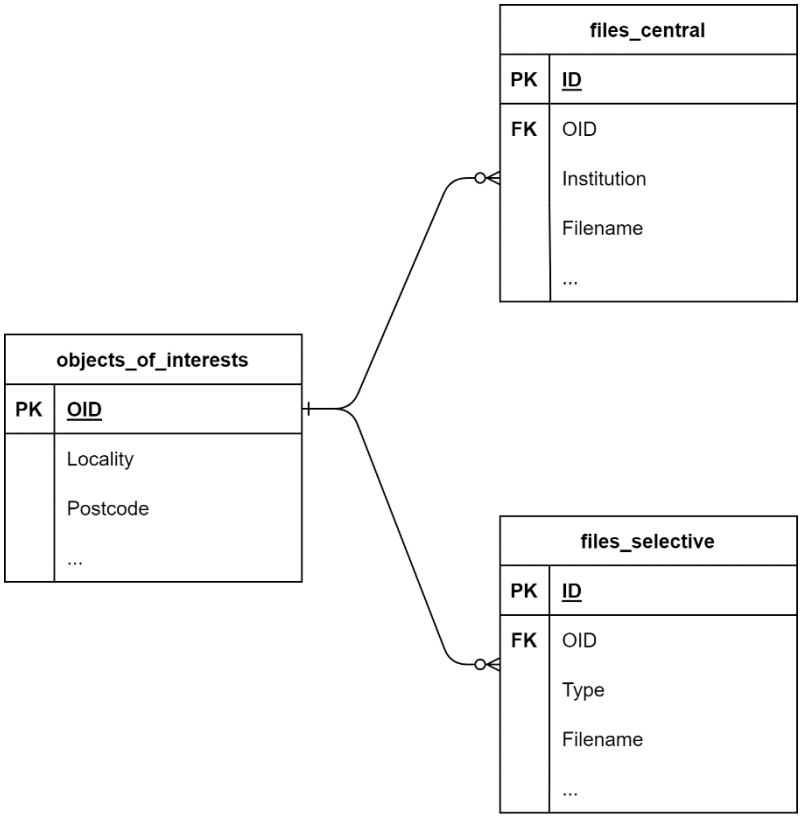

Fig. 3 – Selective database entity relationship diagram.

The publication database is deployed from the selective database supplemented by point geometry. The database is driven by SQLite file-based format extended by OGC Geopackage specification[1].

Editorial Web Application

To design the editorial application (Figure 4), the open-source high-level Python web framework Django[2] was used. The editorial application manages the selection of objects from the central database and access to it is authorized. It is therefore intended only for the creators and administrators of the selective database, which contains objects of interest of the VISKALIA project. The editors may view and edit individual records, which can be searched by keywords or filtered by district or region. It is then possible to add new files (photos, documents, models) to a specific record,

[1] OGC GeoPackage https://www.geopackage.org/
[2] Django project https://www.djangoproject.com/

which represents the content of the selective database. The editorial application is regularly synchronized with the central database to guarantee its up-to-dateness.

Fig. 4 – Editorial Web Application.

Web Map Application

Map application (Figure 5) is designed for the general public, so anyone can access it. It allows users to interactively view individual geographically localized records and display information about them using the attribute table or, better, a customized infopanel. Users can switch between base layers (base map, orthophoto and historical orthophoto) or display administrative boundaries (districts, regions or state border). It is also possible to filter between individual records using the already-mentioned attribute table. In addition, the application also allows to measure distances between interactively entered points and determines the size of manually defined areas.

The application generally uses the Czech localization, but the user interface can be switched to English. However, the information displayed for individual objects is taken from a database that is not managed by us, so the possibility of having this information in English in the future seems unfortunately unlikely.

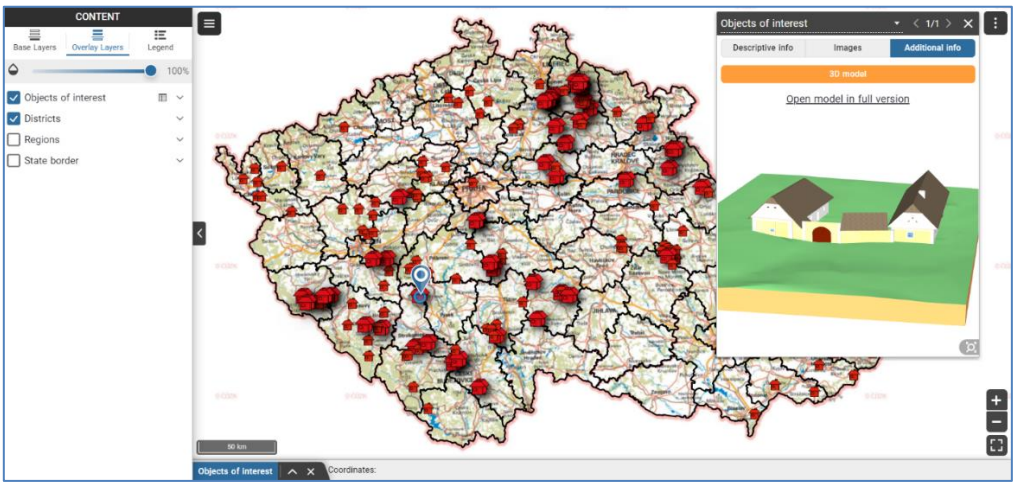

Fig. 5 – Web Map Application.

The combination of QGIS software[3], which was used to create a project with all desired layers (base layers, overlay layers and symbology), and Gisquick[4] publishing platform was used to create the map application. The individual published layers are summarized in Table 2. The Gisquick QGIS plugin was used to upload the project to the publication server. The server can be accessed using a web interface. Three layers were defined as the base and six layers as the overlays. For base layers, Web Map Tile Service (WMTS) was used to get the fastest possible data retrieval. Two of the six overlay layers are not viewable because they do not contain geometry, the layers contain additional information about objects like photographs, plans, spatial models, etc.

Tab. 2 - Overview of the published layers.

Layer	Type	Viewable	Queryable
Base map	Base layer	yes	no
Orthophoto	Base layer	yes	no
Historical orthophoto	Base layer	yes	no
Objects of interest	Overlay layer	yes	yes
Files from central DB	Overlay layer	no	yes
Files from selective DB	Overlay layer	no	yes
Districts	Overlay layer	yes	no
Regions	Overlay layer	yes	no
State border	Overlay layer	yes	no

Gisquick customization (info panel)

Information about a specific object can be displayed more clearly in the aforementioned infopanel, which is displayed in the right part of the map window after clicking on the object of interest. However, in its generic form, it displays information about the objects of interest in a similar way to the attribute table, which was not sufficient in our case, either from an informational or aesthetic point of view. Our goal was to display information about the object not only from the attribute table of the corresponding layer, but also from associated tables containing information about photos and other files of the object. Photographs and other files, such as spatial models or PDF documents, were also intended to be displayed in the infopanel. Therefore, it was necessary to customize the infopanel according to our needs. For the purpose of customization, including the implementation of the required functionality, the JavaScript framework Vue.js[5] was used. To upload the customized infopanel to the Gisquick server, it first had to be compiled into the necessary format. The npm command line utility was used for this compilation.

Unlike the generic infopanel, the customized infopanel consists of three parts. The first part of the infopanel relates to descriptive information such as location, description number, municipality, district, house type or a more specific description of the property. All the information displayed in the first tab is taken from the objects_of_interest relation (Figure 3). The second part is designed for displaying images (historical photographs, plans, etc.) of the object and related information. It allows clicking on the images to view them outside the infopanel in full size or save them to a local device. The files from the central database are the source of information for the second part of the infopanel (files_central relation in Figure 3). The third part is dedicated to additional files (files_selective relation in Figure 3) such as 3D models, PDF documents, additional images not included in the central database and possibly other files (e.g. DOCX, TXT, etc.). In the case that additional files are

[3] QGIS project https://www.qgis.org/
[4] Gisquick publication platform https://www.gisquick.org/
[5] Vue.JS project https://vuejs.org/

uploaded, the third section is further subdivided into one to four sub-sections. The content corresponds to the distribution of each possible file. The second and third parts of the infopanel are shown in Figure 6.

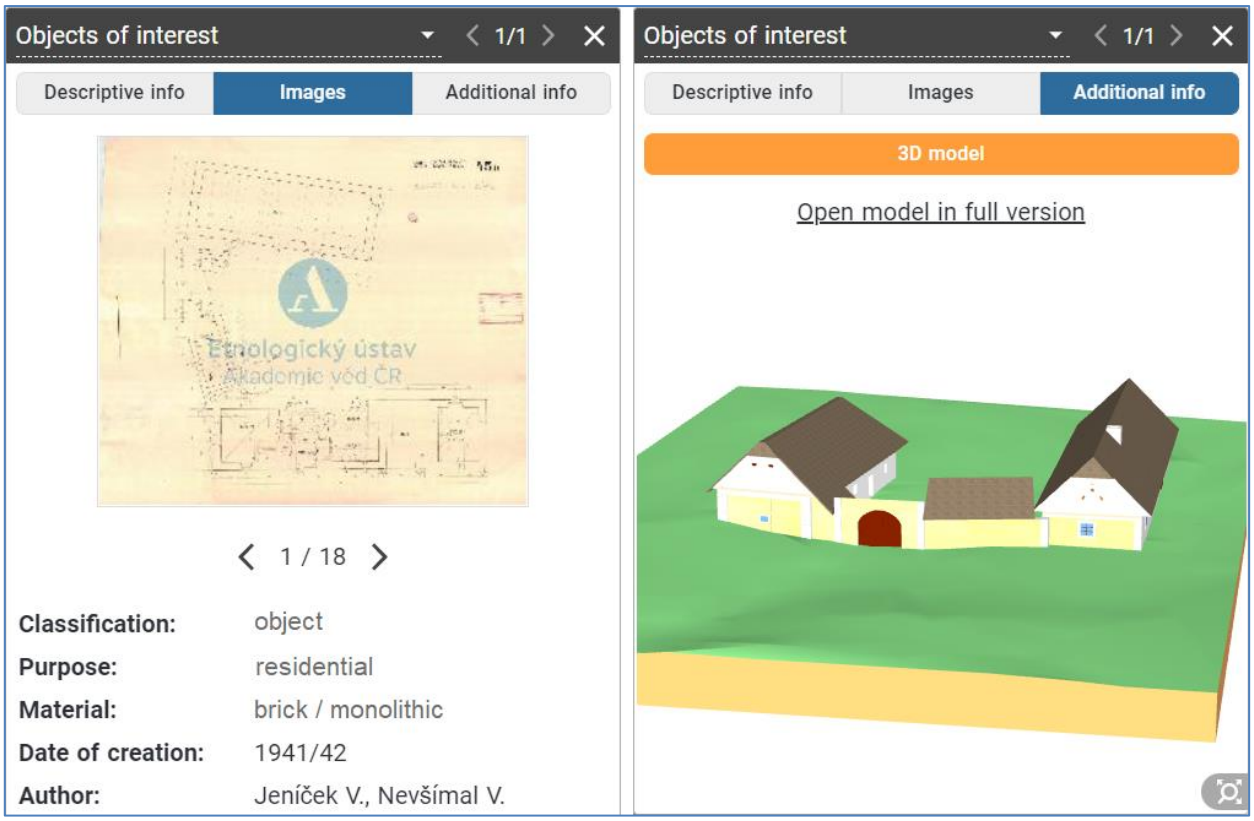

Fig. 6 – The second and the third part of infopanel.

In the preview, the 3D models are only in the basic version, but it is still possible to change the view or zoom in and out of the model. However, there is also a link to the full version of the 3D model providing additional functionality such as showing and hiding different layers of the model (Figure 7). PDF files are displayed in the infopanel similarly to images, where clicking on the preview opens a window with the full version of the PDF file. Any additional files only have a link in the infopanel to either download the file or to display it in a new window if the web browser is capable of doing so.

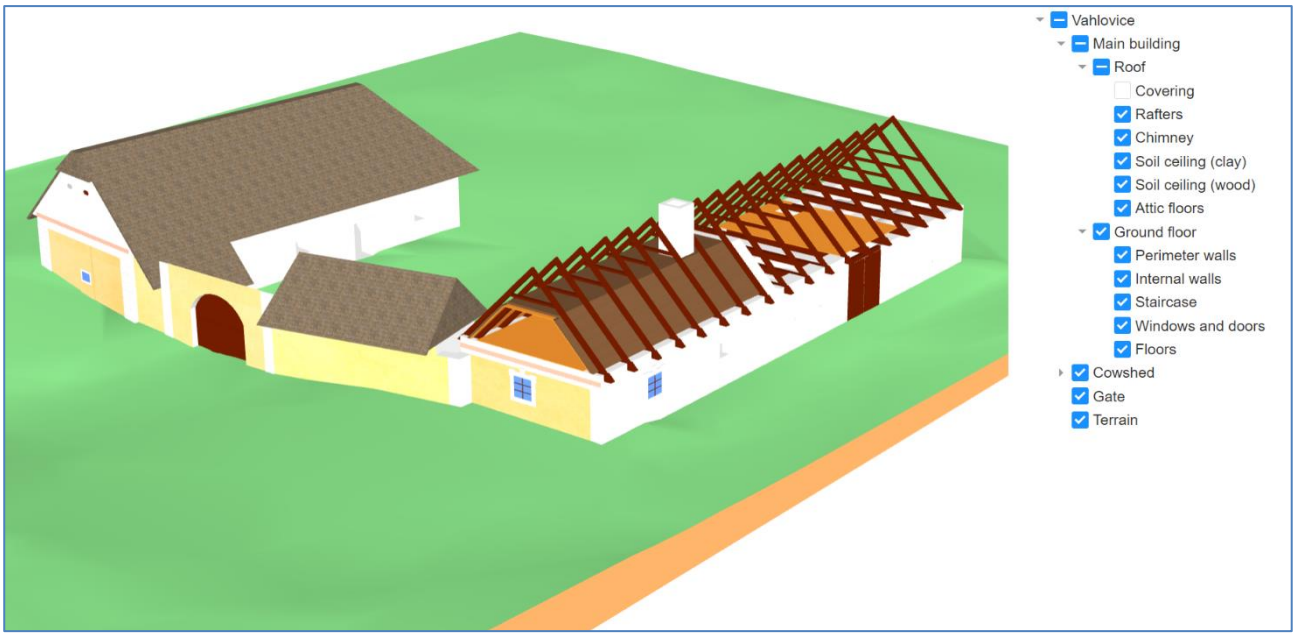

Fig. 7 – Interactive viewing of the 3D model by layers.

CONCLUSION

The article describes the creation of software for the implementation of a web-based open-air museum of vernacular architecture in the Czech Republic. The basis of the open-air museum called VISKALIA are two separate applications that provide all the necessary functions for the management and presentation of its content. The content management application (https://skansen.fsv.cvut.cz/editapp/) is intended for authorized editors who fill the selection database with guaranteed content. The application for the presentation of the content of the open-air museum (https://skansen.fsv.cvut.cz) is intended for all those interested in vernacular architecture, i.e. both the general public and experts.

At present, the virtual open-air museum contains general information on approximately 200 buildings, of which detailed spatial models have been created for 18 buildings. A total of 15 of these models were created on the basis of surviving plan documentation using CAD tools. The remaining three models were created by digitizing existing physical models using the photogrammetric method Structure-from-Motion.

The number of building objects integrated into the virtual open-air museum can be freely expanded according to the needs without the need to modify the software solution. Only open-source tools were used for the development, management and presentation of the open-air museum. The chosen basis for working with spatial data is the QGIS platform, extended by the Gisquick publishing platform. In order to present the content of the virtual museum in an attractive way, it was necessary to perform specific programming modifications to standardized tools, especially to the content of the integrated infopanel.

The whole system is modular and easily transferable to other technical equipment. While the development and testing of the web applications took place on the technical equipment of the Czech Technical University in Prague (the workplace of the system developers), the production version of the museum will be deployed on the infrastructure of the National Museum (the workplace of the system administrators). The easy portability of the applications and all the interconnected software is ensured by the chosen solution based on Docker containers.

The created virtual open-air museum VISKALIA presents selected information about important objects of rural architecture in a unified way. We assume that in the future the number of presented objects and information will gradually increase. We expect that the practical experience

of the users of the virtual open-air museum will also provide valuable suggestions for its further development.

We believe that the created virtual open-air museum will contribute to the popularization of vernacular architecture among the general public and will become an interesting platform for the professional community.

ACKNOWLEDGEMENTS

This work was supported by the Ministry of Culture of the Czech Republic from the Program for the Support of Applied Research and Development of National and Cultural Identity for the Years 2016-2022 (NAKI II), grant project "VISKALIA – Virtual Open-air Museum of the Vernacular Architecture ", No. DG20P02OVV003.

REFERENCES

[1] VISKALIA project. Available online in Czech: http://viskalia.fsv.cvut.cz/projekt/index.html (accessed on 20 October 2022)

[2] Poloprutský Z., Frommeltová E., Münzberger J., & Sedlická K., 2022. 3D Digital Reconstruction of Defunct Rural Buildings Based on Archival Sources. The Civil Engineering Journal 31(1), 196–210, Prague. DOI: https://doi.org/10.14311/CEJ.2022.01.0015

[3] Ammendola J., Dipasquale L., Ferrari E. P., Mecca S., Montoni L., & Zambelli M, 2022. A collaborative Web App to foster a knowledge network on vernacular herit-age, craftspeople, and sustainability. DOI: https://doi.org/10.4995/HERITAGE2022.2022.14951

[4] Dhonju H. K., Xiao W., Mills J. P. & Sarhosis V., 2018. Share Our Cultural Heritage (SOCH): Worldwide 3D Heritage Reconstruction and Visualization via Web and Mobile GIS. ISPRS Int. J. Geo-Inf., 7, 360. DOI https://doi.org/10.3390/ijgi7090360

[5] Mantegari G., Palmonari M. & Vizzari G, 2010. Rapid prototyping a semantic web application for cultural heritage: the case of MANTIC. In Extended Semantic Web Conference (pp. 406-410). Springer, Berlin, Heidelberg. DOI: https://doi.org/10.1007/978-3-642-13489-0_33

[6] Chalkidou, S., Arvanitis, A., Patias, P. & Georgiadis, C., 2021. Spatially Enabled Web Application for Urban Cultural Heritage Monitoring and Metrics Reporting for the SDGs. Sustainability, 13(21), 12289. DOI: https://doi.org/10.3390/su132112289

[7] Guarnieri A., Pirotti F. & Vettore A., 2010. Cultural heritage interactive 3D models on the web: An approach using open source and free software. Journal of Cultural Heritage, 11(3), 350-353. DOI: https://doi.org/10.1016/j.culher.2009.11.011

[8] Nishanbaev I. (2020). A web repository for geo-located 3D digital cultural heritage models. Digital Applications in Archaeology and Cultural Heritage, 16, e00139. DOI: https://doi.org/10.1016/j.daach.2020.e00139

[9] Rattanarungrot S., White M., Patoli Z. & Pascu T., 2014. The application of augmented reality for reanimating cultural heritage. In international conference on virtual, augmented and mixed reality (pp. 85-95). Springer, Cham. DOI: https://doi.org/10.1007/978-3-319-07464-1_8

[10] Selmanović E., Rizvic S., Harvey C., Boskovic D., Hulusic V., Chahin M. & Sljivo, S, 2020. Improving accessibility to intangible cultural heritage preservation using virtual reality. Journal on Computing and Cultural Heritage (JOCCH), 13(2), 1-19. DOI: https://doi.org/10.1145/3377143

[11] Jílková P., Cajthaml J., 2019. Database of Historical Atlases: An Interactive Web Application. In: Proceedings of the International Cartographic Association. Tokyo: International Cartographic Association, 2019, vol. 2. ISSN 2570-2092. DOI: https://doi.org/10.5194/ica-proc-2-52-2019

[12] Proměna venkovské architektury [online]. Available online in Czech: http://venkov.fsv.cvut.cz/projekt/index.html (accessed on 20 October 2022)

[13] Soukup P., Sýkora K., 2020. Development of Rural Architecture – Design and Creation of a Web Database. The Civil Engineering Journal, 29(4), 490–499, Prague. paper: http://venkov.fsv.cvut.cz/projekt/publikace/2020_PS_KS_CEJ.pdf

[14] Landa M., Kavka P., Strouhal L., & Cepicky J. (2017). Building a Complete Free and Open Source GIS Infrastructure for Hydrological Computing and Data Publication Using GIS.lab and Gisquick Platforms. International Archives of the Photogrammetry, Remote Sensing & Spatial Information Sciences, 42. DOI: https://doi.org/10.5194/isprs-archives-XLII-4-W2-101-2017

[15] Vale T., Crnkovic I., De Almeida E. S., Neto P. A. D. M. S., Cavalcanti Y. C., de Lemos Meira S. R., 2016. Twenty-eight years of component-based software engineering. Journal of Systems and Software, 111, 128-148. DOI: https://doi.org/10.1016/j.jss.2015.09.019
[16] JavaScript 3D Library. Available online: https://threejs.org/ (accessed on 20 October 2022)
[17] Martin A., Raponi S., Combe T., Di Pietro R., 2018. Docker ecosystem – Vulnerability Analysis, Computer Communications, Volume 122, Pages 30-43, ISSN 0140-3664, DOI: https://doi.org/10.1016/j.comcom.2018.03.011

APPENDIX A

Tab. A1 - List of objects modeled from the plan documentation.

Id	Village	No.	District	Localization	Exist
1	Bukovina nad Labem	29	Pardubice	50.1220700N, 15.8202439E	no
2	Bukovno	6	Mladá Boleslav	50.4460500N, 14.8392292E	no
3	Francova Lhota	67	Vsetín	49.2079658N, 18.1195658E	no
4	Hlavatce	10	České Budějovice	49.0672028N, 14.2631239E	no
5	Kundratice	60	Semily	50.5815156N, 15.4261467E	yes
6	Náklo	27	Olomouc	49.6525242N, 17.1232369E	no
7	Ostravice	102	Frýdek-Místek	49.5234169N, 18.4025003E	no
8	Petrovice	14	Domažlice	49.4422497N, 12.8915386E	yes
9	Smilkov	14	Benešov	49.6022808N, 14.6168611E	no
10	Šťáhlavice	7	Plzeň-jih	49.6598903N, 13.5249767E	yes
11	Telecí	16	Svitavy	49.6777831N, 16.1960297E	yes
12	Vahlovice	3	Strakonice	49.4460400N, 13.9447031E	yes
13	Zbečno	22	Rakovník	50.0415297N, 13.9207711E	yes
14	Zbožice	2	Havlíčkův Brod	49.6560347N, 15.5633075E	no
15	Zlámanec	12	Uherské Hradiště	49.1284622N, 17.6297361E	no

Tab. A2 - List of objects modeled from physical models.

Id	Village	District	Interier	Note
1	Hlinsko	Chrudim	no	small cottage
2	Orlová	Karviná	yes	wooden cottage
3	Vysoké Mýto	Jablonec nad Nisou	no	town hall

CIVIL ENGINEERING JOURNAL

Article no. 42

THE CIVIL ENGINEERING JOURNAL 4-2022

AN EXPERIMENTAL STUDY ON SHEAR PERFORMANCE OF ADHESIVE INTERFACE BETWEEN STEEL PLATES AND CFRP

Yi Yang, Qianziyang Zhou, Jiahao Bai and Xinyan Guo

School of Civil Engineering and Transportation, South China University of Technology, Guangzhou 510640, China; liyang01245@126.com

ABSTRACT

CFRP (Carbon Fiber Reinforced Polymer) is widely used in steel structural reinforcement. For steel structures strengthened with CFRPs, except the cases the structures have defects before strengthening, the adhesive interface is the weakest part and CFRP debonding is the most common failure mode. In order to investigate the failure mechanism of CFRP strengthened steel structures, this paper presents an experimental study on shear performance of adhesive interface between CFRPs and steel plates by twin shear model. Six steel plates strengthened with CFRP are divided into two groups, one has no damage, another has a gap at the mid. The specimens are tested under tensile loadings. The experimental results show that, the plates with a gap failed for CFRPs debonding, the cracking loading and breaking loading are 14.85kN, and 17.88kN respectively; the strain-loading curves had long linear stages, two strains decreased, and other strains of another side increased rapidly at the cracking loading, then they both rose until the plates failed.

KEYWORDS

Adhesive interface, CFRP, Steel plate, Shear stress, Experimental study

INTRODUCTION

As a new kind of reinforcing composite materials, CFRP has some advantages such as light weight, high strength and elasticity, easy construction, corrosion resistance, low thermal conductivity, electrical isolation, and has been used wildly in structural strengthening. The researches on the steel structural strengthening with CFRP are focus on bending reinforcement, tension reinforcement and fatigue reinforcement [1].

Narmashiri et al. investigated the failure modes of CFRP strengthened steel I-beams by four-points bending test and numerical simulation by ANSYS [2]. They found the failure modes depended on the specifications of CFRP plates. Siwowski and Siwowska compared the flexural behaviour of steel beams reinforced with CFRP in two strengthening schemes: adhesive-bonded passive plates and adhesive-bonded prestressed or active plates [3]. It found that the failure modes comprised CFRP plates debonding or plates rupture depending on the strengthening system and some system parameters. Colombi and Fava performed an experimental study on the fatigue property of cracked steel beams reinforced by CFR. The results shown that CFRP can reduce the fatigue crack growth and raise the fatigue life [4].

Sundarraja et al. made an experimental study and a numerical simulation on the axial CFRP-strengthened steel tubes with hollow square sections under compression load [5]. It concluded that the

increase in the CFRP strips thickness effectively delayed the local buckling of the tubes and led to the inward buckling rather than outward one. Niu and Jin made an analytical study on the buckling loading about the neutral axis with the maximum moments of inertia for a square steel tube with flange outsides wrapped by CFRPs based on Ježek method and considered an initial imperfection [6].

Some researches focus on the strengthening performance of steel structures with damage or cracks reinforced by CFRP. Hou et al. investigated the flexural behaviour of CFRP strengthened damaged steel beams by experimental study and finite element analysis [7]. Furthermore, they discussed the effect of prestress CFRP on the damaged steel beams [8]. Xie studied the capacities and interfacial crack propagation law of notched steel beams and notched steel plates strengthened with CFRPs by the finite element method [9]. In the finite element model, a mixed-mode cohesive law was employed to depict adhesive behaviour. Li and Li investigated the buckling performance of steel compression members with multiple local damages strengthened with CFRP under axial loading [10]. The elastic buckling load considered various boundary conditions was presented by using energy approach. Hu et al. proposes fatigue design guides and programs for CFRP-strengthened steel structures with initial cracks based on existing design codes and guidance for pure steel under fatigue loading [11]. Some typical design examples were given out for reference. Wang investigated the fatigue behaviour of central-cracked and double-edge-cracked steel structures strengthened with CFRPs by experimental study, numerical simulation and theorical method [12].

The authors' research group has been working on the strengthening technology of CFRP in engineering structures for over twenty years. The studies include the fatigue performance of reinforced concrete member strengthened with CFRP, strengthening technic of prestressed CFRP [13], fatigue crack propagation law of RC beams and steel plates with initial cracks strengthened with CFRP [14], and fatigue behaviour of the interface between CFRP and concrete beams under hygrothermal environment [15].

The adhesive interface is the weakest park of CFRP strengthened steel plates, in most cases, the debonding failure of the adhesive interface first occurs in the failure of the components [16-17]. Therefore, studying the mechanical properties of the adhesive interface is important to understand the overall mechanical properties of CFRP strengthened steel structures. This paper provides an experimental investigation on the shear performance of adhesive interface between CFRP and steel plates.

The remainder of the paper is organized as follows. Section 2 describes the experimental program in detail, including material properties, how specimens prepared, and experimental set-up and testing procedures. Experimental results are given out in Section 3. Failure characteristics are described, strain-loading curves are analyzed, and results discussion are presented in this section. The paper closes with brief conclusion in Section 4.

EXPERIMENTAL PROGRAMS

There are some experimental methods for bonding strength of steel structures strengthened with CFRP, such as simple shear model, twin shear model and beam type test. Comparing with simple shear model, twin shear model has simple and clear stress state and influenced few by normal stress. So, a twin shear model, as shown in Figure 1, is applied in this experiment to ensure the adhesive interface subjected to shear stress only.

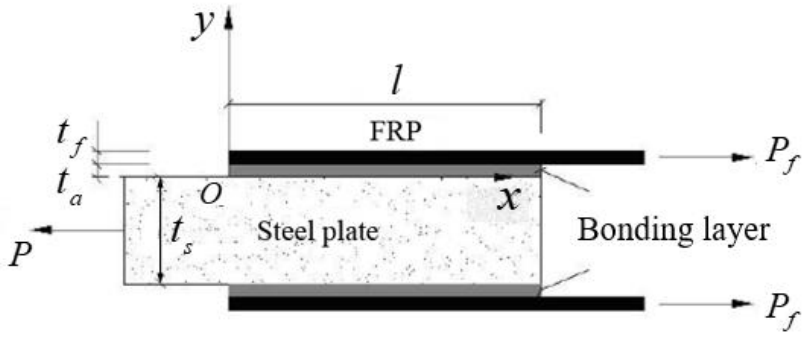

Fig. 1 - Twin shear model

Material properties

In this study, six steel plates strengthened with CFRPs are designed and tested under tensile loadings. The plates are made of Q345 No.10 I-steel, produced by Liuzhou Iron and Steel Company, with effective length of 200mm, width of 15mm, and nominal thickness of 3.5mm. Figure 2 shows the schematic of a steel plate. The mechanical properties of the steel, CFRP and adhesive are shown in Table 1. CFRP is used to strengthen the steel plates. The laminate has 200mm length, 15mm width, and 1.3mm calculating thickness. The carbon fiber silk is UT70-30, which is produced by Toray Company (Tokyo, Japan). Epoxy S-02 of Sikadur®-31SBA, produced by Sika Group, is used as adhesive for bonding the CFRP to the steel plates.

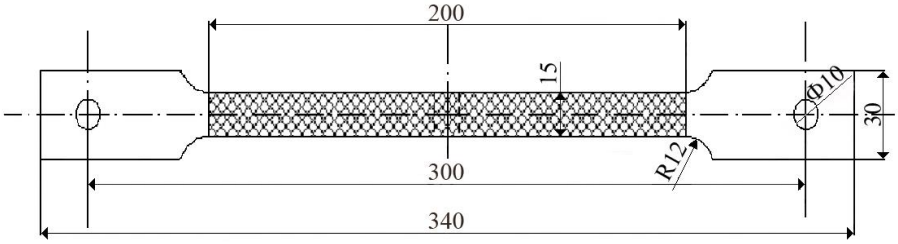

Fig. 2 - Schematic of a steel plate

Tab. 1 - Material properties of components

	Steel	CFRP	Adhesive
Tensile strength (MPa)	455	3780	
Yield strength (MPa)	345		
Shear strength (MPa)			15
Young's modulus (GPa)	206	230	5
Poisson's ratio	0.3	0.25	0.38
Thickness (mm)	3.5	1.3	1.0

Preparation of specimens

Two groups of steel plates with three specimens for each are prepared. The specimens in group A have a gap, with length 3.5mm, at the mid-span as shown in Figure 3. After being abrasive blasted, cleared by abrasive paper and acetone, the plates are bonded with CFRPs at both sides. The CFRPs should be blasted to increase the surface roughness, cleared by dry cloth to get rid of the

residue, cleaned by acetone, and then cut into size 200mm × 15mm, bonded to the plates by using the epoxy. The specimens in group B have no damage and bonded with CFRPs to compare with the specimens in group A. Resistance strain gages, with resistance 10ohms and sensitivity coefficient 2.0, are stick on the CFRPs. The stick locations are shown in Figure 4. For A-specimens, strains at the mid-span are tested and the gages are stick beside the gaps; for B-specimens, strains along CFRPs are considered and the gages are stick at the mid-span and two ends of CFRPs.

Fig. 3 - A steel plate with a gap at the mid-span

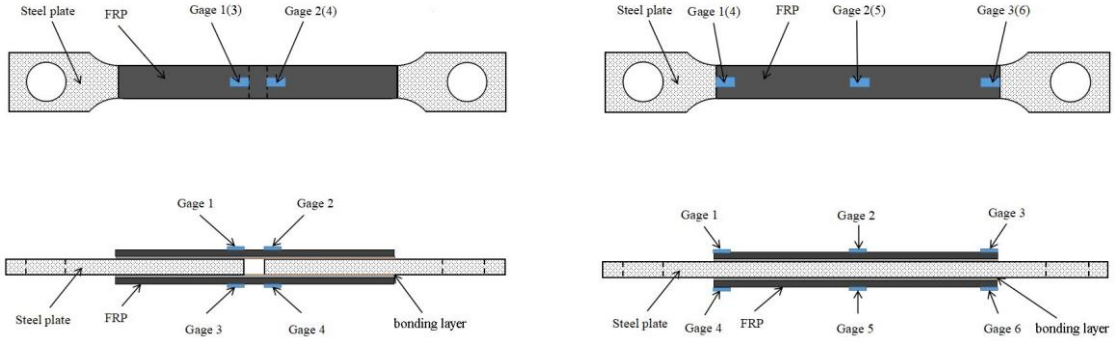

(a) *(b)*

Fig. 4 - Schematic of (a) steel plates with a gap, and (b) without damage bonded with CFRPs and strain gages

Experimental set-up and testing procedures

All the specimens are tested under tensile loadings by SANS's CMT5105 electronic universal testing machine. The machine has high testing precision and sensitivity in the measurement and control of loading, deformation and displacement, and is usually used to test metal specimens with loading under 100kN. The experimental equipment is shown in Figure 5. The strains of CFRPs are recorded by DataTaker's OM4B-DT85G Geologger data collecting system and TMR-7200 dynamic measurement software, as shown in Figure 6.

(a) (b)

Fig. 5 - (a) Testing machine and, (b) a specimen installed in the machine in (a)

Fig. 6 - Data Taker Geologger data collecting system

In this experiment, tension loadings are applied at the steel plates and the stresses transmit to the CFRPs via the adhesive interface. Shear stress appears at the interface between CFRP and steel plate and governs the specimens' failure. The details of testing procedure are listed as following:

(1) Install a specimen in the testing machine, check all the wires are connected correctly.

(2) Debug the data collecting system and let the initial strains be $\pm 4\mu\varepsilon$.

(3) Apply 5% of the maximum loading as initial loading to check if all the machines are working.

(4) Resume loading and control the loading speed at 0.5mm/min.

(5) Observe the CFRPs' debonding and the specimens' failure.

EXPERIMENTAL RESULTS AND DISCUSSION

Failure characteristics

For group A, the three specimens haven't obvious yield and shrinkage stages, and perform tensile behaviour of plastic materials without obvious yield stage. When the loading comes to a cracking loading, a crack appears at the end of the gap which cut through the bonding layer along 45° degree and expand along the interface between CFRP and bonding layer. The average cracking loading and crack strain of the cracked side are 14.85kN and 2728 $\mu\varepsilon$. After cracked, the strain of the cracked side would decrease rapidly and that of uncracked side would continue to increase. Finally, the specimens fail for CFRP debonding and the interface between steel and bonding layer are still undamaged. The cracking loadings and breaking loadings are listed in Table 2 and a failed specimen is shown in Figure 7(a).

Tab. 2 - Failure modes

Serial number	Cracking loading /kN	AVG Cracking loading /kN	Breaking loading /kN	AVG breaking loading /kN	Failure mode
A-1	14.93		--		Cracked at gap
A-2	14.76	14.85	17.81	17.88	Cracked at gap
A-3	14.85		17.96		Cracked at gap
B-1	--		21.50		Plate broken
B -2	--		21.45	21.47	Plate broken
B -3	--		21.48		Plate broken

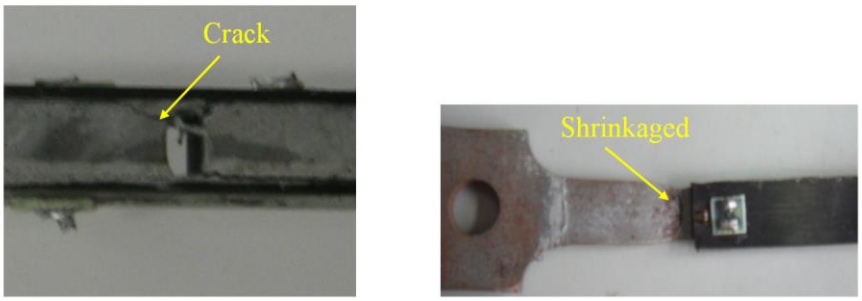

(a) *(b)*

Fig. 7 - (a) A specimen in group A failed for crack expanding, and (b) a specimen in group B failed for plate breaking

For group B, the three specimens perform tensile behaviour of plastic materials, i.e., the specimens go through four stages of elasticity, yield, reinforcement and shrinkage, and break at the end of CFRP. The bonding parts of CFRP and steel are undamaged. A broken specimen is shown in Figure 7(b). At the ends of CFRP, the steel plate has the minimum cross-section and they are possible failure parts. The maximum tension loading capacity of the steel plate is

$$F_{\max,t} = 455 \times (15 \times 3.5) = 21.5\text{kN} \quad (1)$$

The maximum shear loading the interface can bear is

$$F_{\max,s} = 15 \times (15 \times 100) = 22.5\text{kN} \quad (2)$$

The maximum tensile loading the CFRP can have is

$$F_{\max,FRP} = 3780 \times (15 \times 1.3) = 73.7\text{kN} \quad (3)$$

Because there are two adhesive interfaces and CFRPs bonded are two sides of plate, the possible loading for interface failure and CFRP break should be the double values in Eqs. (2) and (3). So, for the undamaged plates, they would fail for steel breaking. The breaking loadings are listed in Table 2 too.

Strain-loading curves

The strain gages stick on the plates in group B are all failed since the gages didn't stick firmly-cemented and deboned in the testing. The strain data of group B are unusable. This section will discuss the relationships between strain and loading for the plates in group A. Figure 8(a) shows the curves of strain-loading of plate A-1, where ε_1, ε_2, ε_3 and ε_4 denote the strain of gage 1, 2, 3 and 4, respectively. When the loading is less than 14.93kN, the curves are almost linear. When the loading comes 14.93kN, ε_1, ε_2 decrease rapidly, and ε_3, ε_4 increase fast. There is a crack appears at the interface between the steel and the bonding layer under gage 1 or 2, then it cut through the bonding layer and expand to the end of CFRP. The tensile stresses of CFRPs of the cracked side fall down, and the CFRP of another side sustains all the tensile loading which makes ε_3 and ε_4 increase. The machine stop loading at the time, and the specimen hasn't a breaking loading. Figure 8(b) is the displacement-loading curve of plate A-1. It shows that the deformation of steel plate is linear to the loading. Steel and CFRP have similar Young's modulus and the specimen is working in linear elastic stage. It can be concluded that the strains of plate are linear and close to that of CFRP.

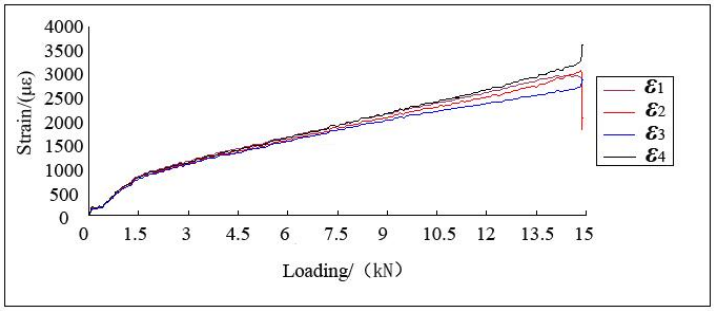

(a)

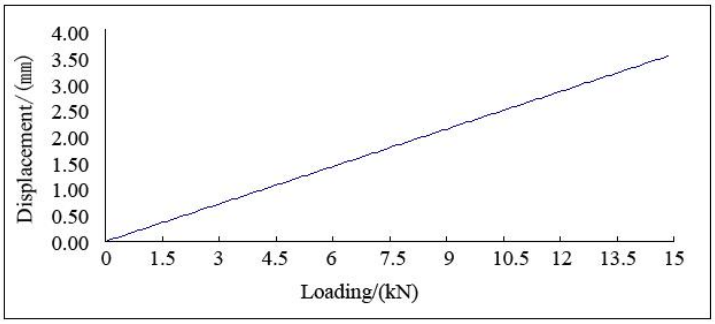

(b)

Fig. 8 - (a) Strain-loading curves and (b) displacement-loading curve of plate A-1

Figure 9 shows the strain-loading curves of plate A-2. When the loading is less than 14.76kN, the curves are almost linear. When the loading comes 14.76kN, ε_1 and ε_2 reduce 13% since a crack appears at the bonding layer of this side, and ε_3, ε_4 rise markedly. Then all the strains rise again when the loading increase but ε_3 and ε_4 are steeper. The specimen fails when the loading is 17.81kN and ε_3, ε_4 drop down to zero.

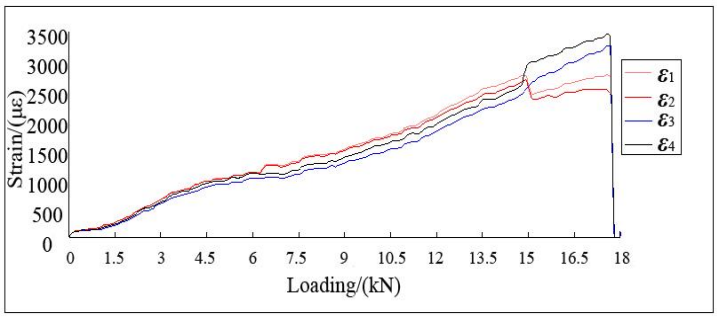

Fig. 9 - Strain-loading curves of plate A-2

For the loading applying is controlled by displacement, when the bonding layer of ε_1 and ε_2 side cracking, the deformation and length of the whole specimen doesn't change, but the length of unbonded CFRP increases which leads to the stiffness of this region decrease. So, ε_1 and ε_2, the strains of this region, decrease abruptly, and the CFRP of another side bears more stress which leads to ε_3, ε_4 increase. As the crack propagating, the strains increasing with the loading. The slopes of ε_1 and ε_2 become gentler, and that of ε_3 and ε_4 have no change.

Figure 10 shows the strain-loading curves of plate A-3. The cracking loading is 14.85kN. Like the curves of plate A-2, ε_1 and ε_2 reduce 15% and ε_3, ε_4 risen markedly when the loading comes to it, then all the strains increases again with the loading and the specimen fails when the loading is 17.96kN.

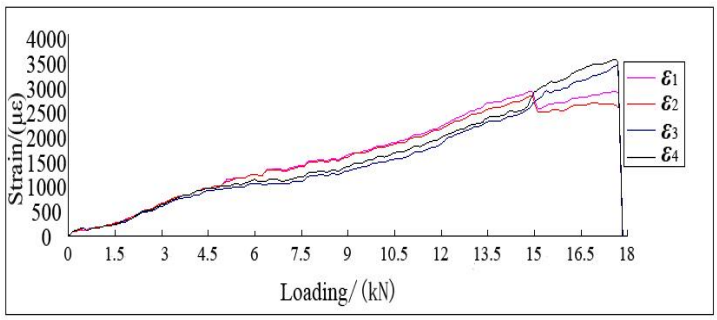

Fig. 10 - Strain-loading curves of plate A-3

The four strain gages in each specimen of group B are stick symmetrically and their values are supposed to be equal. In fact, the strains have differences in 5% at the same side and in 12% at different sides. The main reasons mainly lie in three aspects: 1) there are installation deviations of strain gages; 2) there are installation errors of specimens; 3) there are manufacturing deformations of specimens. The differences of gages lie in acceptable range, so the testing data are valid.

CONCLUSION

This paper provided an experimental investigation on the shear performance of adhesive interface between steel plate and CFRP. Six steel plates strengthened with CFRPs were prepared for the experiment, including three undamaged specimens and three with a gap. Twin shear model were applied in the test under tensile loadings. The experimental results showed that: (1) the undamaged plates broke for tensile failure, the CFRPs and the bonding layer were undamaged; (2) the plates with a gap failed for CFRPs debonding, a crack appeared at the end of the gap, cut through the bonding layer along 45° degree, and expanded along the interface between the CFRP and bonding layer; (3) the specimens with a gap cracked at 14.85kN and failed at 17.88kN; (4) the strain-loading curves had long linear stages, two strains decrease and other strains of another side increased rapidly at the cracking loading, then they both rose until the plates failed. This study will offer scientific basis and important consults to the strengthening design and research on steel structures reinforced by CFRP.

ACKNOWLEDGEMENT

This research was funded by the National Natural Science Foundation of China through Award (Nos. 12172134, 11872185) and the Natural Science Foundation of Guangdong Province through Award No. 2021A1515010037.

REFERENCES

[1] Teng, J.G., Yu, T., Fernando, D. (2012): Strengthening of steel structures with fiber reinforced polymer composites. *Journal of Constructional Steel Research*, vol. 78, pp. 131-143. *DOI:* 10.1016/j.jcsr.2012.06.011

[2] Narmashiri, K., Jumaat, M.Z., Sulong, N.H.R. (2011): Failure modes of CFRP flexural strengthened steel I-beams. *Key Engineering Materials*, vol. 471-472, pp. 590-595. *DOI:* 10.4028/www.scientific.net/KEM.471-472.590

[3] Siwowski, T.W., Siwowska, P. (2018): Experimental study on CFRP-strengthened steel beams. *Composites Part B: Engineering*, vol. 149, pp. 12-21. *DOI:* 10.1016/j.compositesb.2018.04.060

[4] Colombi, P., Fava, G. (2015): Experimental study on the fatigue behaviour of cracked steel beams repaired with CFRP plates. *Engineering Fracture Mechanics*, vol.145, pp. 128-142. *DOI*: 10.1016/j.engfracmech.2015.04.009

[5] Sundarraja, M.C., Sriram, P., Prabhu, G.G. (2014): Strengthening of hollow square sections under compression using FRP composites. *Advances in Materials Science & Engineering*, vol. 2014, pp. 1-19. *DOI:* 10.1155/2014/396597

[6] Niu, P., Jin, C.F. (2015): Analytical solutions on ultimate bearing capacity of a square CFRP-steel tube member with initial imperfection. *Engineering Mechanics,* vol. 32, no. s1, pp. 236-240. (in Chinese)

[7] Hou, W.Y., Wang, L.G. and Shi, D. (2022): Flexural behaviour of strengthened damaged steel beams using carbon fibre-reinforced polymer sheets. *Scientific Reports*, vol. 12, pp. 10342. *DOI*: 10.1038/s41598-022-14471-9

[8] Hou, W.Y., Wang, F.C. and Wang, L.G. (2021): Test and Numerical Analysis on Damaged Steel Beam Strengthened with Prestressed CFRP Sheet. *Advances in Civil Engineering*, vol. 2021, article ID: 6711877. *DOI*: 10.1155/2021/6711877

[9] Xie, Z.H. (2016): *Finite Element Analysis of interfacial stresses of cracked steel structures strengthened with CFRP plate*. Guangzhou: Guangdong University of Technology. (in Chinese)

[10] Li, B., Li, C.X. (2017): Investigation on the anti-buckling behavior of steel compression members with multiple local damage by FRP strengthening. *Industrial Construction*, vol. 47, no. 1, pp. 168-173. (in Chinese)

[11] Hu, L.L., Feng, P., Zhao, X.L. (2017): Fatigue design of CFRP strengthened steel members. *Thin-Walled Structures*, vol. 119, pp. 482-498. *DOI:* 10.1016/j.tws.2017.06.029

[12] Wang, H.T. (2016): *Study on the fatigue behavior of CFRP plate-strengthened steel structures and its design method*. Nanjing: Southeast University, 2016. (in Chinese)

[13] Guo, X.Y., Wang, Y.L., Huang, P.Y., Shu S.Y.H. (2020): Fatigue behavior of RC beams strengthened with FRP considering the influence of FRP-concrete interface. *International Journal of Fatigue*, vol. 143, pp. 105977. *DOI:* 10.1016/j.ijfatigue.2020.105977

[14] Yang, Y., Huang, C.H., Huang, P.Y. (2018): Surface crack propagation rules of CFL-strengthened steel plate under fatigue loading. *IOP Conference Series: Materials Science and Engineering*, vol. 392, no. 2, pp. 0220258. *DOI:* 10.1088/1757-899X/392/2/022028

[15] Chen, Z.B., Huang, P.Y., Guo, X.Y., Zheng, X.H., Yang, Y. (2020): Fatigue equation of structural materials and members under hot-wet environment and cyclic bending loads. *Strength, Fracture and Complexity*, vol. 12, no, 2-4, pp. 119-125. *DOI:* 10.3233/SFC-190241

[16] Jiang, X., Luo, C.W., Qiang, X.H., Kolstein, H., Bijilaar, F. (2017): Effects of Adhesive Connection on Composite Action between FRP Bridge Deck and Steel Girder. *Journal of Engineering*, vol. 2017, article ID: 6218949. *DOI*: 10.1155/2017/6218949

[17] Lozano, C.M., Riveros, G.A. (2019): Effects of Adhesive Bond-Slip Behavior on the Capacity of Innovative FRP Retrofits for Fatigue and Fracture Repair of Hydraulic Steel Structures. *Materials*, vol. 12, no. 9, pp. 1495. *DOI*: 10.3390/ma12091495

CIVIL ENGINEERING JOURNAL

Article no. 43

THE CIVIL ENGINEERING JOURNAL 4-2022

DAM BREACH ANALYSIS AND PARAMETER SENSITIVITY ANALYSIS ALONG A RIVER REACH USING HECRAS

Ashok Karki[1], Santosh Bhattarai[1], Pradhumna Joshi[1], Mukesh Raj Kafle[1] and Rajesh Bhattarai[2]

1. *Tribhuwan University, Institute of Engineering, Pulchowk Campus, Department of Civil Engineering (hydropower) Pulchowk, Lalitpur, Nepal; ashokkarki789@gmail.com, santoshsumi9@gmail.com, pradhumnajoshi@gmail.com, mkafle@pcampus.edu.com*
2. *Hydro Engineering and Management Service Private Limited, Buddhanagar, Kathmandu, Nepal; dexraj147@gmail.com*

ABSTRACT

A dam break is a low-probability, high risk catastrophe event that is extremely destructive and has a substantial negative socio-economic impact on downstream and nearby areas. Simulating dam breach and analyzing flood propagation downstream from those events is vital for identifying and minimizing the risks associated downstream of dam location. This study intended to anlayse the effect of overtopping failure of dam for two scenarios (a) base-case scenario (scenario with average value of dam breach parameters from their range) and (b) worst case scenario (the breach with largest geometry, shortest formation time and highest peak outflow magnitude). Further, a hydrodyanmic modelling is perfomed to investigate the sensitivity analysis (local and global) of five dam breach parameters (dam breach elevation, dam breach width, breach formation time, weir coefficient, trigger failure elevation) on breach outflow in a proposed hydropower project located in Nepal. Aeronautical Reconnaissance Coverage Geographic Information System (ArcGIS), Hydraulic Engineering Center River Analysis System (HEC-RAS) and OriginPro 2022b are utilized to analyse the effect of dam breach and parameter sensitivity.

Generation of outflow hydrograph shows that worst case scenario has devasting effect downstream with innudation of 1047 of househols and 50.83 kilometers of roads. The breach velocity was recorded as 15.16 m/s and 20.85 m/s for base and worst case respectively. The minimum depth and maximum depth of flooding downstream from dam location was found to be 24.51 m and 73.6 m for base case and 47.43 m and 106.75 m for worst case. Due to backwater effect at Bheri river, peak flow at 14 km downstream from dam reduces significantly to 124852.57 m^3/s and 244204.41 m^3/s for base and the worst case respectively. From local sensitivty analysis it has been found that, dam breach elevation is more sensitive and triggering failure elevation is less sensitive for peak outflow hydrograph. Whereas dam breach width seems more sensitive and TFE seems least sensitive for peak outflow using Monte Carlo Simulation for gloal sensitivity.

KEYWORDS

2D-HEC-RAS modelling, Dam breach, Inundation mapping, Local sensitivity analysis, Global sensitivity analysis

INTRODUCTION

Dams and waterway impoundments provide public benefits through the storage of water for flood control, recreation, drinking water, generation of hydroelectric power, stormwater management, wildlife habitat creation and irrigation [1]. A significant hazard to the downstream region is unavoidably present in the event of a dam breach event because of the enormous, stored water

volumes. Concrete gravity dam failures are generally more disastrous because there are fewer visible indicators prior to failure, and collapse can occur quickly with little or no warning [2]. A dam break is a low-probablity, high risk catastrophe event that is extremely destructive and has a substantial negative socio-economic impact on downstream and nearby areas [3]–[5]. Worst of all, the collapse of such a massive dam would be a catastrophic disaster for a country like Nepal, which is economically poor [6].

Failure is unacceptable for dams since it endangers people's lives and incurs huge financial risk. Overtopping, seismic failure, internal erosion, poor management, quality problems, disasters and foundation failure are some of the several failure modes [7]. Failure modes of concerte gravity dam are overtopping, piping/seepage, foundation defects, overturning, cracking and equipment failure [8]. From the world wide historical dam failure's database study performed by up to February 2020, 57.76 percent of gravity dams were failed, out of that 40.86 percent failed due to overtopping [9]. Overtopping failure has been found to be the most crucial cause mainly with respect to time of failure [10][11].

The estimation of dam breach geometry, which involves making decisions about variables like breach width, breach formation time, breach height, breach side slope, weir coefficient, side slope of breach, and trigger failure elevation, is a crucial step in the creation of hypothetical dam breach scenarios. The components that are included in dam breach analysis are; assessment of the dam breach parameters, estimation of the outflow hydrograph, routing of the downstream dam brach hydrograph and estimation of the magnitude and severity of the downstream flooding [12]. The availability of information about the model parameters and the complexity of the model influences the choice and use of the uncertainty approaches. Before choosing acceptable methods, it may be necessary to look at the model's parameters and complexity [13]. Hydrlogic Engineering Center-River Analysis System(HECRAS) model is widely used to simulate flow in river channels and floodplains and found to be an effective model for predicting downstream flooding impacts from an upstream event [14]–[17]. The model's use can save time in model calibration and will be easy to route floods and anticipate flood levels [18]. The model can conduct 2D hydrodynamic unsteady flow routing using the Saint Venant equation or the Diffusion wave equation [8].

The negative impact of dam failure can be mitigated by providing the community with accurate flood inundation maps [19]. A dam failure inundation map shows the area of the downstream from a dam that could reasonably be expected to be inundated in the case of a breakdown of the dam [20]. A wide variety of end users use the maps for planning and as a tool for responding to determine the effects of dam failure in downstream communities. In addition, a dam categorization exercise considered the incremental areas flooded as a result of dam failure. Creating emergency action plan, planning flood evacuation, creating breach inundation zone mapping, choosing suitable spillway design flood are the uses of inundation studies.

The results of sensitivity analysis (SA) of the model output may be used to determine the degree to which the current uncertainties allow a certain mechanism to be clearly defined [21]. Sensitivity analysis is a method for predicting the outcome of a decision if a situation turns out to be different from the key predictions**.** The SA method evaluates how uncertainties in one or more input variables may affect uncertainties in the output variables in a numerical (or other) model. By examining the qualitative and/or quantitative responses of the model to changes in the input variables or via comprehending the phenomenon under study by the analysis of interactions between variables, this analysis helps the model's prediction or reduces it [22]. By focusing on the sensitivity close to a set of factor values, local sensitivity analysis (LSA) determines the local influence of input factor variation on model response [23]. When analyzing the local sensitivity of an input factor, the values of other input factors are held constant while the gradients or partial derivatives of the output functions are used to measure the sensitivity [23]. A study by N. B. Lucie Pheulpin demonstrates that the first order, local approach which is generally still relevant for uncertainty analysis of hydrodynamic risks remains applicable despite the nonlinearity of river flow processes, especially in the presence of significant parameter uncertainty [24]. The Global Sensitivity Analysis(GSA) is a quantitative technique that ignores models and is based on estimating the percentage contribution

of each input factor to the variance of the model's output while also taking interaction terms into consideration [25].

The purpose of this study is to determine breach hydrograph due to overtopping failure of NHP dam under different scenarios and to investigate the impact of a possible failure with prediction of inundation levels (depth, velocity, WSE and arrival time) at a given location using HEC-RAS and ArcGIS. To determine the most sensitive and least sensitive breach parameter on peak outflow by using local and global sensitivity analysis is one of the major objectives of the study.

STUDY AREA

The proposed Nalgad Hydropower Project is located in Nalgad, Jajarkot district, Karnali Province, Nepal. In the Karnali River Basin, Nalgad is one of the primary tributaries of the Thuli Bheri River. The Nalgad gets its name from the Chakhure Lek, a high mountain range that runs across the Jajarkot and Jumla districts of Nepal. The project is a roller compacted concrete dam of 248 m height. The reservoir is created by the storage, which has a total storage volume of 474 MCM and a live storage volume of 350 MCM. The main dam has a spillway that allows a flood up to PMF to flow through, with a crest width of 64.2 m. The dam site of the project is located just downstream of the confluence of Andheri Khola, which is approximately 9.25 km upstream from the confluence of the Nalgad and the Thuli Bheri River and the powerhouse is located on the left bank of Nalgad River approximately 500 m upstream from the suspension bridge at Dalli.

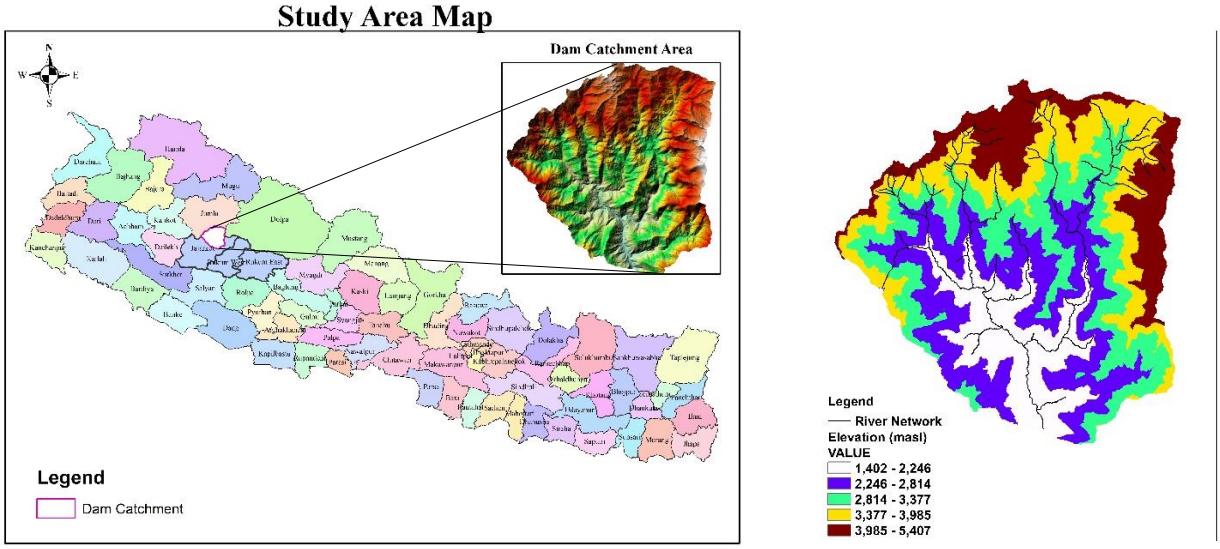

Fig. 1- (a) Map of Nepal (b) Dam catchment and river networks

The catchment area at dam location is 569 km^2. Almost half of the basin is below 3,000 m elevation. The catchment area experiences the annual rainfall of 2018 mm with average monthly flow of 27.3 m^3/s in Nalgad river. Based on the Digital Elevation Model (DEM) the elevation of the catchment varies from 1402 masl to 5407 masl. The dam do not pose a risk of Glacier Lake Outburst Floods (GLOF) [26].

METHODS

Data Collection

Most of the data was compiled from NHP office that includes updated feasibility study report (UFSR) (a study submitted by a joint venture of SMEC International Pvt. Ltd and Australia and MWH

International INC, USAF). Data collected for modelling was grouped into three parts, namely; hydrologic data, spatial data and geometric data.

The peak flow of 24-hr- Probable Maximum Flood (PMP) was the highest among other PMP's thus 24-hr PMP with peak flow of 5102m^3/s was taken as input in this study. The inflow from the Bheri river was taken into consideration as inflow hydrograph. The constant flow hydrograph of 150 m^3/s was provided at the boundary conditions of Bheri river. The Digital Elevation Model (DEM) from Alaska Satellite Facility (ASF) of 12.5 m high resolution terrain corrected from Advanced Land Observing Satellite Phased Array L-band Synthetic Aperture Radar (ALOS PALSAR) dataset were chosen. The topographic map of the project area was acquired from PAHAR mountains of central Asia digital dataset. Land cover data of Nepal 2019 of 30 m resolution was taken from International Centre for Integrated Mountain Development (ICIMOD). Storage area elevation vs storage data was obtained from the UFSR of NHP. The geometric data of dam is presented in

Tab. 1 below.

Tab. 1 - Geometric Data of Dam (Sorce:UFSR)

Type	Curved Gravity Roller Compacted Concrete (RCC) Dam
Maximum height above foundation	248 m
Crest Elevation	1588 masl
Length of crest	495 m
Width of crest	10 m

Watershed delineation and discretization

The high-resolution terrain corrected DEM data was processed in Geographic Information System (GIS) to merge the raster data. The combined data is clipped and made ready to use as DEM input in HEC-RAS. Using the hydrology capabilities in the ArcGIS geoprocessing toolkit, watershed delineation and discretization were carried out in ArcGIS to demonstrate the delineation of watershed and stream networks based on digital elevation models. Several datasets that together characterize the drainage patterns of the basin are derived using the hydrology tools. The digital elevation model underwent geoprocessing analysis to generate data on streams, stream segments, watersheds, flow direction, and flow accumulation. The information is then utilized to create a vector representation of drainage lines and catchments from chosen places. Later the outputs from the HEC-RAS were imported for inundation mapping.

HEC-RAS modelling

For two-dimensional (2D) analysis, at first the projection data was provided to River Analysis System (RAS) mapper. It is easier to use RAS Mapper tool to import necessary terrain data directly to the model. Storage area shape file from the ArcGIS was imported into the geometry and volume elevation relations could be obtained from the loaded terrain. Because of the availability of volume elevation relation, it was directly provided to the storage area. Also, 2D flow area was created with the grid size of 30m by 30m. 11,537 cells in total were used for the analysis. Additionally, the Manning's n value on related land cover grid was imported into the HEC-RAS geometry editor interface. The manning's n value for different land cover type was taken from HECRAS user manual. For a perfect characterization of unstable flow events over the simulation period, the roughness change caused by flood waves cannot be incorporated into the model.

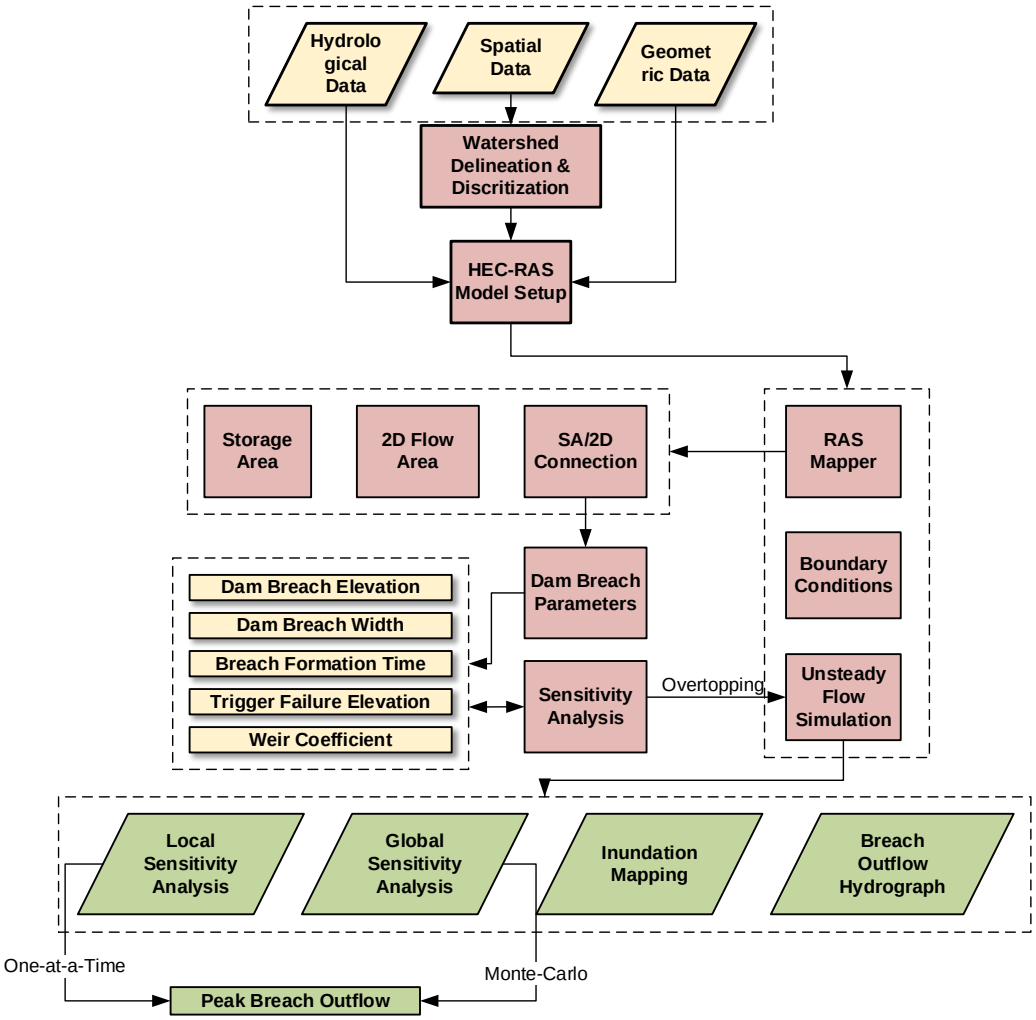

Fig. 2 - Methodological flowchart of the study

The dam was used to connect SA/2D flow area. The geometrical information will all be identical. SA and 2D flow area connections are capable of functioning as a particular kind of a dam structure. It is necessary to model the link as the dam structure using weir embankment data. Weir width, weir coefficient, weir crest shape, spillway height and design energy head are the required storage area connection weir data provided. Modeling the dam breakdown also requires the addition of the breaching plan data. The analysis of the 2D dam break model used different breaching conditions for different scenarios. Storage area connection breach data was provided. The mode of failure was considered as overtopping. Breach progression was set to sine wave. For breach data different breach parameters value were used based on scenarios created. Based on the data two scenarios, base-case scenario and worst-case scenario were created. The range of values of dam breach parameters were taken according to Federal Energy Regulatory Commission (FERC) as stated on HEC-RAS user manual.

Tab. 2 shows range of value for different dam breach parameters, the value of dam breach parameters for the base-case and worst-case scenario taken for the study. The value of the base-case was chosen in such a way that the value was the average of the range of dam breach parameters value. The worst case is defined as the breach with the largest geometry, shortest breach formation time, largest dam breach height, higher trigger failure elevation so that highest peak outflow magnitude occurs.

Tab. 2 - Different values of dam breach parameters based on scenarios

SN	Dam Breach Paramters	Range	Base-Case Scenario	Worst-Case Scenario
1	Dam Breach Width	0.1L to 0.5L	148.5 m	248.5 m
2	Dam Breach Elevation	1470 masl to 1510 masl	1490 masl	1470 masl
3	Breach Formation Time	0.1 hour to 0.5 hour	0.2 hour	0.1 hour
4	Weir Coefficient	1.1 to 1.8	1.44	1.8
5	Trigger Failure Elevation	1588.3 masl to 1588.7 masl	1588.5 masl	1588.7 masl
6	Left Side Slope	Vertical	Vertical	Vertical
7	Right Side Slope	Vertical	Vertical	Vertical
8	Failure Mode	-	Overtopping	Overtopping

Setting up the external boundary conditions was the initial stage in utilizing HEC-RAS to model the downstream channel of the Nalgad Hydropower Project Dam. The upstream limit was chosen so that it could exist independently of the conditions further downstream. The location of the downstream border was chosen to be independent of the flow characteristics below the boundary. All the scenarios on HECRAS model require the same flow and boundary conditions. A boundary line and a normal depth boundary condition have been established for the downstream 2D flow area connection. Upstream boundary condition was provided at dam connection where lateral inflow hydrograph (PMF) was provided. At downstream end of the study area normal depth boundary condition was considered. Also, boundary condition at the Bheri river was created. Storage area initial conditions was set at full supply level of reservoir as 1580 masl.

Unsteady Flow Simulation

The starting date and time of simulation time window was taken from 1st January, 2022 00:00:00AM to 1st January, 2022 1:00:00 PM. 0.2 seconds of fixed time step computation interval was taken. Mapping output interval was taken as 10 seconds whereas hydrograph output interval and detailed output interval was taken as 1 second.

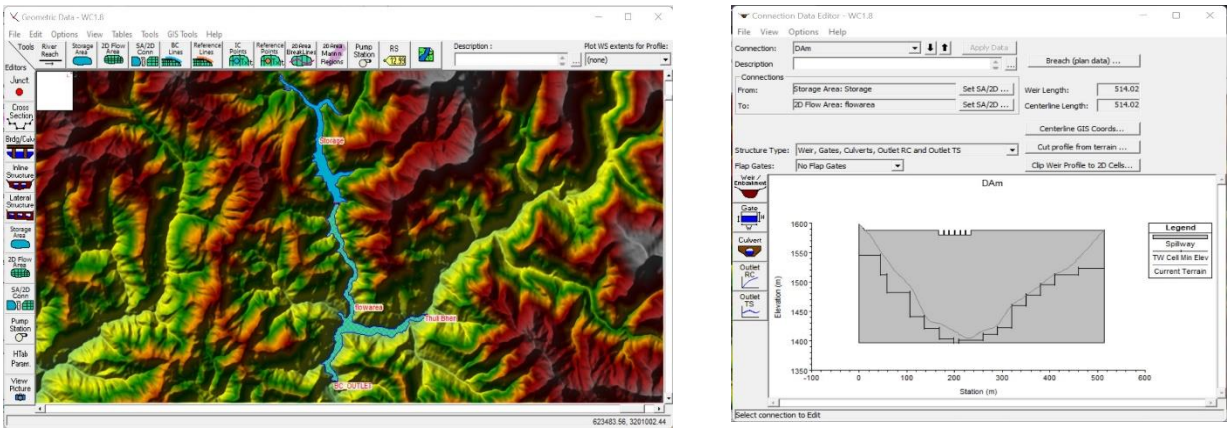

Fig. 3 - (a)Geometry of HEC-RAS model (b)Connection data editor

From the output of HECRAS, dam breach hydrograph can be obtained. Mapping of worst-case scenario downstream of dam was performed after exporting results from HEC-RAS to ArcGIS. Based on results sensitivity (SA) analysis was performed.

RESULTS

The condition, when the reservoir is at full supply level and then peak of the PMF impinges over reservoir is the most critical situation chosen in this study. For this case, it is assumed that the dam is just overtopped by PMF and then the dam is failed due to breaching. The important point in the breach analysis is to estimate accurate outflow hydrograph and downstream inundations area. Sensitivity analysis is used to assess sensitivity of hydrodynamic results to different breach parameters. The results obtained are classified based on following sub headings.

Breach Outflow Hydrograph

2D HEC-RAS analysis of dam break event based on breaching parameters (as mentioned in Tab. 2) gave hydrograph output at the dam structure between the storage area and river reach. Breach initiation had begun to occur on January 1st, 2022, at 9:54:47 AM for base case and at 10:19:11 AM for worst case. Total flow obtained at the full shaped dam break was 194036.2 m^3/s and 515976.8 m^3/s for base and worst case respectively. Fig. 4 (a) shows breach hydrograph for both scenarios.

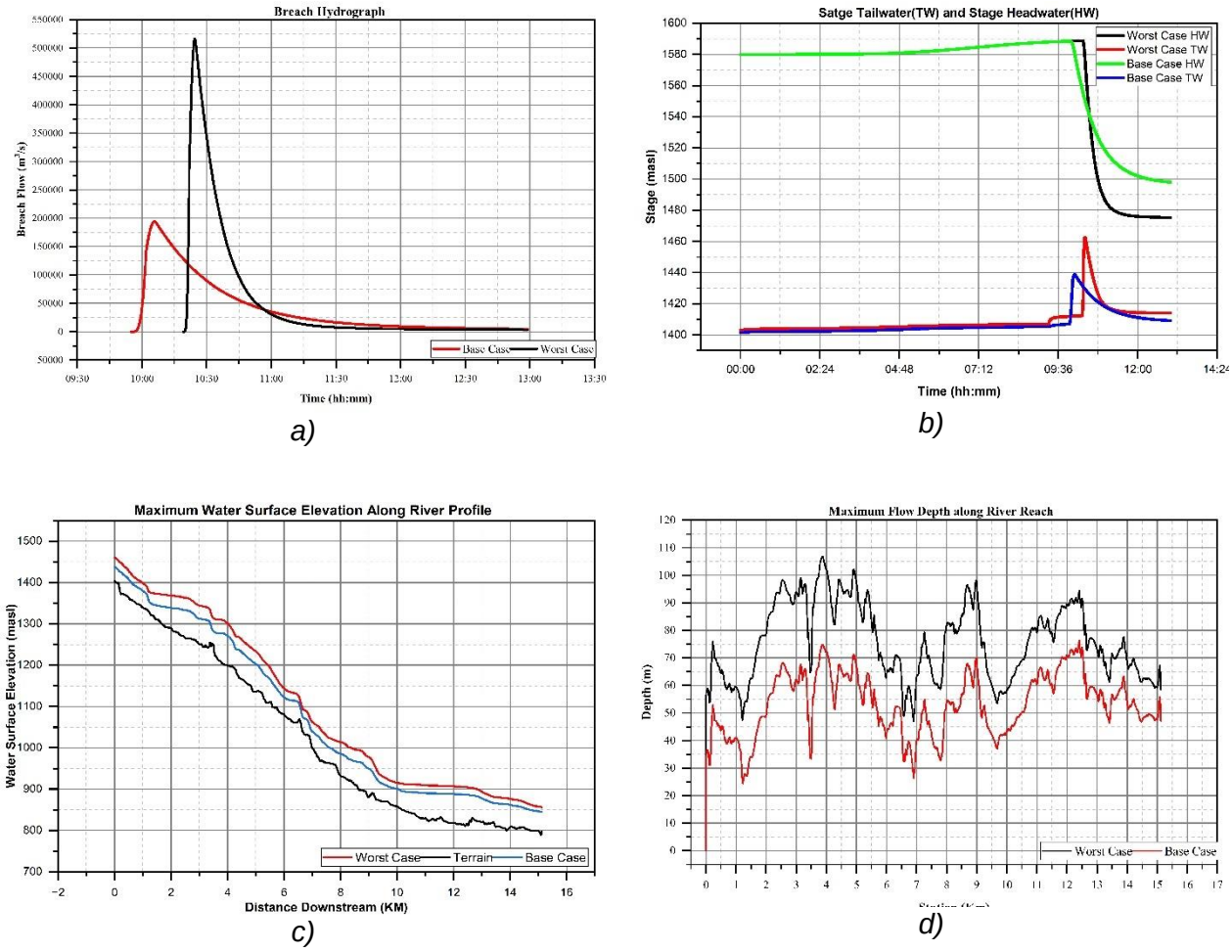

Fig. 4- (a)Breach Hydrograph (b)Stage HW and TW Curve (c)Maximum WSE along river (d)Maximum depth distribution along river

The Head Water (HW) stage, Tail Water (TW) stage, maximum velocity through breach, maximum depth and mimimum depth along river profile for base case and worst case was obtained as; 1588.52 masl and 1588.7 masl, 1438.77 masl and 1460.56 masl, 15.16 m/s and 20.85 m/s, 76.36 m and 24.45 m, 106.762 m and 47.061 m respectively. Maximum Water Surface Elevation (WSE)

of the worst case seems to be greater as more breach flow passes through dam than base case. Fig. 4 (b), (c), (d) shows HW and TW curve, WSE and depth distribution along river profile respectively.

For overtopping failure flood hydrograph routing has been analyzed at seven chainage points, at 2 km downstream, at 4 km downstream, at 6 km downstream, at 8 km downstream, at 10 km downstream, at 12 km downstream and at 14 km downstream to show the effect of flood under overtopping at downstream of the dam.

Tab. 3 - Peak flow at different section from dam location

Distance from Dam (km)	Base-Case		Worst-Case	
	Peak Flow (m3/s)	Time in Peak (hh:mm:ss)	Peak Flow (m3/s)	Time in Peak (hh:mm:ss)
2	191806.17	10:06:40	492765.31	10:25:20
4	189632.05	10:08:00	478351.47	10:26:40
6	189153.06	10:09:10	476006.03	10:27:20
8	188719.44	10:09:50	471609.63	10:28:00
10	187132.53	10:11:00	463447.34	10:28:50
12	125311.30	10:24:40	245582.08	10:37:10
14	124852.57	10:26:30	244204.41	10:38:40

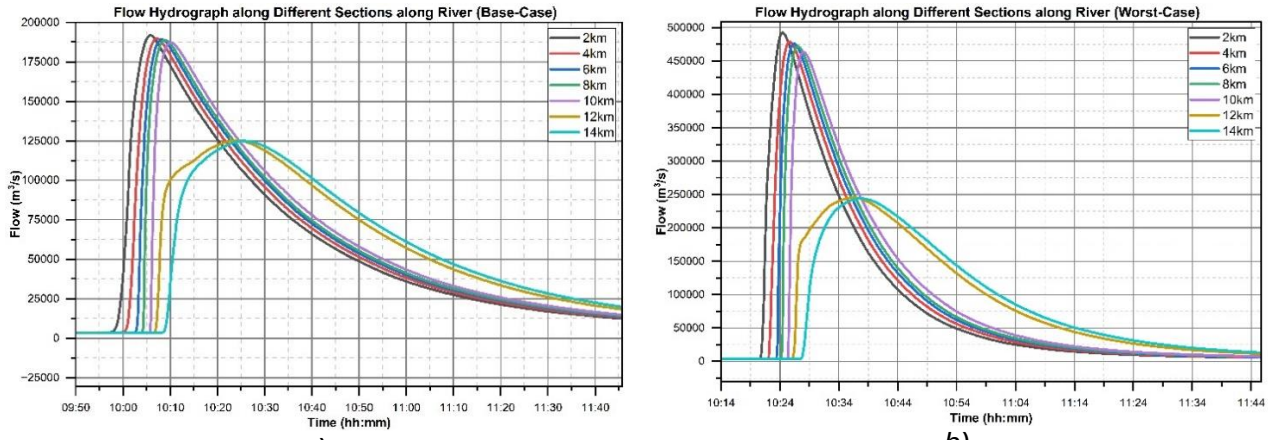

a) *b)*

Fig. 5 - (a)Flow hydrograph (Base-Case) at downstream sections (b) Flow hydrograph (Worst-Case) at downstream sections

Inundation mapping

Mapping of the worst-case scenario downstream of the dam was performed after exporting results from HEC-RAS to ArcGIS. Inundation mapping was done on RAS Mapper on HECRAS and later exported to GIS for further analysis and reporting purpose to identify the potential risk and safe settlement areas from the flow of the dam breach of the worst-case scenario was performed. Municipality based analysis on number of buildings, roads, landcover and area inundated are mapped. The data of buildings and roads was obtained from Geofabric de, open street map data of Nepal and land cover data 2019 was obtained from the ICIMOD.

The significant failure scenario which leads large flood plain according to the study is the worst-case scenario. So, mapping based on the worst-case scenario has been carried out. In

general, high-water depth occurred along the main channel and spreads gradually to the floodplains. The total area inundated after the arrival of PMF into the storage area and the dam breach including reservoir storage was 14.478 square kilometers as seen in Fig. 6. Within the downstream study area two municipality (Nalgad and Athbiskot) and one rural municipality (Barekot) were inundated with inundation area of 6.514 km^2, 1.655 km^2 and 6.309 km^2 respectively. It was found that the depth is higher in storage area of the dam. The model result gave a flood depth 0.0012 m as the minimum to a critical height of 106.762m downstream from dam location. Velocity of flow increases as the dam breaks at downstream of the dam. The velocity was higher at the narrow region of the river and reduces at wider sections. The maximum velocity observed was 78.03 m/s and minimum was zero at storage.

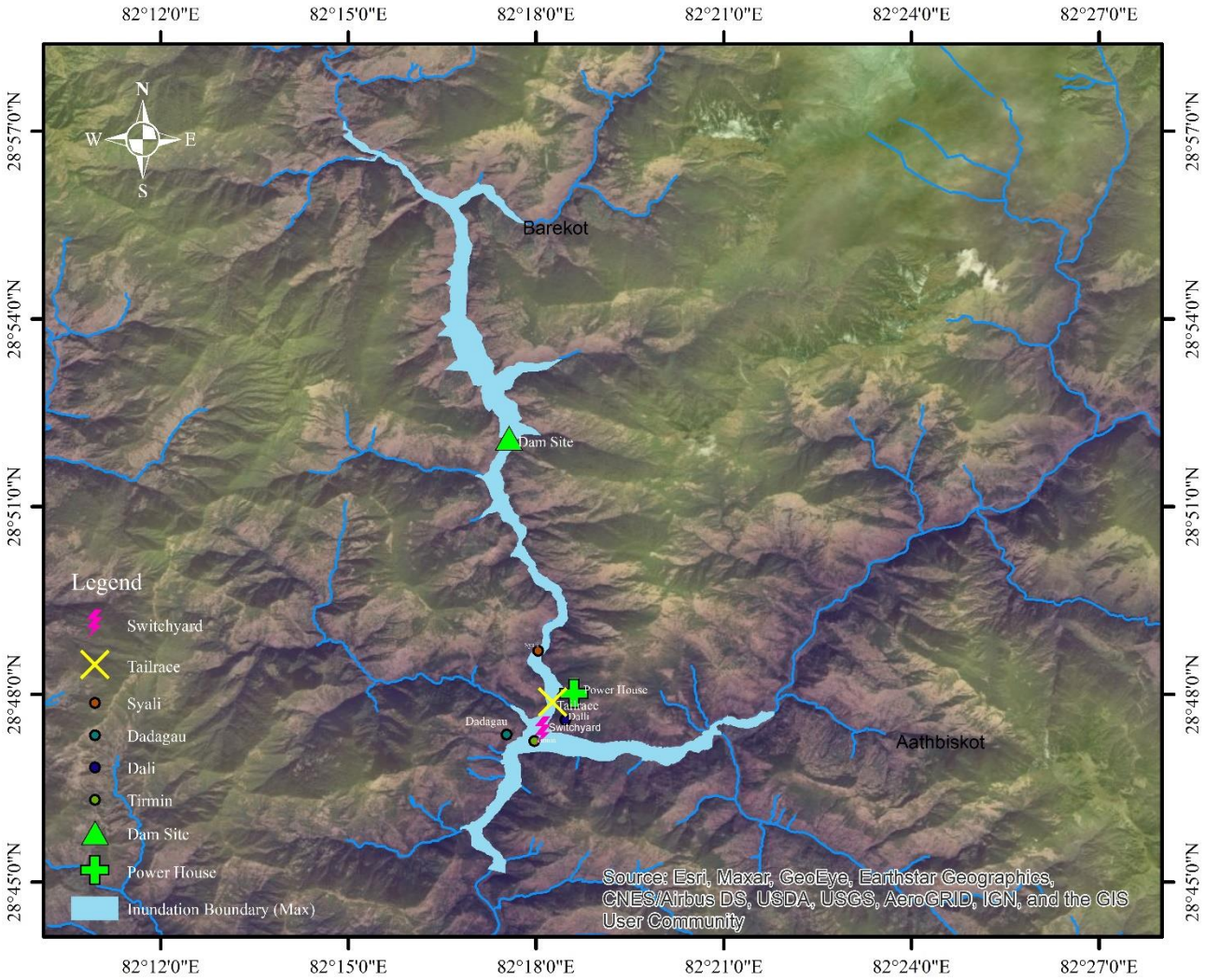

Fig. 6 - Inundation mapping

Fig. 7 (a) and (b) show inundation of buildings and roads across the study reach from the dam location respectively. Municipality based number of buildings and length of road inundated is presented in Tab. 4 and

Tab. 5 respectively. After the arrival of PMF at the dam on 1st January, 2022 at 12:00AM and the dam breached at 10:19:10AM. Arrival time of flood is maximum at upstream of the Bheri river due to backwater effect from flow in the river and at the end of downstream area taken under the study. Fig. 8 (a) and (b) show the depth and arrival time mapping along the study area.

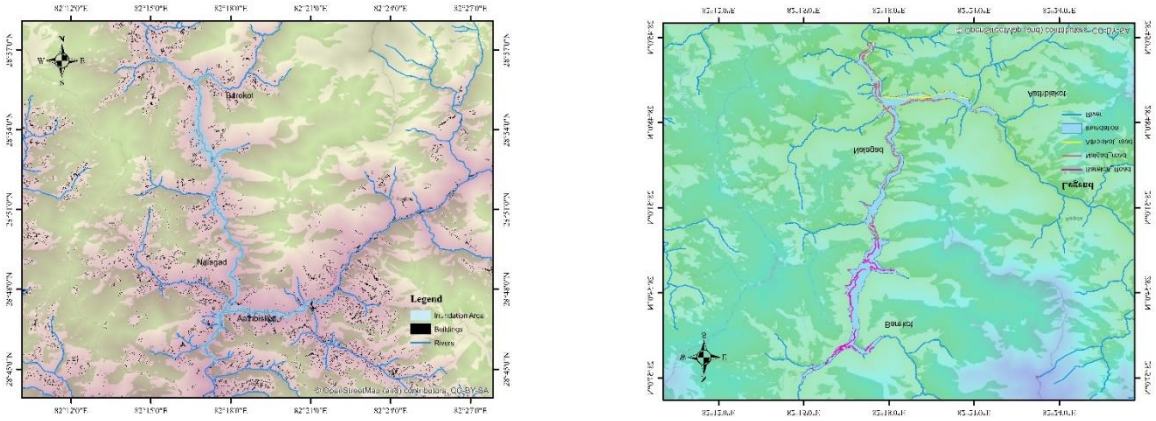

a) *b)*

Fig. 7-(a) Inundation of Buildings (b) Inundation of roads

Tab. 4 - Number of buildings inundated based on municipalities

Municipality/Rural Municipality	Total Number of Buildings	Total Number of Buildings Affected	Percentage Affected
Aathbiskot Municipality	9601	188	1.96
Barekot Rural Municipality	4738	298	6.81
Nalgad Municipality	8008	561	7

Tab. 5 - Inundation of roads along municipalities

Type of Roads/Municipality	Tertiary (m)	Path (m)	Footway (m)	Track (m)
Aathbiskot Municipality	6132.155	51.734	1260.5572	309.9702
Barekot Rural Municipality	-	14069.7715	-	4366.0556
Nalgad Municipality	3972.3097	16624.792	72.087	3974.8811

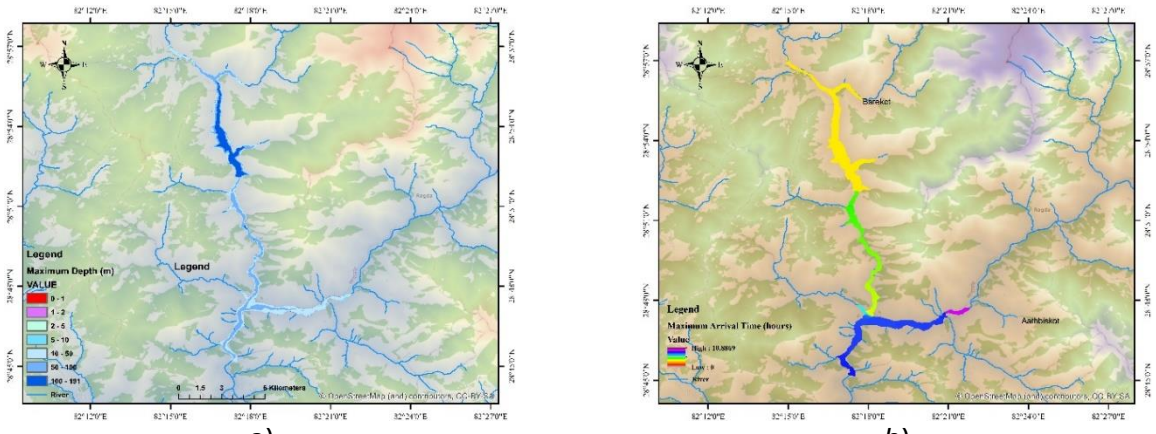

a) *b)*

Fig. 8-(a) Maximum depth (b) Maximum arrival time

Local sensitivity analysis (LSA)

Local sensitivity analysis examines sensitivity only with regard to point estimates of parameter values, which results in the sensitivity measure being affected by the choice of breach parameters. In local sensitivity, first a base case (BC) was set with the breach parameters value as mentioned in the Tab. 2. Sensitivity analysis was performed by changing the breach parameter value one at a time (OAT) keeping all other parameters constant.

Tab. 6 - Values of dam breach parameters taken for LSA

SN	Dam Breach Width	Dam Breach Elevation	Breach Formation Time	Weir Coefficient	Trigger Failure Elevation
1	247.5	1510	0.1	1.1	1588.3
2	198	1500	0.15	1.27	1588.4
3	148.5	1490	0.2	1.44	1588.5
4	99	1480	0.25	1.6	1588.6
5	49.5	1470	0.3	1.8	1588.7

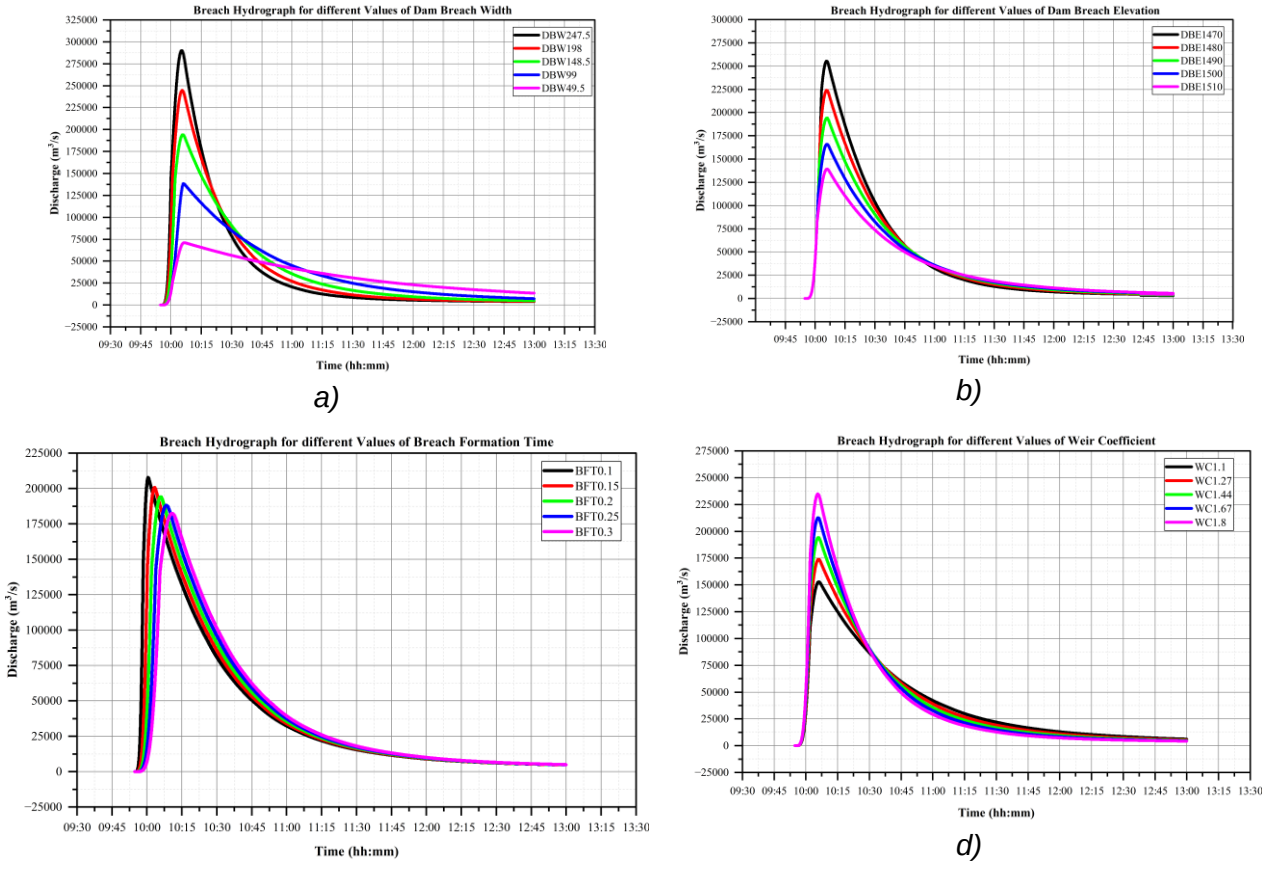

Fig. 9-Breach Hydrograph for different values of (a)dam breach Width (b)dam breach elevation (c)breach formation time (d)weir coefficient

Sensitivity was observed on peak breach flow at dam. Percentage change in output and percentage change in input was calculated and the ratio of percentage change in output to input which is sensitivity index, was determined. Different breaching parameters described the dam break peak flow, implying that the breaching parameters had a significant impact on peak flow estimation.

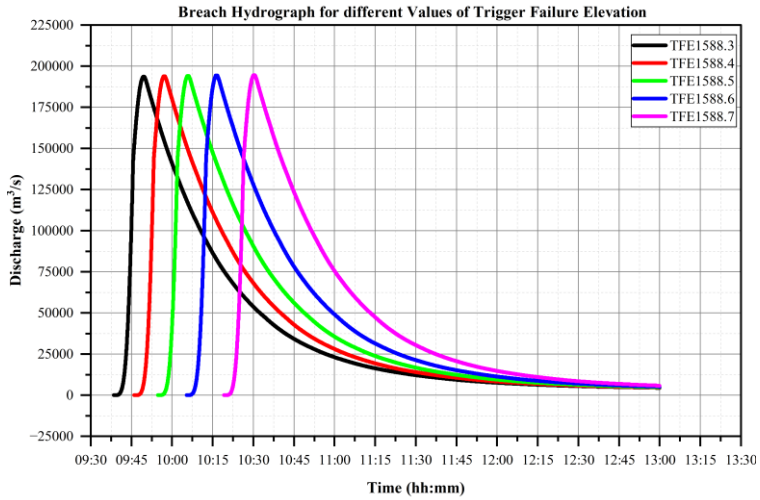

Fig. 10 - Breach hydrograph for different values of trigger failure elevation

Fig. 9 and Fig. 10 show the different peak flow hydrograph based on the different values of dam breach paramters. The mean of ratio of percentage change in output to percentage change in input for maximum peak outflow, for each parameter considered for local sensitivity analysis was calculated as shown in

Tab. 1. Dam breach elevation was found to be the most sensitive parameters followed by weir coefficient, dam breach width and breach formation time. Trigger failure elevation was found to be the least sensitive parameter.

Tab. 7 - Mean of ratio of percent change in output to input

Sensitivity On	Dam Breach Elevation	Weir Coefficient	Dam Breach Width	Breach Formation Time	Trigger Failure Elevation
Peak Outflow	1.17	0.87	0.667	0.129	0.025

Global sensitivity analysis (GSA)

The dam breach phenomenon is a complex one and parameters value for realistic breach of concrete gravity dam by overtopping failure is even more complicated. In global sensitivity analysis, first the input and output parameters were fixed. Dam breach parameters were fixed as input parameters and peak breach flow as output parameters. The input parameters that are considered for the sensitivity analysis are: dam breach elevation, dam breach width, breach formation time, weir coefficient and trigger failure elevation. Based on that, each parameter with maximum, minimum and mean value was taken and 3×3×3×3×3 plan was created based on these parameter values. The relation between considered parameter with breach outflow were obtained by non linear regression analysis where the outputs of the permutation plans from (243 cases) were used. Monte Carlo (MC) sensitivity analysis was performed in OriginPro 2022b. The input parameters distribution was considered to be normal distribution. Sensitivity graph based on plot between percentage change in

variation of standard deviation of input parameters and standard deviation of peak putflow was given directly by the software. From the graph, parameters sensitivity was determined.

200000 samples of inputs were randomly generated between the ranges and simulated to get the output parameter values. Mean of the output from two lakh inputs was 188532.58 m^3/s and standard deviation of 44111.595. represents the standard deviation of peak outflow versus percent change in variation on standard deviation of breach parameters. The difference in standard deviation of DBE, BFT, DBW, WC and TFE on peak outflow were found to be 2931.12, 568.72, 3803.39, 1342.33 and 17.47 m^3/s respectively. The contribution of DBW to peak outflow was found to be maxmimum. So, DBW was the most sensitive and TFE was the least sensitive among other breach parameters.

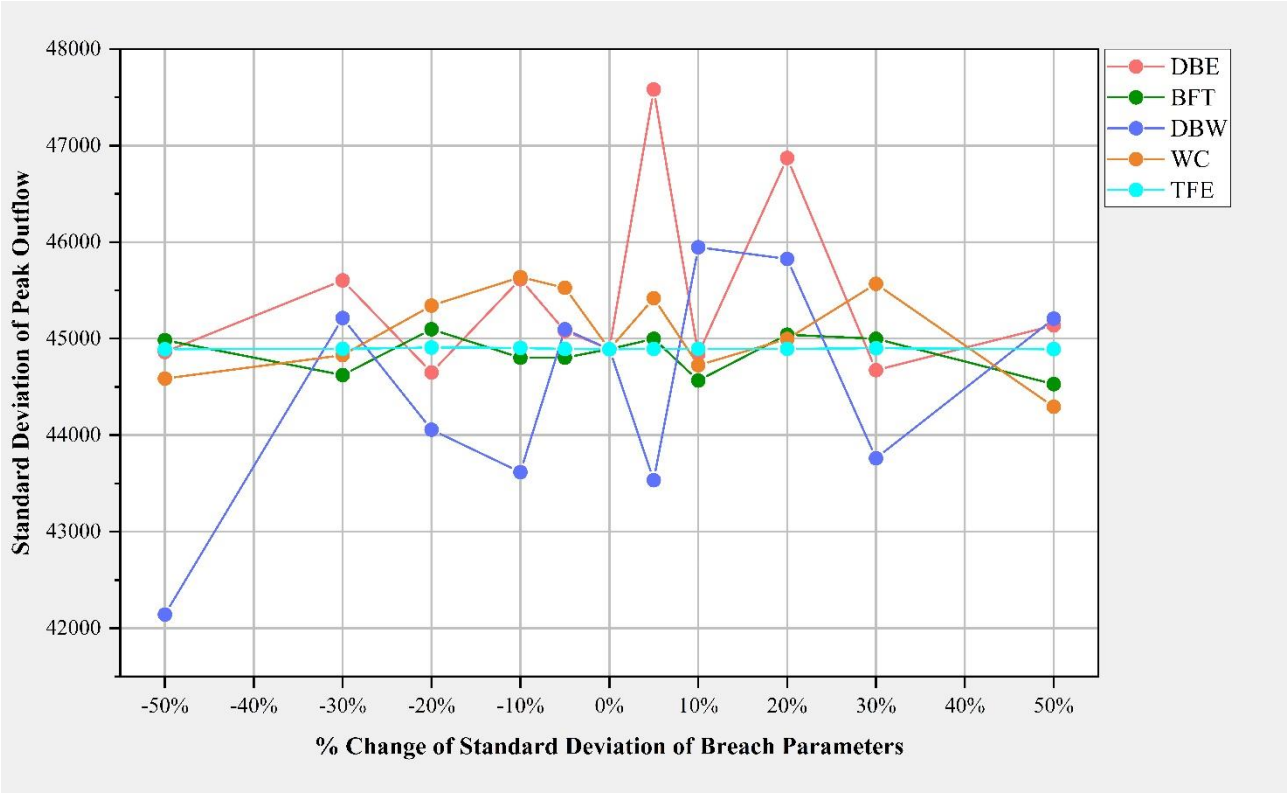

Fig. 11 - Standard deviation of peak outflow Vs Percent change in standard deviation of breach parameters

CONCLUSION

HEC RAS was used to simulate the dam breach and parameter sensitivity analysis for the proposed Nalgad Hydropower Project. The result of this study shows that, a slight change in dam breach parameters resulted in significant changes in peak flows at the dam site and WSE, velocity and arrival time at the specified reach stations in downstream channel at different kilometers.

Based on the results obatined from dam breach analyses and parameter sensitivity analyses the following conclusions were drawn.

- A maximum breach flow of 194036.2 m^3/s was noted for the base-case scenario with 12.036 km^2 area of inundation. Due to worst-case scenario maximum breach flow from dam was noted as 515976.8 m^3/s and a total of 14.478 km^2 was inundated. The output such as water depth, peak discharge, velocity, arrival time, duration was used for generation of inundation maps. Avereage flood depth along entire study area of base case including storage area was 59.62 m for base case and 59.72 m for worst case. High water depth occurred along the main channel and spreads gradually to the floodplains.

- A total of 1047 buildings from three municipalities: Aathbiskot municipality (188), Nalgad municipality (561) and Barekot rural municipality (299) were estimated to be inundated by worst-case scenario. Around 50.83 Km of road (including tertiary road, path, footway and track) were also estimated to be inundated across these municipalities.
- Human settlement area such as Tirmin and Syali, switchyard, tailrace was flooded due to overtopping failure of NHP dam. Power house was found to be one of the safe places from the flood. People from Tirmin and near switchyard area can be safer at Monika hotel whereas people from the Syali will have to move around 118 m to be safer from flood with warning time of 8.41 minutes.
- An increase in the values of dam breach width and weir coefficient increase the peak outflow. BFT and DBE were inversely proportional to peak breach flow. TFE has very less effect on peak outflow.
- The sensitivity analysis of dam breach parameters on peak outflow was undertaken by local and global sensitivity analysis. According to LSA, dam breach elevation was the most sensitive among others. TFE and BFT have least impact than DBE on breach outflow. GSA on peak outflow, the overall effect on outflow while changing all breach parameters, dam breach width was found to be the most sensitive parameters and triggering failure elevation being least sensitive.

Future study may focus on following aspects;

- Determining population at risk, economic valuation of potential damages of downstream infrastructures, land and vegetation and sediment transported by flood should be carried out for determining the actual adverse effect of the flood in wider extent.
- Consideration should also be given to different hydrologic scenarios such as different year return year floods, 30% to 50% reduction in PMF's and sunny day dam break event which helps in determining remedial measure accordingly and preparing emergency action plan.
- Instead of using overly generalized "rules of thumb" or guidelines, potential failure modes assessment should be utilized to establish the most acceptable breach size. To enable sensitivity analysis in the dam break modeling, a range of probable breach geometries should be indicated.
- In cases where there is insufficient or no geological and geotechnical information of dam site, the possibility of the complete failure of dam should be considered.
- In this study, the sensitivity analysis in the downstream river was conducted solely using a two-dimensional unsteady flow routing technique. Similar to this, the reservoir routing was carried out using an only one modeling software and single method. The modeling program has a variety of restrictions and presumptions. So, considering different modelling tools and different methods, results can be compared.
- LSA and GSA on other hydrodynamic outputs like water surface elevation, velocity and arrival time of flood should be carried out.

ACKNOWLEDGEMENTS

We would like to thank all the esteemed faculty members of Department of Civil Engineering, Pulchowk Campus for guiding and encouraging throughout the study. We are thankful to Dr. Divas B. Basnyat for providing detailed feasibility report of Nalgad Hydropower Project that required for the study.

REFERENCES

[1] T. A. Atallah, "MASTER OF SCIENCE N HYDROSYSTEM ENGINEERING A REVIEW ON DAMS AND BREACH PARAMETERS ESTIMATION," 2002.

[2] D. A. H. A. NajmObaidSalim Alghazali, "Mathematical Model of Rcc Dam Break Bastora Rcc Dam As

a Case Study," *Int. J. Civ. Eng. Technol.*, vol. 10, no. 3, pp. 1–14, 2013.
[3] D. Mirauda, R. Albano, A. Sole, J. A.- Water, and undefined 2020, "Smoothed particle hydrodynamics modeling with advanced boundary conditions for two-dimensional dam-break floods," *mdpi.com*, Accessed: Aug. 31, 2022. [Online]. Available: https://www.mdpi.com/692902.
[4] W. Li, Z. Li, W. Ge, S. W.- Water, and undefined 2019, "Risk evaluation model of life loss caused by dam-break flood and its application," *mdpi.com*, 2019, doi: 10.3390/w11071359.
[5] W. Ge *et al.*, "A method for fast evaluation of potential consequences of dam breach," *mdpi.com*, Accessed: Aug. 31, 2022. [Online]. Available: https://www.mdpi.com/560530.
[6] S. Dhiman and K. C. Patra, "Evaluation of Empirical Equations for Dam Breach Parameters," *E-proceedings 37th IAHR World Congr.*, no. 1, 2017.
[7] L. Zhang, M. Peng, D. Chang, and Y. Xu, "Dam Failure Mechanisms and Risk Assessment," *Dam Fail. Mech. Risk Assess.*, pp. 1–476, Jan. 2015, doi: 10.1002/9781118558522.
[8] "User´s Manual HEC-RAS 6.0," *Hydrologic Engineering Center*. 2021.
[9] M. Bernard-Garcia and T.-F. Mahdi, "A Worldwide Historical Dam Failure's Database," Jul. 2020, doi: 10.5683/SP2/E7Z09B.
[10] V. Bellos, V. K. Tsakiris, G. Kopsiaftis, and G. Tsakiris, "Propagating dam breach parametric uncertainty in a river reach using the HEC-RAS software," *Hydrology*, vol. 7, no. 4, pp. 1–14, 2020, doi: 10.3390/hydrology7040072.
[11] G. Tsakiris and M. Spiliotis, "Dam- Breach Hydrograph Modelling: An Innovative Semi- Analytical Approach," *Water Resour. Manag. 2012 276*, vol. 27, no. 6, pp. 1751–1762, May 2012, doi: 10.1007/S11269-012-0046-9.
[12] FERC, "Dam Breach Analysis," 2014.
[13] J.-T. Kuo, B.-C. Yen, Y.-C. Hsu, and H.-F. Lin, "Risk Analysis for Dam Overtopping—Feitsui Reservoir as a Case Study," *J. Hydraul. Eng.*, vol. 133, no. 8, pp. 955–963, Aug. 2007, doi: 10.1061/(ASCE)0733-9429(2007)133:8(955).
[14] L. P. Gyawali, D.R. and Devkota, "Dam Break Analysis USING HEC-RAS: A CASE STUDY of Proposed Koshi High Dam," 2015.
[15] M. S. Khattak, F. Anwar, T. U. Saeed, M. Sharif, K. Sheraz, and A. Ahmed, "Floodplain Mapping Using HEC-RAS and ArcGIS: A Case Study of Kabul River," *Arab. J. Sci. Eng.*, vol. 41, no. 4, pp. 1375–1390, 2016, doi: 10.1007/s13369-015-1915-3.
[16] M. Heydari, A. Shahiri Parsa, M. S. Sadeghian, and M. Moharrampour, "Flood Zoning Simulation by HEC-RAS Model (Case Study: Johor River-Kota Tinggi Region)," *J. River Eng.*, vol. 1, no. 1, p. 6, 2013, [Online]. Available: http://www.scijour.com/page/download-e-AfqLK9Ipw.artdl.
[17] S. E. Yochum, L. A. Goertz, and P. H. Jones, "Case Study of the Big Bay Dam Failure: Accuracy and Comparison of Breach Predictions," *J. Hydraul. Eng.*, vol. 134, no. 9, pp. 1285–1293, 2008, doi: 10.1061/(asce)0733-9429(2008)134:9(1285).
[18] F. E. Hicks and T. Peacock, "Suitability of HEC-RAS for Flood Forecasting," *Can. Water Resour. J.*, vol. 30, no. 2, pp. 159–174, 2005, doi: 10.4296/cwrj3002159.
[19] B. Balaji and S. Kumar, "Dam break analysis of kalyani dam using HEC-RAS," *Int. J. Civ. Eng. Technol.*, vol. 9, no. 5, pp. 372–380, 2018.
[20] Colorado dam safety branch 2010, "Guidelines for Dam Breach Analysis," 2010. Accessed: Aug. 23, 2022. [Online]. Available: https://scholar.google.com/scholar?hl=en&as_sdt=0%2C5&q=colorado+dam+safety+branch+2010&btnG=.
[21] A. Saltelli, "Sensitivity analysis: Could better methods be used?," *J. Geophys. Res. Atmos.*, vol. 104, no. D3, pp. 3789–3793, Feb. 1999, doi: 10.1029/1998JD100042.
[22] C. Pichery, "Sensitivity Analysis," *Encycl. Toxicol. Third Ed.*, pp. 236–237, Jan. 2014, doi: 10.1016/B978-0-12-386454-3.00431-0.
[23] X. Zhou and H. Lin, "Local Sensitivity Analysis," *Encycl. GIS*, pp. 616–616, 2008, doi: 10.1007/978-0-387-35973-1_703.
[24] N. B. Lucie Pheulpin, Vito Bacchi, "Uncertainty and sensitivity analysis for hydraulic models with dependent inputs | Enhanced Reader," *uropean Geosciences Union General Assembly, EGU*, 2019. .
[25] M. Ratto, S. Tarantola, and A. Saltelli, "Sensitivity analysis in model calibration: GSA-GLUE approach," *Comput. Phys. Commun.*, vol. 136, no. 3, pp. 212–224, May 2001, doi: 10.1016/S0010-4655(01)00159-X.
[26] Nalgad, "Updated Feasibility Study Report," 2018.

CIVIL ENGINEERING JOURNAL

Article no. X

THE CIVIL ENGINEERING JOURNAL Y-20ZZ

STUDY ON PREFABRICATED CONNECTOR OF DOUBLE-LAYER RECIPROCAL FRAME

Zifei Li[1], Lin Qi[2], Yongcheng Huai[2]

1. China Hebei Construction & Geotechnical Investigation Group Ltd, Hebei, China.
2. Civil Aviation University of China, Tianjin, China.
lzf_tmgc@163.com; qilin1208@vip.163.com; 758066153@qq.com;

ABSTRACT

A kind of lattice-type steel member is presented and a kind of prefabricated connector suitable for the connection between lattice-type steel members are proposed. The mechanical properties of the connectors are analyzed by using the finite element numerical simulation software ABAQUS. The connectors meet the design goals of the stiffness of connection stronger than members. Parameterized analysis is carried out on the prefabricated connector, and the flexural stiffness expression of the connector is obtained. The suggested values of each component of the prefabricated connectors are given based on the size of connected lattice-type steel members.

KEYWORDS

Double-layer reciprocal frame; Prefabricated structure; Prefabricated connector; Steel structure

INTRODUCTION

The number and variety of members and joints in the traditional large span spatial structure are numerous. The complexity of the structure leads to special shape of the member and the complexity of joints. It is often the case that lots of members are converged at one joint, which causes the consequence that difficulty and the cost of construction both are increased largely [1-3]. Figure 1 shows the roof structure of Beijing Daxing Airport Terminal in China.

The hex-tri reciprocal frame is a special structure of rotational symmetry. The members support each other, each member not only supports the adjacent members but also is supported by another adjacent members, so all members are subjected to the similar mechanical characteristics [4-6]. Members of reciprocal frame are interconnected, which makes the forms of members and joints simple and unified [7-8]. The large span spatial structure can be realized by assembling small-size members of the reciprocal frame, which has a promising future in prefabricated building [9-10].

Fig. 1 - The Roof Structure of Beijing Daxing Airport Terminal

Reciprocal frame is of a long history. The unique structure makes its connections play a crucial part to ensure the reliability of reciprocal frame [4-5]. The joints of reciprocal frame are various. A model of arch bridge connected by inter-locked is shown in Figure 2 [3]. This type of connection depends on frictional force to guarantee the reliability of the structure. This kind of friction-driven connections is very simple. However, the strength and rigidity of the structure is weak which results in the short span of reciprocal frame [11-12]. With the development of reciprocal frame, lashed connection and notched connection appeared [5]. Because the low strength and small rigidity of the connection, reciprocal frame cannot reach larger span [14-15].

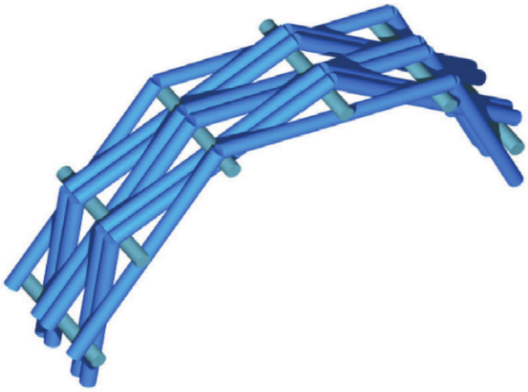

Fig. 2 - Model of Chinese laminated beam bridge

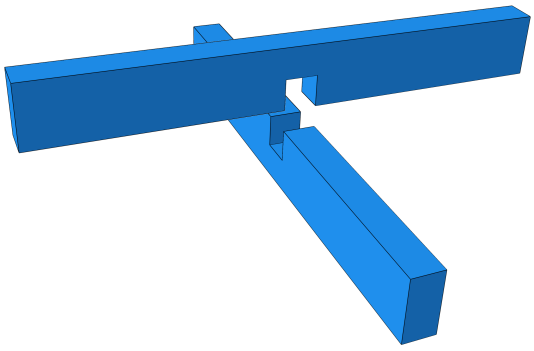

Fig. 3 - Notched connection

In 1976, the first patent of connector in reciprocal frame, bolted connectors, was proposed by Bijnen. He suggested to loop the circular hollow sections via threaded pins to form reciprocal frame [14-15]. The connector is very simple, and is of high strength and great rigidity. However, this connector requires high precision of reserved holes and threaded pins which results in great difficulties for construction and even reducing the efficiency of construction. In addition, two adjacent members connected by this connector rotate result in small rigidity and low strength of the whole structure [15]. The adjustable connector is a kind of prefabricated connection. The strength and rigidity of this kind of connector is much higher, and the unique structure compensates for installation error of the members [15]. However, the adjustable connector is only suitable for single-layer reciprocal frame, which cannot reach large span.

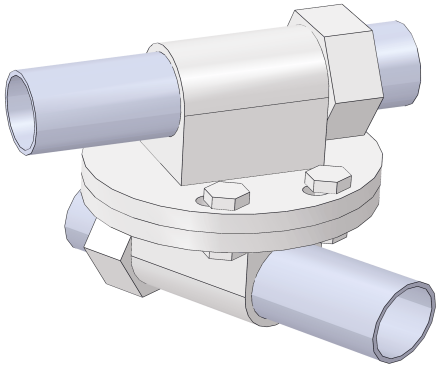

Fig. 4 - Adjustable connector

Fig. 5 - Single-layer reciprocal frame

The extant buildings of reciprocal frame, whether roof structures or landscape structures, are single-layer reciprocal frames. Due to low strength and low stiffness of members, the span of the structure is small. The members of single-layer reciprocal frame are mainly subjected to bending moment, but the bending stiffness of the member is low, which is the main reason for low stiffness of the single-layer reciprocal frame [16-18]. As shown in Figure 6, by transforming the members to lattice-type members, the transformation of the single-layer reciprocal frame to the double-layer reciprocal frame is realized, and the stiffness and strength of the structure have been improved. The double-layer reciprocal frame retains the features and advantages of the reciprocal frame and the strength and stiffness have been improved [17-19].

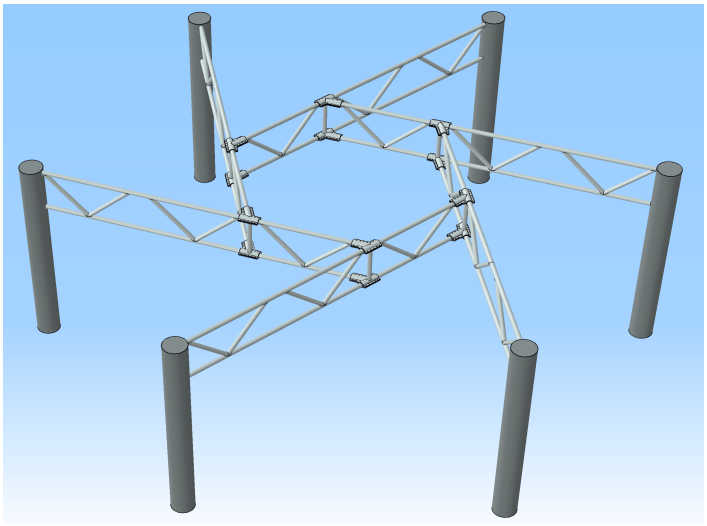

Fig. 6. - A fan of double-layer of reciprocal frame

PREFABRICATED CONNECTOR

Prefabricated Connector

The reliability of the structure connection is crucial. In order to get over the shortcomings of existing joints of reciprocal frame, a kind of prefabricated connector is invented, which is rigid and suitable for alignment between lattice-type members, as shown in Figure 7. The prefabricated connector consists of upper structure, middle structure and lower structure: upper clamping structure 1, middle supporting structure 2 and lower clamping structure 3. The

upper clamping structure and lower clamping structure have the same structural form. The upper clamping structure and the lower clamping structure are parallel intervals set. The middle supporting structure is set vertically with the clamping structures.

As shown in Figure 7 and Figure 8, the two holes with circular sections in each clamping structure are formed by tightening high-strength fastening bolts. The external force works on the upper clamping structure. By setting middle supporting structure, the force can be bear by top and bottom chord. Because the middle supporting structure transmits part of the external force to the bottom chord, the concentration phenomenon of stress at the joints of the lattice type members has been reduced, the material utilization rate has been improved.

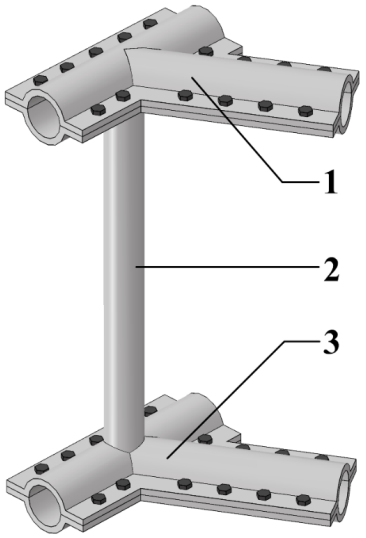

Fig. 7 - Prefabricated connector

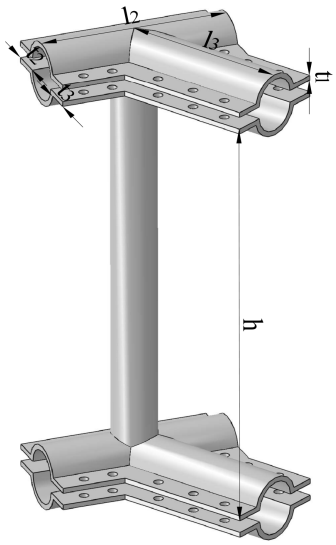

Fig. 8 - Parameters of prefabricated connector

Lattice type member

The bending moment is mainly beared by the members of reciprocal frame. In order to solve the problems that low stiffness of the single-layer reciprocal frame. A lattice type steel member suitable for double-layer reciprocal frame is designed, as shown in Figure 9. The position of prefabricated connectors is reserved in the chord member to facilitate the connection between the lattice type steel member and the prefabricated connectors. And some of the bending moment in the member is converted into axial force. The utilization rate of material has been improved and the stiffness and strength of the structure has been enhanced.

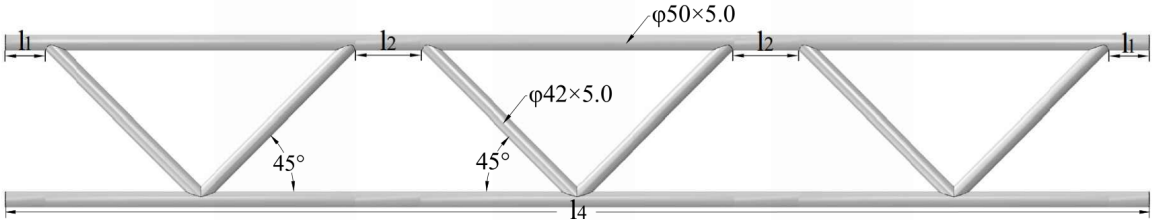

Fig. 9 - Lattice type member

NUMERICAL ANALYSIS OF PREFABRICATED CONNECTOR

As is shown in Figure 10, a three dimensional entity model of a reciprocal frame fan including the prefabricated connectors and the lattice type steel members made of Q235 steel has been created, using the finite element model software Abaqus CAE, to study the mechanical properties of the prefabricated connector. The parameters of each part of the prefabricated connector and the lattice type steel member are shown in table1. The vertical loads are mainly borne by double-layer reciprocal frame which are transmitted to the whole structure by the connectors. Fixed constraints are applied to the ends of the lattice type members, and the vertical downward pressure is applied to the upper surface of the connectors and the gravity of the connectors and members is applied to the numerical model to study the mechanical characteristics of the connectors. In Figure 11, the ratio of the vertical direction displacement of section A to l_1 is the connector's rotation angle around the x-axis.

Tab. 1: The parameters of each part of the connector and the lattice type steel

Geometric Parameters	t_1	t_2	t_3	t_4	l_1	l_2	l_3	l_4	h
Value	8	34	26	6	158	230	230	4420	500

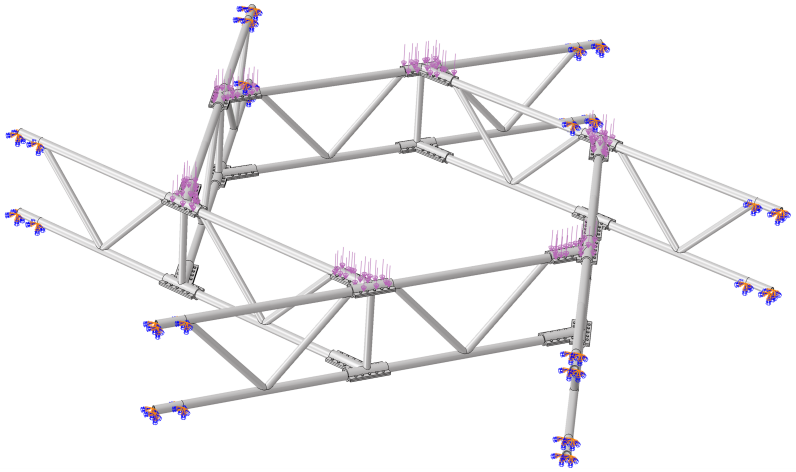

Fig. 10 - The numerical model of reciprocal frame

Fig. 11 - Section A of the connector

In order to study the characteristics of the prefabricated connectors and the failure mechanism of the double-layer reciprocal, the pressure has been constantly increased. When the plastic hinge was formed, the pressure was increased to 2.46 MPa. In the fan of reciprocal frame, every member and connector are in the same condition of stress, so a lattice type steel member and an prefabricated connector are taken to analyse the stress condition.

As can be seen from Figure 12, the connecting part of the web member and upper chord of the lattice-type steel member has shown that the stress of the full section has been reached to 235 MPa and the plastic hinge has been formed, so that the lattice-type steel member has been damaged.

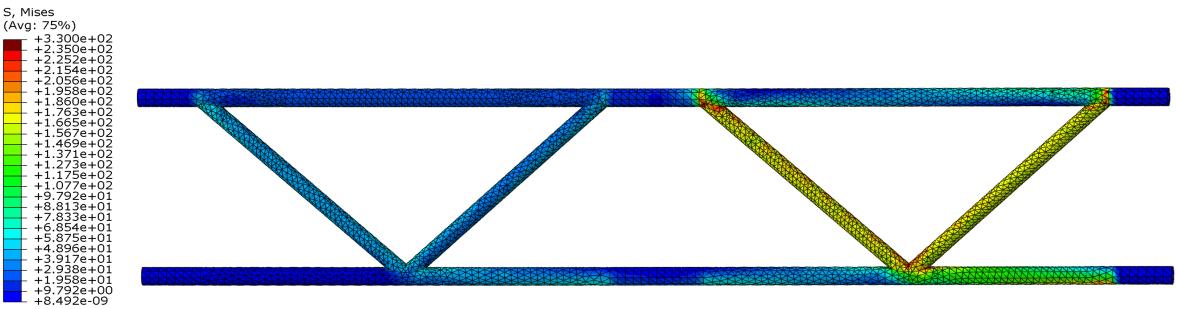

Fig. 12 - Stress nephogram of the lattice type member under pressure/Pa

It can be seen from Figure 13 that most stress elements of the prefabricated connectors are still in the elastic stage, and few of the stress elements of the edge part exceeds 235 MPa. In conclusion, the strength of the connection is higher than the strength of the members. The rotation angle of the connector is only 1.01×10^{-3}rad while the plastic hinge of the member was formed. Hence the rigidity of the prefabricated connector of the X-axis is very large.

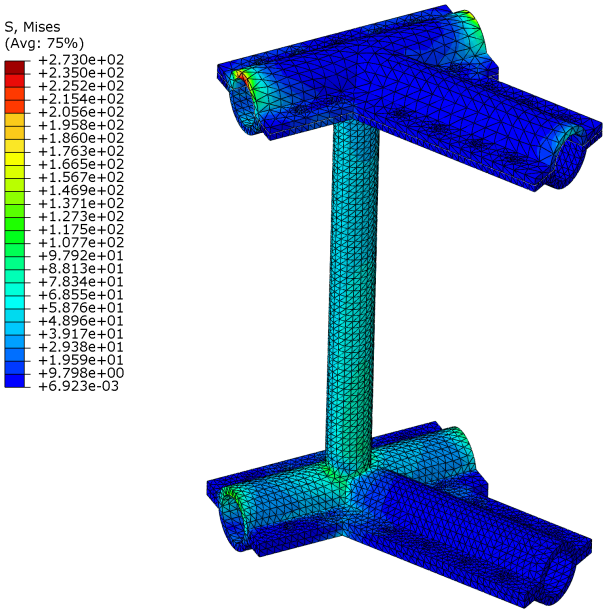

Fig. 13 - Stress nephogram of the prefabricated connector/Pa

CALCULATION MODEL OF THE CONNECTOR

As can be seen from the analysis in the previous section, when plastic hinge is generated at the connecting part of the web member and the upper chord of the lattice steel member, almost all stress elements in the prefabricated connectors are still in the elastic stage.

After finite element analysis, parameters l_3, l_2, l_4, and h have little effect on the finite element analysis of the prefabricated connector. Therefore l_3=l_2= 230 mm, l_4= 4420 mm, h= 500 mm are fixed values. And using this type lattice-steel member of these parameters, when the lattice-steel member is damaged, the stress element of the connector is about to reach the yield stress of 235 Mpa. The problem that the lattice-steel member is too strong and the failure of the prefabricated connector occurs before the lattice-steel member enters the yield stage is

avoided, and the problem that the stress of the prefabricated connector is too small when the lattice-steel member is damaged is avoided.

In order to analyze the complete mechanical characteristics of the prefabricated connectors, the size of each part of the connectors were changed respectively, and the mechanical properties of the prefabricated connectors were analyzed according to the arc length method. The other values of each part in numerical model of parametric analysis are shown in Table 2.

Tab. 2 - Values of connectors in numerical model of parametric analysis

No.	1	2	3	4	5	6	7	8	9	10
t_1/mm	6	8	10	12	14	8	8	8	8	8
t_2/mm	34	34	34	34	34	30	32	34	36	38
t_4/mm	6	6	6	6	6	6	6	6	6	6
l_1/mm	168	168	168	168	168	168	168	168	168	168
l_2/mm	250	250	250	250	250	250	250	250	250	250
f/MPa	235	235	235	235	235	235	235	235	235	235
No.	11	12	13	14	15	16	17	18	19	20
t_1/mm	8	8	8	8	8	8	8	8	8	8
t_2/mm	34	34	34	34	34	34	34	34	34	34
t_4/mm	4	6	8	10	12	6	6	6	6	6
l_1/mm	168	168	168	168	168	158	163	168	173	178
l_2/mm	250	250	250	250	250	250	250	250	250	250
f/MPa	235	235	235	235	235	235	235	235	235	235

No.1-5 in Table 2 are used to establish three-dimensional solid numerical models of ABAQUS. Grave force has been applied and pressure has applied to the connectors. In Model 1-5, only the parameter t_1 has been changed and other parameters remain unchanged. Thus only t_1 is the factor affecting the flexural rigidity of prefabricated connectors. It can be seen from Figure 14 that the rotation angles of the prefabricated connectors around x-axis are approximately directly proportional to the bending moments on section A, and the flexural rigidity of the connector has been increased obviously with the increase of t_1. After analysis and calculation, the flexural rigidity curve of prefabricated connectors with different sizes of t_1 is shown in Figure 15.

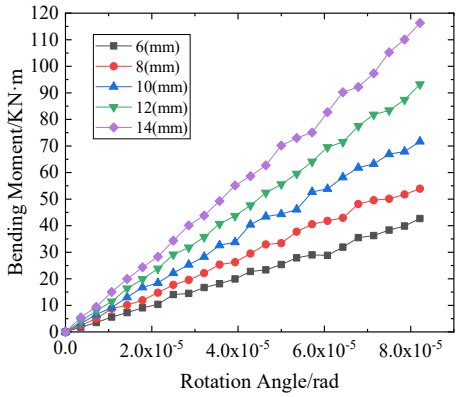

Fig.14 - No.1-5 Numerical model of rotation angle

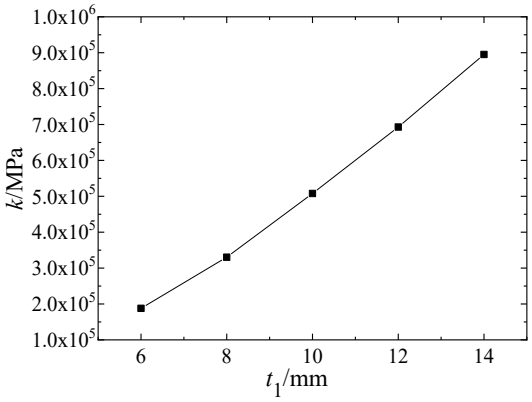

Fig.15 - No.1-5 Relation curve

As shown in the Figure 15, the flexural rigidity k of the prefabricated connector of the x-axis is of an approximate linear relationship with t_1, and the formula is shown below:

$$k=90626t_1+44781 \quad (3.1)$$

Related coefficient: $R^2=0.98$

The relationship between t_2 and k is analyzed in the same way. The bending moment on section A and the Angle curve of prefabricated connectors are shown in Figure 16. It can be seen from Figure 16 that the rotation angle of the prefabricated connectors around the x-axis is directly proportional to the bending moment, and the rigidity of the prefabricated connector is weakly increased with the increase of t_2. After analysis and calculation, the flexural rigidity curve of prefabricated connectors with different sizes of t_2 is shown in Figure 17.

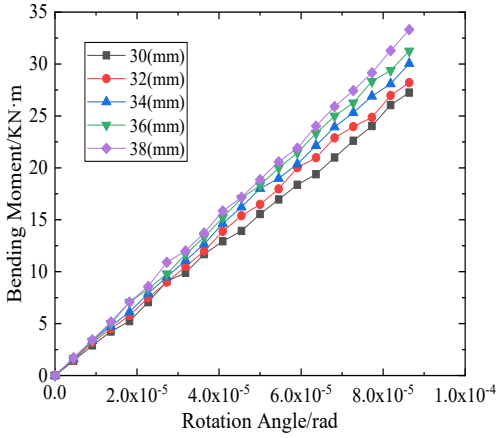

Fig. 16 - No.6-10 Numerical model of rotation angle

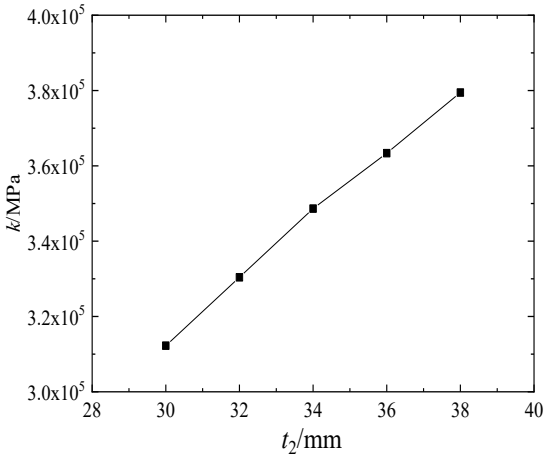

Fig. 17. No.6-10 Relation curve

As is shown in Figure 17, the flexural rigidity k of the prefabricated connector of the x-axis is of an approximate linear relationship with t_2, and the formula is shown below:

k=1640t_2+277890 (3.2)

Related coefficient: R^2=0.97

The relationship between t_3 and k is analyzed in the same way. The bending moment on section A and the Angle curve of connectors are shown in Figure 18. It can be seen from Figure18 that the rotation angle of the connectors around the x-axis is directly proportional to the bending moment, and the flexural rigidity of the prefabricated connector is weakly increased with the increase of t_4. After analysis and calculation, the flexural rigidity curve of prefabricated connectors with different sizes of t_4 is shown in Figure19.

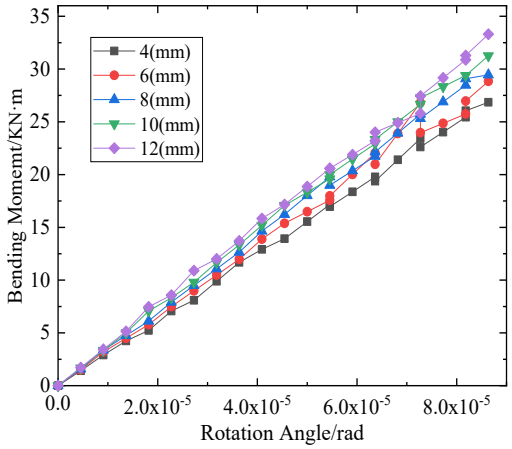

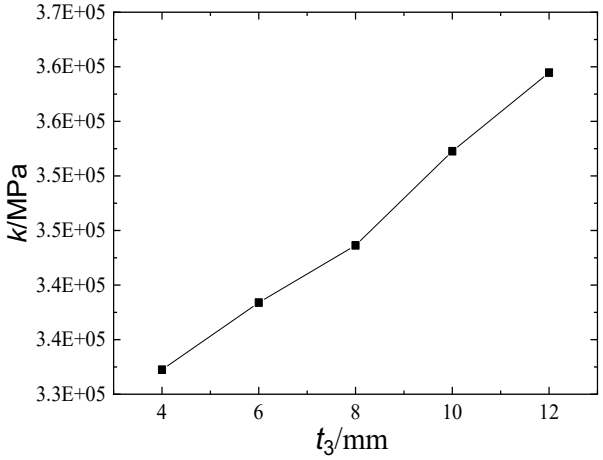

Fig. 18 - No.11-15 Numerical model and rotation angle *Fig. 19 - No.11-15 Relation curve*

As is shown in Figure 19, the flexural rigidity k of the prefabricated connector of the x-axis is of an approximate linear relationship with t_3, and the formula is shown below:

k=2623t_3+322655 (3.3)

Related coefficient: R^2=0.95

The relationship between I_1 and k is analyzed in the same way. The bending moment on section A and the Angle curve of prefabricated connectors are shown in Figure 20. It can be seen from Figure 20 that the rotation angle of the prefabricated connectors around the x-axis is directly proportional to the bending moment, and the flexural rigidity of the prefabricated connector is significantly increased with the increase of I_1. After analysis and calculation, the flexural rigidity curve of prefabricated connectors with different sizes of I_1 is shown in Figure 21.

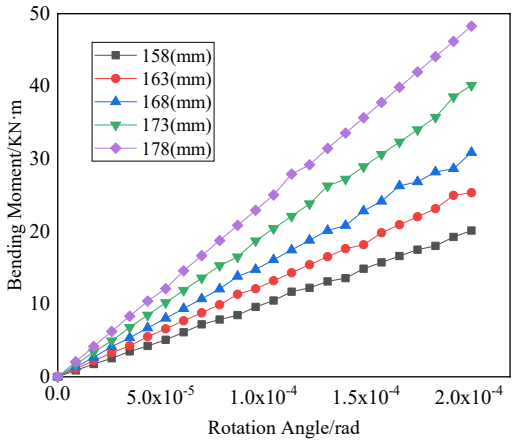

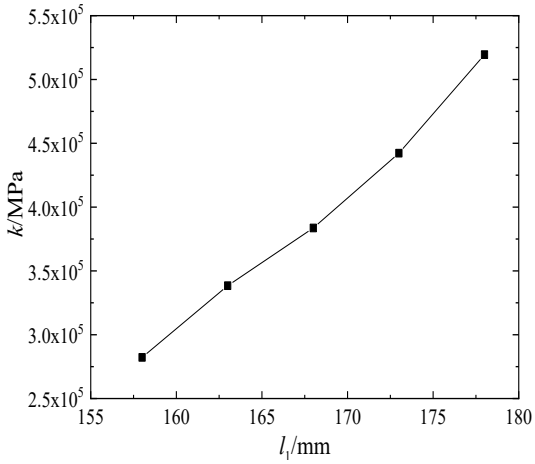

Fig.20. No.16-20 Numerical model of rotation angle Fig.21. No.16-20 Relation curve

As is shown in Figure 21, the flexural rigidity k of the prefabricated connector of the x-axis is of an approximate linear relationship with l_1, and the formula is shown below:

$$k=29652l_1+163655 \quad (3.4)$$

Related coefficient: $R^2=0.96$

The relationship between l_2 and k is analyzed in the same way. The bending moment on section A and the Angle curve of prefabricated connectors are shown in Figure 22. It can be seen from Figure 22 that the rotation angle of the prefabricated connectors around the x-axis is directly proportional to the bending moment, and the flexural rigidity of the prefabricated connector is significantly increased with the increase of l_2. After analysis and calculation, the flexural rigidity curve of prefabricated connectors with different sizes of l_2 is shown in Figure 23.

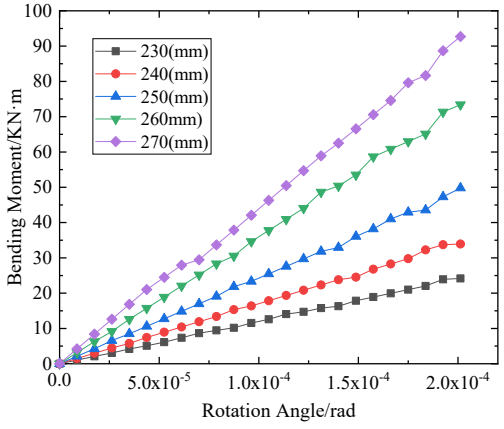

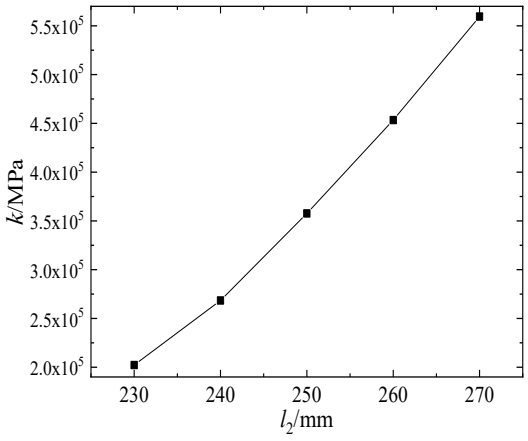

Fig. 22 - No.21-25 Numerical model of rotation angle Fig. 23 - No.21-25 Relation curve

As is shown in Figure 23, the flexural rigidity k of the prefabricated connector of the x-axis is of an approximate linear relationship with l_2, and the formula is shown below:

$$k=7251l_2+74353 \quad (3.5)$$

Related coefficient: R^2=0.97

The relationship between *f* and *k* is analyzed in the same way. The bending moment on section A and the Angle curve of connectors are shown in Figure 24. It can be seen from Figure 24 that the rotation angle of the connectors around the x-axis is directly proportional to the bending moment, and the flexural rigidity of the connector is significantly increased with the increase of *f*. After analysis and calculation, the flexural rigidity curve of prefabricated connectors with different sizes of l_2 is shown in Figure 25.

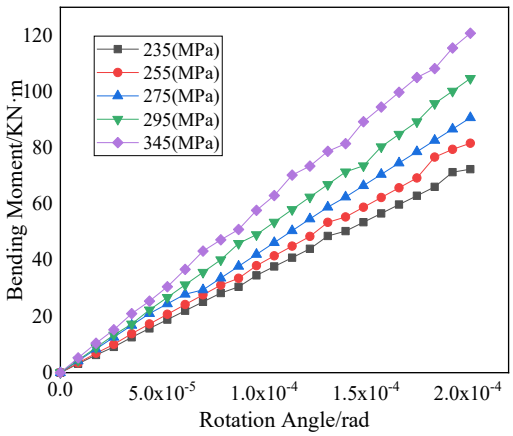

Fig.24 - No.26-30 Bending moment and rotation angle

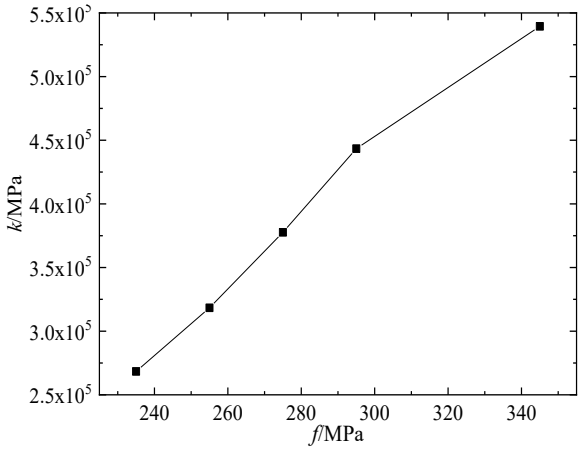

Fig.25 - No.26-30 Relation curve

As is shown in Figure 25, the flexural rigidity *k* of the prefabricated connector of the x-axis is of an approximate linear relationship with *f*, and the formula is shown below:

$$k=6843f+86219 \tag{3.6}$$

Related coefficient: R^2=0.94

As can be seen from the above expressions, the coefficient of k with t1 is 90626, much higher than the coefficient of *k* with t_2, t_4, l_1, l_2 and *f*. Therefore the value of flexural stiffness k is taken to be most influenced by the change in parameter t_1.

As can be seen from the above analysis, it can be concluded the rigidity *k* of the prefabricated connector is of a linear relationship with the parameters t_1、t_2、t_3、l_1、l_2 and *f*. However, according to the formulas, the degree of influence of each parameter on the flexural rigidity *k* is different, the coefficient of *k* with t_1 is 90626, much higher than the coefficient of *k* with t_2, t_3, l_1, l_2 and *f*. Therefore, the value of the flexural rigidity *k* is most affected by the change of the parameter t_1. The formula of $\frac{k}{t_2 t_3 l_1 l_2 f}$ and t_1 are as follows:

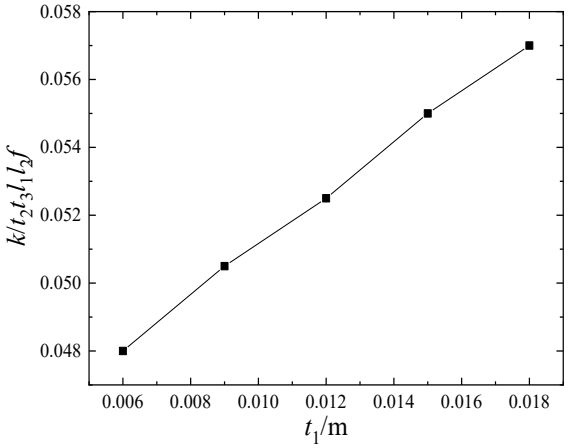

Fig. 26 - Curve of $\frac{k}{t_2 t_3 l_1 l_2 f}$ and t_1

The formula is shown below:

$$\frac{k}{t_2 t_3 l_1 l_2 f} = 0.81 t_1 + 0.02 \tag{3.7}$$

Related coefficient: R^2=0.9985.

In conclude, the formula of flexural rigidity k of the prefabricated connector is as follows:

$$k = t_2 t_3 l_1 l_2 f\left(0.81 t_1 + 0.02\right) \tag{3.8}$$

For the selection of the size of the prefabricated connector, the design goal is to ensure that the prefabricated connector is still in elastic state when the lattice type steel member is damaged, and at the same time, to reduce the size of each part and reduce the use of materials. The chord and web member of the lattice type steel member are circular hollow sections. The outer diameter of the steel pipe is d_s, and the wall thickness is t_s. The diameter of the web member is $0.8d_s$, and the wall thickness is t_s. After calculation and analysis, the suggested sizes of each part of the prefabricated connector are t_1=1.4t_s, t_2=8t_s, t_3=1.2t_s, t_4=1.2t_s, l_1=5d_s+5t_s, l_2=3d_s+5t_s. The diameter of the fastening bolt is 4t_s, and the thickness of bolt protection layer is 4t_s. Specification of fastening bolt should not be smaller than M16 type high strength bolt.

DOUBLE-LAYER HEX-TRI PREFABRICATED RECIPROCAL FRAME

The grid of hex-tri reciprocal frame

As is shown in Figure 27, the grid of hex-tri reciprocal frame is regular and can be extended infinitely to all sides through the annular array. Under the requirements of rigidity, strength and stability, the double-layer hex-tri reciprocal frame can be extended to the outer ring and reach a larger span according to the expansion law of the hex-tri grid of reciprocal frame.[21]

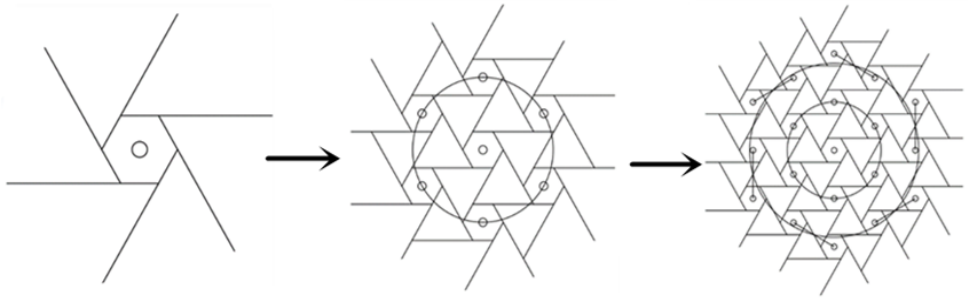

(a) The basic configuration (b)Once extension (c)Twice extension

Fig. 27 - The law of extension of hex-tri grid of reciprocal frame

Double-layer hex-tri prefabricated reciprocal frame

The existing reciprocal frame examples are mainly single-layer reciprocal frame. Due to low strength and low stiffness of members, the span of single-layer reciprocal frame is small. The members of single-layer reciprocal frame are mainly subjected to bending moment, but the bending stiffness of the member is low, which is the main reason for low stiffness of the single-layer reciprocal frame. By transforming the members to lattice-type members, the transformation of the single-layer reciprocal frame to the double-layer reciprocal frame is realized, and the stiffness and strength of the structure have been improved. The double-layer reciprocal frame retains the features and advantages of the reciprocal frame and the strength and stiffness have been improved.

As is shown in Figure 28, according to the geometric extension law of the grid of hex-tri reciprocal frame, the double-layer hex-tri prefabricated steel reciprocal frame can be built, using the prefabricated connectors and lattice type steel members designed in this paper. The joints of the structure are crucial, and the reliability of the prefabricated connector can be guaranteed, and the formula of flexural rigidity of the prefabricated connector has been calculated.

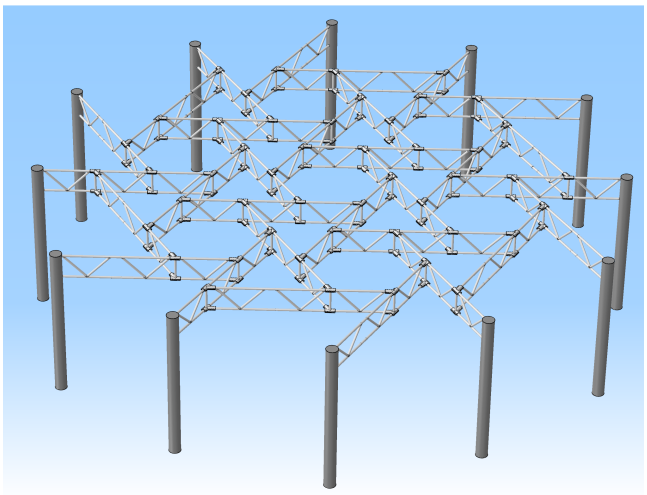

Fig. 28 - Double-layer reciprocal frame

Double-layer hex-tri prefabricated steel reciprocal frame stress cloud

The calculated bending stiffness equation of prefabricated connector (3.8) was input into the ABAQUS finite element connector. Based on the once extension of the hex-tri grid, the finite element numerical model of ABAQUS of double-layer hex-tri steel reciprocal frame was established based on beam elements and hinged connectors. The element type of the finite element numerical model is B31, and the material is Q235 steel. The total length of the members in the numerical model is 4140 mm, the diameter of the circular hollow section is 50mm, and the wall thickness is 5 mm, and the diameter of the circular hollow section web member is 42 mm and a wall thickness of 5mm. Fixed constraints were applied external endpoints of the numerical model, and the roof load of 0.9 kN/m^2 was evenly applied at the joints.

The stress of the double-layer hex-tri steel reciprocal frame formed by the once extension is shown as Figure 29. The stress of the lower chord at the support is the largest, which is 100.4 MPa, less than the yield strength of Q235 steel.

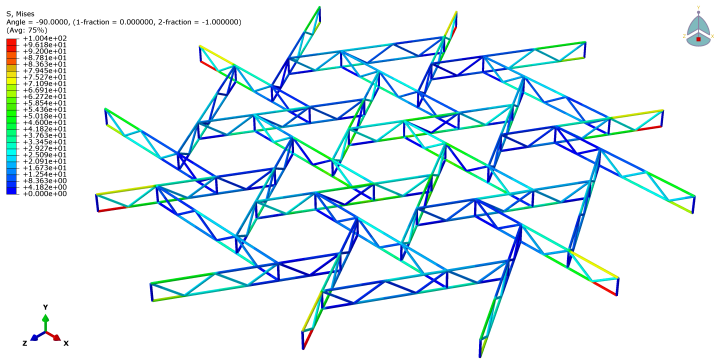

Fig. 29 - Double-layer hex-tri prefabricated steel reciprocal frame stress cloud

CONCLUSION

(1) A lattice-type steel member is presented and a kind of prefabricated connector suitable for the connection between lattice-type steel members are proposed. The mechanical properties of the connectors are analyzed by using the finite element numerical simulation software ABAQUS. The connectors meet the design goal of the strength and rigidity of joints stronger than members.

(2) Parameterized analysis is carried out on the prefabricated connector, and the formula of flexural rigidity of the prefabricated connector has been calculated. The suggested values of each part of the prefabricated connectors are given based on the size of connected lattice type steel members

(3) According to the geometric extension law of the grid of hex-tri reciprocal frame, the double-layer hex-tri prefabricated steel reciprocal frame can be built, using the prefabricated connectors and lattice type steel members designed in this paper.

DECLARATION OF COMPETING INTEREST

The authors declare that they have no known competing financial interests or personal relationships that could have appeared to influence the work reported in this paper.

ACKNOWLEDGEMENTS

This work is supported by National Key Research and Development Plan of China (2021YFB2600500).

REFERENCES

[1] Zhang Ailin, Wang Xiaoqing, Liu Weinong, Zhu Zhongyi, Qiang Shen, Jiang Ziqin, Feng Shuo. Shaking table test on overall-scale model of long-span steel structure of Beijing Daxing International Airport terminal[J]. Journal of Building Structures, 2021, 42(03): 1-13.

[2] Zhao Xianzhong, Xu Xiang-Bin, Yan Shen, Wang Bin, Chen Yiyi, Fan Zhong, Peng Yi, Li Li. Experimental study of complex multiplanar tubular joints[J]. Engineering Mechanics, 2010, 27(S2): 207-211.

[3] Zhang Ailin, Shao Dinan, Zhang Yanxia, Shu Weinong, Zhu Zhongyi, Li Zhenxing. Research on mechanical performance of complex tubular joints of Beijing New Airport Terminal C type column[J]. Journal of Building Structures, 2018, 40(03): 210-220. (in Chinese)

[4] Popovic O. Reciprocal Frame Architecture[M]. Burlington: Elsevier, 2008.

[5] Rizzuto J P, Popovic O L. Connection Systems in Reciprocal Frames and Mutually Supported Elements Space Structure Networks[J]. International Journal of Space Structures, 2010, 11(4): 243-256. doi: 10.1260/0266-3511.25.4.243.

[6] Larsen, Olga Popovic.Reciprocal Frame (RF) Structures: Real and Exploratory[J].Nexus network journal: Architecture and mathematics,2014,16(1):119-134. doi: 10.1007/s00004 -014-0181-0.

[7] Bertin V. Leverworks : one principle, many forms [M]. Beijing: China Architecture & Building Press, 2012. 11-11.

[8] Simon Gelez, Victoire Saby. Workshop « Ateliers Design » : « Nexorades, Facing an Emergency Situation »[J]. International Journal of Space Structures,2012,26(4).

[9] Song, P.,-Wing Fu, C., Goswami, P., et al. Reciprocal frame structures made easy[J].ACM Transactions on Graphics,2013,32(4 CD/ROM):94-1-94-10.

[10] Kai Tai Wan, Honggang Zhu, Terry Y.P. Yuen, Binmeng Chen, Chuanlin Hu,Christopher K.Y. Leung,Jun Shang Kuang. Development of low drying shrinkage foamed concrete and hygro-mechanical finite element model for prefabricated building fasçade applications[J]. Construction and Building Materials,2018,165.

[11] Rizzuto J P, Popovic O L. Connection Systems in Reciprocal Frames and Mutually Supported Elements Space Structure Networks[J]. International Journal of Space Structures, 2010, 11(4): 243-256.

[12] Aicher, S., Garrecht, H., Reinhard, H.-W. (2014): Materials and Joints in Timber Structures. Springer, New York, pp. 129-134.

[13] Joel Gustafsson. Connections in Timber Reciprocal Frames[D].Gothenburg, Sweden: Chalmers University Of Technology, 2016.

[14] Bijnen A. Een geodetiese knoopkonstruktie[P]. Octrooiraad Nederland, Terinzagelegging. Aanvrage, No 7603046. 1976.

[15] Lin Qi, Zifei Li, Lingtong Li, Hui Pan, Zhenzhou Xie, Xin Huang. Study on adjustable connector of reciprocal frame[J]. Civil engineering Journal, 2021, 28(2): 378-392.

[16] Bernard Vaudeville,Simon Aubry,Simon Gelez.Nexorade or Reciprocal Frame System Applied to the Design and Construction of a 850 m2 Archaeological Shelter[J]. International journal of space

structures,2011,26(4):303-311. doi: 10.1260/0266-3511. 26.4.303.

[17] Rizzuto J P. The Structural Behaviour of Mutually Supported Elements in Space Structures[D]. Coventry: Coventry University, 2005.

[18] Pugnale A, Sassone M. Structural Reciprocity: Critical Overview and Promising Research/Design Issues[J]. Nexus Network Journal, 2014, 16(1): 9-35.

[19] Lin Qi, Zifei Li, Hui Pan, Zhenzhou Xie, Lingtong Li, Xin Huang. Study on double-layer hex-tri timber reciprocal frame of mortise-tenon connections[J/OL]. Journal of Building Structures, 1-9[2021-09-14].https://doi.org/10.14006/j.jzjgxb.2021.0131. (in Chinese)

[20] GB50017-2017. Code for design of steel structures [S]. 2017.

[21] Lin Qi, Wenbo Zhang, Zifei Li, Ronglai Sun, Xin Huang. GEOMETRY CONSTRUCTION METHOD OF HEX-TRI RECIPROCAL FRAME[J]. Civil Engineering Journal, 2019, 28(4).

CIVIL ENGINEERING JOURNAL

Article no. 45

THE CIVIL ENGINEERING JOURNAL 4-2022

DIGITIZATION OF PHYSICAL MODELS OF RURAL ARCHITECTURE

Ing. Vojtěch Cehák

CTU in Prague, Faculty of Civil Engineering, Department of Geomatics, Thákurova 7/2077, Prague 6, Czech Republic; email: vojtech.cehak@fsv.cvut.cz

ABSTRACT

Working with objects in digital spatial form is gradually becoming a standard in many fields. In addition to the advantage of easier object manipulation, digital representation can also be used for presentation purposes or better cataloguing. In the case of objects from museum collections, it can serve as a basis for restoration or for conducting deeper research into detailed structures. The method of photogrammetry allows 3D modelling of real objects without physical contact with them, while at the same time making use of affordable equipment. However, the disadvantage of this method is the size of the output data (even hundreds of megabytes), which can be a barrier to easy web sharing. This paper presents an efficient workflow for the 3D digitization of smaller physical objects and the subsequent process of generalizing the resulting triangular model to reduce the data volume. Finally, the model generalization is utilized when publishing the model in a web environment to make it available to the widest possible range of users. The whole procedure is applied to a physical model of a cottage from the village of Orlová (Karviná district, Czechia) from the collection of the Czech National Museum (scale reduction of a vernacular building at a scale of approximately 1:20).

KEYWORDS

3D modeling, Photogrammetry, Cultural heritage, Vectorization, Generalization, Web presentation, SketchUp

INTRODUCTION

With the gradual development of technology, the requirements for the creation of documents in digital 3D form arise. This applies both to the planned form of future objects and products (plans in construction or robotic production in industry) and to existing objects. One of the frequent applications of digital copies of existing objects is heritage conservation, that is, the management of historical buildings and smaller items [1], [2], [3]. For such objects, detailed spatial documentation is used for possible reconstruction or restoration [4]. However, it can also serve a promotional [5] and marketing purpose – it can make the work (and the institution) more visible or present objects that are not exhibited and not accessible to the public. Promotion using 3D models for marketing purposes is common, for example, in the retail sector. Examples of commercial use can be the offers of online stores[1] or even web models of shopping centers[2]. Finally, digital models are also used in

1 https://www.nike.com/cz/u/custom-nike-metcon-8-by-you-10001328/8164255504

2 https://thedubaimall.com/en/map

healthcare, education, industry, culture, and many other sectors. Thus, the presentation of objects using 3D models is commonly used among industries. The purpose of this paper is to build on the knowledge of 3D modelling of smaller objects for heritage purposes and further connect it with the experience of sharing 3D content for promotion purposes.

The main disadvantage of modelling 3D physical objects in the past was the complexity of the workflow, which until now required the work of specialists with expensive equipment. In some cases, it was possible to use other methods to help – for example, if good quality printed documentation in the form of drawings and other technical documents was available, a model could be created using these sources [6]. However, the rapid development of computer technology has brought about the possibility of generating spatial data from photographs and thus expanded the application of the field of photogrammetry.

Photogrammetry, specifically the Structure-from-Motion (SfM) method, allows the creation of 3D digital models of physical objects using a camera and powerful hardware [4]. A specialized program calculates the position of each point in space from images that capture the object from as many directions as possible (Figure 1). In recent years, sophisticated programs and rapidly evolving computing technology have made this method more accessible than ever [2]. Even for a large number of appropriately captured images, the image alignment process is reliable and often fully automatic. The method also benefits from decreasing cost of acquiring high-quality digital cameras. Due to these advantages, the technique is gaining in popularity, thus overtaking other methods such as terrestrial laser scanning or geodetic surveying. The product of the photogrammetric method is a highly detailed textured 3D triangular model (mesh) containing millions of points. The accuracy and detail of the model has one drawback, namely, the large volume of output data (hundreds of megabytes or more).

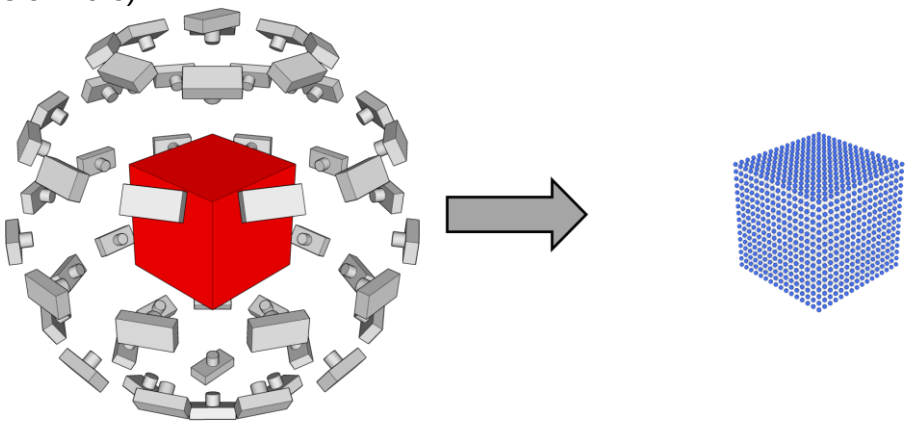

Fig. 1 – Structure-from-Motion method, optimal layout of imaging positions (from all directions to the object)

Today, the Internet is the primary medium for sharing digital content, where a high-quality user experience depends on fast loading and smooth operation. This depends on the speed of data transfer and the volume of data transferred [3]. Therefore, part of the project involved generalizing the detailed triangular model into a form that kept the resulting file size around 10 MB while not significantly reducing the quality of the geometry and textures. The data volume limit was empirically determined with respect to the normal data connection speed in our conditions. It can be assumed that this limit will increase rapidly.

The developed technological procedure was applied to the photogrammetric digitization of a physical model of a vernacular house (with dimensions of approximately 60×100×70 cm, Figure 2) and the subsequent modification of the model (generalization) so that the file complies with the size condition mentioned. All this is done with an emphasis on simplicity and automation of the workflow, which can then be easily applied when digitizing other models with similar parameters. The digitized model has a detachable roof, under which the interior with four rooms and furniture is hidden.

Fig. 2 – Model of a vernacular building from the village of Orlová, Karviná district, Czechia

RELATED WORK

Current research on photogrammetric documentation of historical objects is mostly devoted to building objects of real size (tens of meters). Separately, attention is paid to the digitization of smaller objects. However, the work on the model of a scaled-down building combines the specifics common to both of these fields. In addition, current research hardly focuses on the digitization of the interiors of such physical models, which, due to the high granularity and overall inaccessibility of the small space, represent a challenging environment for the method used.

Karachaliou et al. [1] used the UAV photogrammetry method to create a 3D representation of the "Averof's Museum of Neohellenic Art" building in Metsovo, Greece. In the next step, they converted the model to the HBIM (Historic Building Information Modelling) system to create an effective visualization with a high level of detail for efficient building management and at the same time a high-quality documentation for reconstruction purposes [1], [7]. They highlight the use of photogrammetry as an inexpensive means of producing accurate and detailed 3D documentation of physical objects. They also highlight the importance of HBIM in terms of the increasing frequency of research in this field in recent years.

Moreover, Jeong et al. [7] performed a 3D photogrammetric documentation of a building (traditional timber building), this time to evaluate the reliability of this method. They agree with the advantage of non-contact data acquisition, and their procedure goes on to discuss basic CAD vectorization using cut planes at regular intervals.

Poloprutský et al. [6] present a procedure for creating a 3D building model by combining multiple data types. In addition to the 3D photogrammetric data itself, they also present modelling possibilities using old building plans. This method is quite inexpensive, but it is redeemed by the amount of time spent searching the archives and subsequent manual modelling (adding the third dimension). In addition, the plans for old buildings are often different from reality due to various reconstructions [4]. The resource also stresses that this procedure should be used in cases where a historic building is partially or completely destroyed.

Photogrammetric imaging of 3D objects is often done manually (manual determination of camera position). However, a certain degree of automation can be used to save time and improve the quality of acquired data [3]. Tannús J. [2] proposed a low-cost semi-automated photogrammetric solution containing a camera, tripod, motorized turntable, softbox, and photographic background. This device captures smaller objects using a turntable and a static camera (with an angle of 11° between each frame) to produce image data with regular angular spacing. According to this research, switching from manual scanning to this new procedure saved 20% of the total time. In addition, part of the process (imaging) was performed automatically without the need for human supervision. Furthermore, Marshall et al. [3] designed and built a device for automated image data collection. With it, they tested the relationship between the degree of image overlap and the quality of the output or the duration of the process to find a compromise in the choice of these parameters (finding this compromise is a common dilemma in photogrammetry) [2]. They also took care of the

software design and implementation of safety features to prevent object-camera collisions. The commercial project CultArm3D [8] is very far along in this area of research. It uses a robotic arm for 3D digitization, providing a fixed attachment of the camera while allowing its arbitrary positioning in space.

The software used also plays an important role in 3D modelling, both in terms of the quality of the results, the speed of processing, and the user-friendliness of the interface. In his research, Kingsland K. [9] paid attention to comparing the capabilities of three main programs for 3D modelling from image data. The research shows that although Agisoft Metashape did not achieve the lowest processing time, it was evaluated as the most versatile, both in terms of alignment quality, noise filtering, variability of settings during processing, integration of a robust 3D editor, and finally a more favorable pricing policy. Basically, it can be said that the longer time required for (automatic) processing is compensated for the lower time spent on manual editing of the outputs. Also, Vacca G. [10] tested the data processing software of the Structure-from-Motion method, specifically open-source licensed programs. However, since these two groups of programs are compared separately, it is not possible to reliably compare the results between them.

The final stage of the work is the presentation of the outputs. To distribute the product to as many users as possible, it is best to publish it on the web. In this case, the user only needs basic equipment such as a PC and an internet connection to view the product. Other options to present 3D data include 3D printing [3], [11] (cannot be distributed over the Internet) or VR/AR [5] (requiring expensive hardware). Nishanbaev I. [12] linked existing web technologies to create a web archive for digital 3D models tailored to cultural heritage objects. In his research, he discusses, among others, the available web-based 3D frameworks and libraries (CesiumJS, Three.js, Babylon.js) or file formats suitable for sharing 3D data. Furthermore, Rahaman et al. [5] set out a workflow for non-expert users to create image-based 3D models (photo acquisition, 3D reconstruction), share online and visualize in VR/AR. They highlight specifically the focus on non-expert users (e.g., museums and hobby institutions), for whom digitization and content sharing can help both the preservation of cultural heritage objects and their promotion. For users without code-writing skills, using one of the commercial web repositories with 3D models (Sketchfab [13], 3D Warehouse [14], etc.) is also a good solution. Champion et al. [15] provide a clear comparison of these commercial services and their features, including controls, supported formats, and upload file size limits.

METHODS

The 3D modelling process used is based on the Structure-from-Motion method, which uses calculations to create a 3D model from 2D photographs. For proper functioning, high-quality images with sufficient overlap and clearly identifiable ground control points with precisely known positions (points determine the position and size of the model and characterize its accuracy) are a prerequisite. The calculations (alignment of the images and calculation of the detailed triangular model) were performed in Agisoft Metashape [1], [2], [16], evaluated as the ideal choice of one of the sources [9]. The following sections (Measurement and Computation sections) are devoted to this initial processing. The generalization of the detailed triangular model was performed manually in Trimble SketchUp [17] and is the subject of the third section, Modelling.

Measurement part

According to the research of Hruška et al. [18], who tested the identifiability of six targets (ground control points) of different size, coulor, reflectivity, and pattern, under different conditions, the best recognizable target is in the form of a black and white checkerboard array of 2×2 squares with the center at the intersection of four coloured segments. They also stated that the detectability of a target depends mainly on its size and reflectivity. Therefore, the recommended pattern was chosen and then printed on hard matte paper in a size of 50×50 mm, which sufficiently exceeds the requirement of six times the pixel size established by the source [18]. Numbers were added in the

corners to facilitate identification (Figure 3). Eight targets were mounted on a flat imaging board (Figure 4), and the relative position of each was calculated by planar adjustment from 28 distance measurements (all combinations of distances between points were measured with an empirically determined standard deviation of 0.5 mm). The standard deviation of the resulting coordinates did not exceed 0.2 mm (the least squares method in GNU Gama [19] software was used to calculate the adjusted coordinates).

Agisoft Metashape allows printing of special coding targets with automatic center position detection. This feature can save a lot of time during the process, but its reliability is not verified under various conditions. Therefore, two test targets with automatically detectable patterns were placed near the targets described above (Figure 3). These points were used only to test automatic detection, not as ground control points.

Fig. 3 – Manual detection target (left), automatic detection target

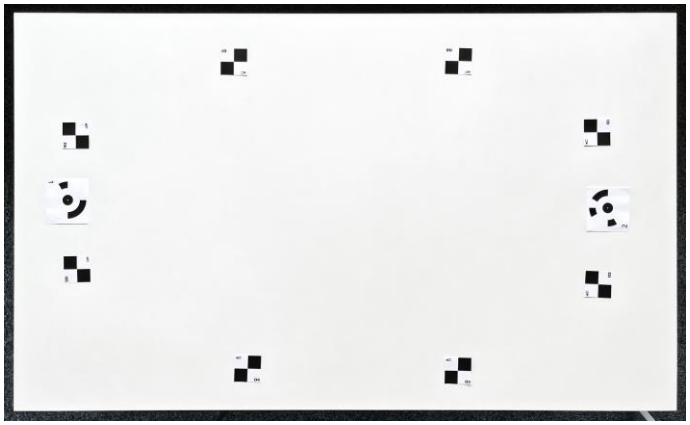

Fig. 4 – Distribution of ground control points on the imaging board (object placed in the center)

Images can be taken handheld, but this approach has many pitfalls (risk of blurring the image with longer exposure times, difficult lighting, etc.). It is therefore preferable to shoot using a tripod and to move the subject between shots by placing it on a turntable. The shooting scene was therefore arranged in this way, with the camera at such a distance from the subject that it was entirely in the frame (the lens used, with a focal length of 40 mm, corresponded to approximately 2 m distance). Illumination was provided by a pair of 50 W LED spotlights with a light color of 4000 K (neutral white) directed at the subject from the same direction as the camera (Figure 5). The subject was rotated at a constant 10° during the imaging, which ensured sufficient image overlap. Thus, rotating the object horizontally produced 36 images (for one elevation setup, see below). This layout of the imaging scene has the great advantage (in contrast to handheld imaging) of simplicity of workflow and therefore ease of reproducibility. Another advantage is the constant position of the lighting (elimination of shadows) or the choice of any exposure time without affecting the sharpness of the image. The disadvantage is the necessary manipulation with the subject, which is therefore exposed to a certain risk of damage. A comparison of the two scene schemes is given below (Figure 5).

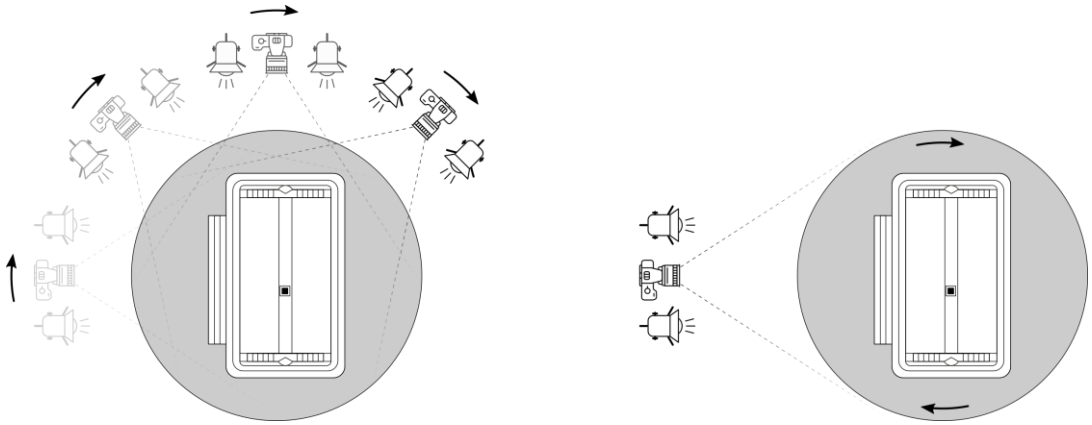

Fig. 5 – Plan view of the shooting scene – handheld (left) and tripod shooting

To precisely capture the object's structure in the vertical direction, the camera was placed in two additional height levels, each time performing one additional horizontal rotation. Finally, additional images were taken covering areas that were difficult to reach (the bottom of the object was not captured [3]). This was followed by imaging of the interior, a difficult environment for the photogrammetry method, with very limited visibility (the necessary view is often obstructed by walls and furniture) and many small details. Only one set of 36 images (horizontal rotation) was captured for each room and the missing vertical dimension was added by a single vertical distance measurement in each room. In total, 121 images for the exterior and 144 images for the interior of the building were taken and used to calculate a detailed triangular model.

Computation part

Today, a variety of programs can be used to process photogrammetric images. Agisoft Metashape is a popular software for image-based modelling. A good quality image set and an appropriate setting of computational parameters are essential for successful model processing. The procedure consists of several steps: initial alignment of the images (sparse cloud), then identification of the ground control points, calculation of the dense point cloud, and finally calculation of the triangular model (mesh) with texture. During the identification of the ground control points, automatic detection was performed for two test points. The results of this function were successful in only 47% of the cases. Examination of the unsuccessfully detected cases showed that failure occurs when the target is not visible in its entirety or is captured from a too sharp angle.

During the processing, it is advisable to clean the model from noise and other objects (base, surrounding environment). The result is a textured, highly detailed 3D model of the object. Individual sets of images (exterior and 4 rooms of the interior) were processed separately, and then the models were aligned in a unified coordinate system (cloud-to-cloud method) and merged. Some of the interior locations were not visually accessible (covered by furniture) and the image coverage at these locations was not sufficient to generate the model. At these locations, the calculation failed, and the triangular model does not contain geometry.

Although the triangular model in this form is sufficient as a good 3D documentation, it would be difficult to present it in a web environment due to its file size. Therefore, the next stage was to create a compact generalized model. Although the model loses detail, it is much more economical in terms of data volume.

Modelling part

Agisoft Metashape features a tool for uniform model generalization. In this process, it reduces the point density but does not consider the logical subdivision of the model. It does not preserve important edges and leaves flat parts too dense (Figure 6), which is not an optimal solution.

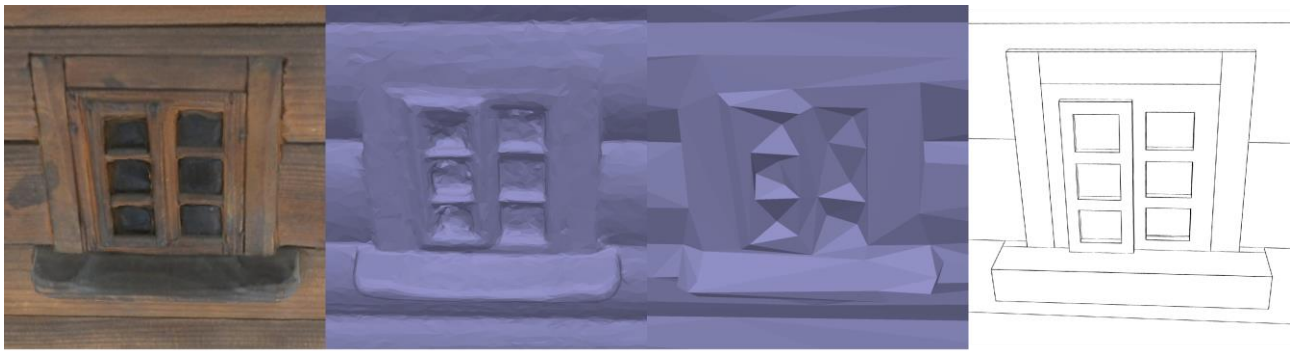

Fig. 6 – Types of geometry generalization

For these reasons, the Trimble SketchUp modelling program with the Scan Essentials plugin was used. Geometry was manually modelled directly into the point cloud. During the modelling process, generalization techniques were used to replace flat parts with planes (the reduction of the number of points was in this case in a ratio of up to 10^6:1), as well as alignment of surfaces along the axes (orthogonality), geometry simplification of some elements (elimination of detailed structures) or regularization of the dimensions of elements (e.g. constant stair spacing). A special approach was given to the thatched part of the roof, where the generalization techniques described above were ineffective due to the irregular structure. Therefore, this part was generalized by uniformly reducing the number of points of the original triangular model to a point spacing of 10 mm. Although all above-mentioned generalization techniques degraded the accuracy of the model in some areas, they contributed significantly to the overall clarity and topological correctness of the model. Due to the reduction in geometry, the resulting generalized model saved 663.9 MB (99.7%) compared to the original triangular model from Agisoft Metashape; the comparison of the parameters of the two models is shown below (Table 1). Data volumes refer to files in DAE text format.

Tab. 1 - Comparison of model data volumes (exterior + interior)

	No. of points	No. of faces	File size [MB]
Detailed triangular model	4 691 084	9 343 001	666,0
Generalized model	11 411	23 639	2,1

Fig. 7 – Orthogonal projections of textures onto the generalized model

Orthogonal projections from the four horizontal directions and from below were used to texture the generalized model (Figure 7). This method can be used if the model has an orthogonal shape (the main walls are perpendicular to each other). Since the triangular model is the basis for both the generalized model and the projected textures, the position of the modelled elements corresponds to the projected textures. These can therefore be applied to all geometry of the selected wall after initial alignment.

Visually inaccessible parts of the interior could not be covered with texture (Figure 8). However, given the purpose of the generalized model, it was not appropriate to leave these areas blank. Therefore, these parts were covered using graphics editor tools (Affinity Photo software was used). Copies of sections from other suitable parts of the image were used to replace larger areas. Smaller elements such as colour differences and other poorly rendered parts were smoothed out with the retouching functions. All interior textures (20 textures in total, 4 walls, and the floor in each room) were refined in this way, giving the model a better look for presentation purposes.

Fig. 8 – Corrections to the orthogonal projection of one of the walls, "before" (left) and "after"

Another weakness of textures was their size (data volume). To maintain the final size of the model specified, it was necessary to reduce it. Raster image files can be effectively compressed by using a suitable format, reducing resolution, reducing colour depth, or increasing compression (for some formats). The effect of changing each factor on the overall file size was tested (tested on the texture in Figure 8); the results are summarized in the table below (Table 2). As can be seen in Figure 9, reducing the resolution and increasing the compression rate have different impacts on the visual quality of the image file. Although the two compared texture sections were extracted from a file of similar size (approximately 600 kB), the sample located on the right shows significantly worse visual quality. Reducing the colour depth had a negligible impact on the file size. Therefore, to reduce the volume of texture data, the resolution was preserved and the JPG compression value was set to 30.

Tab. 2 - Dependence of texture file size on resolution and compression intensity (texture data from Figure 8, each file was modified from the original, IrfanView program used)

		Resolution [px]				
		5000×2949	4000×2359	3000×1770	2000×1180	1000×590
Quality (JPG)	100	5151 kB	3604 kB	2386 kB	1290 kB	377 kB
	85	2243 kB	1567 kB	1022 kB	539 kB	156 kB
	70	1516 kB	1075 kB	701 kB	360 kB	100 kB
	55	1157 kB	818 kB	532 kB	268 kB	73 kB
	40	927 kB	649 kB	420 kB	210 kB	56 kB
	25	658 kB	459 kB	293 kB	145 kB	39 kB

Fig. 9 – Texture detail for different compression parameters (detail of Figure 8)

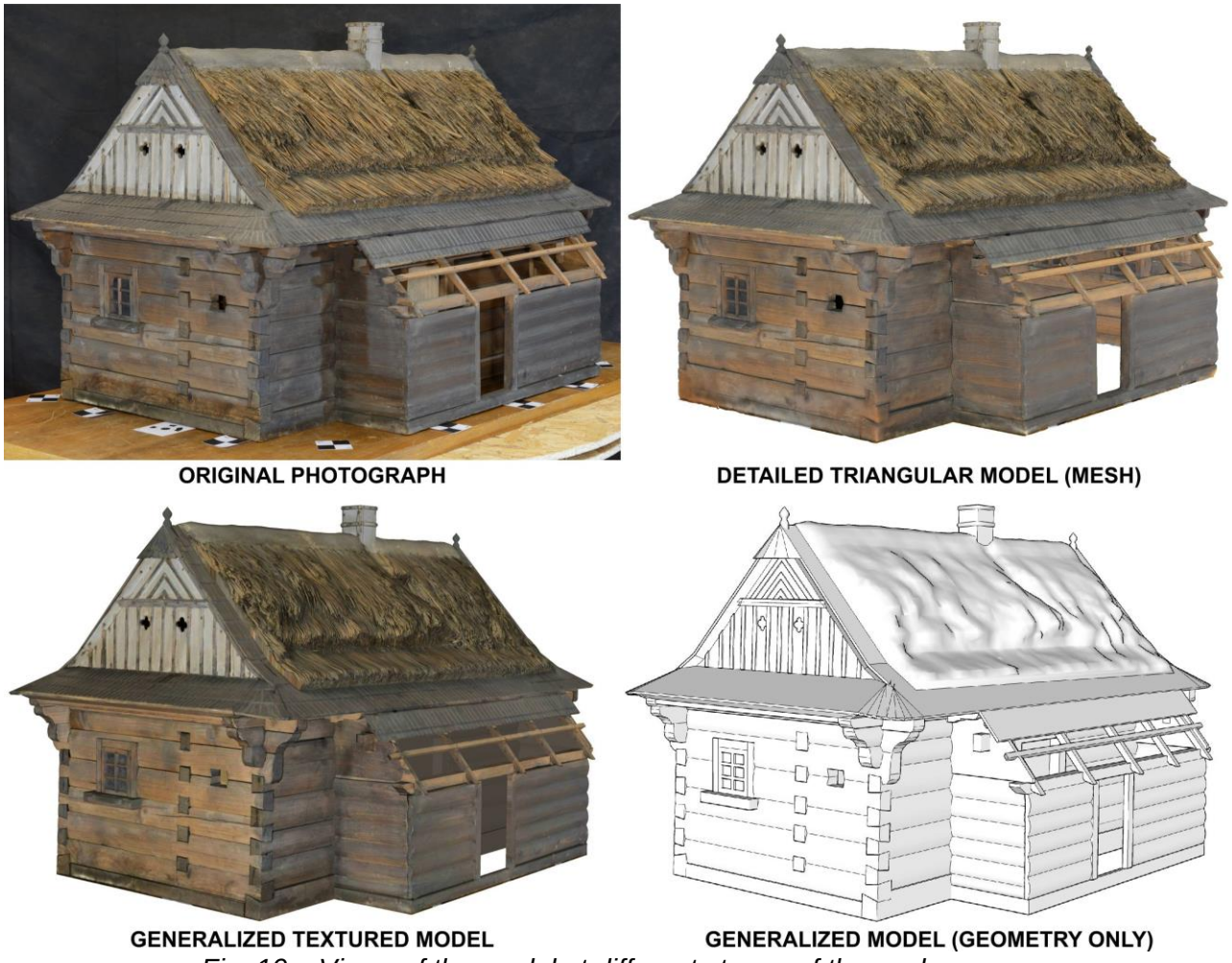

Fig. 10 – Views of the model at different stages of the work process

In total, 5 textures were created for the exterior and 20 for the interior. Each of them required editing with retouching tools due to incompleteness. In total, the image files for the model included 6.1 MB of data (JPG format). The total size of the textures in their original form (full resolution, low compression) was 193.5 MB, so 97% of the data was saved by graphical processing of the files. After adding the vector geometry of the model (DAE format), the total size of the generalized model was 11.4 MB. In this form, it meets the size and texture quality criteria (the quality can be visually compared in Figure 10).

The main objective of the described technological procedure was the presentation of the 3D model in a web environment. For this purpose, the JavaScript library Three.js [20] and its ColladaLoader function were used. This function loads 3D data in Collada format (DAE extension) into the web browser window [6]. Since the model contains an interior that is initially covered by the roof, it was necessary to add controls to the loaded page, allowing the model to be displayed both in its complete form and in its uncovered form (interior revealed by removing the roof). The resulting output is an HTML file executable in a web browser in the form of a web page containing a generalized textured 3D model. In the upper right corner, the page contains checkboxes with a label for each layer (part of the model), each of which can be clicked to change the visibility of the layer (Figure 11). The content of the web page takes approximately 3 seconds to load with a normal internet connection speed. There is no need to include user instructions, as the interface is simple and intuitive.

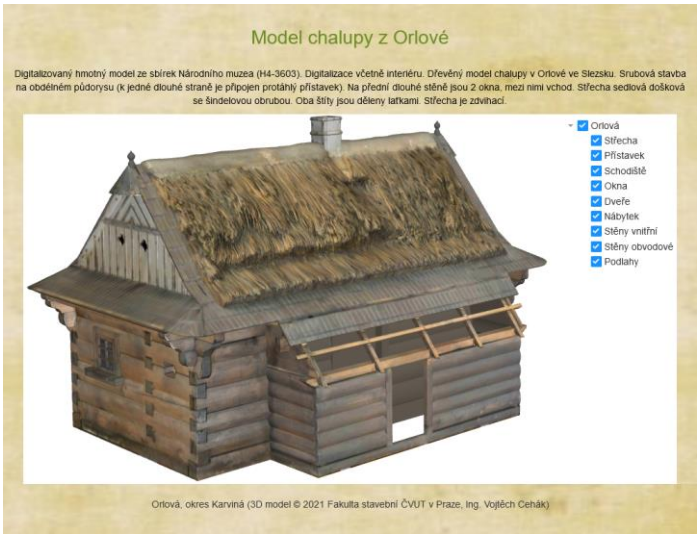

Fig. 11 – Presentation of the generalized model in a web environment

RESULTS AND CONCLUSION

The paper presents the methodology of the technical procedure for digitizing a physical model of approximately 1:20 scale of a building using photogrammetry (exterior and interior). Furthermore, the generalization of the resulting triangular model is carried out in both the form of geometry reduction and the reduction of the texture data volume. The use of photogrammetry ensures high accuracy and detail of the output, as well as the efficiency of the workflow.

The generalization process was performed by manual modelling using a detailed point cloud in Trimble SketchUp. The generalization saved 99% of the data volume compared to the original triangular model (the size of the resulting textured model was 11.4 MB). The resulting model could thus be published and presented as a lightweight web application based on the features of the Three.js library, including a user-friendly environment for switching layer visibility.

The developed procedure from digitization to presentation is applicable to physical models of buildings or other objects of similar dimensions. Thanks to the use of a turntable and a static camera position, it can be performed even by a person with no knowledge of photogrammetry. In future work,

it is planned to further improve the procedure technologically – for example, by testing a light diffusion device (softening the shadows in the image) or using a green screen to mask the background to speed up the calculation [2]. It is also worth exploring technological improvements to the generalization process. The latter involves difficult decisions about which elements to keep and which to omit, depending on the structure and subdivision of the digitized object. It requires an individual approach and is, therefore, time-consuming and difficult to automate.

ACKNOWLEDGEMENTS

This work was supported by the Ministry of Culture of the Czech Republic from the Program for the Support of Applied Research and Development of National and Cultural Identity for the Years 2016-2022 (NAKI II), grant project "VISKALIA – Virtual Open-air Museum of the Vernacular Architecture", No. DG20P02OVV003.

REFERENCE

[1] KARACHALIOU, E., GEORGIOU, E., PSALTIS, D. and STYLIANIDIS, E. UAV for Mapping Historic Buildings: From 3D Modelling to BIM. The International Archives of the Photogrammetry, Remote Sensing and Spatial Information Sciences. Online. 31 January 2019. Vol. XLII-2/W9, p. 397–402. DOI 10.5194/isprs-archives-XLII-2-W9-397-2019.

[2] TANNUS, Julia. Optimizing and Automating Computerized Photogrammetry for 360° 3D Reconstruction. In : 2020 22nd Symposium on Virtual and Augmented Reality (SVR). Online. Porto de Galinhas, Brazil : IEEE, November 2020. p. 267–271. ISBN 9781728192314. DOI 10.1109/SVR51698.2020.00048.

[3] MARSHALL, M. E., JOHNSON, A. A., SUMMERSKILL, S. J., BAIRD, Q. and ESTEBAN, E. Automating Photogrammetry for the 3D Digitisation of Small Artefact Collections. The International Archives of the Photogrammetry, Remote Sensing and Spatial Information Sciences. Online. 23 August 2019. Vol. XLII-2/W15, p. 751–757. DOI 10.5194/isprs-archives-XLII-2-W15-751-2019.

[4] PAVLOVSKIS, Miroslavas, MIGILINSKAS, Darius, KUTUT, Vladislavas and ANTUCHEVICIENE, Jurgita. Initial data preparation for 3D modelling of heritage building. In : Online. Vilnius Gediminas Technical University, 3 December 2019. DOI 10.3846/mbmst.2019.049.

[5] RAHAMAN, Hafizur, CHAMPION, Erik and BEKELE, Mafkereseb. From photo to 3D to mixed reality: A complete workflow for cultural heritage visualisation and experience. Digital Applications in Archaeology and Cultural Heritage. Online. June 2019. Vol. 13, p. e00102. DOI 10.1016/j.daach.2019.e00102.

[6] POLOPRUTSKÝ, Zdeněk, FROMMELTOVÁ, Eva, MÜNZBERGER, Josef and SEDLICKÁ, Kateřina. 3D Digital Reconstruction of Defunct Rural Buildings Based on Archival Sources. Stavební obzor - Civil Engineering Journal. Online. 30 April 2022. Vol. 31, no. 1, p. 196–210. DOI 10.14311/CEJ.2022.01.0015.

[7] JEONG, Gi Young, NGUYEN, Tan No, TRAN, Dang Khai and HOANG, Thi Bich Huyen. Applying unmanned aerial vehicle photogrammetry for measuring dimension of structural elements in traditional timber building. Measurement. Online. March 2020. Vol. 153, p. 107386. DOI 10.1016/j.measurement.2019.107386.

[8] CULTLAB3D. Digitization made easy. CultArm3D. Online. 2022. Available from: https://www.cultarm3d.de/

[9] KINGSLAND, Kaitlyn. Comparative analysis of digital photogrammetry software for cultural heritage. Digital Applications in Archaeology and Cultural Heritage. Online. September 2020. Vol. 18, p. e00157. DOI 10.1016/j.daach.2020.e00157.

[10] VACCA, G. Overview of Open Source Software for Close Range Photogrammetry. The International Archives of the Photogrammetry, Remote Sensing and Spatial Information Sciences. Online. 23 August 2019. Vol. XLII-4/W14, p. 239–245. DOI 10.5194/isprs-archives-XLII-4-W14-239-2019.

[11] BALLETTI, Caterina, BALLARIN, Martina and GUERRA, Francesco. 3D printing: State of the art and future perspectives. Journal of Cultural Heritage. Online. July 2017. Vol. 26, p. 172–182. DOI 10.1016/j.culher.2017.02.010.

[12] NISHANBAEV, Ikrom. A web repository for geo-located 3D digital cultural heritage models. Digital Applications in Archaeology and Cultural Heritage. Online. March 2020. Vol. 16, p. e00139. DOI 10.1016/j.daach.2020.e00139.
[13] SKETCHFAB. Sketchfab. Online. 2022. Available from: https://sketchfab.com/
[14] TRIMBLE INC. 3D Warehouse. Online. 2022. Available from: https://3dwarehouse.sketchup.com/
[15] CHAMPION, Erik and RAHAMAN, Hafizur. Survey of 3D digital heritage repositories and platforms. Virtual Archaeology Review. Online. 8 July 2020. Vol. 11, no. 23, p. 1. DOI 10.4995/var.2020.13226.
[16] AGISOFT. Agisoft Metashape. Discover intelligent photogrammetry with Metashape. Online. 2022. Available from: https://www.agisoft.com
[17] TRIMBLE INC. SketchUp. 3D Design Software, 3D Modeling on the Web. Online. 2022. Available from: https://www.sketchup.com/
[18] HRUSKA, Jonas, PADUA, Luis, ADAO, Telmo, PERES, Emanuel, MARTINHO, Jose and SOUSA, Joaquim J. Target Influence on Ground Control Points (GCPs) Identification in Aerial Images. In : IGARSS 2020 - 2020 IEEE International Geoscience and Remote Sensing Symposium. Online. Waikoloa, HI, USA : IEEE, 26 September 2020. p. 6487–6490. ISBN 9781728163741. DOI 10.1109/IGARSS39084.2020.9324222.
[19] GNU Operating System. GNU Gama. Online. 2022. Available from: https://www.gnu.org/software/gama/
[20] Three.js – JavaScript 3D Library. Online. 2022. Available from: https://threejs.org/

CIVIL ENGINEERING JOURNAL

Article no. 46

THE CIVIL ENGINEERING JOURNAL 4-2022

RESEARCH ON TRANSPORTATION SAFETY OF PREFABRICATED BUILDING COMPONENTS BASED ON SPA-ABC

Meng Li and Zheng Guo

School of Management, Wuhan University of Science and Technology, Wuhan, Hubei, China, limengwd@126.com, 2621185695@qq.com

ABSTRACT

Aiming at the safety problem of the transportation of prefabricated components in prefabricated buildings, set pair analysis (SPA) and Pareto analysis (ABC) are used to propose a transportation safety evaluation model for prefabricated components in prefabricated buildings based on SPA-ABC. Based on the existing research results, the risk factors in the three stages of transportation preparation, transportation work and storage work are sorted out, and the evaluation index system of transportation safety is established. Combining the status quo of transportation operations, SPA is used to determine the index weights. Based on the ABC theory, risk factors are divided into major risk factors (type A), secondary risk factors (type B) and general risk factors (type C), and recommendations are made based on the major risk factors. The results show that ten risk indicators such as transportation operators, transportation plans, and fixing measures for prefabricated components are type A risk factors, which are the focus of prefabricated construction transportation operations.

KEYWORDS

Prefabricated building, Transportation of prefabricated components, Safety evaluation system, Set pair analysis method (SPA), Pareto analysis method (ABC)

INTRODUCTION

Since the goal of “striving to make the proportion of prefabricated buildings exceed 30% in 10 years” was put forward in 2016 [1], clear arrangements for prefabricated construction work have been made across the country. This year has entered the "second half" of achieving this goal. China's support for prefabricated buildings has also been further increased. Yunnan, Sichuan, Anhui and other places have introduced a series of related policies and implementation measures to support the construction of prefabricated buildings [2]. At the same time, the requirements for all aspects of prefabricated buildings are getting higher and higher. In terms of engineering safety, although prefabricated buildings are safer than traditional cast-in-place buildings, safety accidents still occur from time to time, so prefabricated buildings have their own unique risks [3]. Prefabricated buildings have increased a large number of hoisting operations and transportation operations. The safety of hoisting operations "occupies a major position" in frequent accidents, and has always been an important object of people's attention. In contrast, transportation safety issues are often overlooked by people. However, the safety and efficiency of the transportation link is also an issue that cannot be ignored for the development of prefabricated building safety. Once there is a problem in this link, it will have a significant impact on the construction safety, quality and schedule of the entire project [4].

In recent years, scholars at home and abroad have also made a lot of in-depth explorations on the safety of prefabricated buildings. These studies mainly focus on two aspects, one is the safety study of the whole process of prefabricated buildings, and the other is the detailed study of safety during the hoisting phase of prefabricated buildings. In contrast, there are very few studies on the transportation safety of prefabricated building components. Wang et al. [5] used the importance-performance analysis method to study the risk factors affecting the development of prefabricated buildings in China. Factors such as unreasonable transportation conditions, insufficient coordination during transportation, and transportation tools were taken into consideration. Jin et al. [6] used Netica software to compile Bayesian network models and sensitivity analysis methods to analyze each type of risk factor to compare the degree of influence of these risk factors on the safety of prefabricated buildings. The results pointed out that the risk level of the transportation stage belonged to level 3, where the lack of fixing measures during the transportation of prefabricated components was the most influential risk factor. Duan et al. [7] used the structural equation model to study the main factors of the safety of prefabricated buildings. They believed that the on-site transportation, unloading and stacking of prefabricated structures were key issues affecting construction safety, but off-site transportation was not considered. Li et al. [8] simultaneously adopted the structural equation model and confirmatory factor analysis theory, and believed that the risks in the transportation and storage stages were greater than those in the production and installation stages, and the biggest safety problem in transportation stage was transportation vehicles. Liu et al. [9] used the analytic hierarchy process to analyze the factors affecting the quality of prefabricated buildings from four aspects: design, production, transportation and installation, and concluded that many unnecessary problems could be avoided by strictly implementing national operational standards in the transportation stage. Chang and Chang [10] analyzed the problems existing in the transportation stage of prefabricated components and put forward reasonable suggestions. Wang and You [11] studied the hoisting safety of prefabricated buildings based on the C-OWA operator, and combined the Pareto classification method to classify the factors in the transportation and hoisting stages of prefabricated components. The results showed that the disturbance of the lifting point and the contamination of the pre-buried materials at the lifting point caused by the transportation stage belonged to category C risk. When Wang and Yan [12] studied the construction safety of prefabricated buildings, they also considered the damage caused by transportation. In summary, domestic and foreign scholars have conducted relatively detailed studies on the main influencing factors, risk identification, and safety warnings of prefabricated building safety issues, which has greatly promoted the development of the prefabricated building industry in China. Most of the above studies take the transportation phase into consideration, which illustrates the importance of safety issues during the transportation phase. However, a complete transportation operation safety management system has not yet been formed, and specific risk factors are simply mentioned or ignored.

The paper intends to start from the safety problems existing in the transportation of prefabricated buildings and construct a system of risk factors in the transportation stage. The set pair analysis method (SPA) is used to determine the weight of each indicator, and the Pareto analysis method (ABC) is used to determine the risk factor category. Finally, the authors take a project in Wuhan as an example to prove the feasibility and practicability of this method, and proposed targeted measures for Type A risk factors. The specific process is shown in Figure 1. It is expected to provide reference suggestions for the safety management of prefabricated buildings, especially the safety management of transportation operations.

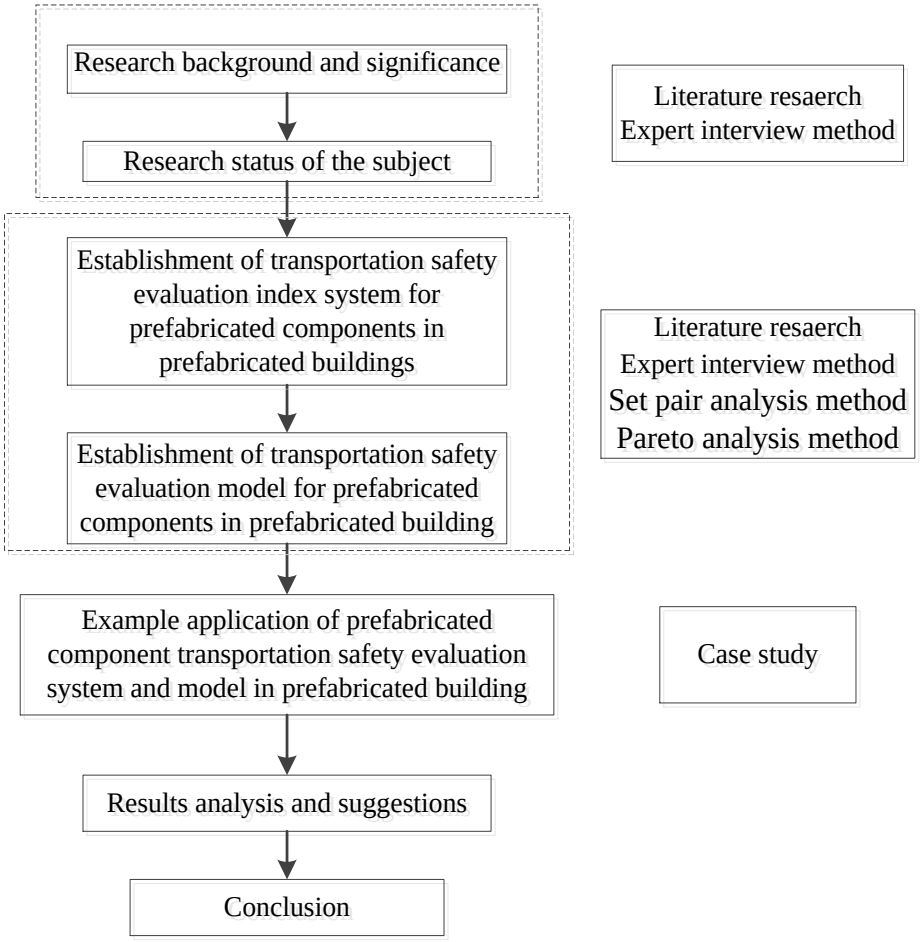

Fig.1 - Transportation safety evaluation process of prefabricated components in prefabricated buildings

TRANSPORTATION SAFETY MODEL OF PREFABRICATED BUILDING COMPONENTS BASED ON SPA-ABC THEORY

Determination of indicator weight

The SPA proposed by Zhao Keqin is a mathematical method that comprehensively considers and studies the certainty and uncertainty of the system [13]. It combines set theory with dialectics of nature. The basic idea is: when studying a problem, use the degree of connection to express the certainty and uncertainty of a research object, and consider the two and their transformation as a system for comprehensive research [14]. Compared with the analytic hierarchy process, the use of set pair analysis to determine the index weight is easier to distinguish and comprehensively evaluate [15].

Its connection degree expression is as follows:

$$\begin{cases} \mu = a + bi + cj, (i \in [-1,1],\ j = -1) \\ a + b + c = 1 \end{cases} \quad (1)$$

Where a, b, and c represent the degree of identity, degree of difference, and degree of opposition, respectively; i and j represent the coefficient of uncertainty and the degree of opposition, respectively. By affecting the value of c, j affects the size of a; the values of i and j are also affected

by a, b, and c [16]. In short, these few parameters are a whole. They influence and restrict each other to form a complex system.

This model transforms the uncertainty of related issues into specific mathematical theories. At the same time consider the certainty and uncertainty of the system. This makes the determined index weights more objective and authentic. The following will list the specific steps of applying the set pair analysis method to determine the index weight: This section should describe in detail the study material, procedures and methods used.

(1) The construction of the judgment matrix

Suppose there are r related professionals, and the evaluation index set is:

$$X = \{X_K\}, k = (1,2,3\cdots n) \tag{2}$$

Then, using the 9-scale method, professionals are invited to compare each indicator pair by pair and evaluate its importance. So as to get the elements of the judgment matrix and construct the corresponding judgment matrix $M_{kl}^{(r)}$..

$$M_{kl}^{(r)} = \begin{pmatrix} x_{11} & x_{12} & \cdots & x_{1n} \\ x_{21} & x_{22} & \cdots & x_{2n} \\ \vdots & \vdots & \ddots & \vdots \\ x_{n1} & x_{n2} & \cdots & x_{nn} \end{pmatrix} \tag{3}$$

Where r represents the judgment matrix obtained by the rth expert. And exist $x_{ij} = 1/x_{ji}$.

(2) Determination of connection degree model

When evaluating various indicators, there is no situation in which different experts have diametrically opposite evaluation opinions on two indicators. That is, there is no expert who thinks x_1 is extremely important than x_2, while another expert thinks that x_2 is extremely important than x_1. Generally speaking, the situation of similar opinions but differences is more in line with the actual situation. Therefore, it is considered that j=0, and the same-different model is adopted: μ=a+bi.

The connection degree model determined by the matrix form of the above-mentioned similarity and difference model:

$$\mu_{ij} = A_{ij} + iB_{ij}$$

$$= \begin{pmatrix} a_{11} & a_{12} & \cdots & a_{1n} \\ a_{21} & a_{22} & \cdots & a_{2n} \\ \vdots & \vdots & \ddots & \vdots \\ a_{n1} & a_{n2} & \cdots & a_{nn} \end{pmatrix} + i \begin{pmatrix} b_{11} & b_{12} & \cdots & b_{1n} \\ b_{21} & b_{22} & \cdots & b_{2n} \\ \vdots & \vdots & \ddots & \vdots \\ b_{n1} & b_{n2} & \cdots & b_{nn} \end{pmatrix} \tag{4}$$

$$a_{ij} = \begin{cases} \min\{x_{ij}^{(r)}\}, x_{ij}^{(r)} \geq 1 \\ \max\{x_{ij}^{(r)}\}, x_{ij}^{(r)} \leq 1 \end{cases} \tag{5}$$

$$b_{ij} = f(x) = \begin{cases} \left|\max\{x_{ij}^{(r)}\} - \min\{x_{ij}^{(r)}\}\right|, x_{ij}^{(r)} \geq 1 \\ -\left|\max\{x_{ij}^{(r)}\} - \min\{x_{ij}^{(r)}\}\right|, x_{ij}^{(r)} \leq 1 \end{cases} \tag{6}$$

$$(r = 1,2,3\cdots n; i = 1,2,3\cdots n; j = 1,2,3\cdots n)$$

In formula (4), A_{ij} represents the identity matrix; B_{ij} represents the difference matrix.

In formula (5): exists $x_{ij} = 1/x_{ji}$, therefore, $\max\left\{x_{ij}^{(r)}\right\} = 1/\min\left\{x_{ij}^{(r)}\right\}$, and $a_{ij} = 1/a_{ji}$

(3) Consistency treatment of identity matrix

Compared with the analytic hierarchy process, using the compatibility matrix method for consistency processing can simplify the calculation process. It does not require a consistency check to obtain a matrix that meets the consistency requirements. Compatibility matrix $D = \left(d_{ij}\right)_{n\times n}$.

$$d_{ij} = \sqrt[n]{\Pi_{m=1}^{n} a_{im} \times a_{mj}} \quad (7)$$

Where $d_{ij} = 1/d_{ji}, d_{ij} = d_{im} \times d_{mj}, d_{ii} = 1$

(4) Calculation of index weight

$$\omega_i = c_i \Big/ \left(\sum_{p=1}^{n} c_p\right) \quad (8)$$

$$c_p = \sqrt[n]{\Pi_{j=1}^{n} d_{ij}} \quad (9)$$

ABC method risk classification

ABC classification method (Pareto analysis method), or primary and secondary factor analysis method. As the name suggests, it focuses on distinguishing the primary and secondary, seizing the key influencing factors among many factors, and implementing corresponding measures [17]. According to the Pareto principle, this method holds that most of the harvest comes from the few efforts, and most of the output comes from the few inputs. Similarly, the majority of risks come from the minority of reasons, as long as the cumulative majority of risks are found, the main cause of the minority can be obtained [18]. The advantage of the ABC classification is that it simplifies our workflow and reduces our workload [19]. Because we can identify the major risk factors, we can focus on those risk factors instead of focusing on all the risk factors all the time. Therefore, the analysis objects are divided into three types: A, B, and C. Corresponding to major risk factors, secondary risk factors, and general risk factors. Among them, the cumulative weight value of A risk is less than 60%, the B risk is between 60% and 90%, and the C risk is between 90% and 100%.

CONSTRUCTION OF RISK FACTOR SYSTEM FOR PREFABRICATED BUILDING COMPONENT TRANSPORTATION OPERATIONS

Prefabricated building is a type of building in which some of its prefabricated components are manufactured in a designated plant according to the demand plan, transported to the construction site by special transportation vehicles, and assembled on site using some connection technology. At present, the prefabricated building components generally prefabricated in the factory include prefabricated beams, walls and floor slabs and other main components; prefabricated stairs, bay windows or kitchens and toilets and other special-shaped components. Most of these main building components are cast-in-place in traditional buildings, but are prefabricated in prefabricated buildings. Therefore, a lot of transportation work is inevitably required. Coupled with the characteristics of large weight, large volume, and irregular shape of the prefabricate components, this has caused difficulties in transportation operations. This article is based on the characteristics of prefabricated building transportation operations and existing research results, combined with the traditional five aspects of building safety influencing factors "people, materials, machines, management and environment". Analyze the risk factors of transportation operation of prefabricated construction from three stages of transportation preparation, transportation operation and storage work.

Transportation preparation

Transportation preparation is very important for subsequent transportation operations, and whether it is fully prepared directly affects the entire transportation process. The main risks at this

stage are: (1) Inadequate training for transport operators, lack of safety awareness, and negligence of labor protection measures; (2) Insufficient capabilities of transport management personnel, poor organization and coordination capabilities, lack of sufficient management knowledge and Corresponding professional knowledge; (3) Lack of emergency plans or incomplete emergency plans, and no field drills on the plans formulated, and unskilled; (4) Inadequate attention to transportation operations, resulting in rough and incomplete transportation plans.

Transport operations

(a) Integral transport frame

(b) A type transport frame

Fig.2 - Type of transport frame

(a) Fixing measures and pads

(b) No fixing measures

Fig.3 - Suitable and unsuitable fixing measures

Various details in transportation have always been the focus of attention. The key to whether the transportation work is completed smoothly and safely lies in whether these details can be done. The main risk factors at this stage are: (1) Failure to select suitable transport vehicles according to the specifications, shapes, weights, etc. of the prefabricated components; (2) The selection of loading and unloading equipment is inappropriate or cannot meet the requirements for carrying capacity; (3) The transport frame designed or manufactured cannot meet the stress requirements of the corresponding components; Under normal circumstances, the transport frame used to transport the components is shown in Figure 2. (4) The prefabricated component fixing measures are not considered adequately, and measures such as protection and shock absorption are not adopted; This is shown in Figure 3. (5) In order to reduce transportation costs, blindly pursue short transportation routes, resulting in unreasonable route planning. Or not survey the route on the spot to verify whether the special location of the road can meet the transportation requirements. For example, the radius of gyration of the road and the bearing capacity of the bridge; (6) The crack resistance of the most unfavorable section of the component has not been checked to understand the force form of the unfavorable section of the precast component; (7) The construction site is uneven; (8) In terms of social environment, if the transportation route passes through urban arterial roads and other busy roads, it is easy to cause traffic congestion, which will cause huge safety hazards to urban traffic and people; (9) Weather conditions during transportation will affect transportation work, such as strong winds, heavy rain, heavy snow, etc.

Storage work

Since the storage work is directly related to the loading and unloading work in the transportation phase, it is also taken into consideration. If the storage work is perfunctory, one is to cause damage to the components, which will affect the safety of the follow-up work. Second, the components tilt or collapse when they are stacked, which will inevitably cause safety hazards to nearby workers. The main influencing factors at this stage are (1) The stacking location is not specified or the stacking location is not planned in the appropriate order, resulting in the secondary handling of the components. Furthermore, the stacking site is uneven and the drainage measures are not adequate; (2) Failure to adopt appropriate stacking methods according to the shape and force form of the components, causing damage to the components; (3) Insufficient protection measures when stacking components . Figure 4 shows an example of the above three factors

(a) Storage space clutter

(b) Prefabricated stairs placed vertically without fixed measures

(c) Unsuitable pad position

Fig.4 - Misbehavior in the storage work

Tab. 1 - Risk factors for transportation operations in prefabricated building

Target layer	Criterion layer	Index layer
Safety Evaluation of Prefabricated Building Transportation	Transportation preparation A_1	transportation operators A_{11}
		transportation management personnel A_{12}
		emergency plans A_{13}
		transportation plans A_{14}
	Transportation operation A_2	transportation vehicles A_{21}
		loading and unloading equipment A_{22}
		transportation racks A_{23}
		prefabricated component fixing measures A_{24}
		transportation routes A_{25}
		checking component strength, construction site A_{26}
		construction site A_{27}
		social environment A_{28}
		natural environment A_{29}
	Storage work A_3	stacking location A_{31}
		stacking method A_{32}
		stacking component protection measures A_{33}

From the above analysis, we can know the risk factors of each stage of the transportation operation of prefabricated components. Transportation preparation stage: transportation operators, transportation management personnel, emergency plans, transportation plans. Transportation operation stage: transportation vehicles, loading and unloading equipment, transportation racks, prefabricated component fixing measures, transportation routes, checking component strength, construction site, social environment, and natural environment. Storage work stage: stacking location, stacking method, stacking component protection measures. Based on this, the risk factor system of transportation operations is presented in Table 1.

Tab 2 - Indicator weight

Criterion layer	Indicator	Index layer	Indicator	Relative weight	Comprehensive weight
Transportation preparation A1	0.4089	A11	0.4570	0.1523	0.0623
		A12	0.1611	0.0537	0.0220
		A13	0.0995	0.0332	0.0148
		A14	0.2824	0.0941	0.0420
Transportation operation A2	0.4464	A21	0.1164	0.0388	0.0173
		A22	0.0948	0.0316	0.0141
		A23	0.1211	0.0404	0.0180
		A24	0.1584	0.0528	0.0236
		A25	0.1387	0.0462	0.0206
		A26	0.1305	0.0435	0.0194
		A27	0.0710	0.0237	0.0106
		A28	0.0798	0.0266	0.0119
		A29	0.0893	0.0298	0.0133
Storage work A3	0.1447	A31	0.2453	0.0818	0.0118
		A32	0.4093	0.1364	0.0197
		A33	0.3454	0.1151	0.0167

CASE ANALYSIS OF TRANSPORTATION SAFETY MODEL OF PREFABRICATED BUILDING BASED ON SPA-ABC THEORY

The following will analyze the transportation safety model of prefabricated buildings based on the SPA-ABC theory, taking the transportation of prefabricated building components of an affordable housing project in Wuhan as an example. The beams, slabs, roof trusses, stairs and other components of the project are all prefabricated. The 16 risk indicators (Table 1) in the three stages of transportation preparation, transportation and storage of this project are selected to construct the evaluation index system of this project.

Determine the index weight

Based on the SPA method, 3 experts and scholars and 2 relevant managers are invited to compare each index in Table 1 with each other to obtain a judgment matrix. Because in the process of evaluating the importance of indicators, it is easy to be affected by subjective factors. So this research will adopt an anonymous method and make full use of the professional knowledge and work experience of experts. Let experts make independent judgments and minimize the influence of unnecessary factors. According to the above-mentioned SPA method to determine the weight, the weight value of each indicator of the project and the weight value of these three stages (A_1, A_2, A_3) can be obtained as shown in Table 2. Among them, since the evaluation results of experts are not much different, *i* can be taken as 0.5[20].

Risk factor classification

According to the weights determined above, normalize the weights and calculate the cumulative weights. Based on the ABC analysis method, the risk factors are classified. The risk indicators of Type A, Type B and Type C are respectively determined as shown in Table 3 and Figure 5.

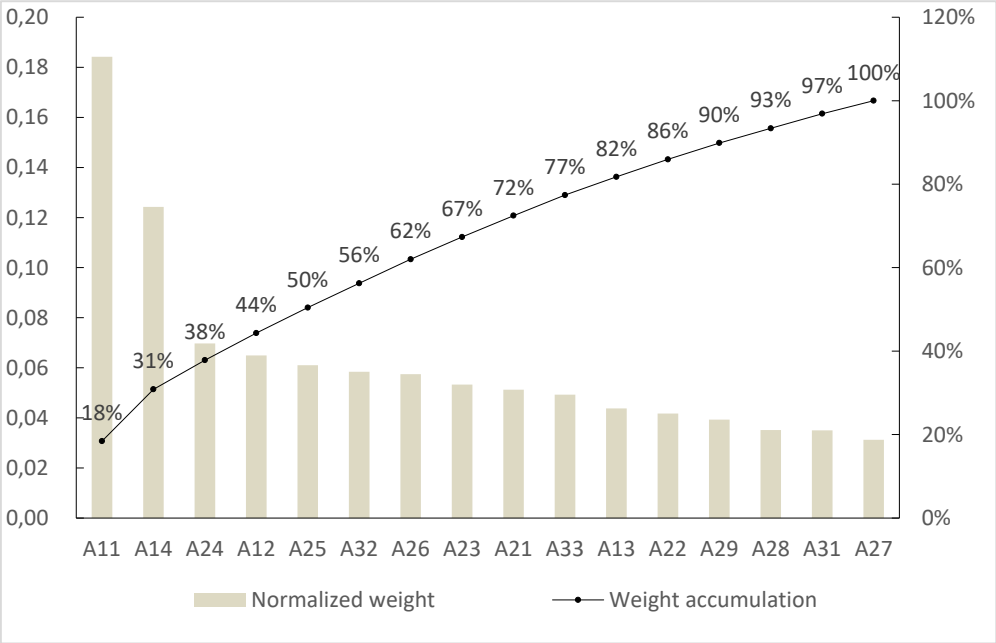

Fig.5 - Pareto chart

According to the above data, there are six indicators for Type A risk factors: transportation operators A_{11}, transportation plans A_{14}, fixing prefabricated components A_{24}, transportation management personnel A_{12}, transportation routes A_{25}, and stacking methods of components A_{32}. These indicators are the "critical few" of the factors that affect the transportation safety of prefabricated components of prefabricated buildings. In future work, these risk factors should be regarded as the main objects of concern. And corresponding measures should be taken to prevent them. There are seven type B indicators and three type C indicators, which are the "general majority" of the factors affecting the safety of transportation operations. Although the importance of these factors is after Type A risk factors, they cannot be ignored.

ANALYSIS AND RECOMMENDATIONS

In the above case analysis, six main risk factors are derived. Among them, the transportation plan, transportation operators and transportation management personnel belong to the transportation preparation stage; the prefabricated component fixing measures and transportation routes belong to the transportation operation stage; the stacking method of the components belongs to the storage stage. The following will focus on the six factors in these three stages and put forward corresponding suggestions.

(1) Transportation preparation stage

When designing a transportation plan, the transporter needs to comprehensively analyze the types, quantities, and arrival time of the required components according to the needs of the construction party to ensure the smooth and safe completion of the transportation tasks.

For transportation operators, the most important thing is to cultivate their safety awareness. Therefore, strengthening training assessment and supervision is essential. During the training, some typical accident cases should be displayed frequently or experts should be invited to explain on the spot. During the assessment, the actual operation assessment should be combined with the theoretical assessment. Considering the cultural level of the general operating staff, the method of face-to-face inquiry can be adopted. Labor insurance products must be distributed to operators in a timely manner, and they must also be supervised whether they are used correctly at work.

In terms of management personnel, problems in safety management in construction projects have always been the main cause of human and material safety accidents. Therefore, managers should also regularly conduct regular and irregular training, learn management knowledge and corresponding transportation expertise, cultivate their organization and coordination capabilities, and enhance their sense of responsibility.

(2) Transportation operation stage

When the transportation components are fixed by lashing to prevent the components from moving, the contact points should be provided with protective measures such as pads. At the same time, in order to reduce the damage of components due to road bumps during transportation, some shock absorption measures can be taken. For example, a shock-absorbing shelving frame is set, a hydraulic method is used on the transport vehicle, or an air spring is set on the bottom of the transport vehicle. Before leaving the factory, these fixing measures should be further checked.

The transportation route should be planned with full consideration of the size and weight of the transportation vehicle. After selecting an optimal route, site surveys should be conducted on the route, especially bridges, culverts, etc. At the same time, plan an alternative route to prevent emergencies.

(3) Storage work stage

Different types of components adopt different storage methods. Transverse members can be stacked on hardened ground or steel frame. However, spacers should be arranged between the components, especially flexible gaskets should be inserted at the rigid resting point to prevent rigid contact between the components. And the number of layers should not exceed 6 layers. Vertical components can be used with special stacking racks to ensure stable storage and avoid "slip and fall" accidents. Prefabricated stairs, balconies and other components can be laid flat.

CONCLUSION

Compared with traditional buildings, prefabricated buildings have significant advantages in terms of safety. In recent years, the construction industry at home and abroad has developed rapidly. Although there has been a lot of research on its safety, there is a lack of research on the safety of transportation operations. Based on the SPA-ABC theory, this paper establishes a transportation

safety model for prefabricated components of prefabricated buildings, and verifies the feasibility of this model through practical application.

(1) This model develops a prefabricated component transportation operation safety evaluation system based on the characteristics of prefabricated building transportation operations and existing research results.

(2) This article introduces the set pair analysis method, combined with the compatibility matrix method to determine the connection degree model of the relevant problem index weight. Comprehensive consideration of the identity and difference, certainty and uncertainty of experts' knowledge, so as to further reduce the influence of experts' subjective arbitrariness.

(3) Classify each risk factor through ABC analysis method. According to the results of the Pareto chart, it can be seen that the main risk factors (type A) of the "critical minority" include six factors such as transportation operators, transportation plans, and prefabricated component fixing measures. In addition, corresponding measures are implemented for the main risk factors. In this way, companies can use limited resources to obtain the greatest return on the safety management of transportation operations. The method is simple but not lacking in practicability.

ACKNOWLEDGEMENTS

This work is supported by the Humanities and Social Sciences Research Project of the Ministry of Education in China (21YJCZH069).

REFERENCES

[1] Wang, Y. J., 2016.The State Council deploys 8 key tasks to vigorously develop prefabricated buildings: strive to use about 10 years to make prefabricated buildings account for 30% of the newly built building area. China Investigation & Design, no.11:8.

[2] Gao, Y. Y., 2021-07-21 Support for the development of prefabricated buildings is still active everywhere. China Construction News Network. https://www.chinajsb.cn.

[3] Jeong, G., Kim, H., Lee, H. S., et al., 2021. Analysis of safety risk factors of modular construction to identify accident trends. Journal of Asian Architecture and Building Engineering. 1-13.

[4] Li, Q. N., Chen, R. J., Ma, M. C., 2021. Transportation risk assessment of fabricated building parts based on combined weight. Journal of Civil Engineering and Management. Vol.38, no.01, 52-57.

[5] Wang, Z. L., Shen, H. C., Zuo, J., 2019. Risks in prefabricated buildings in China: importance-performance analysis approach. Sustainability. Vol.11, no.12, 3450.

[6] Jin, Y., Zhang, J., Sun, L., 2019. Safety risk assessment of prefabricated building construction based on bayesian network. IOP Conference Series: Earth and Environmental Science. Beijing: IOP Publishing. Vol.371, no.3, 032052.

[7] Duan, Y. H., Zhou, S. Y., Guo, Y. B., et al., 2020. Safety Risk and Strategy of Prefabricated Building Construction Based on SEM. Journal of Civil Engineering and Management. Vol.37, no.02, 70-75, 121.

[8] Li, H. Y., Li, Q. M., Lu, Y., 2019. Analysis of key safety risks in prefabricated building construction based on structural equation model. China Safety Science Journal, Vol.29, no.04, 171-176.

[9] Liu, Z. K., Sun, G. S., Liu, Y. Z., 2019. Quality evaluation of prefabricated concrete construction. Journal of Liaoning University of Technology (Social Science Edition). Vol.21, no.04, 47-50.

[10] Chang, C. G., Chang, S. Q., 2019. Research on the safety management of the transportation and hoisting process of prefabricated building components. Shenyang University of Architecture and Construction (Social Science Edition). Vol.21,no.02, 141-147.

[11] Wang, D. H., You, Y. Y., 2020. Study on safety production management of prefabricated building hoisting. Value Engineering. Vol.39, no.01, 55-57.

[12] Wang L zhi, Yan L j.,2020. Safety evaluation of prefabricated bunding construction based on combination weighting and Variable fuzzy sets. Journal Safety Science and Technology, Vol.16, no.11: 103-109.

[13] Feng, Y. J., Du, S. Z., Zhang, J. Y., 2019. Safety evaluation and prediction of prefabricated building construction based on EW-SPA. China Safety Science Journal. Vol.29, no.05, 85-90.
[14] Yan, F., Xu, K., 2018. A set pair analysis based layer of protection analysis and its application in quantitative risk assessment. Journal of Loss Prevention in the Process Industries. Vol.55: 313-319.
[15] Wu, J. J., Cai, Y., Liu, Z. J.,2010. Set-pair analysis of index weight in formal safety assessment. Navigation China. Vol.33, no.03, 60-63.
[16] Zhao, K. Q.,2000. Set pair analysis and its preliminary application. Hangzhou: Zhejiang Science and Technology Press. 1-43.
[17] Zhang, J. X., Zhao, R. Y., 2017. A talk on application of pareto diagram and fishbone diagram in the quantitative and qualitative analysis of instruments and equipment inventory loss. Research and Exploration in Laboratory. Vol.36, no.04, 276-279.
[18] Balaji K, Kumar V S S, 2014.Multicriteria inventory ABC classification in an automobile rubber components manufacturing industry[J]. Procedia CIRP, Vol.17: 463-468.
[19] Vujović, A., Đorđević, A., Gojković, R., & Borota, M. 2017. ABC classification of risk factors in production supply chains with uncertain data. Mathematical Problems in Engineering, 2017.
[20] Wang, Z. Q., Zhang, Q. M., Wang, G. Q., et al.2018. Safety evaluation of prefabricated building construction based on FTA-SPA-Grey clustering. Safety and Environmental Engineering. Vol.25 no.02, 166-173.

CIVIL ENGINEERING JOURNAL

Article no. 47

THE CIVIL ENGINEERING JOURNAL 4-2022

STRATA SUBSIDENCE CHARACTERISTICS OF SHIELD TUNNELING IN COASTAL SOFT SOIL AREA

Qingming Xiang [1], Youqian Gao[1], Jiaxuan Su[2], Xiaoshuang Li[3] and Xuansheng Cheng[3]

1. *Wenzhou Traffic Engineering Management Center, No. 2, East Road, Nanbaixiang Street, Ouhai District, Wenzhou, China; 347363807@qq.com; gaoyouqian@qq.com*
2. *Wenzhou Traffic Engineering Test and Inspection Limited Company, No. 110, Haitong Road, Wenzhou Economic and Technological Development Zone, Wenzhou, China; 164528647@qq.com*
3. *School of Civil Engineering, Lanzhou University of Technology, No. 287, Langongping Road, Lanzhou, China; 2857309418@qq.com; chengxuansheng@gmail.com*

ABSTRACT

In order to study the subsidence characteristics caused by large diameter shield tunnelling in coastal soft soil area, based on the project of North Oujiang shield tunnel, the displacement field, seepage field and stress field of surrounding rock during shield tunnel construction under fluid-solid coupling were analyzed by using finite difference method. The results show that when the shield tunnelling passes through the monitoring section of the tunnel, the surrounding rock in a certain range of this section above the tunnel will be uplifted. Shield tail grouting can effectively control the settlement of the strata, and the increase of the ground settlement decreases gradually. With the advance of the shield the pore water pressure increases, and the pore water pressure in the soil layer will rise sharply due to the shield tail grouting. When the shield passes through the monitoring section of the tunnel, the strata stress above the tunnel increases due to uplift extrusion, and the strata stress below the tunnel decreases due to stress release. When the shield tail grouting is completed and the shield machine gradually moves away from the monitoring section, the stress release leads to the decrease of the ground stress around the tunnel, and the strata stress distribution is funnel-shaped.

KEYWORDS

Coastal soft soil area, Shield tunnel, Numerical simulation, Displacement, Pore water pressure, Stress

INTRODUCTION

With the continuous development of shield technology, slurry shield technology is widely used in the construction of the submarine tunnel in soft clay strata. In the process of shield tunnelling, the disturbance to the surrounding soil layer will inevitably occur. If the disturbance is too large, it will pose a threat to the safety of the surrounding buildings or adjacent structures, and it is not conducive to the stability of the tunnel structure in the later period. Therefore, it is of great engineering significance to study the displacement field, seepage field and stress field in the surrounding rock during the shield tunnelling.

Scholars at home and abroad have studied the ground settlement of tunnel construction with different methods. Peck [1] induced and analyzed the surface settlement of tunnel construction based on the measured data of the project, and showed that the shape of settlement trough in tunnel construction of non-cohesive soil and cohesive soil layer presented error function or normal distribution curve shape. Due to its clear concept and simple calculation, this formula has been

widely applied in practical engineering and has been continuously improved by some scholars [2-10]. Rowe and Kack [11] adopted the finite element method to simulate the ground settlement during shield construction, and analyzed the influence of segment weight, soil parameters, formation loss, and shield tail grouting on the ground settlement. Zhang and Huang [12] summarized stratum response caused by excavation disturbance, synchronous grouting, seepage and creep behavior of soft soil during shield tunnelling. Sagaseta [13] assumed that the soil was homogeneous, isotropic and linearly elastic incompressible material in a semi-infinite space. Combined with the Mindlin solution and the virtual mirroring technology of fluid mechanics, the analytical solution of formation displacement caused by formation loss was obtained. Liu and Zhang [14] applied the random medium theory to the prediction of ground subsidence caused by tunnel construction,and gave two-dimensional and three-dimensional analytical formulations for settlement prediction. Later some researchers analyzed the ground settlement of shield tunnel under the influence of different soil layers and construction conditions, and further developed the theory [15-19]. Chen et al. [20] combined with practical engineering used empirical formula (assuming that the settlement curve above the tunnel is a Gaussian distribution curve) and finite element analysis to conduct reverse analysis to the surface settlement of the tunnel. Based on the Mindlin solution, Liang et al. [21] considered the influence of the supporting force on the shield tunnel face, the non-uniform lateral friction between shield shell and soil in the process of shield tunnelling, the shield tail grouting pressure and other factors on the ground settlement. The vertical and horizontal displacement prediction formulas of the ground during shield tunnelling were obtained. Lv et al. [22] took the shield tunnel project of Guangzhou Metro Line 8 and studied the settlement of shield construction in the composite strata of upper soft and lower hard by using the finite element simulation and combining with the monitoring data of the project. They concluded that with the decrease of the height ratio of soft and hard rocks (soft rock height/hard rock height), the ground settlement decreased and the settlement trough became shallower. At present, the researches of scholars both domestic and foreign on the horizontal displacement of the stratum are relatively few, and the prediction results mostly reflect the settlement in the later stage of shield construction, and it cannot reflect the disturbance to the soil layer in the shield advancing process. And most of the studies do not consider the influence of water seepage in surrounding rock mass on stratum settlement.

The displacement field, seepage field and stress field of surrounding rock during shield tunnel construction under fluid-solid coupling were analyzed by using finite difference method combined with the actual project of North Oujiang tunnel of S2 railway line in Wenzhou city. This paper will provide theoretical guidance for the construction and design of similar underwater tunnel engineering.

NUMERICAL EXAMPLES

Numerical model and boundary conditions

The shield construction process at the typical section in the middle section of the river is simulated. The excavation diameter of shield machine is 14.9m, the outer diameter D of the tunnel is 14.5m, and the inner diameter d is 13.3m. The tunnel is buried 20m below the riverbed, and the water depth above the riverbed is 12m. A three-dimensional numerical model of tunnel construction is established by finite difference method. Due to the symmetry of the structure, half of the structure model is selected for calculation and analysis. In order to eliminate the influence of boundary effect, the distance between the left and right boundary and the lower boundary of the model and the tunnel axis is 3~5 times of tunnel diameter. Figure 1 shows the numerical model of shield construction and its dimensions.

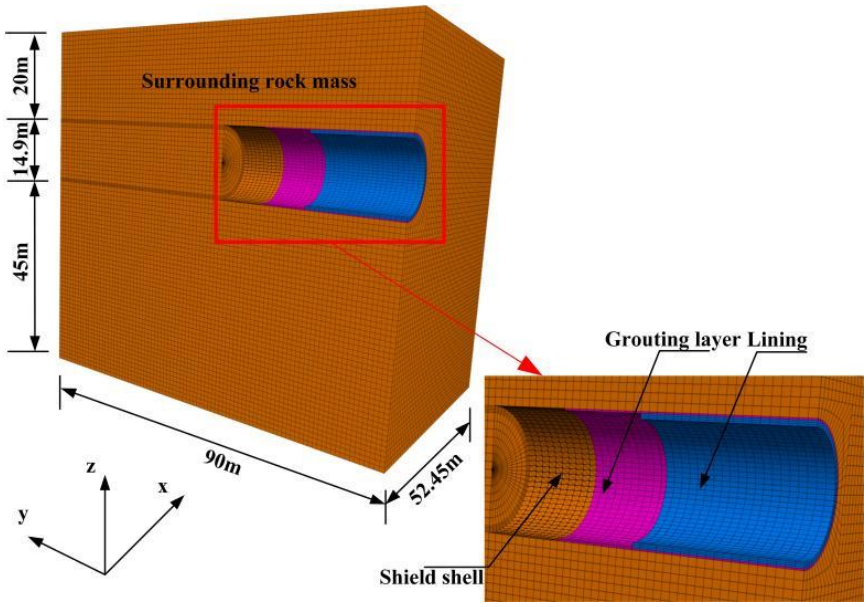

Fig. 1 – Numerical model of shield construction

The elastic constitutive models are used for the lining, grouting layer and shield of the tunnel, and the Mohr-Coulomb model is used for the surrounding rock mass, and the 8-node solid element is used for the lining, grouting layer and surrounding rock mass, and shell element is used to simulate shield shell of the shield machine. Physical parameters of surrounding rock are shown in Table 1. The selection of material parameters and elements such as shield shell, shield tail grouting body and lining are shown in Table 2. Considering the influence of staggered assembled segments and bolt connection on the stiffness of lining structure, the reduction coefficient of bending stiffness is selected as 0.8. The boundary conditions are that the top of the model is free, and the water level is above the riverbed surface depending on the specific water level. The horizontal displacement of the left and right sides and the two sides perpendicular to the axis of the tunnel are constrained, while the vertical displacement of the bottom is constrained. The sides and the bottom are set as impervious boundaries. The boundary conditions are shown in Figure 2.

Tab. 1 - Physical parameters of surrounding rock mass

The soil	Natural gravity γ/(kN/m^3)	Thickness of soil /m	Internal friction angle φ/(°)	Cohesive force c /kPa	Poisson's ratio v	Modulus of elasticity E/MPa	Porosity n	Permeability coefficient k_s/(m/s)
②^{1}Mud	16.4	14	3	6	0.4	10	0.63	7×10^{-7}
②^{2}Mud	16.7	12	3	6	0.4	10	0.6	5×10^{-7}
③^1 Silt clay	17.2	12	4	8	0.35	15	0.58	1×10^{-7}
④^{2}Clay	18.2	7	7	12	0.3	20	0.5	6×10^{-8}
⑥^{3}Tuff	25	>50	-	-	0.25	1500	0.3	2×10^{-8}

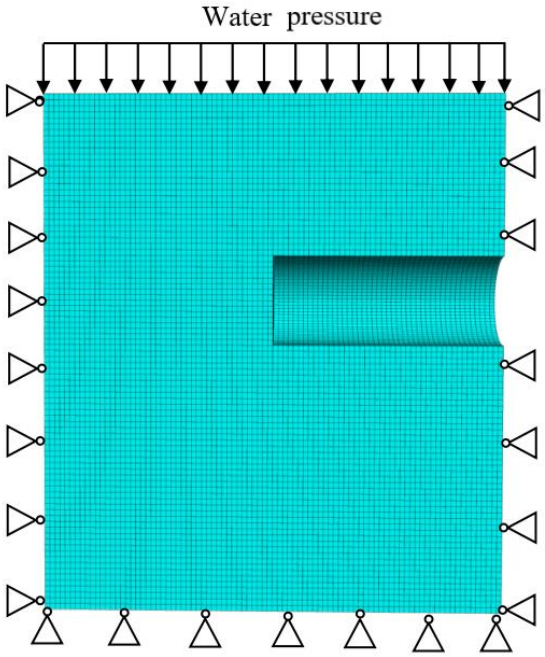

Fig. 2 – Model boundary condition

Tab. 2 - Material parameters

Material	Gravity γ/(kN/m^3)	Thickness /mm	Poisson's ratio v	Modulus of elasticity E/MPa	Unit
Lining（C50）	25	600	0.2	2.67×10^4	8-node element
Shield shell	78.5	60	0.3	2.1×10^5	Shell element
Grouting material (Beginning)	21	200	0.46	0.4	8-node element
Grouting material (Condensation)			0.2	4	

Shield construction load parameter and construction simulation

Slurry pressure in the slurry tank: The calculation results show that the support pressure at the center of the excavation face is 545.456kPa, and the change gradient of the support pressure on the excavation face is 15.537kPa/m. The grouting pressure is taken 1.1 times of the water and soil pressure, and the grouting pressure at the central axis of the tunnel is 532.434kPa, with a gradient of 16.998kPa/m. The weight of shield shell: The slurry pressure balance shield machine is selected the total weight is 2126t. The weight of the whole shield machine is evenly distributed on the whole shield shell, and the uniform weight is 71.342kPa.

The 30 rings excavation process of shield tunnel is simulated and the length of each ring is 2m. The coupling calculation between fluid and solid is adopted to carry out mechanical calculation and seepage calculation at the same time, and the actual shield construction process is simulated and analyzed. Firstly, the in-situ stress balance is carried out for the model without considering the seepage in the surrounding rock. After tunnelling and excavating, seepage calculation and mechanical calculation are carried out simultaneously, and the fluid modulus is set as 2×10^6 kPa. The empty model is used to excavate each ring of the tunnel. The supporting pressure is set on the tunnel face, and the shell element is used to generate shield shell on the excavation ring to support the excavated soil layer. The excavation is carried out step by step. When tunnelling to the sixth

ring, the shield shell element of the first ring is deleted to generate the lining of the first ring and the grouting layer of the first ring. Grouting pressure is set on the soil and lining of the upper and lower surfaces of the grouting layer of the first ring respectively to carry out fluid-soild coupling calculation. In this way, the excavation is carried out step by step to support each ring and grouting behind the ring. The grouting pressure is set behind the ring for the fluid-soild coupling calculation until the excavation of the 30th ring is completed.

CALCULATION RESULTS AND ANALYSIS OF RESULTS

The shield construction process of 30 rings of underwater tunnel excavation is numerically simulated. According to the five stages of shield tunnel construction, the displacement field, seepage field and stress field of the surrounding rock are analyzed. In order to eliminate the influence of the boundary on each field of the surrounding rock, the position of the 15th ring (Y=30m plane) is taken as the monitoring section.

Displacement field

Taken the 15th ring section (Y=30m plane) as the monitoring cross section, the stratum settlement of monitoring section after the completion of 14th ring (shield close to monitoring section), 16th ring (shield through the monitoring section), 18th ring (transition), 21st ring (shield tail grouting stage), 23rd ring (hardening stage 1), 30th ring (hardening stage 2) are respectively selected. The formation depths of Z =0m, 10m and 18m are selected to analyze the laws of ground subsidence in the process of shield tunnelling, and the calculation results are shown in Figure 3.

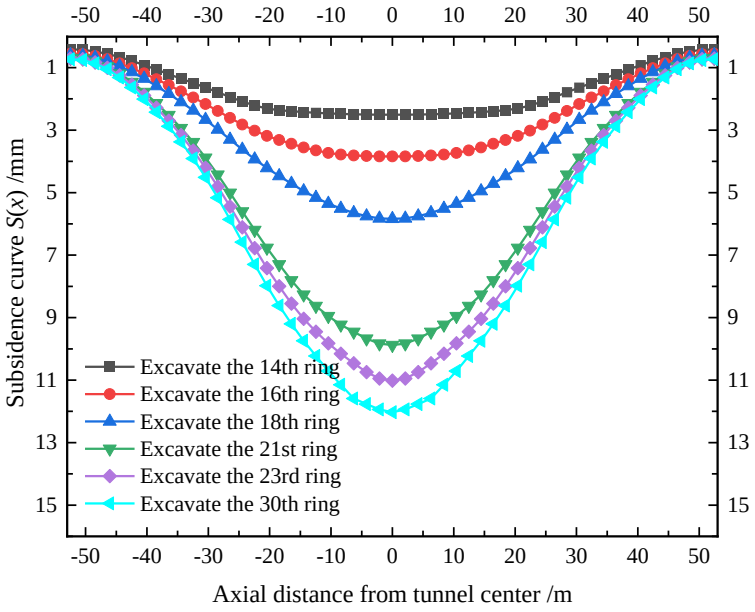

(a) Formation depth z=0m

Fig. 3 – Subsidence curve during excavation

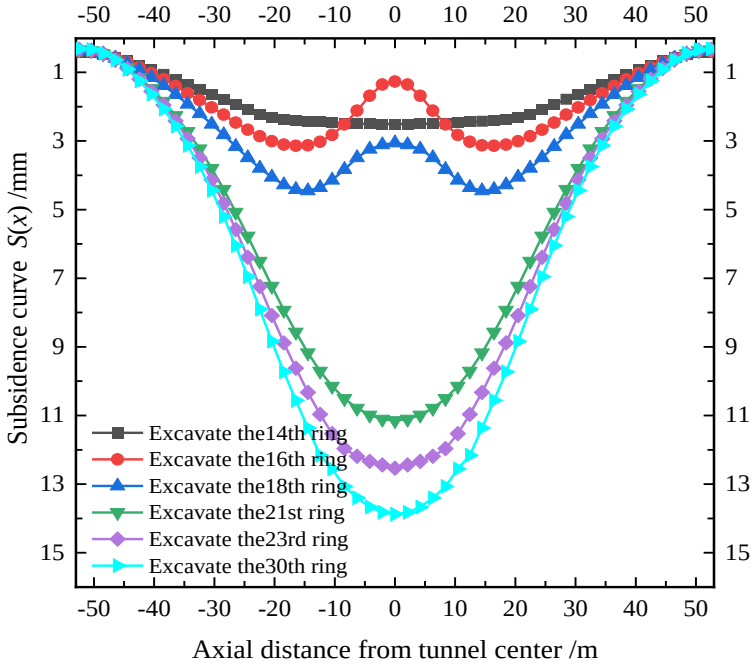

(b) Formation depth z=10m

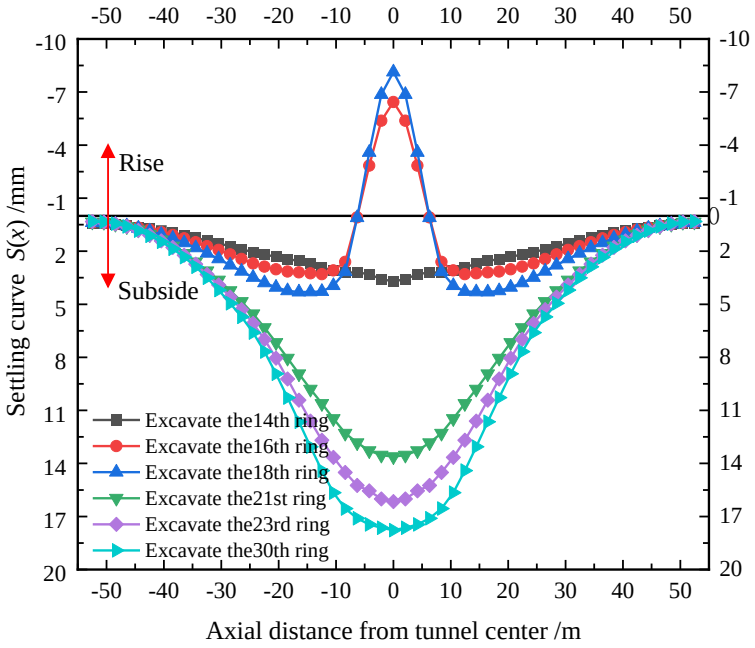

(c) Formation depth Z=18m plane

Fig. 3 – Subsidence curve during excavation

The Figure 3(a) shows that with shield advancing step by step, the settlement stratum (z = 0 m plane) is slowly growing, the settlement curve is basically the same in each shield stage, which all fit to Gaussian normal distribution of Peck curve, and the largest settlement occurs in the center of the tunnel axis. And after completion of the 14th ring, 16th ring, 18th ring, 21st ring, 23rd ring and 30th ring shield tunnelling, the maximum settlements on the plane z=0m are 2.6 mm, 3.8 mm, 5.8 mm, 9.9 mm, 11.0 mm and 12.3 mm respectively，which indicates that the settlement at the bottom plane of the river mainly occurs between 14th ring and 21st ring (the period of shield machine crossing and shield tail leaving the monitoring section) during shield construction, and the

settlement at the bottom plane of the river is small during grouting completion and slurry consolidation, which shows selection of grouting pressure is appropriate, and strata subsidence can be controlled. Combined with Figure 3 (b) and (c), it can be seen that after the completion of the 16th and 18th rings of shield tunnelling, the settlement curve in the ground does not conform to the Gaussian normal distribution, and the curve shows the shape of gradually decreasing around and bulging in the middle, which is related to the upward floating of the machinery caused by the stress redistribution in the construction process of the shield tunnelling, so it is necessary to carry out counterweight on the shield machine in the process of shield construction to anti-floating. After the completion of shield tunnelling in the 21st, 23rd and 30th rings, the settlement curve at any depth of the stratum still conforms to the Gaussian normal distribution because the formation stress has been released due to the existence of the grouting layer. The existence of buffer layer reduces the pressure difference between the top and bottom of the tunnel, so that the floating effect will no longer occur. As can be seen from the figure, in the whole process of shield construction, with the shield gradually approaching the monitoring section, the ground will be disturbed and vertical settlement will occur. With the shield tunnelling passing through the tunnel section, A certain range of the surrounding rock above the tunnel will be uplifted, but the settlement of the riverbed will continue to increase. With the shield tail grouting gradually away from a tunnel section, the shield tail grouting can effectively control the subsidence of the ground. The subsidence of the ground is still gradually increasing, but after the condensation and hardening of the grouting layer, the subsidence of the ground will gradually tend to be stable.

Pore water pressure

The positions above the central axis of the tunnel, which are 2 m, 6 m, 10 m, 14 m, 16 m, 18 m and 20 m from the bottom of the river, are selected to study the change of pore water pressure in surrounding rock soil caused by the whole excavation process, as shown in Figure 4.

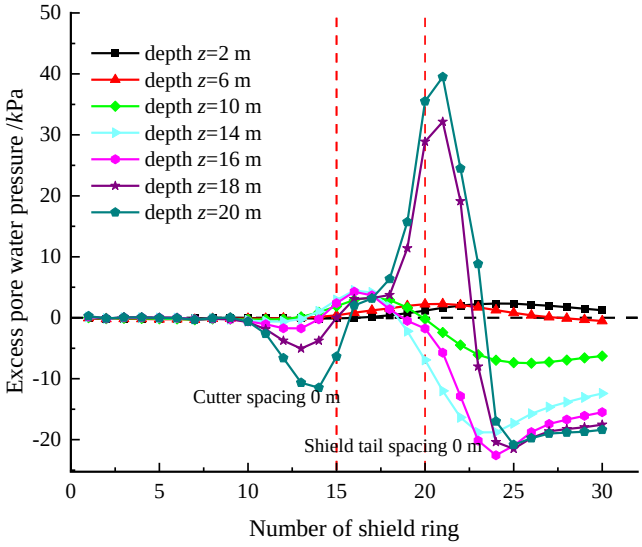

Fig. 4 – Change curve of pore water pressure during excavation

As can be seen from Figure 4, during the shield tunnelling, as the cutter head gradually approaches the tunnel excavation face, the pore water pressure in the formation will gradually decrease due to shield disturbance. When the shield passes through the tunnel face, the excess pore water pressure will be formed in the formation due to the disturbance, and the pore water pressure will increase with the shield advancing. When the grouting at the tail of the shield is removed, the pore water pressure in the soil layer within 4m of the upper part of the tunnel will rise sharply, and the maximum excess pore water pressure is 39.5kPa. As the shield tail gradually moves away, the pore pressure in the upper strata of the tunnel gradually decreases, then increases and finally tends to be stable. The final pore water pressure is less than the original

hydrostatic pressure. By contrast, the pore water pressure at the top of the tunnel eventually decreases by 18.4kPa. It can be roughly seen from the figure that the influence range of pore water pressure is roughly within the range of 10m above.

Stress field

Distribution of transverse stress field

Figure 5 is the vertical stress in the transverse direction at the position of the monitoring section (Y=30m plane) during shield construction

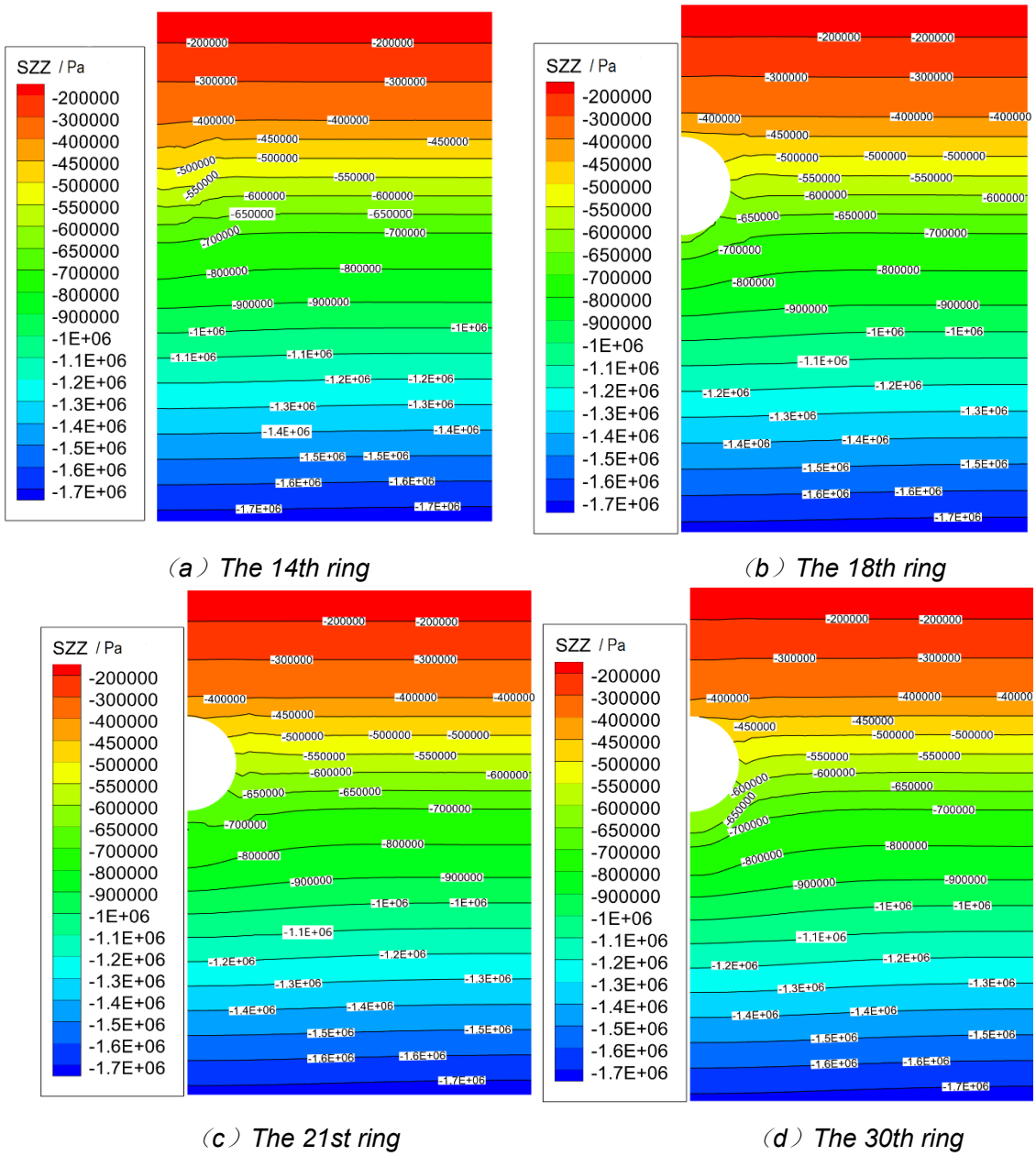

（a）The 14th ring　　（b）The 18th ring

（c）The 21st ring　　（d）The 30th ring

Fig 5 – Transverse stress distribution during shield construction

According to Figure 5 (a), when the shield approaches the tunnel face (the 14th ring), the vertical stress of the stratum decreases slightly compared with the initial stress, and the shield has begun to affect the soil in front of the tunnel face. As can be seen from Figure 5 (b), when the shield passes through the tunnel face, the vertical stress of the upper soil layer increases due to the

extrusion of the floating effect and presents an upward protrusion, while the bottom decreases due to the release of the stress. It can be seen from Figure 5 (c),and Figure 5(d) that when the shield tail moves away, there is a stratum loss between the strata. The existence of the gap leads decrease of the stress due to the release of the strata stress around the tunnel, and the disturbance also gradually decreases from the tunnel position to both sides, and the surrounding vertical stress presents funnel shape. Also it is seen from Figure 5 (d) that after the grouting body solidifying and hardening, the vertical stress of the formation is basically the same and tends to be stable.

Distribution of axial stress field

Figure 6 is the vertical stress on the longitudinal section where the tunnel axis is located during shield construction, and the vertical stress of the stratum in the shield construction process is analyzed.

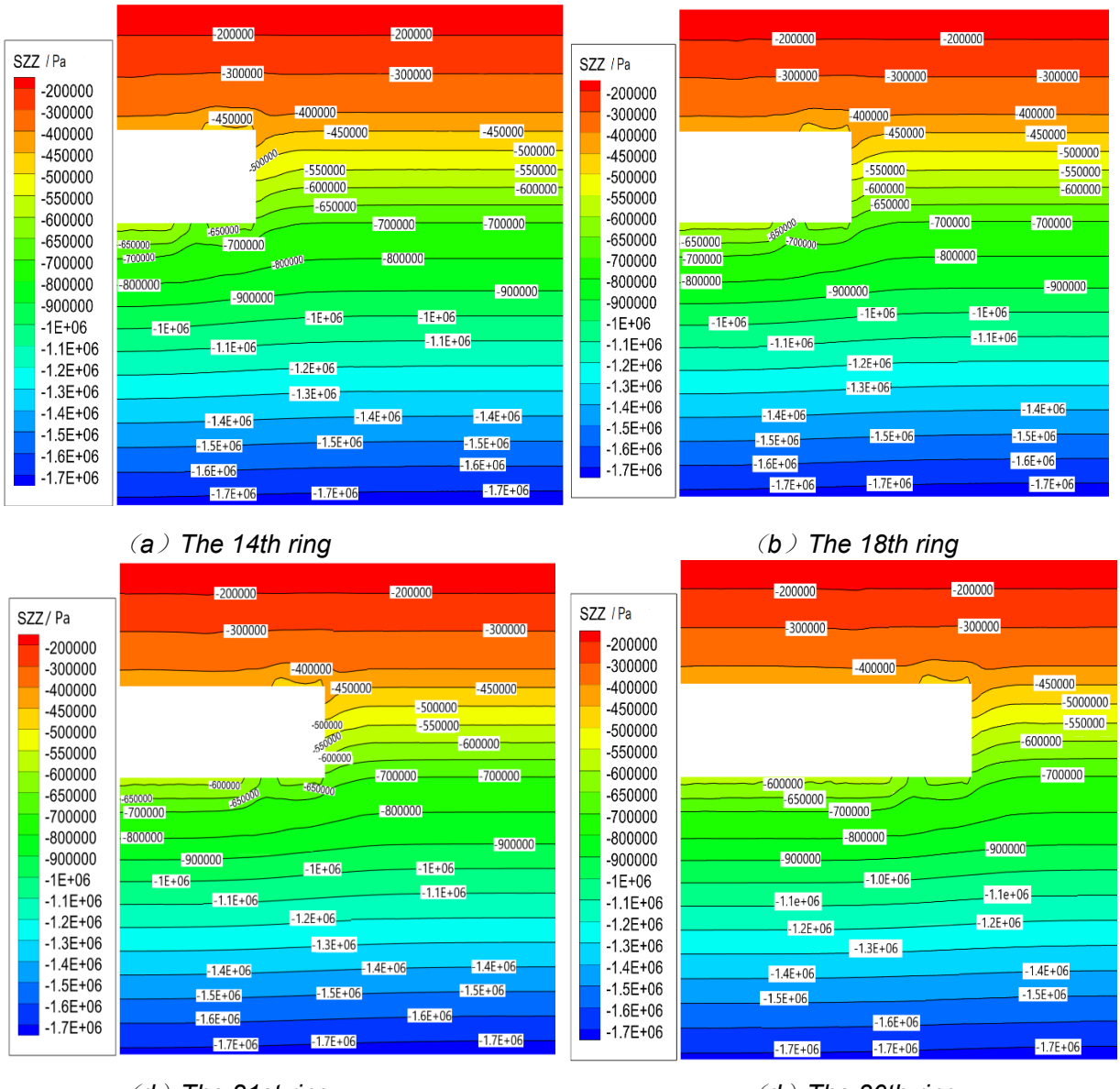

(a) The 14th ring *(b) The 18th ring*

(d) The 21st ring *(d) The 30th ring*

Fig. 6 – Axial stress distribution during shield construction

The Figure 6 (a) shows as the tunnelling approaches the tunnel face, the degree of disturbance increases, and the stress release of the formation in front of the tunnel face increases, and the formation stress distribution presents a funnel shape. In Figure6 (b), the stress in the range around 8m in front of the shield face decreases due to the stress release, and the undisturbed area is still in

the initial stress state. The formation stress at the shield tail gradually tends to be stable with the gradual advancing of the shield. When the shield passes through the strata, the stress of the upper soil above the tunnel increases due to the floating effect, and the stress of the bottom soil under the tunnel decreases due to the stress release. The distribution of vertical stress in Figure 6 (d) is almost the same as that in Figure 6 (c), and the formation stress tends to be stable as the shield tail gradually moves away.

CONCLUSIONS

(1) During the shield tunnelling, as the shield gradually approaching to the monitoring section, the strata will be disturbed and vertical subsidence will occur. When the shield tunnelling passes through the monitoring section, the surrounding rock soil in a certain range above tunnel uplifts, but the settlement of the strata under the riverbed will continue to increase. Shield tail grouting can effectively control the subsidence of the strata, the increasing range of the strata subsidence gradually decreases, and the strata subsidence tends to a stable state with the consolidating and hardening of the grouting layer.

(2) As the shield approaching to the tunnel monitoring section, the pore water pressure of the formation decreases gradually due to the shield disturbance. When tunnel shield passes through the monitoring section, excess pore water pressure will be formed in the stratum. With the shield advancing, pore water pressure will also increase. The pore water pressure of the soil will rise sharply when the shield tail grouting. With the shield moving away from the monitoring section, the pore pressure in the stratum above the tunnel gradually decreases, then increases and finally tends to be stable.

(3) With the shield advancing the monitoring section, the vertical stress of the stratum around the tunnel decreases due to disturbance. When the shield passes through the monitoring section, the stress in the strata above the tunnel increases due to uplift extrusion, and the soil stress under the tunnel arch bottom decreases due to stress releasing. When the shield is away from the monitoring section, the formation loss occurs around the tunnel, and the stress decreases in the surrounding stratum due to the stress release and shows a funnel-shaped distribution.

(4) For the shield tunnelling in soft soil area, it is suggested that the support force of tunnel face and grouting pressure should be set as 1.1 times the original lateral and vertical soil and water pressure respectively, which can minimize the disturbance of the stratum.

ACKNOWLEDGEMENTS

This paper is supported in part by the National Natural Science Foundation of China (Grant number: 51968045), and the Science and Technology Planning Project of Zhejiang Traffic Quality Supervision Industry(Grant number: ZJ201906).

REFERENCES

[1] Peck R. B., 1969. Deep excavations and tunneling in soft ground. In the 7th ICSMFE. Mexico, 311-375.

[2] Mair R. J., Taylor R. N., Bracegirdle A., 1993. Subsurface settlement profiles above tunnels in clays. Géotechnique , Vol. 43: 315-320. https://doi.org/10.1680/geot.1993.43.2.315

[3] Celestino T. B., Gomes R. A. M. P., Bortolucci A. A., 2000. Errors in ground distortions due to settlement trough adjustment . Tunnelling and Underground Space Technology, Vol. 15:97-100. https://doi.org/10.1016/S0886-7798(99)00054-1

[4] Jiang X. L., Zhao Z. M., Li Y., 2004. Analysis and calculation of surface and subsurface settlement trough profiles due to tunneling. Rock and soil mechanics, Vol. 5: 1542-1544. https://doi.org/10.1007/BF02911033

[5] Qu J. L., Ge X. R., 2005. Analysis of characteristics of settlement trough induced by shield construction in soft soil area. Industrial Construction, Vol. 35: 42-46.

[6] Zhang Z. X., Zhang H., Yan J. Y., 2013. A case study on the behavior of shield tunneling in sandy cobble ground. Environmental Earth Sciences, Vol. 69: 1891-1900. https://doi.org/10.1007/s12665-012-2021-4
[7] Li Z. C., Chen R. P., Meng F. Y., et al., 2015. Tunnel boring machine tunneling-induced ground settlements in soft clay and influence of excavation parameters. Journal of Zhejiang University, Vol. 49:1268-1275. https://doi.org/10.3785/j.issn.1008-973X.2015.07.010
[8] Shen Y. S., He Y. H., Zhao L., et al., 2017. Improvement of Peck formula of surface construction settlement of rectangular tunnel in soft soil area. Journal of Railway Science and Engineering, Vol. 14: 1270-1277.
[9] Cai Y., Zhang C. P., Min B., et al., 2019. Deformation characteristics of ground with voids induced by shallow metro tunnelling. Chinese Journal of Geotechnical Engineering, Vol. 41: 534-543.
[10] Lu D. C., Lin Q. T., Tian Y., et al., 2020. Formula for predicting ground settlement induced by tunnelling based on Gaussian function. Tunnelling and Underground Space Technology, Vol. 103: 1-22. https://doi.org/10.1016/j.tust.2020.103443
[11] Rowe R. K., Kack G. J., 1983. Theoretical examination of the settlements induced by tunnelling: four case histories. Canadian Geotechnical Journal, Vol. 20: 299-314. https://doi.org/10.1016/0148-9062(83)90716-7
[12] Zhang D. M., Huang X.,2018. Proceedings of GeoShanghai 2018 International Conference: Tunnelling and Underground Construction. Springer Nature Singapore Pte Ltd, Singapore.
[13] Sagaseta C.,1987. Analysis of undrained soil deformation due to ground loss. Géotechnique, Vol. 37: 301-320. https://doi.org/10.1680/geot.1987.37.3.301
[14] Liu B. C., Zhang J. S., 1995. Random medium method for surface subsidence caused by near surface excavation. Chinese Journal of Rock Mechanics and Engineering, Vol. 14: 289-296.
[15] Yang J. S., Liu B. C., 1998. Surface movement and deformation caused by extrusion shield tunneling. Rock and soil mechanics, Vol. 19:10-13.
[16] Zhu Z. L., Zhang Q. H., Yi C. H., 2001. Stochastic theory for predicting longitudinal settlement in soft - soil tunnel. Rock and soil mechanics, Vol. 22:56-59.
[17] Shi C. H., Peng L. M., 2004. Application of stochastic medium theory to predicting settlement in longitudinal surface due to tunnel construction by shield. Rock and soil mechanics, Vol. 25: 320-323. https://doi.org/10.1007/BF02911033
[18] Fang T., Xu X. C., 2015. Improved calculation of parallel twin tunnel settlement based on stochastic medium theory. Urban Mass Transit, Vol. 18:19-23.
[19] Liu B., Yang W. H., 2019. Prediction model and application of three-dimensional ground surface settlement induced by tunnel excavation considering time effect. Journal of Mining Science, Vol. 4: 384-393.
[20] Chen S. L., Gui M. W., Yang M. C., 2012. Applicability of the principle of superposition in estimating ground surface settlement of twin- and quadruple-tube tunnels. Tunnelling and Underground Space Technology, Vol. 28:135-149. https://doi.org/10.1016/j.tust.2011.10.005
[21] Liang R. Z., Xia T. D., Lin C. G., et al., 2015. Analysis of ground surface displacement and horizontal movement of deep soils induced by shield advancing. Chinese Journal of Rock Mechanics and Engineering, Vol. 34: 583-593. https://doi.org/10.13722/j.cnki.jrme.2015.03.016
[22] Lv J. B., Li X. L., Fu H. L., et al., 2020. Influence of shield tunnel construction on ground surface settlement under the condition of upper-soft and lower-hard composite strata. Journal of Vibroengineering, Vol. 22: 1126-1144. https://doi.org/10.21595/jve.2020.20967

CIVIL ENGINEERING JOURNAL

Article no. 48

THE CIVIL ENGINEERING JOURNAL 4-2022

STOCHASTIC TRAFFIC DEMAND PROFILE: INTERDAY VARIATION FOR GIVEN TIME AND DAY OF WEEK

Igor Mikolášek

Brno University of Technology, Faculty of Civil Engineering, Institute of Road Structures, Veveří 95, 602 00 Brno, Czech Republic; igor.mikolasek@vutbr.cz

ABSTRACT

Traffic demand prediction is one of the major elements of traffic planning and modelling. Traffic surveys routinely estimate the profile of traffic demand on a certain road section, showing the expected evolution of the demand over a day or week. However, the actual demand fluctuates around this value on day-to-day basis and thus can exceed otherwise sufficient capacity and consequently cause congestion due to the capacity drop. This type of traffic demand variability has not yet been properly studied although it can play significant role in traffic modelling and engineering. The relevance of this variability is further increasing with the growing popularity of stochastic traffic models. This paper presents results of a statistical analysis of the demand variability in five-minute aggregation intervals. Normal, lognormal and gamma distributions all show reasonably well fit to the data for individual intervals and often do not differ on statistically significant level. Based on the count of the best fits, the lognormal distribution seems to be most suitable, while the gamma distribution is the most universal and with generally acceptable fit. There appears to be a pattern where certain distributions have better fit in different times of the day and week. The regularity and magnitude of demand probably both play a role in this, as well as the aggregation interval. Two simple models for modelling the variability are proposed for practical applications when there is not enough data to perform similar analysis.

KEYWORDS

Random traffic demand, Probability distribution, Traffic model, Goodness-of-fit

INTRODUCTION

The paper deals with the variability of traffic demand around its time-varying mean value given by the traffic demand profile. Traffic demand profiles are commonly estimated via a traffic survey at specific location for workday or weekend. They show the estimated average progression of traffic demand over the whole day based on the collected data, which are usually extrapolated and transformed using coefficients of daily or seasonal variation specified in TP 189 [1] in the Czech Republic. This data can further be used to calculate annual average daily traffic (AADT). However, there is usually no information about the possible variation of the traffic volumes from day to day at any time. This variability can play important role if the intensity is close to capacity levels. Once the capacity, which is also a stochastic variable [2–4], is exceeded, the capacity drops to queue discharge flow level [5–7], making it more difficult for the congestion to resolve even after the demand drops again.

Most of the existing research on traffic demand focused on OD (origin-destination) matrices. Those model the traffic relations among points of interest on the traffic network on variable scale and are then used (mostly) in the four-stage traffic models as one of the inputs for modelling traffic flow [8]. Historically, mostly deterministic OD matrices, which, at best, reflected the difference between the morning and afternoon peak hours, were used. In the past two decades, many new more dynamic models were developed, which utilize the development of IT and big data [9]. While researches were

dealing with the randomness of morning peak even earlier, practitioners preferred simple deterministic models which were sufficient for the applications at the time, according to Alfa [10].

If only local road section is modelled, the traffic demand or intensity cannot be modelled via the four-stage model and must be defined otherwise. This is often resolved by simply using a uniform distribution or at best with an exponential distribution with constant parameter based on an expected hourly volume in the peak hour. However, for stochastic models the traffic demand should be also modelled in more detailed statistical manner, especially if methods such as Monte Carlo simulation are used. Such model then allows, for example, to estimate the probability of TF breakdown at given time of day/week or development of a queue, or to accurately model behaviour of a traffic actuated system such as traffic lights, variable message signs and others. Using a fixed TF intensity would contradict the purpose of such model.

The problem of variability of traffic flow (TF) intensity on given day of week and time of day across following weeks, which could be called stochastic traffic demand profile, have not yet been significantly dealt with in the literature. While researchers and practitioners were and are certainly both aware of the random fluctuations on day-to-day and week-to-week basis, little attention is paid to it. If such variability is concerned, it is usually in the form of a random multiplicative coefficient with normal distribution and zero mean, e.g. Brilon [11] used random coefficient coming from N~(1, 0.1).

Better understanding of the phenomenon and the variability patterns could lead to better traffic modelling and prediction or to optimization of different traffic control algorithms, as well as more accurate traffic-engineering evaluations and designs.

METHODS

The traffic flow intensity (demand) data used for this study come from overhead ASIM by Xtrail tri-tech (microwave, infrared, ultrasonic) traffic detectors on motorway D5 at km 32.9, direction Prague, from June to December 2015 (29 weeks in total). Traffic congestions do not regularly occur in this location or on nearby on- or off-ramps. Therefore, the measured intensity can be considered as equal to the traffic demand with reasonable reliability. The original data is aggregated in 5-minute intervals and differentiates 6 vehicle categories. Firstly, the different categories were merged and transformed to passenger cars by using passenger car equivalent (PCE) PCE = 2 for trucks and busses to take their larger effect on the TF into consideration. Hence, pc/h was used as a unit of TF intensity. All the TF records were grouped into groups based on day-of-week, hour, and starting minute, together reflecting the whole week-long TF demand profile segmented into 5-minute intervals. Therefore, 2016 groups (7 days × 24 hours × 12 5-minute intervals) were created, each with up to 29 measurements. The outliers with Z-score > 3 were discarded from each group.

Each of the groups was fitted with five different random distributions using R script: normal (norm), gamma, Weibull (Weib), inverse Weibull (invWeib) and log-normal (lognorm). Those five were chosen based on theoretical assumptions and histograms of few randomly chosen groups as possible candidates for reasonable fit. The parameters of each of the fitted distribution for each of the group, along with the Akaike information criterium (AIC) which describes the goodness-of-fit of the model with the underlying data, were obtained as a result.

The choice of the best-fitting distribution was run in several phases as it turned out that the results are far from unambiguous. The best distribution was to be chosen based on the number of groups for which it had the best fit (lowest AIC). Since the first results led to no clear conclusions, each of the groups was expanded with data from the neighbouring groups, assuming they are highly correlated in terms of the TF intensity. That allowed to triple the sample size in each group (up to 87 measurements) at the cost of negligible bias, leading to more accurate fitting of the distributions. All the presented results are based on the data with extended groups. To further clarify the conclusions, groups from the night hours and weekends were omitted from the evaluation for two reasons. First, they can be reasonably assumed to have different statistical distribution thanks to different traffic patterns and second, they play little role in traffic engineering application. Eventually, the counts of best fits were also evaluated for each day and even hour, separately, and for each of the subset of

groups, the average AIC was also calculated for each of the distributions. That allows to compare to what extent is the best distribution better than the others. Small AIC difference means both (or more) distributions are almost equally good at fitting the data.

RESULTS AND DISCUSSION

Tab. 1 presents the aggregated results after expanding the groups with the neighbouring intervals for both whole week and for only workdays from 6 AM to 6 PM.

The overall results of the performed analyses are provided in Tab. 2. The left side of each table a-e (one for each workday) shows the count of best fits of each model within each time interval, the right side shows the average AIC of each model within the corresponding interval.

Tab. 1: Summary of the counts of best fit among the five probability distributions with and without the night and weekend intervals.

Distribution	norm	gamma	Weib	invWeib	lognorm
No. of best fits (Mon-Sun)	475	615	215	60	651
No. of best fits (Mon-Fri 6-18 h)	221	150	63	33	253

The relative likelihood of each model is given by $\exp((AIC_{min} - AIC_i)/2)$ where AIC_{min} is the AIC of the seemingly best-fitting model and AIC_i of the *i*-th model. It gives the probability that the *i*-th model minimizes the loss of information better than the model with lowest AIC and can be used to choose the best model(s) based on statistical significance. Unlike likelihood-ratio test, the compared models do not need to be nested, but the fitted data set obviously must be the same, i.e. the comparison can only be made within each time interval, e.g. compare the models on Friday 17-18 (Tab. 2 e). If the common level of significance 0.05 is used, the difference needed for the model with higher AIC to be statistically significantly worse than the one with the lowest AIC is circa 6. Therefore, if the difference in AIC is less than 6, we can say the two given models are not significantly different. In the case of Friday 17-18 this means that while gamma distribution seems to have the best fit, both normal and lognormal distributions are not statistically significantly worse in representing the empirical data. The same conclusions can be made for most of the presented intervals even though the best model differs. In few cases the Weibull distribution has the best fit but that seems more like a coincidence within the overall results.

Tab. 2 (a-e): Aggregated results of goodness-of-fit on hour-to-hour and day-to-day basis for each workday between 6 AM and 6 PM. Tables a-e show results for individual workdays. The results are colour-coded for each section (and separately for each line on the right side) for better clarity.

(a)

Monday	norm	gamma	Weib	invWeib	lognorm	norm	gamma	Weib	invWeib	lognorm
Sum 6-18	44	31	20	7	42	719.60	721.45	726.61	751.44	724.34
6-7	3	0	9	0	0	740.81	757.11	737.89	825.59	768.93
7-8	5	0	7	0	0	773.28	791.70	771.53	865.11	805.19
8-9	9	0	3	0	0	748.45	757.38	751.50	815.24	765.09
9-10	7	3	1	0	1	699.82	701.47	705.07	734.60	703.85
10-11	2	8	0	0	2	727.38	726.05	734.89	748.09	726.92
11-12	2	4	0	0	6	707.81	705.61	717.13	723.74	705.74
12-13	9	3	0	0	0	683.93	684.58	689.25	711.56	686.15
13-14	2	5	0	0	5	688.50	686.11	698.76	700.38	686.00
14-15	0	2	0	2	8	693.79	689.75	705.84	693.27	688.56
15-16	0	1	0	3	8	721.37	715.86	734.69	718.83	714.15
16-17	4	3	0	0	5	720.51	718.44	730.05	739.04	718.90
17-18	1	2	0	2	7	729.55	723.37	742.64	741.86	722.62

(b)

Tuesday	norm	gamma	Weib	invWeib	lognorm	norm	gamma	Weib	invWeib	lognorm
Sum 6-18	41	21	1	14	67	744.71	742.48	753.32	762.15	743.20
6-7	10	2	0	0	0	749.33	752.29	752.30	792.58	756.48
7-8	9	2	1	0	0	765.42	770.41	769.68	819.42	775.91
8-9	10	2	0	0	0	775.36	778.07	780.29	820.87	782.57
9-10	7	2	0	0	3	754.09	754.95	760.26	792.84	758.19
10-11	3	4	0	0	5	732.26	730.23	739.10	753.25	731.09
11-12	0	1	0	3	8	736.49	730.32	748.13	736.09	728.66
12-13	1	1	0	0	10	737.04	732.28	748.25	742.70	731.26
13-14	1	0	0	1	10	724.38	720.02	736.90	730.29	719.04
14-15	0	1	0	0	11	765.15	759.22	775.85	763.83	757.60
15-16	0	0	0	5	7	756.32	749.19	769.30	748.55	746.81
16-17	0	4	0	5	3	719.37	714.83	729.31	717.35	713.48
17-18	0	2	0	0	10	721.36	717.90	730.51	728.07	717.28

(c)

Wednesday	norm	gamma	Weib	invWeib	lognorm	norm	gamma	Weib	invWeib	lognorm
Sum 6-18	52	31	7	1	53	730.69	731.07	737.47	757.84	733.21
6-7	9	3	0	0	0	742.48	745.36	745.28	784.92	749.69
7-8	8	0	4	0	0	805.89	811.91	806.48	855.89	818.03
8-9	10	1	1	0	0	790.46	802.47	793.31	873.02	814.16
9-10	4	4	0	0	4	737.96	736.66	746.07	761.61	737.89
10-11	0	4	0	1	7	728.70	725.25	738.47	737.43	724.67
11-12	3	2	1	0	6	724.60	722.98	732.82	742.58	723.31
12-13	4	2	0	0	6	735.87	734.47	744.15	757.02	735.36
13-14	4	4	0	0	4	736.64	735.37	745.00	760.13	736.21
14-15	7	2	0	0	3	707.79	707.94	714.03	735.26	709.45
15-16	0	4	1	0	7	701.25	698.91	708.90	714.82	699.04
16-17	1	3	0	0	8	678.32	675.55	688.33	685.12	675.08
17-18	2	2	0	0	8	678.38	675.91	686.82	686.28	675.60

(d)

Thursday	norm	gamma	Weib	invWeib	lognorm	norm	gamma	Weib	invWeib	lognorm
Sum 6-18	62	22	32	4	24	722.44	727.49	727.18	770.19	732.70
6-7	7	0	4	0	1	708.10	721.98	708.81	793.07	733.25
7-8	8	0	4	0	0	761.52	778.82	762.31	857.83	792.92
8-9	9	0	3	0	0	779.23	791.27	780.41	852.74	802.06
9-10	8	1	3	0	0	719.05	723.98	721.29	768.27	728.67
10-11	9	1	1	0	1	719.74	722.81	722.44	759.43	726.09
11-12	3	4	1	0	4	687.39	686.11	696.99	708.47	686.60
12-13	2	1	1	1	7	687.67	685.47	698.71	702.90	685.57
13-14	4	1	1	2	4	707.17	706.28	715.49	731.30	707.46
14-15	3	5	1	0	3	720.22	718.89	728.24	745.26	719.77
15-16	3	1	3	1	4	722.99	724.74	729.86	755.82	727.47
16-17	2	8	2	0	0	739.98	740.34	746.11	777.76	743.37
17-18	4	0	8	0	0	716.27	729.15	715.46	789.39	739.13

(e)

Friday	norm	gamma	Weib	invWeib	lognorm	norm	gamma	Weib	invWeib	lognorm
Sum 6-18	22	45	3	7	67	698.42	695.84	706.51	713.31	696.02
6-7	0	3	0	1	8	660.36	656.43	669.03	662.54	655.48
7-8	0	2	0	2	8	698.30	693.08	708.46	701.10	691.82
8-9	0	2	0	0	10	688.56	684.59	698.44	695.04	683.83
9-10	0	1	0	1	10	667.42	663.51	677.42	671.89	662.60
10-11	2	2	1	3	4	674.39	671.92	682.53	685.48	671.90
11-12	4	4	2	0	2	674.73	674.96	679.80	697.84	676.29
12-13	0	5	0	0	7	684.42	681.80	692.80	696.52	681.67
13-14	3	7	0	0	2	718.79	717.54	727.35	746.73	718.72
14-15	2	7	0	0	3	731.76	730.12	739.45	756.21	731.31
15-16	3	4	0	0	5	737.00	734.17	745.81	759.40	734.70
16-17	3	5	0	0	4	749.14	747.19	755.48	772.37	748.33
17-18	5	3	0	0	4	696.20	694.78	701.51	714.58	695.60

The counts of best fits for each model are also highly skewed towards the three distributions while Weibull and especially inverse Weibull distributions lag far behind. In most cases, even their AIC is much higher than that of the three other distributions, while in the cases when they do have the best fit, the three distributions are in most cases not significantly worse. Obviously, if either Weibull or inverse Weibull distribution has good fit, the other has the worst fit by far.

Fig. 1 finally shows an illustrative comparison of goodness-of-fit of three different distributions to one particular group of TF data. The three distributions illustrate good, acceptable, and unsuitable fitting model, using different graphic tools of goodness-of-fit measure. Note that the AIC difference between log-normal and normal distribution is more than 10 but, visually, even the normal distribution has relatively good fit, despite being statistically significantly worse. That shows that often more than one distribution can model the empirical data reasonably well, which is important.

(a)

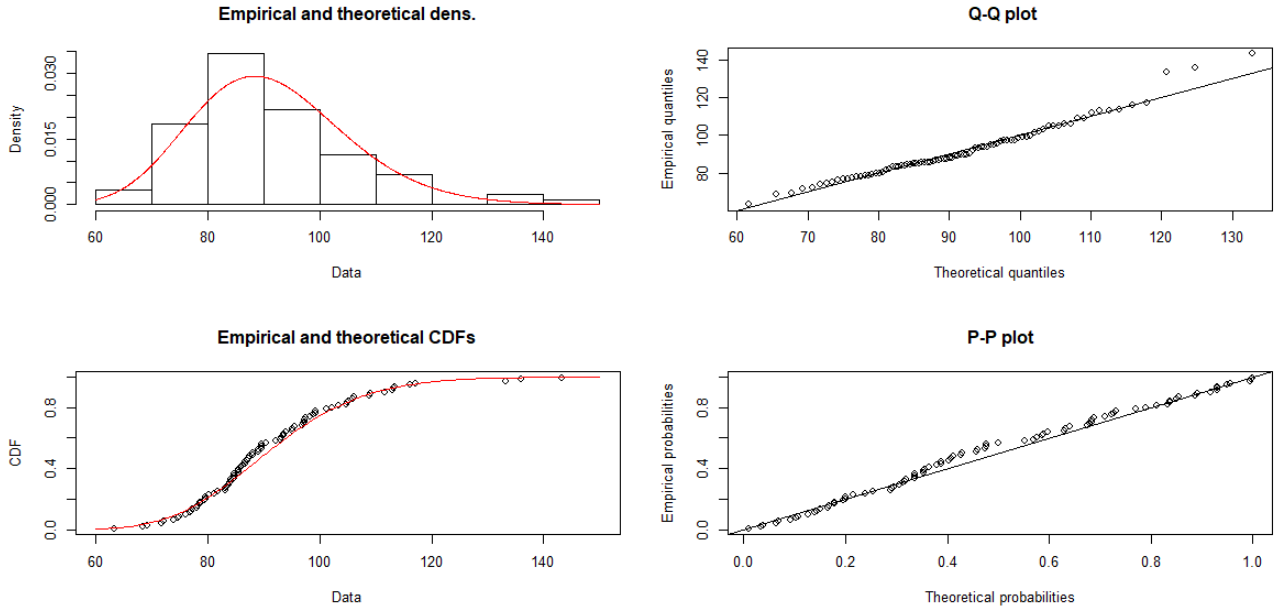
Empirical and theoretical dens.
Density
Data
Q-Q plot
Empirical quantiles
Theoretical quantiles
Empirical and theoretical CDFs
CDF
Data
P-P plot
Empirical probabilities
Theoretical probabilities

(b)

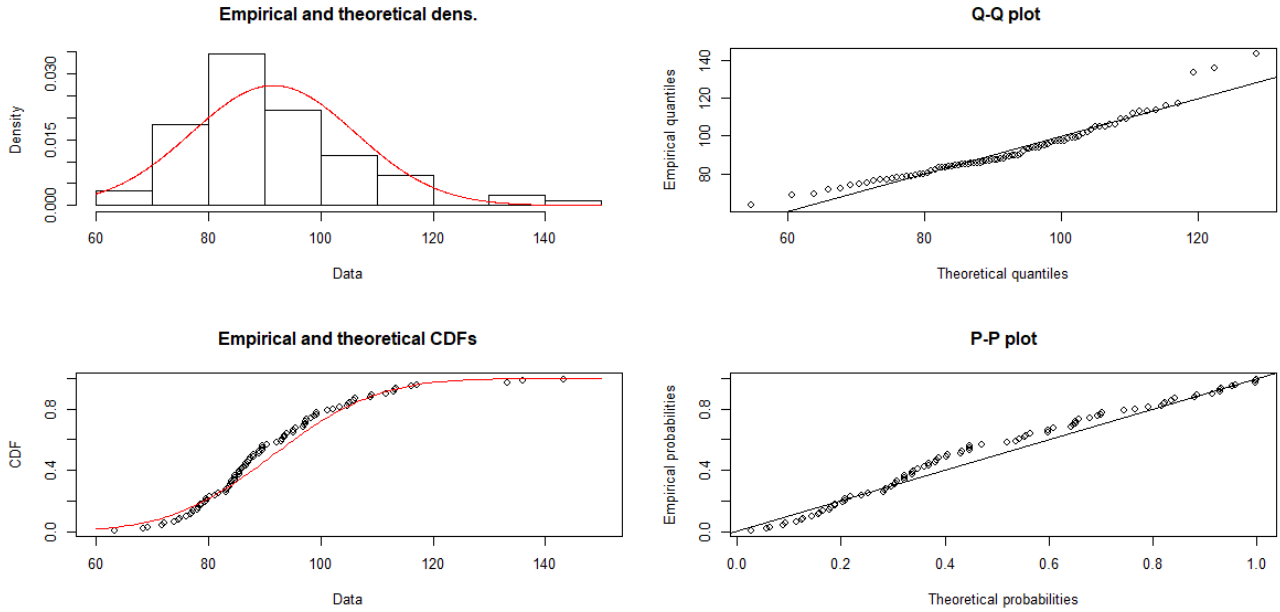
Empirical and theoretical dens.
Density
Data
Q-Q plot
Empirical quantiles
Theoretical quantiles
Empirical and theoretical CDFs
CDF
Data
P-P plot
Empirical probabilities
Theoretical probabilities

(c)

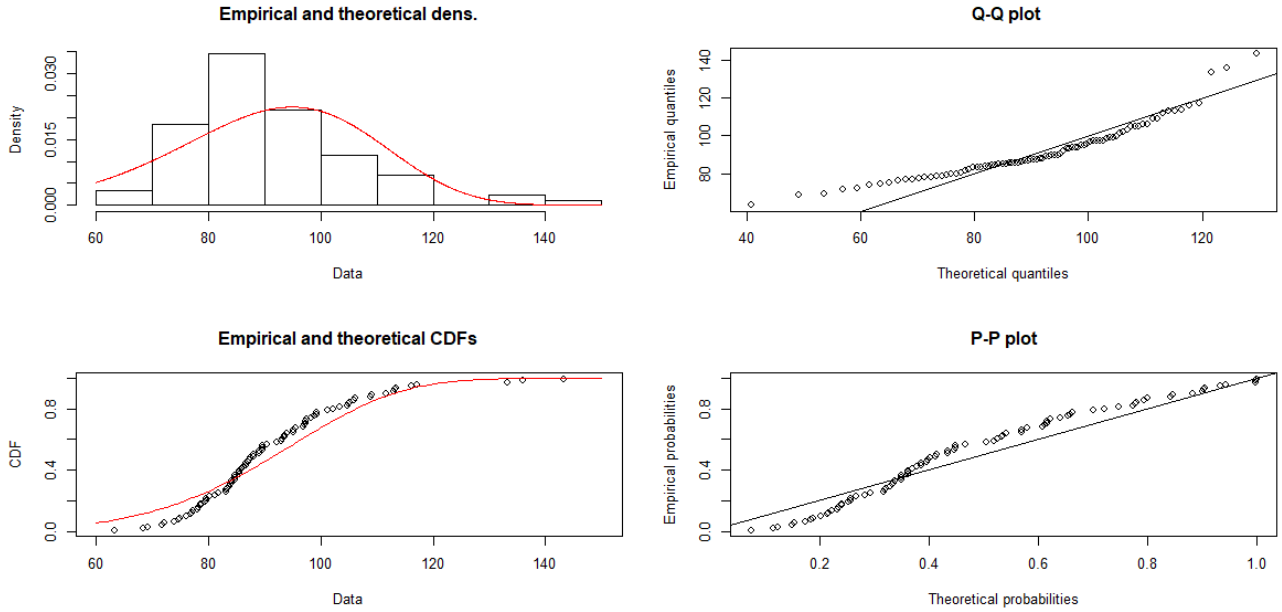

Fig. 1 – Illustrative comparison of three probability distribution functions and Q-Q and P-P plots for the Monday 15:20-15:35 group: (a) log-normal distribution (AIC 706.8), (b) normal distribution (AIC 717.3), (c) Weibull (AIC 735.2).

Based on the results in Tab. 2, there seems to be a trend where normal distribution performs best during the morning peak but after that, gamma or lognormal distribution take over as best fitting, on average. The exception seems to be Friday where gamma, and partially lognormal distribution have the best fit over the whole day. It is possible that this happens due to different patterns in the traffic flow during the morning peak which tends to happen more regularly for various reasons, most obviously due to schools starting at 8 am so parents driving their children always commute at the same time. Further, the capacity of road network may have played a role during certain times of day (especially the morning peak) and the effect would differ on different locations.

Theoretical arguments can be made for all the three distributions – central limit theorem might point to the normal distribution, while right-skewed, lower-bound data suggest lognormal or gamma distributions. However, as gamma distribution is the most flexible (it is in fact a whole family of distributions), it may be the most suitable candidate for modelling this variable. This is supported by the results, where it was almost always among the two best-fitting distributions.

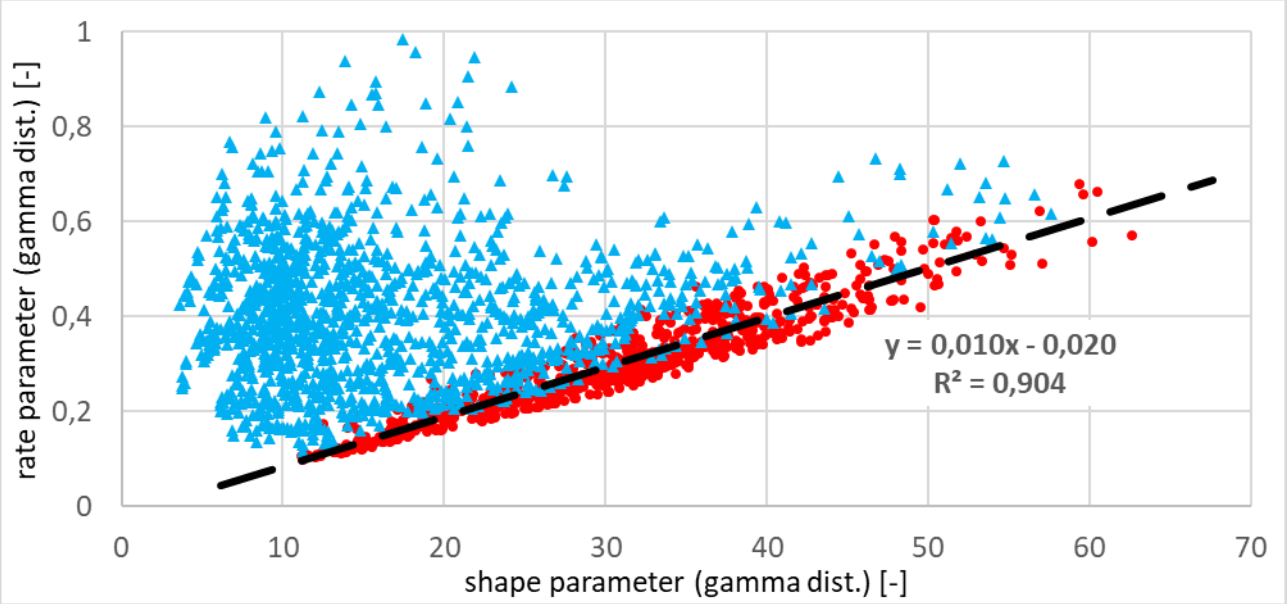

Fig. 2 – Relationship of the shape and rate parameters of gamma distribution. Red circles represent intervals on workdays from 8-18 hours, for completeness, weekends and night intervals are shown as blue triangles.

While understanding what distribution is suitable for modelling this type of data is important, it is only the starting point for any practical application. If there is a large set of historical traffic demand data, it can be used to fit a theoretical distribution to it and later the distribution can be used to generate traffic in a model. However, there is often not enough data (never in the case of manual traffic surveys) to do that. Thus, a generally acceptable model that could be used when only the estimated mean values are known is necessary for many practical applications. As the gamma distribution was regarded as most universal, it is a natural candidate for such a model. Moreover, as Figure 2 shows, there is even very strong corelation (R^2 = 0,904) between the two parameters of the distribution if only intervals with strong and regular traffic (workdays 8-18) are considered. Unfortunately, there is no meaningful way to connect the mean value of expected traffic demand to the shape or scale parameter of the gamma distribution, rendering the gamma distribution unusable if it is not possible to fit it to a large set of data. On the contrary, while it is possible to directly transform the mean expected traffic intensity to the mean of a lognormal distribution, there is much weaker correlation between the parameters of lognormal distribution. In fact, if only the intervals for workdays 8-18 are plotted, they form a circular shape with virtually no correlation.

As was shown earlier, the normal distribution is also a good candidate for modelling the variability and it has a strong benefit in that one of its parameters, the mean, is always known, or rather estimated with varying degree of certainty. Moreover, as Figure 3 shows, there is also fairly strong correlation (R^2=0,84) between the mean and standard deviation. Therefore, only knowing the mean expected TF intensity in any 5-minute interval of a day is sufficient to model its random fluctuations relatively accurately on day-to-day (or week-to-week, depending on the way the mean is calculated) basis.

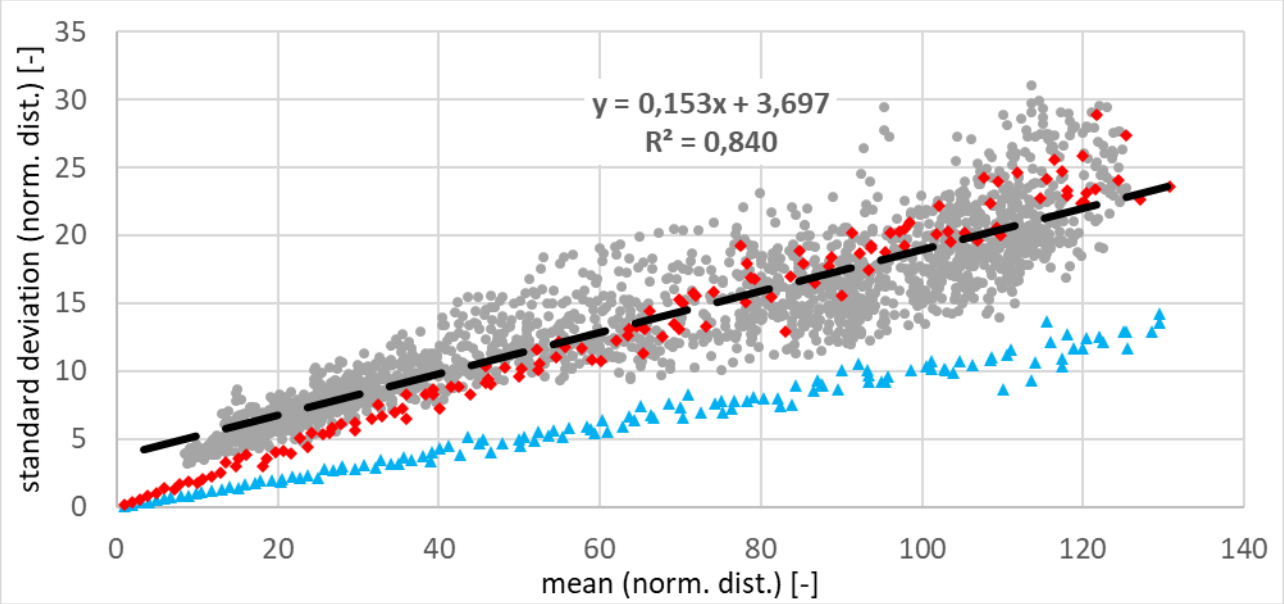

Fig. 3 – Relationship of the mean and standard deviation in grey circles (all 2016 datapoints), interpolated with a black line. For comparison, datapoints modelled based on the Brilon's approach [11] are shown: the original N~(1, 0.1) – blue triangles; modified N~(1, 0.2) red diamonds.

The standard deviation (SD) can be estimated as $3.7 + 0.153 \times \mu$, where μ is the mean expected TF intensity. Figure 3 also compares it to the model implemented by Brilon [11]. He originally used multiplicative coefficient from N~(1, 0.1), which is shown to greatly underestimate the actual variability of the traffic flow intensities, at least for 5-minute intervals. However, if the standard deviation of the random coefficient is increased to 0.2, the result is much closer to the data. The average SD seems to be very similar, but it is underestimated for low intensities and slightly overestimated for high intensities. Overall, the Brilon's modified approach with SD increased to 0.2 is very robust and simple and seems good enough to use if no better data is available. However, for situations similar to that for which this study was based upon (5-minute aggregation interval, motorway), the proposed model N~(μ, 3.7+0.153×μ) should provide more accurate results.

The whole concept discussed in this study is only concerned with the demand variability and assumes that the mean expected demand for given time/day is known with reasonable reliability and won't significantly change within the modelled timeframe. Any significant changes in the mean, such as long-term increase of traffic, new capacity restrictions, or possible detours, should be reflected by other means as they would be normally.

CONCLUSIONS

Based on the presented results, normal, lognormal, and gamma distribution all seem like good adepts for describing the inter-day variability of traffic flow at given time of day with quite similar counts of best fits among them with the other two usually not being statistically significantly worse. On the other hand, both Weibull and inverse Weibull distributions can be dismissed as potential candidates given the presented results. Two different approaches for modelling random day-to-day or week-to-week fluctuations in traffic demand are recommended for situations when only the mean expected values are known.

Based on the case study, the TF distribution seems quite variable during the week and perhaps no single theoretical distribution is perfect for describing it. Even larger data sample, different aggregation intervals, or involving some sort of time series in the modelling might help to bring more clarity in future studies. Further, similar experiments should be performed on various

locations and types of roads to see if the patterns would change with respect to the surrounding road network and its capacity.

ACKNOWLEDGEMENTS

This study was supported by Brno University of Technology from Junior specific research grant FAST-J-20-6145.

REFERENCES

[1] EDIP s.r.o. (2018). *Techical terms TP 189 - Determining traffic flow intensity on roads [in Czech]*. Czech Ministry of Transportation. http://www.pjpk.cz/data/USR_001_2_8_TP/TP_189_2018_final.pdf

[2] Polus, A., & Pollatschek, M. A. (2002). Stochastic nature of freeway capacity and its estimation. *Canadian Journal of Civil Engineering*, *29*(6), 842–852. https://doi.org/10.1139/l02-093

[3] Brilon, W., Geistefeldt, J., & Regler, M. (2005). Reliability of Freeway Traffic Flow: A stochastic Concept of Capacity. *Proceedings of the 16th International Symposium on Transportation and Traffic Theory*, 125–144. https://www.ruhr-uni-bochum.de/verkehrswesen/download/literatur/ISTTT16_Brilon_Geistefeldt_Regler_final_citation.pdf

[4] Lorenz, M. R., & Elefteriadou, L. (2001). Defining freeway capacity as function of breakdown probability. *Transportation Research Record*, *1776*, 43–51. https://doi.org/10.3141/1776-06

[5] Hall, F. L., & Agyemang-Duah, K. (1991). Freeway Capacity Drop and the Definition of Capacity. *Transportation Research Record*, *1320*, 91–98. http://onlinepubs.trb.org/Onlinepubs/trr/1991/1320/1320-012.pdf

[6] Zhang, L., & Levinson, D. (2004). Some properties of flows at freeway bottlenecks. *Transportation Research Record*, *1883*(1883), 122–131. https://doi.org/10.3141/1883-14

[7] Srivastava, A., & Geroliminis, N. (2013). Empirical observations of capacity drop in freeway merges with ramp control and integration in a first-order model. *Transportation Research Part C: Emerging Technologies*, *30*, 161–177. https://doi.org/10.1016/j.trc.2013.02.006

[8] G., M. M. (2007). The Four-Step Model. In D. A. Hensher & K. J. Button (Eds.), *Handbook of Transport Modelling* (Vol. 1, pp. 35–53). Emerald Group Publishing Limited. https://doi.org/10.1108/9780857245670-003

[9] Zhao, Y., Zhang, H., An, L., & Liu, Q. (2018). Improving the approaches of traffic demand forecasting in the big data era. *Cities*, *82*, 19–26. https://doi.org/https://doi.org/10.1016/j.cities.2018.04.015

[10] Alfa, A. S. (1986). A review of models for the temporal distribution of peak traffic demand. *Transportation Research Part B: Methodological*, *20*(6), 491–499. https://doi.org/https://doi.org/10.1016/0191-2615(86)90027-5

[11] Brilon, W., Geistefeldt, J., & Zurlinden, H. (2007). Implementing the concept of reliability for highway capacity analysis. *Transportation Research Record*, *2027*, 1–8. https://doi.org/10.3141/2027-01

CIVIL ENGINEERING JOURNAL

Article no. 49

THE CIVIL ENGINEERING JOURNAL 4-2022

INFLUENCE ANALYSIS OF NATURAL VIBRATION CHARACTERISTICS OF STEEL BOX GIRDER WITH SINGLE CABLE PLANE AND LARGE CANTILEVERS

Kexin Zhang, Xinyuan Shen, Jicheng Liu and Longsheng Bao

Shenyang Jianzhu University, School of Transportation and Geomatics Engineering, Shneyang, No.25 Hunnan Zhong Road, China; jt_zkx@sjzu.edu.cn, baolongsheng710605@163.com

ABSTRACT

In order to study the effect of cable damage on the self-vibration characteristics of steel box girder cable-stayed bridges with a single-cable plane and large cantilevers, a finite element model of the bridge was elaborated using the finite element software Midas/Civil to find out self-vibration characteristics of the cable-stayed bridge. The self-vibration characteristics of the bridge were also analysed for different damages to the cables and for different degrees of the damages to the cables. The structural health of a bridge can be diagnosed and assessed based on self-vibration characteristics of the studied structure.

KEYWORDS

Cable-stayed bridge, Natural vibration characteristics, Vibration mode, Steel box girder

INTRODUCTION

Steel box girder cable-stayed bridges with a single-cable plane and large cantilevers are composed of a composite girder, of a single tower and of stay cables arranged in one plane [1,2]. In order to increase the torsional and flexural capacity of the main girder and tower, main girder and pier are connected together [3-5]. The main girder is composed of stell box, cantilevers and the concrete deck, and the driving lanes are located on cantilevers. The main bridge design adopts a harp (parallel) system of stay cables with distinctive characteristics of the times [6-8]. The analysis of dynamic characteristics is the basis for the study of its dynamic behaviour – natural vibrations as well as dynamic response characteristics. Through the analysis of the self-vibration characteristics of the studied structure, a theoretical basis is provided for the future design of such structure. [9-12]. Ist natural-vibration characteristics determine its dynamic response characteristics. Through the analysis of the natural-vibration characteristics of the studied structure, a theoretical basis is provided for a future design of steel box girder cable-stayed bridges with a single stay cable plane and large cantilevers.

BACKGROUND

The cable stayed bridge is located in Fuyuan City, Heilongjiang Province. Its superstructure is 280 m long, with two spans of 140 m + 140 m and a width of 26.5 m. A longitudinal section of the bridge is shown in Figure 1 and a cross section is shown in Figure 2. The bridge deck is composed of a steel box girder, steel cantilevers and a concrete bridge deck. Carriageways are located on cantilevers on both sides of the structure. The steel box adopts single box and double chamber structure, and the steel cantilevers on the both sides are made as variable height I-girders. The cantilevers are made of Q370qE steel, the bridge deck is made of C50 concrete. The bridge tower

is a single column type with a height of 117 m. The part of the tower above the deck is made of C55 concrete and the part below the deck is made of C50 concrete. Stay cables are arranged in a harp shaped (parallel) system and are made of high-strength and low relaxation steel strands. Their characteristic tensile strength is 1860 MPa and the modulus of elasticity is 1.95×10^5 MPa. The cable spacing on the main girder is 9 m, and the anchorage spacing on the tower is 5.533 m - 5.606 m from the top to the bottom. There are 52 stay cables over the whole bridge, the shortest stay cable is 20.575 m long, and the longest stay cable is 147.651m long. The tower is made of C55 concrete. The section effect of the main girder is shown in Figure 3.

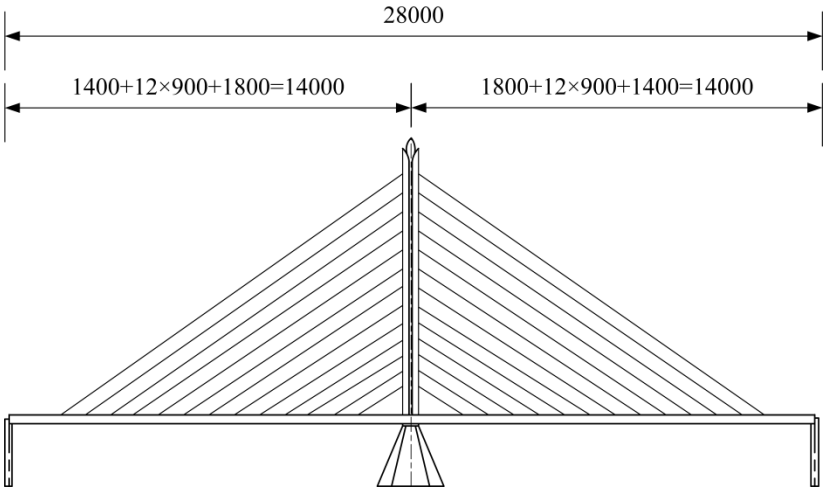

Fig. 1 – Elevation of the bridge

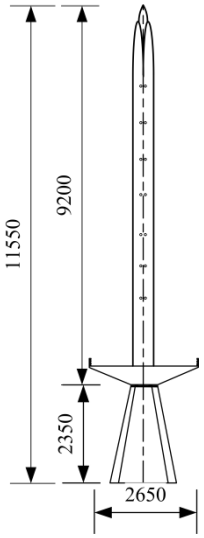

Fig. 2 – Cross section of the bridge

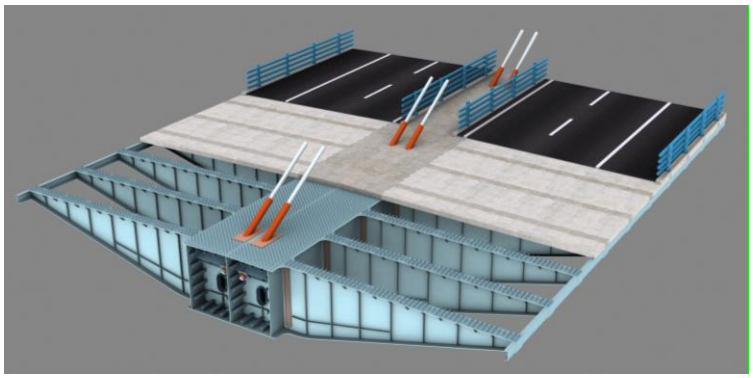

Fig. 3 – Section effect diagram of the main girder

To analyze dynamic characteristics of the bridge, a three-dimensional finite element model of the bridge was elaborated using the finite element analysis software Midas / Civil 2019. The main tower and main girder were simulated using beam units, and the tension cables were simulated using truss units. Totally, 798 beam units and 52 truss units were used. A rigid connection between the deck and the top part of the tower is simulated, stay cables are rigidly connected to the deck, as well as to the bridge tower. An overall view of the bridge finite element model is shown in Figure 4.

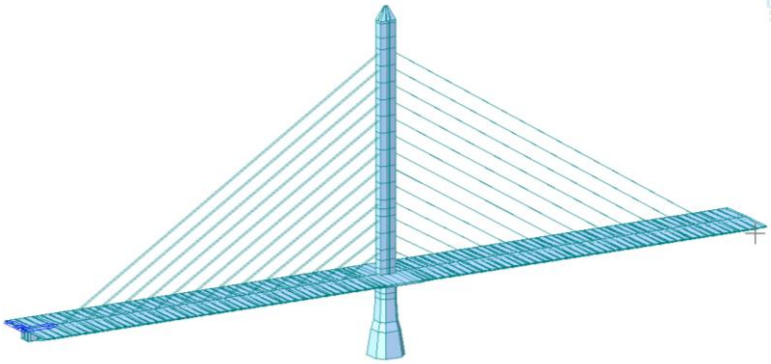

Fig. 4 – Bridge finite element model

ANALYSIS OF BRIDGE NATURAL VIBRATION CHARACTERISTICS

Modal analysis is an analysis method, which describes behaviour of the structure according to the inherent characteristics of the structure, mainly including frequency, damping and modal shape [13-15]. For this, it is necessary to determine natural frequencies and modes of the structure, because any structure has its own natural frequencies and corresponding modes of vibration, which are principal properties of the structure. The first 10 natural vibration modes of the studied structure are shown in Figure 5.

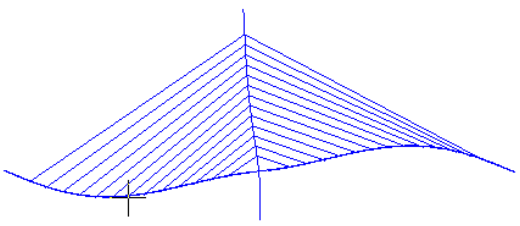

(a) – First order vibration mode (Beam vertical bending)

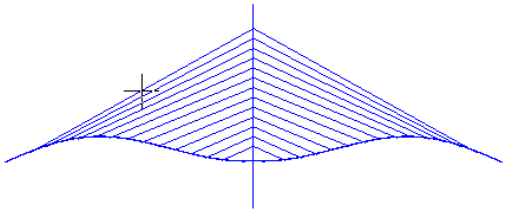

(b) – Second order vibration mode (Beam vertical bending)

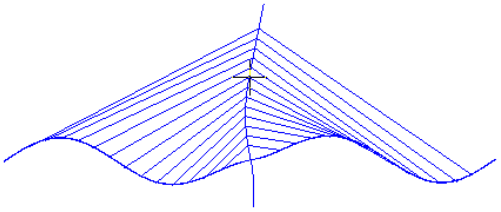

(c) – Third order vibration mode (Beam and tower vertical bending)

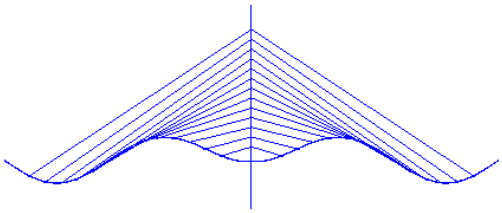

(d) – Fourth order vibration mode (Beam vertical bending)

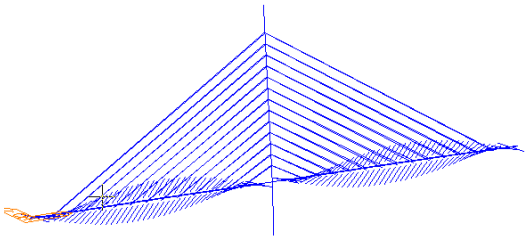

(e) – Fifth order vibration mode (torsion and lateral bending of the girder)

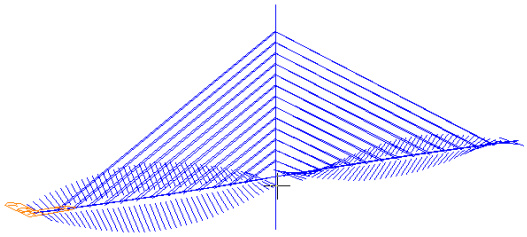

(f) –Sixth order vibration mode (Beam twist)

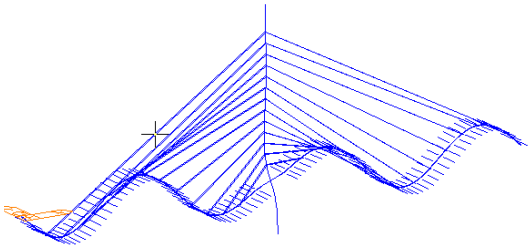

(g) – Seventh order vibration mode (Beam and tower vertical bending)

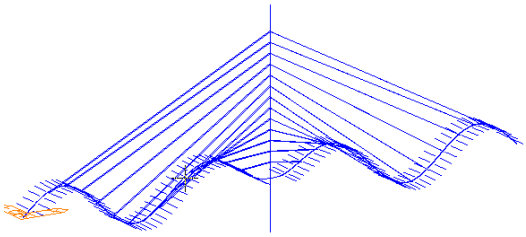

(h) – Eighth-order vibration mode (Beam vertical bending)

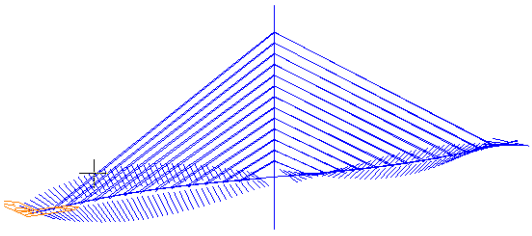

(i) – Ninth order vibration mode (Beam torsion and beam transverse bending)

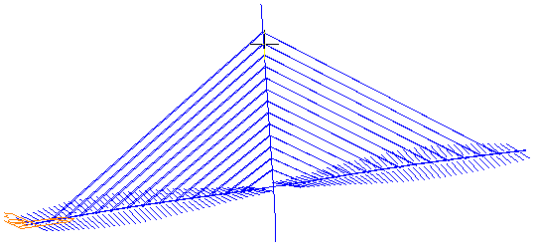

(j) – Tenth order vibration mode (Beam torsion and tower vertical bending)

Fig. 5 – Vibration modes of bridge

The first 10 natural periods and modes of the studied structure are shown in Table 1.

According to the calculation results in Table 1, the basic natural vibration period of the bridge is 1.85s (i.e. the corresponding frequency is 0,54 Hz). Generally, the basic natural vibration period of ordinary cable-stayed bridges is above 2s, while that of beam bridges is about 1s. It shows that the basic natural period of the studied structure is between the value of a continuous girder (rigid frame) and an ordinary cable-stayed bridge [16-17].

From the first 10 natural vibration modes of the model, it can be seen, that the vibration modes of the studied structure are dominated by vertical bending vibrations of the deck, which corresponds to the structural characteristics of a rigid deck and flexible stay cables. The vibration

behaviour of the studied structure is more similar to that of a continuous girder (rigid structure) and other girder bridges, unlike general cable-stayed bridges where the torsion of towers and cables is the main vibration pattern [18].

Tab.1 - Period and vibration pattern at each order of mode

Order	Period/s	Original Natural Frequency/Hz	Vibration patterns
1st	1.85	0.54	Vertical bending of deck
2nd	1.12	0.89	Vertical bending of deck
3rd	0.64	1.56	Vertical bending of deck + *longitudinal* bending of tower
4th	0.57	1.75	Vertical bending of deck
5th	0.36	2.73	Torsion and transverse bending of deck
6th	0.35	2.80	Torsion of deck
7th	0.34	2.93	Vertical bending of deck + *longitudinal* bending of tower
8th	0.31	3.17	Vertical bending of deck
9th	0.31	3.22	Torsion and transverse bending of deck
10th	0.25	3.88	Torsion of deck + lateral bending of tower

EFFECT OF DAMAGE TO ONE SIDE OF THE CABLE ON THE DYNAMIC CHARACTERISTICS

Effect of complete damage to the cables

In order to further understand the dynamic characteristics of the structure, it is necessary to consider the analysis of the factors influencing the dynamic characteristics of the bridge. The influence of a cable damage on natural vibration frequency of the bridge is studied. For a simulation of a cable damage, its modulus of elasticity was considered by the value of 1×10^{-5} MPa. The frequency change of the stay cable after a damage was calculated, while the frequency variation was = (frequency value after damage - frequency value without damage)/frequency value without damage. Some valuable conclusions can be drawn by comparing and analyzing the variation of natural vibration frequencies under various conditions.

There are 13 pairs of stay cables at each side of the tower of the bridge. The cables at each side of tower are numbered from short cables to long cables, S01 to S13 respectively. With S02 and S04 representing short cords, S06 and S08 representing medium cords, and S10 and S12 representing long cords, the frequency values and frequency variation values after damage are shown in Tables 2 and 3. The relationship between the order of different cables and the frequency variation is shown in Figure 6. It can be seen from Table 3 and Figure 5: when one side of a tension cable is completely damaged, the cable damage has a greater effect on the 2nd and 4th order frequency variation of the studied structure, in which the vertical deformation of the main beam occurs both in the 2nd and 4th order. A complete damage of a tension cable has a small effect on the stiffness of the main tower, so the frequency change of the main tower l*ongitudinal* bending modes is not significant and can be ignored. The frequency change curves of the second and fourth order of the main beam are shown in Figure 7 and Figure 8. The second order frequency curve of the main beam is a parabola shape with an upward opening. The minimum natural frequency is 0.86 Hz. The fourth order frequency curve of the main beam is W - shaped. The minimum natural vibration frequency is 1.72 Hz. The second order vertical bending frequency of the main deck decreases first and then rises, and the fourth order vertical bending frequency of

the main deck varies irregularly, while the frequencies of other modes almost do not change. Therefore, the cable damage has a certain effect on the vertical bending mode frequency of the deck.

Tab.2 - Frequency variations after damage of stay cables

Order	Original Natural Frequency/Hz	Frequency Variation after Cable Damage /Hz					
		S02	S04	S06	S08	S10	S12
1st	0.54	0.54	0.54	0.54	0.54	0.54	0.54
2nd	0.89	0.88	0.88	0.87	0.87	0.87	0.88
3rd	1.56	1.55	1.55	1.55	1.55	1.55	1.55
4th	1.75	1.73	1.73	1.74	1.75	1.74	1.74
5th	2.73	2.73	2.73	2.73	2.73	2.73	2.73
6th	2.80	2.80	2.80	2.80	2.80	2.80	2.80
7th	2.93	2.93	2.93	2.92	2.92	2.92	2.93
8th	3.17	3.17	3.17	3.17	3.17	3.17	3.17
9th	3.22	3.22	3.22	3.22	3.22	3.22	3.22
10th	3.88	3.88	3.88	3.88	3.88	3.88	3.88

Tab.3 - Proportional change of frequency after damage of stay cables

Order	Proportional change of frequency/%					
	S02	S04	S06	S08	S10	S12
1st	-0.09	-0.4	-0.67	-0.49	-0.03	-0.53
2nd	-0.21	-1.09	-2.2	-2.64	-1.99	-0.72
3rd	-0.35	-0.55	-0.1	-0.07	-0.35	-0.12
4th	-0.62	-1.19	-0.56	0	-0.32	-0.36
5th	0	0	0	0	0	0
6th	0	0	0	0	0	0
7th	-0.16	0	-0.34	-0.32	0	-0.06
8th	-0.46	-1.09	-0.05	-0.16	0	-0.12
9th	0	0	0	0	0	0
10th	0	0	0	0	0	0

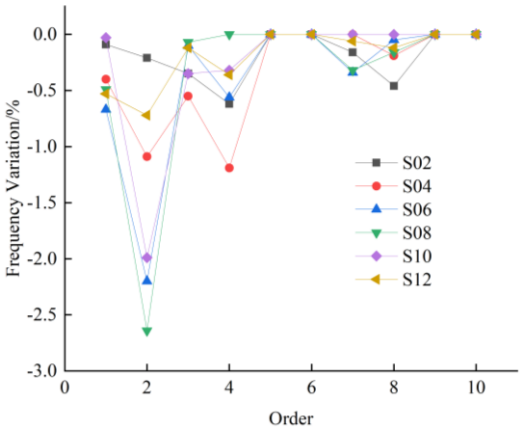

Fig.6 - Relationship between the order variation

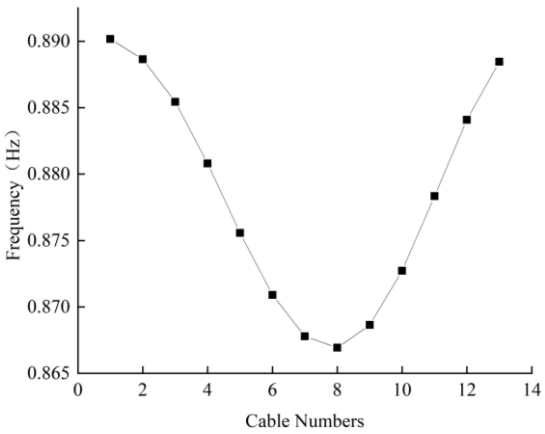

Fig.7 - Natural frequency of deck and frequency with a damaged stay cable – 2nd order

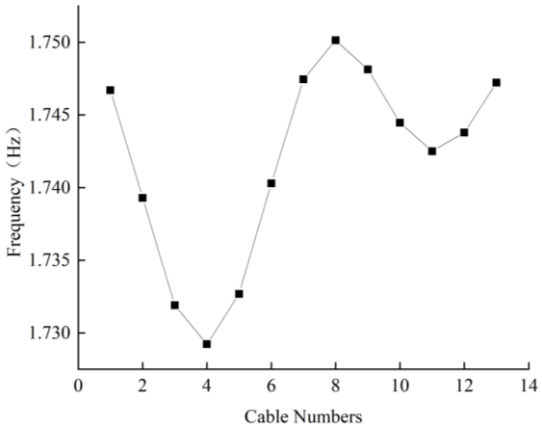

Fig.8 - Natural frequency of deck with a damaged stay cable – 4th order

Influence of different elastic modulus of cable

In order to investigate the effect of different degrees of damage to stay cables at one side of the tower on natural frequencies of the bridge, three different lengths of stay cables are analyzed. Three S03, S04 and S05 are taken as representatives of short cables, three S07, S08 and S09 are taken as representatives of medium and long cables, and three S11, S12 and S13 are taken as representatives of long cables. In order to further study the influence of the elastic modulus of the cable on natural vibration frequencies of the cable-stayed bridge, calculations were made with an elastic modulus ratio of 0.25-1 for each order, so the elastic modulus values were 1.95×10^5, 1.4625×10^5, 0.975×10^5, and 1×10^{-5} MPa, respectively.

Figure 9, Figure 10 and Figure 11 show the relationship between frequency and order for a damage to a short cable, middle cable and long cable. See Figure 12, Figure 13 and Figure 14 for frequency variation curves of S04, S08 and S12 cables. Figures 9 and 12 show that the frequency proportional change of the main beam increases with the increase of a cable damage. When the damage of cable S04 is from 25% to 100%, the change of a vertical bending frequency of the beam increases by 0.55%, which is mainly reflected in the third order. The frequency variation of vertical bending increases by 1.19%, which is mainly reflected in the first, second, fourth and eighth orders. The second and fourth order frequency changes are more significant than the first, third and eighth order frequency changes. Therefore, a cable damage has a great influence on the frequency of the vertical bending mode of the main beam.

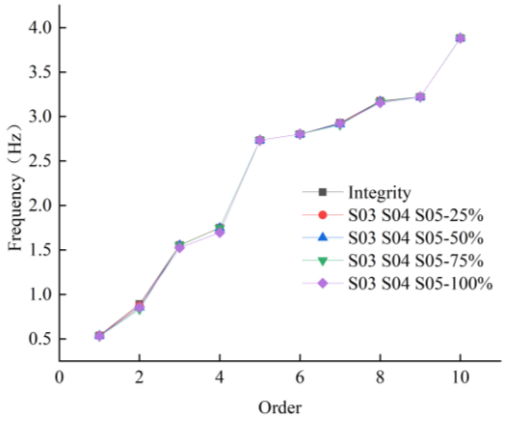

Fig.9 - Relationship between frequency and order for damaged cables S03, S04, S05

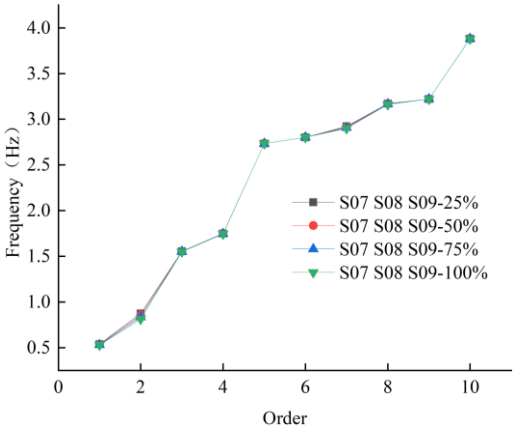

Fig.10 - Relationship between frequency and order for damaged cables S07, S08, S09

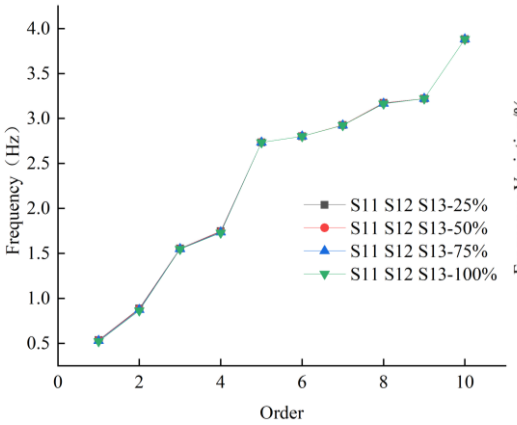

Fig.11 - Relationship between frequency and order for damaged cables S12, S12, S13

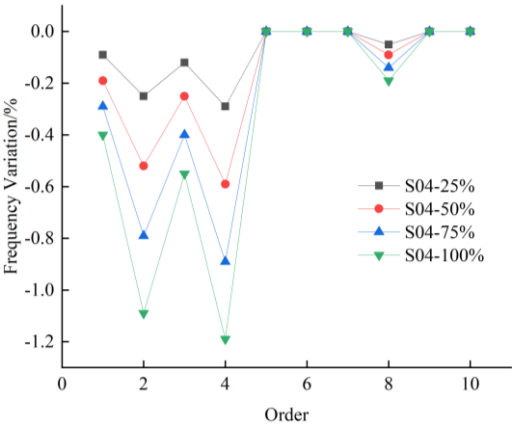

Fig.12 - Curve of frequency change for damaged cable S04

According to Figure 10 and 13, when a damage of S08 cable is from 25% to 100%, the variation of the deck vertical bending frequency increases by 2.64%. The effect is concentrated in the main girder 2nd order vertical bending vibration type. The increase of a cable damage has little influence on the stiffness of the tower, so frequencies of the vertical bending modes of the tower do not change much and can be ignored.

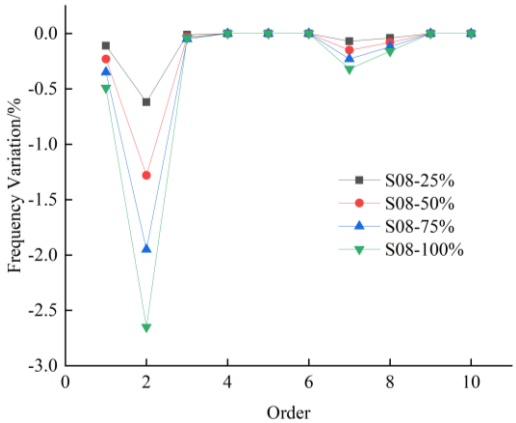

Fig.13 - Curve of frequency change for damaged cable S08

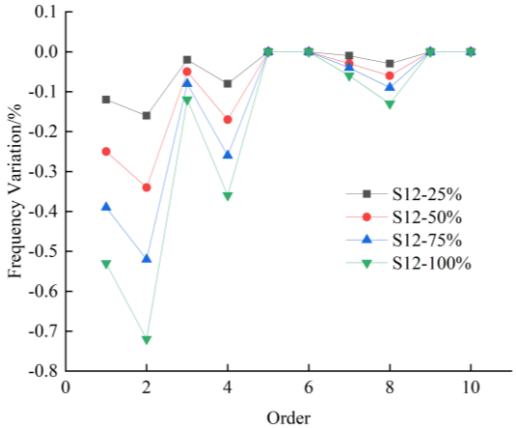

Fig.14 - Curve of frequency change for damaged cable S12

From Figure 11 and Figure 14 can be seen: when a damage of S12 cable is from 25% to 100%, the damage is concentrated in the main beam 1, 2, 4 and 8 stages of vertical bending vibration, for beam transverse bending vibration and tower transverse bending vibration almost no effect. With the increase of cable damage ratio, the first order proportional change of frequency of cable S12 increased by 0.53%, the second order proportional change of frequency increased by 0.72%, the fourth order proportional change of frequency increased by 0.36%, and the eighth order proportional change of frequency increased by 0.12%. Therefore, the cable damage has a certain effect on the frequency of the vertical bending mode of deck.

ANALYSIS OF THE EFFECT OF DAMAGE TO THE TENSION CABLES ON BOTH SIDES OF THE TOWER ON NATURAL -VIBRATION CHARACTERISTICS OF THE CABLE-STAYED BRIDGE

Influence of complete failure of a cable

There are 26 stay cables on both sides of the tower. The cables onboth sides of the tower are numbered from short cables to long cables, D01 ~ D13. D03, D04, D05 for short cables, D07, D08, D09 for medium cables, D11, D12, D13 for long cables. For damaged stay cables, modulus of elasticity considered is 1×10^{-5} MPa. The frequency values and frequency variation values after the damage are shown in Table 4 and Table 5. The relationship between frequency proportional change and order for a damaged cable is shown in Figure 15. It can be seen from Table 5 and Figure 15 that when the cables on the both sides are completely damaged, the cable damage has a great influence on the frequency amplitude of the order 1, 2 and 4 of the studied structure, and the vertical deformation of the main beam occurs at the order 1, 2 and 4. The first, second and fourth order frequency variation curves of the main beam are shown in Figure 16, 17 and 18. The first order frequency curve of the main beam changes irregularly. The minimum frequency of natural vibration occurs under a damage of the long cable D13, which is 0.51 Hz. The second order frequency curve of the main beam is a parabola shape with an upward opening. The minimum value of natural vibration frequency appears in the middle cable D08, which is 0.84Hz. The fourth order frequency curve of the main beam is W - shaped. The minimum natural frequency appears on the short cable D04, which is 1.70 Hz. The change rate of cable D08 is 5.13%.The second order frequency of the main beam decreases first and then rises, and the vertical bending mode frequency of the main beam is significantly affected by the cable damage, so the cable damage has a certain influence on the vertical bending mode frequency of the deck.

Tab.4 - Frequency under cable damage

Order	Original Natural Frequency/Hz	Frequency Variation after Cable Damage /Hz					
		D02	D04	D06	D08	D10	D12
1st	0.54	0.54	0.53	0.53	0.53	0.54	0.53
2nd	0.89	0.89	0.87	0.85	0.84	0.86	0.88
3rd	1.56	1.54	1.54	1.55	1.55	1.54	1.55
4th	1.75	1.73	1.71	1.73	1.75	1.74	1.74
5th	2.73	2.73	2.73	2.73	2.73	2.73	2.73
6th	2.80	2.80	2.80	2.80	2.80	2.80	2.80
7th	2.93	2.92	2.93	2.91	2.91	2.93	2.92
8th	3.17	3.15	3.16	3.17	3.16	3.17	3.17
9th	3.22	3.22	3.22	3.22	3.22	3.22	3.22
10th	3.88	3.88	3.88	3.88	3.88	3.88	3.88

Tab.5 - Frequency variation

Order	Frequency variation /%					
	D02	D04	D06	D08	D10	D12
1st	-0.18	-0.8	-1.31	-0.96	-0.06	-1.16
2nd	-0.41	-2.16	-4.33	-5.13	-3.79	-1.33
3rd	-0.69	-1.04	-0.21	-0.15	-0.73	-0.25
4th	-1.25	-2.39	-1.06	0	-0.61	-0.66
5th	0	-0.01	-0.01	-0.01	0	0
6th	0	-0.01	-0.01	-0.01	0	0
7th	-0.32	0	-0.72	-0.66	0	-0.13
8th	-0.92	-0.36	-0.11	-0.32	0	-0.23
9th	0	0	0	0	0	0
10th	0	0	0	0	0	0

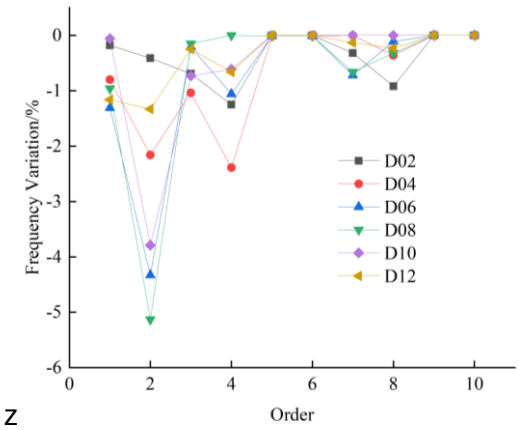

z

Fig.15 - The relation between frequency variation and order

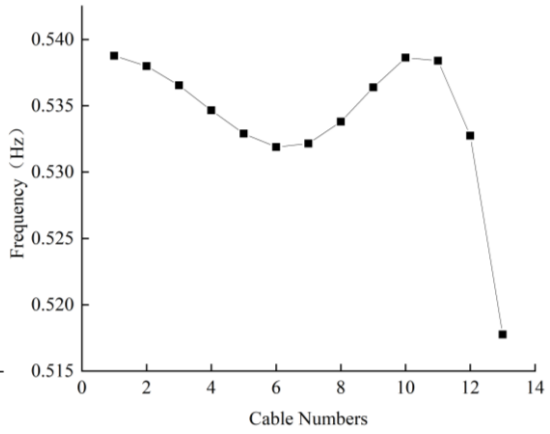

Fig.16 - First order frequency curve of main deck for damaged cable

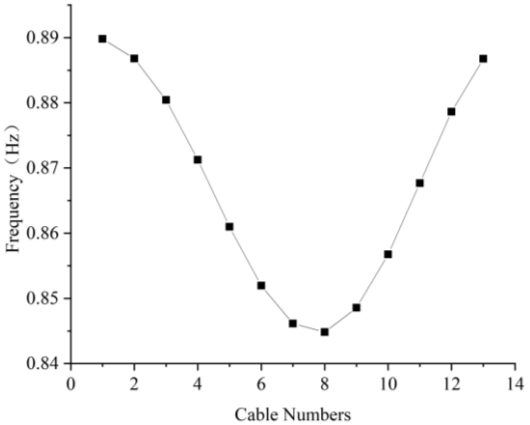

Fig.17 - Second order frequency curve of main deck for damaged cable

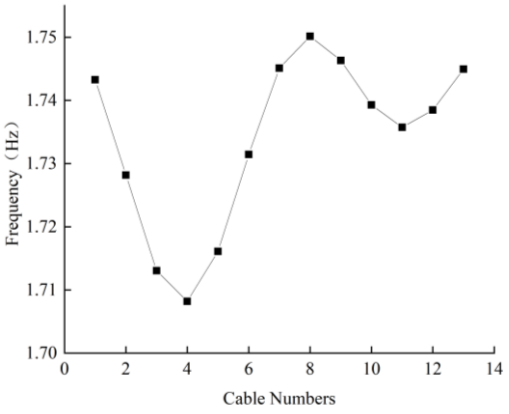

Fig.18 - Fourth order frequency curve of main deck for damaged cable

Influence of different elastic modulus of a cable

In order to explore the influence of different damage degrees of stay cables on both sides of the tower on the natural vibration frequency of the bridge, the damage of three different lengths of

stay cables are analyzed respectively. Three D03, D04 and D05 are taken as representatives of short cables, three D07, D08 and D09 are taken as representatives of medium and long cables, and three D11, D12 and D13 are taken as representatives of long cables. The elastic modulus of the cables was 1.95×10^5, 1.4625×10^5, 0.975×10^5 and 1×10^{-5} MPa, respectively.

Figure 19, Figure 20 and Figure 21 show the frequency values for damaged short cables, middle cables and long cables under different damage degrees. The proportional frequency change curves for damaged cables D04, D08 and D12 cables are shown in Figure 22, 23 and 24. It can be seen from Figure 19 and Figure 22 that the damage of short cables is mainly reflected in the beam vertical bending mode (the 1st, 2nd, 4th and 8th modes) and beam tower *longitudinal* bending mode (the 3rd mode), in which the 2nd and 4th frequencies are more obvious than the 1st, 3rd and 8th frequencies.

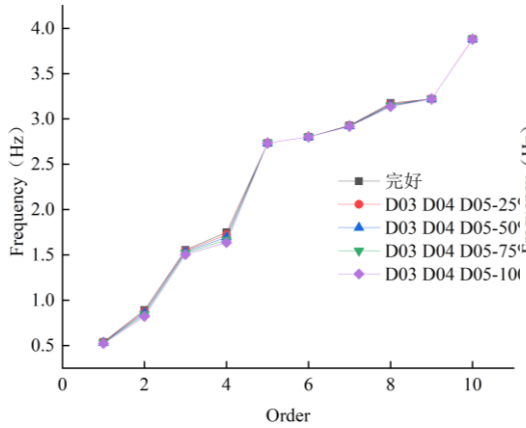

Fig.19 - Relationship between frequency and order for damaged cables D03, D04, D05

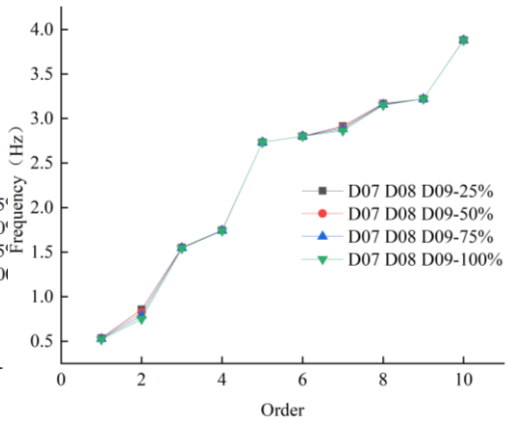

Fig.20 - Relationship between frequency and order for damaged cables D07、D08、D09

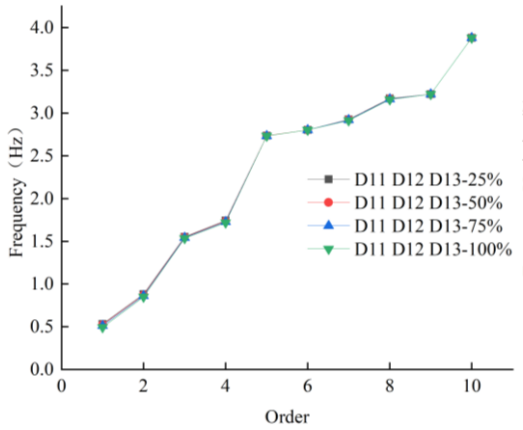

Fig. 21 - Relationship between frequency and order for damaged cables D03, D04, D05

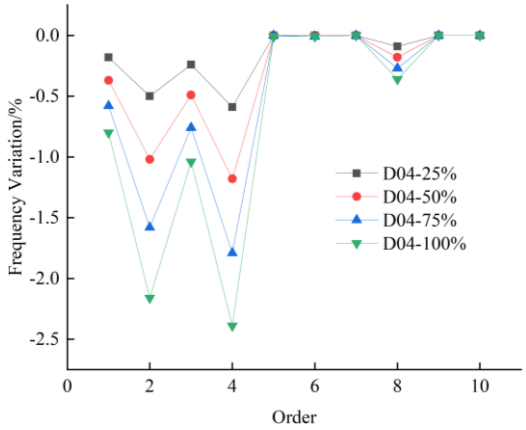

Fig. 22 - Curve of frequency proportional change of for damaged cable D04

From Figure 20 and Figure 23, it can be seen that: the frequency values of different degrees of damage in the cable show regular changes, and the damage is concentrated in the beam vertical bending vibration (1st and 2nd order vibration) and beam vertical bending and tower vertical bending vibration (7th order vibration), where the 2nd order frequency variation is more significant than the 1st and 7th order frequency variation, and with the increase of the degree of damage, the frequency variation is more and more significant. There is almost no effect on the beam and tower transverse bending vibration.

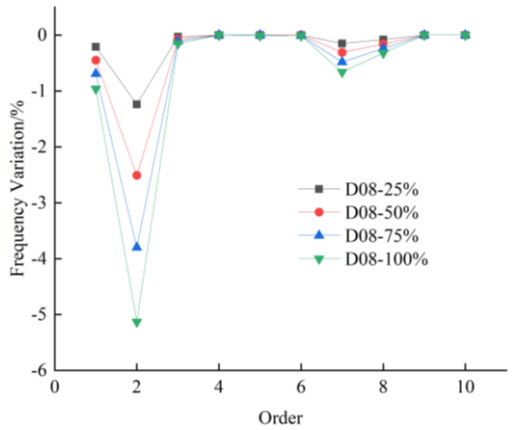

Fig.23 - Curve of frequency proportional change for damaged cable D08

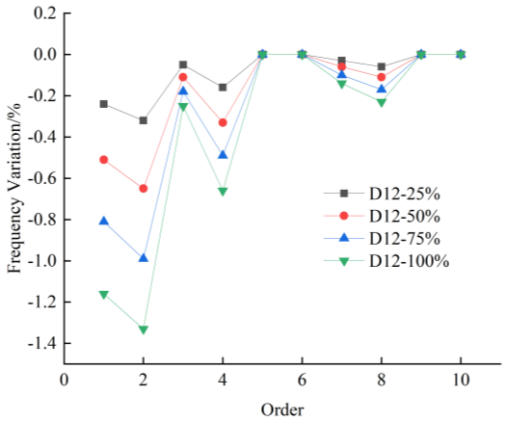

Fig.24 - Curve of frequency proportional change for damaged cable D12

From Figure 21 and Figure 24, it can be seen that the frequency values with different degrees of damage of long cables show regular changes, and the damage is concentrated in the beam vertical bending vibration (1st, 2nd, 4th and 8th order vibration) and the beam vertical bending and tower vertical bending vibration (3rd and 7th order vibration), where the 1st and 2nd order frequency variation is more obvious than the 3rd, 4th, 7th and 8th order frequency variation, and the frequency variation is increasing with the increase of the degree of damage The proportional changes of the 1st and 2nd order frequencies are more obvious than the 3rd, 4th, 7th and 8th order frequencies.

CONCLUSION

This paper analyses natural vibration characteristics of a steel box girder cable-stayed bridge with a single-cable plane and large cantilevers, and studies the influence of various stay cable damages on natural vibration characteristics of the bridge, including the effects of different degree of such damages at one side as well as on the both sides of the tower, which can diagnose and evaluate the health condition of such bridges, which was shown by the results of this research.

(1) The bridge has no main girder torsional vibration type in the first 4- orders, because the main girder is a steel box combined with large cantilevers, the steel box girder size is relatively small, and the stay cables are arranged in the central cable plane, which causes, that the main girder of the studied structure has large torsional stiffness and good resistance to torsional deformation.

(2) The tower side and both sides of the damage cable with the increase in number, the main beam 2nd order vertical bending and main beam 4th order vertical bending frequency variation effect is larger. Main beam 2nd order vertical bending self-oscillation frequency is open upward parabolic change, S08 and D08 cable damage, main beam 2nd order vertical bending self-oscillation frequency is the smallest; Main beam 4th order vertical bending self-oscillation frequency is irregular change, S04 and D08 order main beam vertical bending frequency is the smallest. The second order vertical bending frequency of the main deck decreases first and then rises, and the fourth order vertical bending frequency of the main deck varies irregularly, while the frequencies of other modes almost do not change. Therefore, the cable damage has a certain effect on the vertical bending mode frequency of the deck.

(3) For a short cable at one side as well as at both sides of the tower with different degrees of damage, the damage is concentrated in 1st, 2nd, 4th and 8th order, where the vertical bending modes of the main deck are generated. For beam transverse bending and torsional vibrations almost no effect. With the increase of cable damage ratio, the first order proportional change of frequency of cable S12 increased by 0.53%, the second order proportional change of frequency

increased by 0.72%, the fourth order proportional change of frequency increased by 0.36%, and the eighth order proportional change of frequency increased by 0.12%. Therefore, the cable damage has a certain effect on the frequency of the vertical bending mode of deck.

REFERENCES

[1] Jang, S. , Jo, H. , Cho, S. , Mechitov, K. , Rice, J. A. , & Sim, S. H. , et al. 2010. Structural health monitoring of a cable stayed bridge using smart sensor technology: deployment and evaluation. smart struct syst 6(5-6):439-459. Smart Structures & Systems, 6(5_6), 439-459.

[2] Cho, S. , Park, J. , Jung, H. , Yun, C. , & Seo, J. . 2010. Structural health monitoring of a cable-stayed bridge using acceleration data via wireless smart sensor network.

[3] Ju, Y. Z. , Liu, W. C. , Bai, J. F. , & Chen, J. H. . 2010. Nonlinear static analysis of cable-stayed bridge. IEEE.

[4] Tang, E. , & Hong, H. . 2010. Numerical simulation of a cable-stayed bridge response to blast loads, part i: model development and response calculations. Engineering Structures, 32(10), 3180-3192.

[5] Hong, H. , & Tang, E. . 2010. Numerical simulation of a cable-stayed bridge response to blast loads, part ii: damage prediction and frp strengthening. Engineering Structures, 32(10), 3193-3205.

[6] Yao, C. Y. , Pu, Q. H. , & Yao, Y. D. . 2014. Mechanical features of cable-girder anchorage for long-span railway cable-stayed bridge with steel box girders. Applied Mechanics & Materials, 587-589, 1391-1394.

[7] Jo, H. , Sim, S. H. , Mechitov, K. A. , Kim, R. , Li, J. , & Moinzadeh, P. , et al. 2011. Hybrid wireless smart sensor network for full-scale structural health monitoring of a cable-stayed bridge. Proceedings of Spie the International Society for Optical Engineering, 7981, 798105-798105-15.

[8] Hou, S. B. , Amp, X. R. , & Corporation, B. C. . 2014. Mechanical analysis on large-span cable-stayed bridge under moving load. Transportation Standardization.

[9] Xu, F. , Wang, X. , & Wu, H. . 2012. Inspection method of cable-stayed bridge using magnetic flux leakage detection: principle, sensor design, and signal processing. Journal of Mechanical Science and Technology, 26(3), 661-669.

[10] Park, J. W. , Jung, H. J. , Jo, H. , & Spencer, B. F. . 2012. Feasibility study of micro-wind turbines for powering wireless sensors on a cable-stayed bridge. Energies, 5(12), 3450-3464.

[11] Dai, Gong-lian, YAN, & Bin, et al. 2012. Longitudinal forces of continuously welded track on high-speed railway cable-stayed bridge considering impact of adjacent bridges. Journal of Central South University.

[12] Ho, D. D. , Lee, P. Y. , Nguyen, K. D. , Hong, D. S. , Lee, S. Y. , & Kim, J. T. , et al. 2012. Solar-powered multi-scale sensor node on imote2 platform for hybrid shm in cable-stayed bridge. Smart Structures & Systems, 9(2), 145-164.

[13] Hikami, Y. . 2010. Rain vibrations of cables in cable-stayed bridge. Journal of Wind Engineering, 1986(27), 17-28.

[14] Loh, C. H. , & Chang, C. M. . 2010. Vibration control assessment of asce benchmark model of cable‐stayed bridge. Structural Control & Health Monitoring, 13(4), 825-848.

[15] Cho, S. , Jang, S. A. , Jo, H. , Mechitov, K. , & Seo, J. . 2010. Structural health monitoring system of a cable-stayed bridge using a dense array of scalable smart sensor network. Proceedings of SPIE [16] The International Society for Optical Engineering.

[16] Wickramasinghe, W. R. , Thambiratnam, D. P. , Chan, T. H. , & Nguyen, T. 2016. Vibration characteristics and damage detection in a suspension bridge. Journal of Sound and Vibration, 375, 254-274.

[17] Zhang, K. , Qi, T., Xue, X., Zhu, Z., & Sun, Q. 2020. Study on the influence of cable/sling damage on thenatural vibration characteristics of special-shaped-stayed arch bridge without back cable .Civil Engineering Journal, (4).

[18] Zeng, Y. , Zheng, H., Jiang, Y., Ran, J., & He, X. 2022. Modal analysis of a steel truss girder cable-stayed bridge with single tower and single cable plane. Applied Sciences,12(15), 7627.